

THE EQUIVALENT WAVEFIELD
CONCEPT IN MULTICHANNEL
TRANSIENT ELECTROMAGNETIC
SURVEYING

ANDREW J. S. WILSON

THESIS SUBMITTED FOR THE DEGREE OF
DOCTOR OF PHILOSOPHY

UNIVERSITY OF EDINBURGH

1997



This thesis has been composed by myself and has not been submitted in any previous application for a degree. Except where stated to the contrary, the work reported within was executed by myself.

Andrew JS Wilson

Andrew J S Wilson

1997.

*We shall not cease from exploration
And the end of all our exploring
Will be to arrive where we started
And know the place for the first time*

T.S.Eliot

This thesis is dedicated to Gillian who,
knowing I was a slow and clumsy explorer,
chose anyway to be my companion.

Abstract

The equivalent wavefield concept relates diffusive electromagnetic propagation to non-diffusive propagation, provided equivalent source and boundary conditions are satisfied. This well-known concept is a special case of a more general theorem, proven here, relating the solutions of two systems of partial differential equations that have the same spatial, but different temporal derivatives. In the case we consider, the velocity of the equivalent wavefield is proportional to the square root of the resistivity of the diffusive electromagnetic medium. The use of the concept has two advantages: first, analytical results may be derived more easily in the equivalent wavefield domain; second, interpretation of data is easier after mapping to the equivalent wavefield domain.

In general, electromagnetic fields have an irrotational component that is equivalent to P-wave propagation, and a solenoidal component that is equivalent to S-wave propagation. Using a moment tensor and a dipole moment to represent electromagnetic dipole sources allows comparison with seismic sources. For example, the equivalent wavefield of the magnetic field generated by an electric current dipole in a whole space is generated by a point source of torque, generating shear waves only.

The electric field generated by a switch-off electric current dipole at the surface of a half-space has an equivalent wavefield at the interface equal to a triangle with origin at the switch-off time, peak at the arrival time and zero thereafter. When graphed as a function of space versus time, arrivals in the equivalent wavefield lie on straight lines and can be interpreted using straightforward concepts from the seismic refraction method.

Diffusive to propagative mapping of numerical data requires regularisation to stabilise whatever numerical inversion procedure is used. Approaches include matrix inversion and a new algorithm which uses deconvolution in log time. The latter approach is computationally inexpensive and permits analysis of the distortion of the recovered waveform which is caused by regularisation. Both approaches successfully extract several arrivals when these are well-resolved in the original diffusive synthetic. Diffusive to propagative mapping applied to synthetic electromagnetic responses calculated for a horizontal electric current dipole source over a uniform half-space or simple layered-Earth models yields equivalent wavefields which are interpretable after calibration for waveform regularisation.

Acknowledgements

There are some things which I am probably not very good at, and there are also some things which I am definitely very bad at. Letting people know how much I appreciate them falls into the second category, so I would like to take this opportunity to catch up on some long overdue *thank-yous* to some of the many people without whom I would never have started, let alone finished, this thesis.

Let me begin with those who helped me arrive in a position to start this thesis. During my time as an undergraduate many lecturers and tutors patiently tried to transfer information into my brain. I thank all of them, but I would especially like to thank those who stimulated and nurtured my interest in computational science and in particular Derek Arthur, Douglas Heggie, Ken McKinnon and John Martin. Richard Kenway deserves a special mention; he forgave me for spurning a physics degree and allowed an interloper from mathematics to attend his scientific computing course. Allan Sinclair took a personal interest in my well being and gave me encouragement, advice and eventually the chiding to get started on a PhD.

I owe a debt of thanks to Neil Carmichael for finding the time to interview me (twice) and the scholarship money to support me during my first summer at Edinburgh Parallel Computing Centre (EPCC). During that formative summer Mikeee Norman gave up time from his own work to give Hamish Mills and I a crash-course introduction to doing science on the much-beloved ECS (a transputer-based Meiko supercomputer). At the end of that summer EPCC employed me full-time and over the following two years I was privileged to work on a series of projects for Dick Dalley and Phil Nelson. At EPCC I was educated, stimulated and given room to stretch myself despite the inevitability that some of my learning would be done by making mistakes. I was given some great partners in crime, including Neil Wilson, Tim Harding and Ian Flockhart. During those years I was coached by Kevin Collins, Neil Heywood, Nick Radcliffe and ‘Uncle’ David Wallace who *still* has twice as much energy and enthusiasm as anyone else. Just as I was approaching the point where I could actually do some useful work, they were generous enough to help me realise my ambition to study for a PhD, even though this meant me leaving EPCC.

During much of the preparation of this thesis I was supported by the European Community THERMIE research project *Determination of Reservoir Fluid Content by Combined use of Seismic and Transient Electromagnetic Methods* grant number OG/0305/92/NL-UK and Elf

Enterprise Caledonia contract number CA5527. This exceptional project gave motivation, focus and constructive criticism which immeasurably improved the work in this thesis. I am indebted to Professor Anton Ziolkowski, the leader of the project, and to Dr Bruce Hobbs for their supervision, assistance and advice. The Edinburgh team was later joined by Dave Sharrock who forgave my coding style and evolving notation and finally Ian Chisholm to whom I must stop apologising.

This project would not have been possible without collaborating partners at Compagnie Générale de Géophysique, DeutscheMontanTechnologie, HarbourDom Consulting and The University of Köln. Many people in all of these organisations gave me help and encouragement throughout the project. Pierre Andrieux and Horst Ruter gave me encouragement and constructive criticism which helped shape up my ideas. Special thanks go to Andreas Hördt, who risked his sleeping bag, and Ole Engels who risked his beautiful flat. Andreas and Ole, together with Stefan Bauer and Stefan Helwig, took me into their gîte and under their wing during field operations. Together they initiated me in TEM acquisition and I will always be indebted to them for their patient efforts to make me a part of the team despite my total lack of experience. Special thanks also to Keeva Vozoff for sharing his experience, his whisky and his house in Köln; and to Liz for keeping Keeva in check.

Jean-Claude Ghillon of Elf gave not only his support but also focused our direction and sharpened up our presentations. The help of Gaz de France in planning and carrying out the field operations was invaluable. The cooperation of the Research and Development team in charge of the field site, headed by Frederic Huguet and from the management of the production unit, headed by M. Laroche was vital in ensuring the smooth and efficient running of the survey.

During my time at The Department of Geology and Geophysics at The University of Edinburgh many office-mates suffered my quirks with good humour, including Paul Caban, Rodney Johnston, Beatriz Ortega, Johann Raith, Milos Savic, Ian Sharp and Sergei Zatsepin. As an interloper from another discipline joining a large department midway through term, I was apprehensive. I needn't have been since I found a friendly atmosphere, and many friends willing to act as walking, talking encyclopedic dictionaries. They know who they all are which is as well since there is no space to name them all here, but I owe a special mention to Roger Banks for his sage advice and to Mark Higgins who lent energy and enthusiasm, was never more than 18 hours late, and along with David Bailey, Clare Peters and Olga Savasta gave helpful comments on various parts of this thesis.

This thesis was completed while I was employed by Edinburgh Parallel Computing Centre (EPCC). Thanks to Arthur for his patience and to the thesis police, Mark, Mark and Neil, for their support during these months. EPCC is an interdisciplinary focus for high performance parallel computing projects involving groups within the University of Edinburgh, industrial partners and academic users throughout Europe. The centre is supported by major grants and contracts from industry, the Commission of the European Communities, the Department of

Trade and Industry, the Engineering and Physical Sciences Research Council, the Joint Information Systems Committee of the Higher Education Funding Councils and Scottish Enterprise Software Group.

Many thanks go to Shari Trewin, Simon Chapple and the entire PUL team at EPCC for developing and supporting the PUL-TF parallel utility library of which I made much use, and to Shane for the abuse it gave the workstation cluster. Gordon Cameron and Chris Thornborrow let me bounce some of my wackier ideas off them, were an inspiration for some of my less-disastrous ones and allowed me to leverage their work in modular visualisation environments. I hope that Peilin Jia and Bill Day will one day forgive me for the terrible projects that I made them work on with me.

This thesis would not have been possible without the generosity of others who made available electromagnetic modelling programs into which years of energy and expertise had been invested. I am one of many indebted to Kurt Strack for his landmark textbook *Exploration with Deep Transient Electromagnetics* and accompanying MODALL software. Professor Alan Tripp of the University of Utah gave permission to use the EM3D program. Dean Livelybrooks, Louise Pellerin and Andreas Hördt gave instruction and help in its use. Liming Yu gave his EMAFD program and many hours of help with its use and development.

Throughout this work my family sent unending love and support. Many other people also sent me encouragement and help from beyond Edinburgh. Marijke van Heeswijk sent her copy of Aki and Richards which was vital in the closing months. Ki Ha Lee, Dean Oliver and Adrianus de Hoop sent me vital technical notes and pre-prints. I am indebted to Evert Slob and Benoit Tournier who shared their software and their latest results; these long-distance conversations by email shaped my thinking and raised my spirits.

I am indebted to my examiners, Roger Banks, Peter Weidelt and Sergei Zatsepin, whose careful examination and thoughtful comments greatly improved this thesis.

Finally, I must thank Greta who showed me every day that a little sparkle could be brought to any job.

Contents

Abstract	iv
Acknowledgements	v
Conventions, Notation and Definitions	1
1 Introduction	8
1.1 Electromagnetic Surveying	9
1.1.1 Industrial Applications	9
1.1.2 Acquisition Systems	9
1.1.3 Surveying Configurations	10
1.1.4 Data Processing and Interpretation	12
1.2 The Equivalent Wavefield Concept in Multichannel Transient Electromagnetic Surveying	14
1.3 Outline of This Thesis	15
2 Propagation of Seismic and Electromagnetic Energy in the Earth	17
2.1 Governing Equations	18
2.1.1 Waves in Elastic Media	18
2.1.2 Maxwell's Equations	20
2.2 Solution Using Irrotational and Solenoidal Components	25
2.2.1 The Completeness Theorem	25
2.2.2 Separation of the Diffusive Response into Irrotational and Solenoidal Components	27
2.3 Conclusions	32
3 The Diffusive Response and its Equivalent Wavefield	33
3.1 The Equivalent Wavefield Concept	34
3.1.1 How the Q Transform Works	35
3.1.2 A More Rigorous Derivation	36
3.1.3 Correspondence of Sources	39

3.1.4	The Effect of the Choice of the Time Origin	39
3.2	Conclusions	41
4	Point Sources in Infinite Media	42
4.1	EM Responses to Point Sources in Infinite Media	43
4.1.1	Response to a Directed Point Source Term	43
4.1.2	A Shorter Derivation	47
4.1.3	Representation of EM Sources	48
4.1.4	Magnetic Field of a Transient Electric Current dipole	51
4.1.5	Electric Field of a Transient Electric Current dipole	52
4.2	Comparison of EM Sources and Seismic Sources	55
4.3	Conclusions	57
5	Sources at the Surface of a Uniform Half-Space	58
5.1	Horizontal Electric Current Dipole at the Surface of a Uniform Half-Space	59
5.1.1	EM Response for a Switch-off Transmitter Current Profile	59
5.1.2	Equivalent Wavefield for a Switch-off Transmitter Current Profile	60
5.1.3	EM Response and Equivalent Wavefield for an Impulsive Transmitter Current Profile	63
5.2	Conclusions	64
6	MTEM Acquisition and Pre-processing with TEAMEX	65
6.1	The TEAMEX MTEM Acquisition System	66
6.1.1	Acquisition Configuration	66
6.2	Data Pre-processing	69
6.2.1	Conversion from Bipolar Response	69
6.2.2	Removal of Residual Bias	69
6.2.3	Reduction of Random Noise by Vertical Stacking	70
6.2.4	Reduction of Organised Noise	70
6.3	Noise Environments	71
6.4	Distortions of the Signal	71
6.4.1	Low-pass Filtering	71
6.4.2	Clock Drift	72
6.4.3	Transmitter Waveform Instability	72
6.4.4	Near Surface Heterogeneities	73
6.4.5	Induced Polarisation	73
6.4.6	Pulsed Cathodic Protection	74
6.5	Measurement and Compensation for the System Response	74
6.6	Experience from an Early Time-Lapse Multichannel Survey with TEAMEX	75

6.7	Conclusions	78
7	Diffusive to Propagative Mapping	79
7.1	Diffusive to Propagative Mapping (DPM) as an Ill-posed Inverse Problem	80
7.2	Diffusive to Propagative Mapping (DPM) by Deconvolution of the Q Transform in Logarithmic Time	83
7.2.1	Formulation of the Q Transform as a Convolution in Logarithmic Time .	83
7.2.2	Analytical Demonstration of the Convolutional Relationship	85
7.2.3	Calculating a Deconvolution Filter in the Frequency Domain	86
7.2.4	The Effects of DPM Regularisation on Recovered Waveforms	88
7.2.5	Demonstration of Numerical DPM by Deconvolution in Log Time	89
7.2.6	Self-Similar Scaling of the Equivalent Wavefield	89
7.2.7	Compensating for Waveform Regularisation	91
7.2.8	DPM by Deconvolution in Log Time of 10 Ω m Half Space Synthetics . . .	95
7.2.9	DPM by Deconvolution in Log Time of 50 Ω m Half Space Synthetics . . .	99
7.2.10	DPM by Deconvolution in Log Time in the Presence of Several Arrivals .	101
7.2.11	DPM by Deconvolution in Log Time of 1D Layered Earth Synthetics . . .	103
7.3	Diffusive to Propagative Mapping (DPM) by Singular Value Decomposition of the Q Transform	110
7.3.1	Formulation of DPM as a Matrix Inversion Problem	110
7.3.2	Demonstration of DPM by Singular Value Decomposition	112
7.3.3	DPM by Singular Value Decomposition of 10 Ω m Half Space Synthetics .	115
7.4	Conclusions	118
8	Conclusions	119
A	Time-Lapse Electromagnetics	131
B	Related Problems in Partial Differential Equations	142
B.1	Generalising the Q Transform	142
B.2	Correspondence of Sources	145
B.3	Singular Value Expansion Analysis of The Generalised Q Transform	145
C	Geophysical Modelling and Simulation on High Performance Computers	147
C.1	High Performance (Parallel) Computers	148
C.1.1	Computer Architectures	148
C.1.2	Fine and Coarse Grain Parallelisation Techniques	150
C.1.3	Load Balancing Techniques	153
C.2	Geophysical Modelling with Integral Equations	155
C.2.1	Formulating the EM Induction Problem Using Integral Equations	155

C.2.2	Scope of the Integral Equation Formulation	157
C.3	Geophysical Modelling with Finite Differences	159
C.3.1	Axi-symmetric Finite Difference Formulation	159
C.4	Task Farm Parallelisation of EM Simulation	162
C.4.1	Software Engineering	162
C.4.2	Performance Analysis	165
C.4.3	Large Scale Feasibility Studies	166
C.5	Conclusions	167
D	Feasibility Studies	168
D.1	1D Modelling of a Shallow Gas Storage Reservoir	169
D.1.1	Description of Earth Model	169
D.1.2	Description of the Acquisition Configuration	169
D.1.3	Results	171
D.2	3D Modelling of an Axisymmetric Submarine Reservoir	174
D.2.1	Description of Earth Model	174
D.2.2	Description of Source and Receiver Configuration	175
D.2.3	Results	176
D.3	Conclusions	178
E	Euphrates: A System for Automatic Introduction of Data Parallelism into Modular Applications	179
F	Automatic Parallelisation of Multichannel Transient EM Processing	188

List of Figures

1.1	EM sources and receivers.	10
1.2	Lateral profiling with an electromagnetic sounding tool.	11
1.3	The depth of investigation of an EM sounding tool can be varied by altering its configuration. Changes in Earth properties with depth can be inferred from variations in the EM response measured using different configurations.	11
2.1	James Clerk Maxwell	24
3.1	Response to a directed impulsive point source term in propagative and diffusive media.	34
4.4	Graphical representation of a double-couple source.	55
4.5	Graphical representation of the two couples arising from the curl of a point dipole source.	55
4.1	Graphical representation of a Dirac delta function.	56
4.2	Graphical representation of a couple in 3D space.	56
4.3	The nine possible couples in 3 dimensional space.	56
5.1	Configuration of a grounded dipole source.	59
5.2	The equivalent wavefield of a grounded dipole source.	62
6.1	A TEAMEX receiver unit.	66
6.2	Use of clocks to synchronise transmitter and receiver systems.	67
6.3	Surface to surface MTEM data acquisition configuration.	68
6.4	Location of field area.	75
6.5	Common source gather showing raw and stacked traces.	76
6.6	Processing of common source gather.	76
7.1	Magnitude of frequency components in inverse filter calculated through Fourier domain.	87
7.2	Calculation of inverse filter through Fourier domain.	87
7.3	Numerical demonstration of DPM by deconvolution in log time.	90

7.4	Log-log plot of in-line Ex component for model h10.	92
7.5	Comparison of numerical recoverable equivalent wavefield with the analytic result.	93
7.6	Equivalent wavefield for 10 Ω m model.	94
7.7	DPM of a synthetic for a 10 Ω m half space.	95
7.8	DPM with extrapolation for 10 Ω m half space synthetic.	97
7.9	Equivalent wavefield for 10 Ω m model.	98
7.10	Log-log plot of in-line Ex component for model h50.	99
7.11	Equivalent wavefield for 50 Ω m model.	100
7.12	DPM by deconvolution in log time of synthetic containing two pulses, one twice as fast as the other.	102
7.13	DPM by deconvolution in log time of synthetic containing two pulses, one three times as fast as the other.	102
7.14	DPM by deconvolution in log time of synthetic containing two pulses, one four times as fast as the other.	102
7.15	Earth Model ilq1	103
7.16	Log-log plot of in-line Ex component for model ilq1.	104
7.17	Extrema marked on equivalent wavefield for 200 Ω m model.	105
7.18	Earth Model k44	106
7.19	Log-log plot of in-line Ex component for model k44.	106
7.20	Extrema marked on equivalent wavefield for k44 model.	108
7.21	Extrema marked on equivalent wavefield for h44 model.	109
7.22	DPM by singular value decomposition.	113
7.23	Equivalent wavefield calculated by DPM by singular value decomposition.	114
7.24	DPM by singular value decomposition of 10 Ω m Half Space Synthetic.	115
7.25	Equivalent wavefield for 10 Ω m model.	116
C.1	Schematic DM-MIMD architecture.	149
C.2	Schematic SIMD architecture.	149
C.3	Schematic SMP architecture.	150
C.4	A functional pipeline.	151
C.5	The classic task farm.	151
C.6	Geometric domain decomposition in two dimensions.	152
C.7	Geometric decomposition of an unbalanced problem.	154
C.8	A scattered spatial decomposition distributes work more evenly.	154
C.9	The Green's tensor.	156
C.10	Main program section for sequential version of EM3D.	162
C.11	Main program section for task-farm parallel version of EM3D.	164
C.12	Subroutines to implement task generation, task execution and result collation.	164

C.13 Execution times of the task farm version of EM3D running dike4 model using 36 frequencies.	166
C.14 Speed up of the task farm version of EM3D running dike4 model using 36 frequencies.	166
D.1 Resistivity versus depth profiles for 1D Earth models IL10, IL100 and IL200. . .	170
D.2 Log-log plot of in-line Ex component for model IL200.	171
D.3 Comparison of in-line Ex response for models IL10, IL100 and IL200.	173
D.4 Ratio of in-line Ex components for models IL200 and IL10.	173
D.5 Schematic of axisymmetric sub-marine reservoir.	174
D.6 Vertical section through the smoothed conductivity model for sub-marine model ilm3000b.	175
D.7 Smoothed vertical conductivity profile for sub-marine model ilm3000b.	176
D.8 Zoom on vertical profile of resistive anomaly: maximum resistivity is 75 Ωm . . .	176
D.9 Collinear and broadside source-receiver configurations.	176
D.10 Ratio of total and normal electric field for axisymmetric submarine reservoir model.	177

List of Tables

0.1	Some time domain functions and their Laplace transforms.	7
0.2	Some time domain functions and their q domain equivalents.	7
C.1	Timing Results for dike4 model using 1 frequency.	165
D.1	Layer thicknesses, depths and resistivities for model IL200.	169
D.2	Thicknesses and resistivities for layer 5 of models IL200, IL100 and IL10.	169

Conventions, Notation and Definitions

In general the terminology and conventions presented here follow Hobbs (1992). The term *primary* field refers to a source field which is generated externally to the Earth's surface. A time-varying primary field induces an associated *secondary* field. The *normal* field consists of the primary field plus the secondary field induced in a one-dimensional or layered Earth approximation. The *total* field includes any *anomalous* field, additional to the normal field, which arises due to additional heterogeneities.

Scalar and Vector Quantities

Vector quantities are written in a bold typeface, for example \mathbf{F} , and scalar quantities in normal typeface, for example F .

Space and Time

Let $\mathbf{x} = (x_1, x_2, \dots, x_N)$ denote the position vector in \mathbb{R}^N , and \mathbf{e}_i the i th unit vector so that $\mathbf{x} = \sum_{i=1}^N x_i \mathbf{e}_i$. Let r denote $\|\mathbf{x}\|_2 = \sqrt{\sum_{i=1}^N x_i^2}$. The direction cosine $\gamma_i = x_i/r$ is widely used. Let t denote time.

Differential Operators

Where F is a function only of a single variable, v say, let $F'(v)$ denote the derivative of F with respect to v .

Let ∂_t denote the partial derivative with respect to time, so that

$$\partial_t F(\mathbf{x}, t) = \frac{\partial F(\mathbf{x}, t)}{\partial t} \quad (0.1)$$

and

$$\partial_t^j F(\mathbf{x}, t) = \frac{\partial^j F(\mathbf{x}, t)}{\partial t^j}. \quad (0.2)$$

Let ∂_i denote the partial derivative with respect to the i th spatial component x_i , so that

$$\partial_i F(\mathbf{x}, t) = \frac{\partial F(\mathbf{x}, t)}{\partial x_i} \quad (0.3)$$

and

$$\partial_i^j F(\mathbf{x}, t) = \frac{\partial^j F(\mathbf{x}, t)}{\partial x_i^j}. \quad (0.4)$$

If P is a polynomial with coefficients $a_j, j = 1, \dots, m$ let

$$P(\partial_t)[F(\mathbf{x}, t)] = \sum_{j=1}^m a_j \partial_t^j F(\mathbf{x}, t) \quad (0.5)$$

and similarly for polynomials in ∂_i .

Transforms

Denote the Laplace transform of $\mathbf{F}(\mathbf{x}, t)$ with respect to t with transform parameter s as

$$\hat{\mathbf{F}}(\mathbf{x}, s) = \mathcal{L}[\mathbf{F}(\mathbf{x}, t)](s) \quad (0.6)$$

$$\equiv \int_0^\infty \mathbf{F}(\mathbf{x}, t) \exp(-st) dt \quad (0.7)$$

provided this integral converges. The complex inversion formula for the Laplace transform is

$$\mathbf{F}(\mathbf{x}, t) = \frac{1}{2\pi i} \int_{c-i\infty}^{c+i\infty} \hat{\mathbf{F}}(\mathbf{x}, s) \exp(st) ds, \quad (0.8)$$

when this integral converges. The Laplace transform of the n th derivative of a function $\mathbf{F}(\mathbf{x}, t)$ is

$$\mathcal{L}[\partial_t^n \mathbf{F}(\mathbf{x}, t)](s) = s^n \hat{\mathbf{F}}(\mathbf{x}, s) - \sum_{i=0}^{n-1} s^i \partial_t^{n-1-i} \mathbf{F}(\mathbf{x}, 0). \quad (0.9)$$

Denote the Fourier transform of $\mathbf{F}(\mathbf{x}, t)$ with respect to t with transform parameter ω as

$$\tilde{\mathbf{F}}(\mathbf{x}, \omega) = \mathcal{F}[\mathbf{F}(\mathbf{x}, t)](\omega) \quad (0.10)$$

$$\equiv \int_{-\infty}^\infty \mathbf{F}(\mathbf{x}, t) \exp(i\omega t) dt \quad (0.11)$$

provided this integral converges. Using this convention the inversion formula for the Fourier transform is

$$\mathbf{F}(\mathbf{x}, t) = \frac{1}{2\pi} \int_{-\infty}^\infty \tilde{\mathbf{F}}(\mathbf{x}, \omega) \exp(-i\omega t) d\omega. \quad (0.12)$$

The Fourier transform of the n th derivative of a function $\mathbf{F}(\mathbf{x}, t)$ is

$$\mathcal{F}[\partial_t^n \mathbf{F}(\mathbf{x}, t)](\omega) = (-i\omega)^n \tilde{\mathbf{F}}(\mathbf{x}, \omega). \quad (0.13)$$

Special Functions

$$\delta(v) \quad \int_{-\infty}^{\infty} \delta(x - \eta) f(x) dx = f(\eta) \quad \text{the Dirac delta function}$$

$$\delta(\mathbf{x}) \quad \delta(x_1)\delta(x_2)\delta(x_3) \quad \text{the 3D Dirac delta function}$$

$$\delta_{ij} \quad \delta_{ij} a_j = a_i \quad \text{the Kronecker delta function}$$

$$\text{erf}(x) \quad \frac{2}{\sqrt{\pi}} \int_0^x \exp(-t^2) dt \quad \text{the error function}$$

$$\text{erfc}(x) \quad 1 - \text{erf}(x) \quad \text{complementary error function}$$

$$\mathcal{H}(t) \quad \begin{cases} 0 & t < 0 \\ 1 & t > 0 \end{cases} \quad \text{Heaviside or unit step function}$$

$$\Gamma(z) \quad \int_0^{\infty} \exp(-t) t^{z-1} dt \quad \text{Gamma function}$$

$$\mathcal{I}_{\nu}(z) \quad \sum_{m=0}^{\infty} \frac{(\frac{1}{2}z)^{\nu+2m}}{m! \Gamma(\nu+m+1)} \quad \text{modified Bessel function of the first kind}$$

$$\mathcal{K}_{\nu}(z) \quad \frac{\pi}{2} \frac{\mathcal{I}_{-\nu}(z) - \mathcal{I}_{\nu}(z)}{\sin(\nu\pi)} \quad \text{modified Bessel function of the third kind}$$

SI Base Units

Quantity	Unit	
	Name	Symbol
length	metre	m
mass	kilogram	kg
time	second	s
electric current	ampere	A

SI Derived Units

Quantity	Unit		
	Name	Symbol	Equivalent
frequency	hertz	Hz	s^{-1}
force	newton	N	$kg\ m/s^2$
pressure	pascal	Pa	N/m^2
energy	joule	J	$kg\ m^2/s^2$
power	watt	W	J/s
electric potential	volt	V	W/A
resistance	ohm	Ω	V/A
conductance	siemens	S	A/V
magnetic flux	weber	Wb	V s
inductance	henry	H	Wb/A
electric charge	coulomb	C	A s
capacitance	farad	F	C/V

Symbols

Symbol	Description	Units
A	a matrix	
$\mathbf{B}(\mathbf{x}, t)$	magnetic induction	Wb m^{-2}
$\mathbf{D}(\mathbf{x}, t)$	electric displacement	C m^{-2}
\mathcal{D}	moment of electric dipole	A m
$\mathbf{E}(\mathbf{x}, t)$	electric field	V m^{-1}
E_{\parallel}	component of the electric field parallel to the transmitter dipole	V m^{-1}
E_{\perp}	component of the electric field orthogonal to the transmitter dipole	V m^{-1}
$\mathbf{F}(\mathbf{x}, t)$	a diffusive field	
$\mathbf{G}(\mathbf{x}, t)$	$\sqrt{\pi} \exp(v) \mathbf{F}(\mathbf{x}, \frac{1}{4} \exp(2v))$	
\mathbf{H}	source density of strain	
$\mathbf{H}(\mathbf{x}, t)$	magnetic field	A m^{-1}
$\mathbf{J}^s(\mathbf{x}, t)$	source volume density of electric current	A m^{-2}
$\mathbf{K}^s(\mathbf{x}, t)$	source volume density of magnetic current	V m^{-2}
dHz/dt	rate of change with time of the component of magnetic field parallel to the z axis	$\text{A m}^{-1} \text{s}^{-1}$
$M(v)$	deconvolution (inverse) filter for $W(v)$	
$\mathbf{R}(\mathbf{x}, v)$	$\mathbf{R}(\mathbf{x}, v) = \mathbf{U}(\mathbf{x}, \exp(v))$, a resampled version of the wavefield \mathbf{U}	
$\mathbf{S}, \mathbf{U}, \mathbf{V}$	matrices	
$\mathbf{U}(\mathbf{x}, q)$	a wavefield	
$W(v)$	$4 \exp(-2v) \exp(-\exp(-2v))$, the kernel for the formulation of the Q transform as a convolution equation	
$W'(v)$	$8 \exp(-2v) \exp(-\exp(-2v)) (\exp(-2v) - 1)$, the derivative of $W(v)$	
$\Lambda(v)$	deconvolution (inverse) filter for $W'(v)$	
ϵ	dielectric permittivity	F m^{-1}
μ	magnetic permeability	H m^{-1}
λ, μ	Lamé's constants	
σ	conductivity	S m^{-1}
ρ	resistivity	Ωm
ϱ	volume density of mass	kg m^{-3}
\mathbf{u}	displacement	m
ε_{ij}	strain tensor	
\mathbf{f}	source volume density of force	N/m^3
s, p	Laplace transform parameters	s^{-1}
q	$q = \exp(v) = 2\sqrt{t}$	$\sqrt{\text{s}}$
v	$v = \ln(2\sqrt{t})$	
\forall_i, ν_i	singular values	
$\mathbf{u}_i, \mathbf{v}_i$	left and right singular functions	
$\mathbf{u}_i, \mathbf{v}_i$	left and right singular vectors	

Commonly Employed Results

$$\nabla(fg) = f(\nabla g) + g(\nabla f)$$

$$\nabla.(f\mathbf{A}) = f(\nabla.\mathbf{A}) + \mathbf{A}(\nabla f)$$

$$\nabla \times (f\mathbf{A}) = f(\nabla \times \mathbf{A}) + (\nabla f) \times \mathbf{A}$$

$$\nabla(\mathbf{A}\mathbf{B}) = (\mathbf{A}\nabla)\mathbf{B} + (\mathbf{B}\nabla)\mathbf{A} + \mathbf{A} \times (\nabla \times \mathbf{B}) + \mathbf{B} \times (\nabla \times \mathbf{A})$$

$$\nabla.(\mathbf{A} \times \mathbf{B}) = \mathbf{B}(\nabla \times \mathbf{A}) - \mathbf{A}(\nabla \times \mathbf{B})$$

$$\nabla \times (\mathbf{A} \times \mathbf{B}) = \mathbf{A}(\nabla.\mathbf{B}) - \mathbf{B}(\nabla.\mathbf{A}) + (\mathbf{B}\nabla)\mathbf{A} - (\mathbf{A}\nabla)\mathbf{B}$$

$$\frac{\partial r}{\partial x_i} = \frac{x_i}{r} = \gamma_i$$

$$\frac{\partial \gamma_j}{\partial x_i} = \frac{1}{r}(\delta_{ij} - \gamma_i \gamma_j)$$

$$\frac{\partial}{\partial x_i} \left(\frac{\gamma_j}{r} \right) = \frac{1}{r^2}(\delta_{ij} - 2\gamma_i \gamma_j)$$

$f(t)$	$\hat{f}(s) = \int_0^\infty \exp(-st)f(t)dt$
$\partial_t^n f(t)$	$s^n \hat{f}(s) - \sum_{i=0}^{n-1} s^i \partial_t^{n-1-i} f(0)$
$tf(t)$	$-\frac{\partial \hat{f}(s)}{\partial s}$
$\int_0^t f_1(\tau)f_2(t-\tau) d\tau$	$\hat{f}_1(s)\hat{f}_2(s)$
$\int_0^t f(\tau) d\tau$	$1/s \hat{f}(s)$
$\delta(t-a)$	$\exp(-as)$
$f(t-a)$	$\exp(-as)\hat{f}(s)$
$H(t)$	$1/s$
$t^n \mathcal{H}(t)$	$n!s^{-n-1}$
$\mathcal{H}(t-a)$	$\frac{1}{s} \exp(-as)$
$\operatorname{erfc}(\frac{a}{2\sqrt{t}})$	$\frac{1}{s} \exp(-a\sqrt{s})$
$t^{-1/2} \exp(-\frac{a^2}{4t})$	$\frac{1}{\sqrt{s}} \sqrt{\pi} \exp(-a\sqrt{s})$
$t^{-3/2} \exp(-\frac{a^2}{4t})$	$\frac{2}{a} \sqrt{\pi} \exp(-a\sqrt{s})$
$\left(\frac{a^2}{4} - \frac{t}{2}\right) t^{-5/2} \exp(-\frac{a^2}{4t})$	$\sqrt{s} \sqrt{\pi} \exp(-a\sqrt{s})$
$t^{-5/2} \exp(-\frac{a^2}{4t})$	$\frac{4}{a^2} (\sqrt{s} + 1/a) \sqrt{\pi} \exp(-a\sqrt{s})$
$t^{\nu-1} \exp(-\frac{a^2}{4t})$	$2(\frac{a}{2\sqrt{s}})^\nu \mathcal{K}_\nu(\frac{a}{\sqrt{s}})$

Table 0.1: Some time domain functions and their Laplace transforms.

$f(t) = \frac{1}{2\sqrt{\pi t^3}} \int_0^\infty q \exp(-\frac{q^2}{4t}) u(q) dq$	$u(q)$
$\mathcal{H}(t)$	$q\mathcal{H}(q)$
$\delta(t-0^+)$	$\delta(q-0^+)$
$\frac{1}{2\sqrt{\pi t^3}} \frac{r}{c} \exp(-\frac{r^2}{c^2 4t})$	$\delta(q-r/c)$
$\frac{1}{2\sqrt{\pi t^3}} (1 - \frac{r^2}{c^2 2t}) \exp(-\frac{r^2}{c^2 4t})$	$\delta'(q-r/c)$
$\operatorname{erf}(\frac{r}{c2\sqrt{t}})$	$q\mathcal{H}(r/c-q) + r/c\mathcal{H}(q-r/c)$
$\frac{1}{\sqrt{\pi t}} \exp(-\frac{r^2}{c^2 4t})$	$\mathcal{H}(q-r/c)$
$\operatorname{erf}(\frac{r}{c2\sqrt{t}}) - \frac{2}{\sqrt{\pi}} \exp(-\frac{r^2}{c^2 4t})$	$q\mathcal{H}(r/c-q)$
$\operatorname{erfc}(\frac{r}{c2\sqrt{t}}) + \frac{2}{\pi} \frac{r}{c2\sqrt{t}} \exp(-\frac{r^2}{c^2 4t})$	$q\mathcal{H}(q-r/c)$
$\int_0^t \frac{a}{2\sqrt{\pi}} \tau^{-3/2} \exp(-\frac{a^2}{4\tau}) f(t-\tau) d\tau$	$\begin{matrix} u(q-a) & q > a \\ 0 & q < a \end{matrix}$

Table 0.2: Some time domain functions and their q domain equivalents.

Chapter 1

Introduction

Geophysical methods, such as electromagnetic or seismic surveying of the subsurface, are applied by several industries including hydrocarbons, waste storage, geotechnical, water, minerals, coal and geo-thermal energy. Recent advances have delivered multichannel transient electromagnetic (MTEM) acquisition systems which simultaneously record from one source into several receivers. This is in contrast to the seismic method where development and deployment of systems for multichannel acquisition, processing and interpretation has been ongoing for decades.

Electromagnetic propagation in the Earth is diffusion-dominated over the frequency range which is useful in deep surveying. The equivalent wavefield concept relates diffusive propagation to an equivalent non-diffusive, wave propagation, provided equivalent source and boundary conditions are satisfied. This concept has found application in analysis of the diffusive propagation of electromagnetic, thermal and pressure fields.

This thesis applies the equivalent wavefield concept to relate diffusive electromagnetic propagation in the Earth to a (fictional) equivalent wavefield. The purpose is to enable wave propagation theory and interpretation techniques developed for the seismic method to be applied to the analysis of MTEM surveying.

This chapter introduces electromagnetic surveying, explains the motivation for applying the equivalent wavefield concept and summarises the structure of the rest of this thesis. Further chapters introduce seismic and electromagnetic propagation and apply the equivalent wavefield concept to calculate electromagnetic responses and their equivalent wavefields. Then, using a calibrated numerical calculation, synthetic responses from half-space and layered Earth models are mapped to the equivalent wavefield domain and interpreted using concepts from seismic refraction.

1.1 Electromagnetic Surveying

1.1.1 Industrial Applications

Electromagnetic (EM) methods of surveying the Earth's subsurface have demonstrated their utility to the hydrocarbons industry by providing information on subsurface structure in regions where conditions are unfavourable for the seismic method, and by providing information complementary to that available from the seismic method.

EM methods have been successfully applied to investigations underneath volcanics and in other situations not favourable for the seismic method (Newman, Hohmann & Anderson 1986, Withers, Eggers, Fox & Crebs 1994, Zhdanov & Keller 1994, Warren 1996, Yan, Su & Hu 1997). Replacement of hydrocarbons with saline water, which is often injected into a reservoir during secondary hydrocarbon recovery, causes conductivity changes which may be mapped by EM surveys (Newman & Alumbaugh 1995, Alumbaugh & Morrison 1995*a*). Conductivity changes caused by steam flooding (Vaughan, Udell & Wilt 1993, Butler & Knight 1995) may also be mapped by surface electromagnetic surveys (Wayland, Lee & Cabe 1985, Wayland, Lee & Cabe 1987, Daily & Ramirez 1995, Lee, Xie, Hoversten & Pellerin 1995).

EM methods are also applied in the search for minerals, the characterisation of waste storage and disposal sites, geotechnical investigations, and the detection and monitoring of resistivity anomalies associated with pollutants.

1.1.2 Acquisition Systems

Of the possible acquisition configurations sub-aerial, surface-source-to-surface-receiver methods are perhaps the easiest to implement and have received the greatest attention. Many controlled-source, surface-to-surface systems have been developed for various applications. Commercial manufacturers such as Geonics now offer a wide range of systems. Developments principally for mineral exploration include the University of Toronto UTEM system (West, Macnae & Lamontagne 1984) and the SIROTEM system developed at CSIRO in Australia (Buselli & O'Neill 1977). More recent has been the commercialisation of deep-Earth sounding systems, such as TEAMEX from DMT (Strack 1992, Chapter 5) and the Geonics EM42 and PROTEM systems, which are capable of penetrating to depths of interest to hydrocarbon exploration.

Controlled-source, sub-marine studies have been carried out using the electric dipole transmitter, electric dipole receiver configuration in both the frequency domain (Cox, Constable, Chave & Webb 1986, Constable, Cox & Chave 1986, Constable, Cox & Chave 1987) and the time domain (Evans, Cairns & Edwards 1993). The time domain magnetic dipole transmitter, magnetic dipole receiver configuration has also been used sub-marine (Cheesman, Edwards & Law 1990, Webb, Edwards & Yu 1993).

Most down-hole EM development has focused on cross-hole acquisition (Sena & Toksoz 1990,

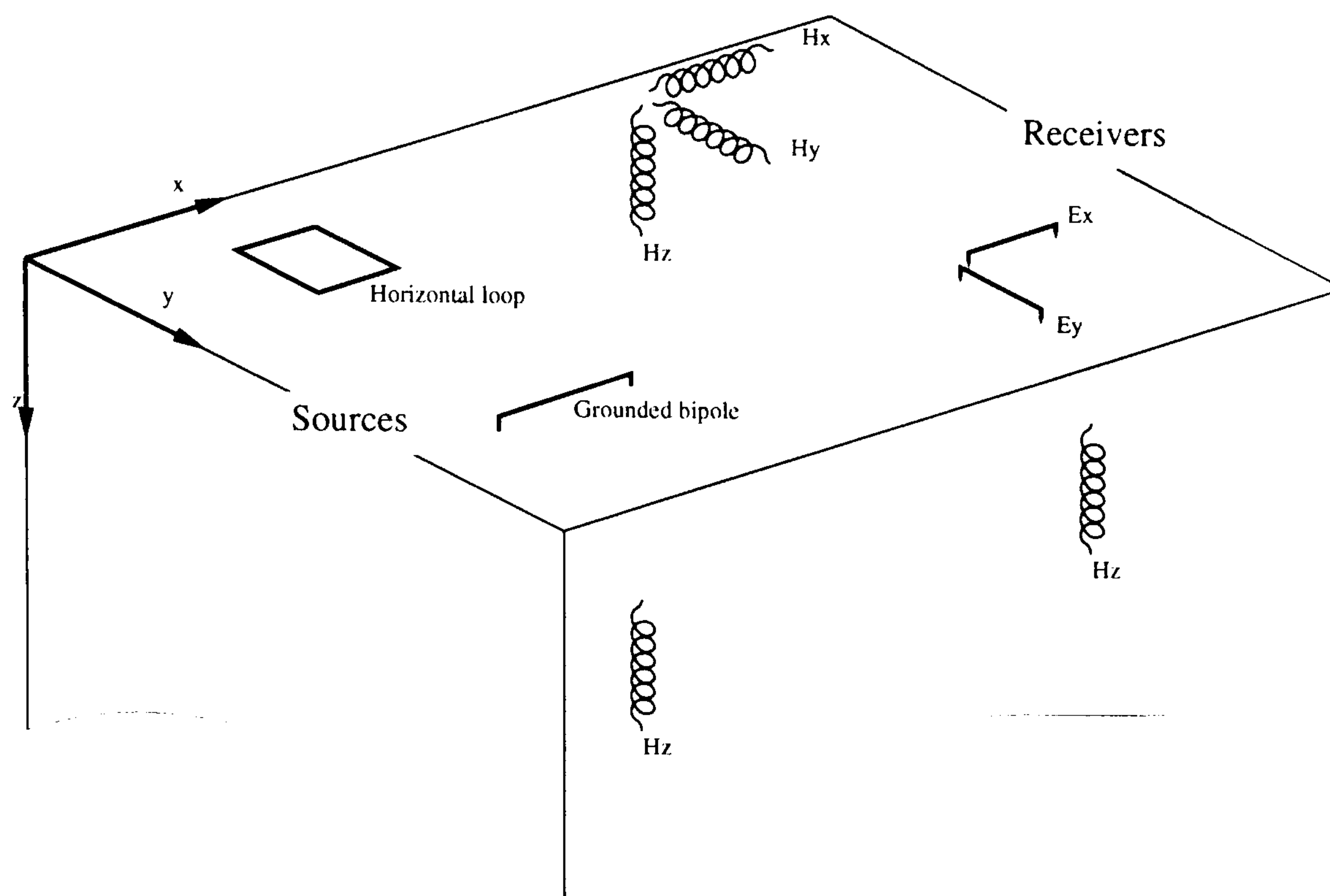


Figure 1.1: Electromagnetic sources and receivers. Grounded wires are used to provide an electric bipole source or receiver. Current flowing in loops of wire generate or measure magnetic fields. Multi-turn coils are often used to give a compact magnetic field transponder with a large equivalent area.

Sakashita & Shima 1993, Nekut 1994, Sakashita, Shima & Gasnier 1994, Alumbaugh, Becker, Deszcz-Pan, Lee, Morrison, Nichols & Wilt 1994, Alumbaugh & Morrison 1995*b*, Alumbaugh & Morrison 1995*a*, Newman & Alumbaugh 1995, Wilt, Morrison, Becker, Teng, Lee, Torres-Verdin & Alumbaugh 1995, Wilt, Alumbaugh, Morrison, Becker, Lee & Deszczpan 1995). Work has also been published on the borehole to surface configuration (Spies & Greaves 1991), examining what can be detected through a metal well casing (Schenkel & Morrison 1994, Wu & Habashy 1994) and proposals for insertion of insulating collars into a steel well casing which allow it to be used as both source and receiver electrode (Nekut 1995).

1.1.3 Surveying Configurations

Electromagnetic surveying may be used for preliminary investigation of an area or a more intensive survey can be designed to delineate an already-identified target.

An electromagnetic sounding system generates a pattern of subsurface current which is changed by the presence of an anomaly. Lateral profiling (Figure 1.2) deploys an EM surveying system at a series of locations across the Earth's surface to identify the lateral location of an anomaly.

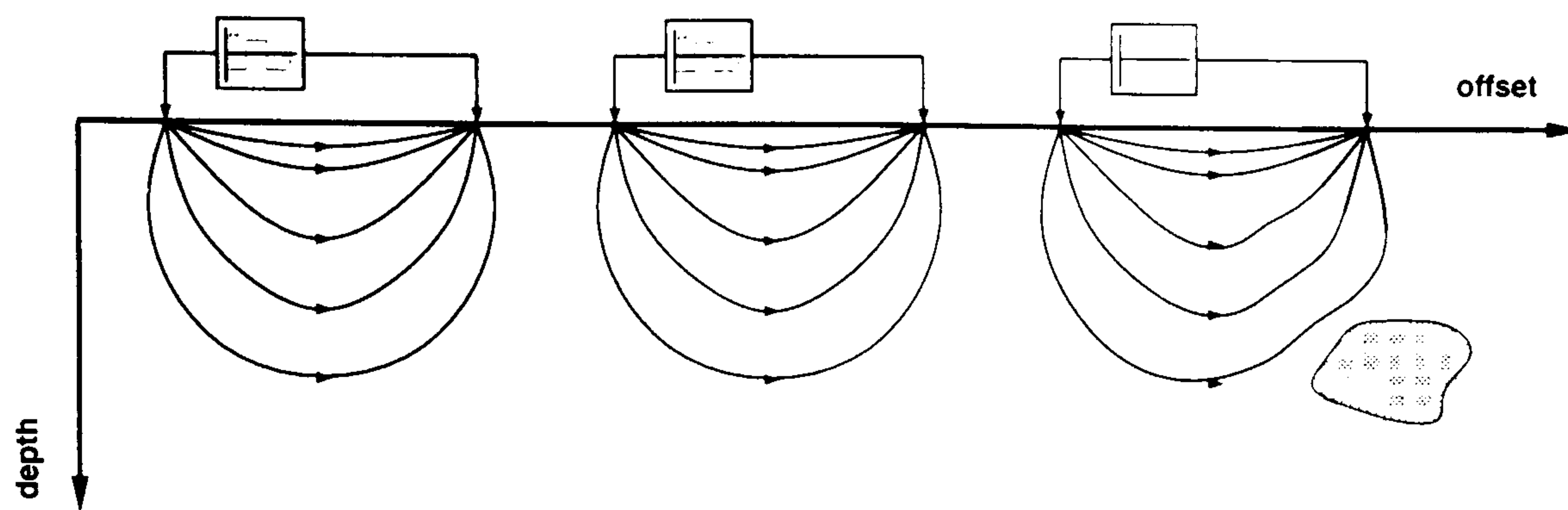


Figure 1.2: The horizontal location of isolated anomalies in a uniform background can be identified by deploying the EM surveying system at a series of locations across the Earth's surface. This allows a lateral profile to be built up, which indicates the lateral location of a targets such as faults, dikes, buried objects or other anomalies.

Spies (1989) demonstrates that the volume and depth of investigation of an EM survey system increases with the foot-print (source-receiver dimensions) of the system and the wavelength of the EM fields employed. Depth profiling (Figure 1.3) deploys an EM system with increasing wavelength and/or foot-print over the same location.

Depth profiling is suitable for detecting geoelectric variations in depth such as the thickness of the weathered layer, the depth to the water-table or a layer of clay.

To delineate a target in both horizontal and vertical dimensions the EM surveying system must be deployed at many different lateral locations *and* with many different depths of investigation. The long offset transient electromagnetic (LOTEM) method is designed to penetrate to depths which are of interest in mineral and hydrocarbon exploration and to detect both resistive and conductive targets. LOTEM surveys employ a grounded electric bipole source at the Earth's surface and a number of surface receivers measuring both electric and magnetic fields. In the LOTEM method the distance between transmitter and receiver is approximately equal to or greater than the exploration depth.

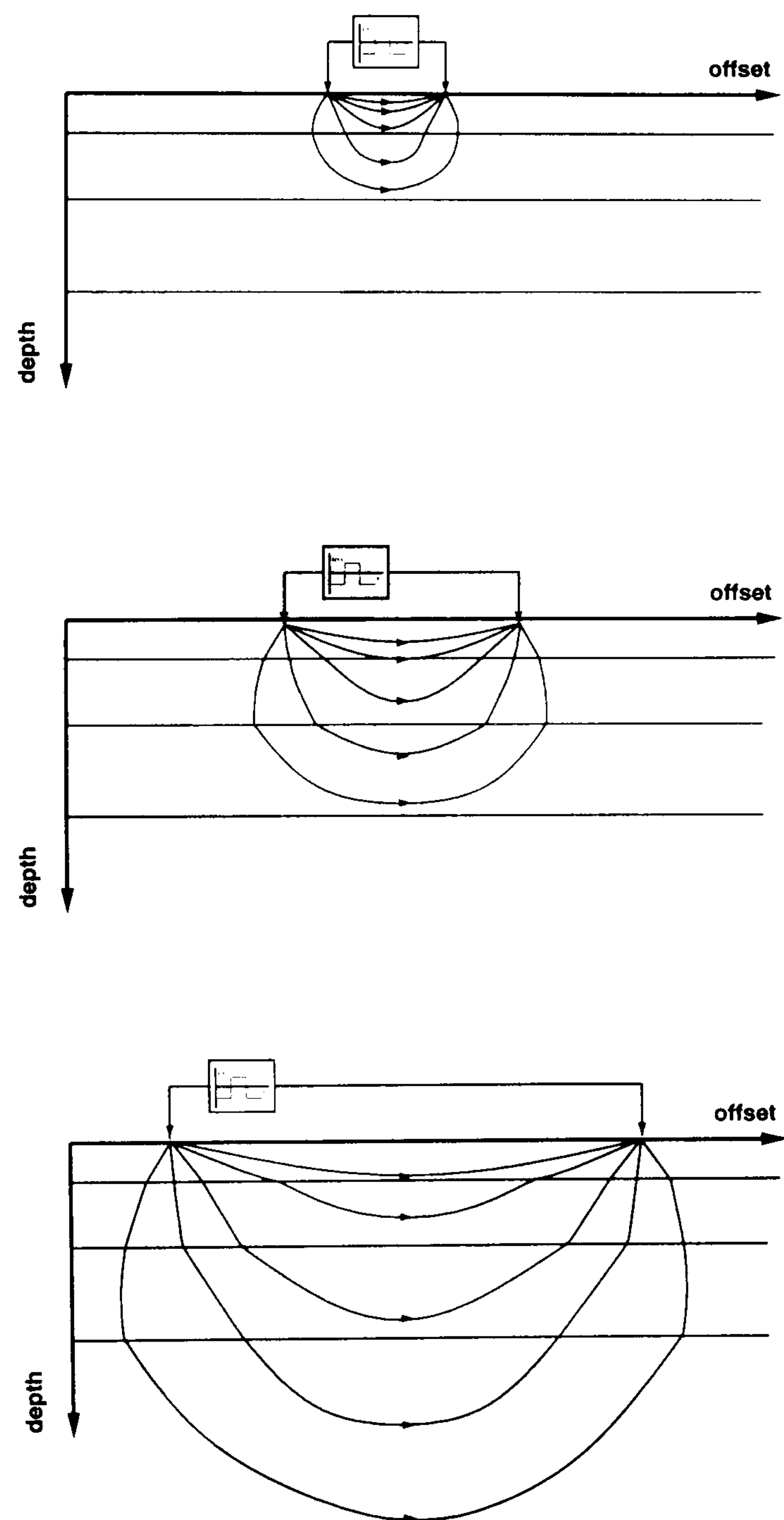


Figure 1.3: The depth of investigation of an EM sounding tool can be varied by altering its configuration. Changes in Earth properties with depth can be inferred from variations in the EM response measured using different configurations.

1.1.4 Data Processing and Interpretation

Apparent Resistivity Transforms

Apparent resistivity transforms offer a quick, simple and computationally inexpensive method of converting a measured voltage into a figure more directly related to a possible Earth model. One definition of apparent resistivity is given by Sheriff (1984)

The resistivity of homogeneous isotropic ground which would give the same voltage-current relationship as measured.

Because apparent resistivity transforms attempt to account for effects of source strength, receiver sensitivity, and source-receiver orientation and offset, they are extremely helpful as a pre-processing step prior to first presentation of data.

Iterative Forward Modelling

Iterative forward modelling is a model-based approach to data interpretation which relies upon the iterative refinement of a model through forward modelling until a good fit with the experimentally acquired data is achieved. Iterative forward modelling (also widely known as inverse modelling) is the mainstay of many EM processing and interpretation schemes despite well understood limitations of the approach.

In many locations a 1D, layered, Earth model is not inappropriate and interpretation using a layered Earth model gives useful results. 1D iterative forward modelling is tractable using moderate amounts of computer power and has become a routine process. Well-understood procedures are available for estimating the degree of confidence with which features in the resulting interpretation, such as the thickness or resistivity of a layer, are resolved by the data (Strack 1992, Chapter 4)(Jupp & Vozoff 1975, Vozoff & Jupp 1975, Lines & Treitel 1984).

Goldman, Tabarovsky & Rabinovich (1994) investigate the interpretation of synthetic LOTEM data calculated for Earth models consisting of two layers with an additional cylindrical basement high or depression and conclude that interpretation of transients from the LOTEM configuration using 1D inversion pseudo-sections does not give reliable results for such situations.

Regions of more complex geology demand the use of a 2D or 3D Earth model. Unfortunately 2D and 3D EM modelling programs are often computationally expensive and difficult to use (Hördt, Druskin, Knizhnerman & Strack 1992). This makes 2D and 3D iterative forward modelling a slow and painful task. The problem is exacerbated by the dramatic increase in data volumes resulting from the multichannel surveys required to resolve 2D and 3D features (Schnegg & Sommaruga 1995, Hördt, Vozoff & Neubauer 1995). Consequently the production of pseudo-sections, by piecing together results from many 1D inversions to give a 2D picture, remains a common technique despite its limitations (Cooper & Swift 1994, Schnegg & Sommaruga 1995).

Iterative forward modelling is probably the most popular development in processing of synthetic and field data for complex geology. However even the most aggressive attacks on the 3D problem, which bring to bear massively parallel supercomputers rated in the top 20 in the world (Newman & Alumbaugh 1996), have not yet tackled large MTEM surveys in the frequency ranges of interest in hydrocarbon exploration and production.

Tomographic Methods

Tomographic inversion methods aim to estimate directly an image of the distribution of subsurface properties as a function of depth. Recently much progress has been made for the magnetotelluric (Journal of Geomagnetism and Geoelectricity 1993) and cross-borehole electromagnetic tomography configurations (Nekut 1994, Sakashita & Shima 1993, Sakashita *et al.* 1994, Alumbaugh *et al.* 1994, Alumbaugh & Morrison 1995*b*, Alumbaugh & Morrison 1995*a*, Wilt, Morrison, Becker, Teng, Lee, Torres-Verdin & Alumbaugh 1995, Wilt, Alumbaugh, Morrison, Becker, Lee & Deszczpan 1995, Côte, Degauque, Lagabriele & Levent 1995). The EM tomography formulation can be applied to surface TEM data (Eaton 1989), however little work has been published applying this to field data, perhaps because the backscattered field is weaker and more difficult to image than the direct field, perhaps because noise levels are higher, and possibly because the proximity of the Earth's surface complicates both modelling and imaging processes.

One of the main difficulties encountered in electromagnetic tomography is the complexity of the phenomena of propagation involved, and, in particular how to take into account the heterogeneous medium. Tomographic methods are usually regarded as expensive in terms of computer time. Computational expense can be reduced by assuming a simplified geometry and/or by employing a simplified propagation theory. The limitations on resolution which are imposed by ignoring diffraction effects are becoming more well appreciated. Côte *et al.* (1995) demonstrate for a cross-hole EM system that the ray theory approximation may be such a bad approximation that it results in predicting an anomaly of opposite sign to that observed.

Full waveform tomographic inversion of transient electromagnetic data is likely to be extremely computationally expensive and its application to surface-to-surface dipole-dipole EM has not yet been published.

Electromagnetic Migration

Electromagnetic migration schemes analogous to pre-stack wave equation migration¹ have been proposed independently by groups originating in the former Soviet Union (Velikov, Zhdanov &

¹Seismic migration algorithms can be categorised into two classes: Kirchhoff integral methods and wave equation-based methods. Kirchhoff integral methods are based around the concept of a travel time from source to receiver. Use of this approximation gives increased flexibility and reduced computational cost. EM propagation in the Earth is diffusive: each frequency in a pulse travels at a different velocity. Therefore the concept of a travel time is more difficult to define for EM propagation and so EM migration schemes analogous to the Kirchhoff integral approach may be more difficult to develop.

Frenkel 1987, Zhdanov & Frenkel 1983, Zhdanov & Frenkel 1988, Zhdanov, Traynin & Portniaguine 1994, Zhdanov, Traynin & Booker 1996) and the United States of America (Lee, McMechan & Aiken 1987). These schemes downward continue the surface EM observations to construct a two-dimensional resistivity image of the medium that produced them.

The downward continuation operator is constructed by drawing a parallel between the EM and acoustic wave equations. Unfortunately this results in an EM downward continuation operator which is unstable and small amounts of noise are amplified by the downward extrapolation.

In order to achieve stability Lee *et al.* (1987) chose to specify the values of the EM fields on two orthogonal edges of their 2D mesh, thus converting an unstable initial value problem to a stable boundary value problem. This stabilisation is achieved at the cost of requiring subsurface field values to be known *a priori*.

Zhdanov *et al.* (1994) apply a regularisation procedure to prevent amplification of noise. Alternatively they propose a migration scheme which has the advantage of being stable, but the disadvantage of giving the wrong amplitudes: information on structure is extracted from phases which are correct.

Both these approaches require an estimate of the background resistivity model. An accurate background resistivity model is important in obtaining accurate results.

Joint Interpretation

Sonic and resistivity logs often show a strong correlation, suggesting that electromagnetic and seismic surveys see the same major geological interfaces (Ziolkowski, Peet, Strack, Andrieux & Vozoff 1992, Nelson & Johnston 1994). The integrated interpretation of seismic and EM surveys to yield improved results over seismic alone has been presented by several authors including (Nagy 1992, Jones 1987, Withers *et al.* 1994, Warren 1996). The use of seismic reflection data to constrain iterative forward modelling of transient electromagnetic data has been demonstrated on large-scale geological units in areas of relatively simple geological structure (Strack, Hanstein, Brocq, Moss, Vozoff & Wolfgram 1989, Strack, Hördt, Vozoff & Wolfgram 1991, Strack & Vozoff 1992).

1.2 The Equivalent Wavefield Concept in Multichannel Transient Electromagnetic Surveying

Recent adaption of technology from multichannel seismic acquisition systems has delivered multichannel transient electromagnetic (MTEM) acquisition systems, which have the capacity to investigate both resistive and conductive targets at depths of interest in hydrocarbon exploration and production. EM explorationists are now presented with systems capable of collecting an unprecedented abundance of data and require to develop a supporting methodology

for designing, acquiring, processing and interpreting such surveys.

The iterative forward modelling, tomography and migration approaches to EM interpretation are active areas of research. To a greater or lesser extent their effectiveness for interpreting a large MTEM survey, probing to depths of interest in hydrocarbon exploration, remains unproved. All are expected to be computationally expensive when applied to a large MTEM survey over a complex geological target.

The equivalent wavefield concept relates diffusive electromagnetic propagation to non-diffusive propagation, provided equivalent source and boundary conditions are satisfied. This thesis applies the equivalent wavefield concept to yield novel analysis, processing and interpretation methods for use in MTEM surveying.

The essential advantage of the equivalent wavefield is that pulses in the equivalent wavefield domain do not disperse. In addition to simplifying analytic calculation, this means that the concepts of wavefield ray theory and travel-times may be applied to produce interpretation approaches which do not require iterative forward modelling.

Following Tournerie & Gibert (1995) we call the process of calculating the equivalent wavefield from the measured EM signals, diffusive to propagative mapping (DPM). DPM is well understood to be an ill-posed problem and the development of efficient algorithms for implementing DPM is an area of active research.

There is no suggestion that DPM can somehow lend electromagnetic surveying the high resolution enjoyed by seismic methods; fundamental limitations on resolution remain. However the equivalent wavefield may be significantly easier to interpret than the original diffusive data.

1.3 Outline of This Thesis

After this opening chapter the theory of the propagation of seismic and EM energy in the Earth is introduced. In general, EM fields have an irrotational component that is equivalent to P-wave propagation, and a solenoidal component that is equivalent to S-wave propagation.

The equivalent wavefield concept is introduced and followed by an informal derivation of the Q transform, which is a prescription for calculating a diffusive field from its equivalent wavefield. The method of derivation is a special case of a more general theorem relating the solutions of two systems of partial differential equations that have the same spatial, but different temporal derivatives. This more general theorem is presented in an appendix.

Using the equivalent wavefield concept, and results from wave theory, the response to a directed impulsive point source is calculated for uniform, isotropic media. The response for physically realistic sources is then calculated by combination with the source description. A moment tensor and a dipole moment are used to model EM sources commonly used in field data acquisition. This representation also allows comparison with seismic sources. For example, the equivalent wavefield of the magnetic field generated by an electric current dipole in a whole

space is generated by a point source of torque, generating shear waves only.

The equivalent wavefield of a grounded horizontal electric current dipole source located at the surface of a uniform half-space is calculated for receivers located at the surface of the half-space.

Following this introduction to the theory of EM and seismic propagation, MTEM field data acquisition methods are discussed for a surface survey employing the new TEAMEX data acquisition system, including source and receiver configuration, pre-processing, noise levels, signal distortions and repeatability.

The problem of transforming a diffusive field to an equivalent wavefield is analysed and seen to be an inherently ill-posed problem. Regularisation methods aim to modify ill-posed problems to yield a solution method which is stable in the presence of noise and also gives a solution which is as close as possible to the “true” solution of the original ill-posed problem. Results are presented from the application of two techniques for numerically estimating the equivalent wavefield, applied to MTEM synthetics generated for half-space Earth models. In both cases the regularisation introduced to stabilise the solution method causes the numerically recovered equivalent wavefield to be smoothed. The simplicity of one technique, deconvolution in log time, allows analysis of this smoothing. When combined with the analytically calculated equivalent wavefield for a source and receivers on the surface of a half space, this calibrates the numerical calculation.

An appendix describes numerical modelling studies using layered Earth models to investigate the feasibility of using MTEM surveys to detect and monitor hydrocarbon reservoirs. These indicate that when drawing an analogy between diffusive EM surveying and the seismic method it is more appropriate to consider wide-angle, refraction seismic than near-offset, reflection seismic surveying.

Using a calibrated numerical calculation synthetic responses from half-space and layered Earth models are mapped to the equivalent wavefield domain and interpreted using concepts from seismic refraction. This interpretation approach exploits, indeed requires, the multi-channel nature of the acquisition.

Discussion of techniques for applying high performance (parallel) computers to numerical simulation of the EM response of a target body is relegated to an appendix. The automatic parallelisation of such MTEM data processing is outlined in an appendix.

Time-lapse MTEM acquisition with the TEAMEX system was demonstrated by field experiment, conducted over an underground gas storage site in the Paris basin. The first of these two surveys is described in an appendix.

Chapter 2

Propagation of Seismic and Electromagnetic Energy in the Earth

The propagation of seismic energy through the Earth can be accurately modelled by the propagation of mechanical disturbances in elastic media. Starting from basic concepts of deformation, strain and stress this chapter derives the elastic wave equation for a homogeneous, isotropic and perfectly elastic solid.

The fundamental empirical relations of electromagnetism for general media and general sources are described by Maxwell's equations. In this chapter Maxwell's equations are introduced and specialised for the case of the diffusion-dominated response of a linear, homogeneous and isotropic imperfect conductor such as is often used to model the EM response of the Earth. From these the equation describing diffusion of the electric and magnetic fields in such media is derived.

When solving the elastic wave equation it is common to divide the wavefield into irrotational (P-wave) and solenoidal (S-wave) components characterised by potentials. The completeness theorem for elastic media asserts that every solution of the elastic wave equation can be written in this way and gives a prescription for calculating these potentials from source terms.

The diffusive field can also be separated into irrotational and solenoidal components characterised by potentials. A completeness theorem for diffusive media is presented here.

2.1 Governing Equations

2.1.1 Waves in Elastic Media

A solid body can be deformed by applying forces to its external faces. The external forces are opposed by internal forces which resist the deformation. As a consequence the body tends to return to its original state when the external forces are removed. This property to resist deformation is called elasticity. A perfectly elastic body is one which recovers completely after being deformed without loss of energy to frictional or viscous forces. To a good approximation rocks can be accurately modelled as perfectly elastic under small deformations.

The displacement vector \mathbf{u} is defined as the vector distance of a particle of the solid body at time t from its position at some reference time t_0 . Displacement does not necessarily imply deformation. For instance, if all the particles in a body are displaced by the same amount, or if the body is rotated, then displacement occurs without deformation. Deformation occurs when the displacements of particles in a body vary from place to place. Displacement is a vector quantity with components (u_1, u_2, u_3) and each component is a function of space and time. As a shorthand we use u_j to denote the component in the \mathbf{e}_j direction where $j = 1, 2$ or 3 . Each component of displacement u_j varies as a function of space. For compactness we write the rate of change of component u_j with respect to the \mathbf{e}_i direction as $\partial_i u_j$ — see Box 1.

The equation of deformation of an elastic solid is

$$\varepsilon_{ij} = \frac{1}{2}(\partial_i u_j + \partial_j u_i) + h_{ij} \quad (2.1)$$

where ε_{ij} is the symmetric¹ strain tensor, \mathbf{u} is the particle displacement and h_{ij} is the source density of strain (Zou 1993, Equation 3.1.3).

The constitutive equation for an elastic solid is a generalisation of Hooke's law and describes the linear relationship between stress and strain as

$$\tau_{ij} = c_{ijpq} \varepsilon_{pq} \quad (2.2)$$

(Nye 1957) where c_{ijpq} is the stiffness tensor of the elastic solid. From the conservation of angular momentum it follows that the stress tensor τ_{ij} is symmetric (Achenbach 1973, Section 2.3.2 pp 51-52).

For an isotropic and perfectly elastic solid

$$c_{ijpq} = \lambda \delta_{ij} \delta_{pq} + \mu (\delta_{ip} \delta_{jq} + \delta_{iq} \delta_{jp}) \quad (2.3)$$

where λ and μ are Lamé coefficients and δ_{ij} is the Kronecker delta function (Achenbach 1973).

¹The strain tensor can be divided into its anti-symmetric component which corresponds to rotation and its symmetric component which corresponds to deformation. In this discussion only the symmetric, rotation-free, strain tensor, sometimes also called the displacement tensor, will be needed.

Box 1 Elasticity, Tensors and the Summation Convention

Consider the process of hanging a weight from a string, which stretches slightly under the increased tension. Adding or removing a little weight changes the tension in the string causing a change in its extension. Hooke's law models the extension of the string as proportional to the tension in the string. That is, extension is a linear function of tension. This is a good model for many materials provided the changes in extension are small.

For a 3D medium the concept of tension generalises to stress τ_{ij} and the concept of extension generalises to strain ε_{ij} . Stress and strain are examples of a tensor: a mathematical object which is characterized by a number of indices (the *order* or *rank* of the tensor) and which obeys well-defined rules for how the tensor components change when there is a transformation of coordinates. Tensors are often used to represent physical quantities. For example, scalars like mass are zero-order tensors, vectors are first-order tensors and stress and strain are second order tensors.

Of the possible linear relationships between stress and strain the most general is that the stress in any given direction is a weighted sum of each component of strain. That is

$$\tau_{ij} = \sum_{p=1,2,3} \sum_{q=1,2,3} c_{ijpq} \varepsilon_{pq}$$

in which c_{ijpq} is called the stiffness tensor. For compactness it is common to assume that a repeated index implies summation and to drop the summation signs:

$$\tau_{ij} = c_{ijpq} \varepsilon_{pq}.$$

This shorthand notation is sometimes called the Einstein summation convention.

Further Reading

H. Jeffreys (1931) *Cartesian tensors* Cambridge University Press, UK.

Substituting (2.3) into (2.2) gives

$$\tau_{ij} = (\lambda \delta_{ij} \varepsilon_{kk} + \mu (\delta_{ip} \delta_{jq} + \delta_{iq} \delta_{jp})) \varepsilon_{pq} \quad (2.4)$$

$$= \lambda \delta_{ij} \varepsilon_{kk} + 2\mu \varepsilon_{ij} \quad (2.5)$$

where ε_{kk} is the cubic dilatation. Substituting the equation of deformation (2.1) into (2.5) yields the relationship between stress and displacement:

$$\tau_{ij} = \lambda \delta_{ij} \varepsilon_{kk} + 2\mu \varepsilon_{ij} \quad (2.6)$$

$$= \lambda \delta_{ij} \left(\frac{1}{2} (\partial_k u_k + \partial_k u_k) + h_{kk} \right) + 2\mu \left(\frac{1}{2} (\partial_i u_j + \partial_j u_i) + h_{ij} \right) \quad (2.7)$$

$$= \lambda \delta_{ij} (\partial_k u_k + h_{kk}) + \mu (\partial_i u_j + \partial_j u_i) + 2\mu h_{ij}. \quad (2.8)$$

The linearised equation of motion of an elastic solid can be written as

$$\partial_j \tau_{ij} - \rho \partial_t^2 u_i = -f_i \quad (2.9)$$

where ρ is the density of the solid and \mathbf{f} is the volume source density of volume force (Achenbach 1973).

Substituting (2.8) into (2.9) gives

$$\partial_j \left[\lambda \delta_{ij} (\partial_k u_k + h_{kk}) + \mu (\partial_i u_j + \partial_j u_i) + 2\mu h_{ij} \right] - \rho \partial_t^2 u_i = -f_i \quad (2.10)$$

$$\lambda \partial_i \partial_k u_k + \lambda \partial_i h_{kk} + \mu \partial_j \partial_i u_j + \mu \partial_j \partial_j u_i + \partial_j 2\mu h_{ij} - \rho \partial_t^2 u_i = -f_i \quad (2.11)$$

$$(\lambda + \mu) \partial_i \partial_k u_k + \mu \partial_j \partial_j u_i - \rho \partial_t^2 u_i = -f_i - \lambda \partial_i h_{kk} - 2\mu \partial_j h_{ij}. \quad (2.12)$$

Rewriting Equation (2.12) in our usual notation we have the elastic wave equation (Aki & Richards 1980, Equation 4.1, page 64)

$$(\lambda + \mu) \nabla (\nabla \cdot \mathbf{u}) + \mu \nabla^2 \mathbf{u} - \rho \frac{\partial^2 \mathbf{u}}{\partial t^2} = -\mathbf{f} - \lambda \nabla \text{trace}(\mathbf{H}) - 2\mu \nabla \mathbf{H} \quad (2.13)$$

where $\text{trace}(\mathbf{H}) = h_{kk}$ is the trace of the source density of strain \mathbf{H} .

2.1.2 Maxwell's Equations

In this section the equations which describe the behaviour of electromagnetic fields are set out. Beginning from the fundamental empirical relations for general media and general sources, the governing equations are derived for media and sources of interest to this study. Ultimately this yields a vector diffusion equation in the electric or magnetic field.

Maxwell's equations are the fundamental relations which have been demonstrated by experiment to describe macroscopic electromagnetic phenomena. They are

$$\nabla \cdot \mathbf{D}(\mathbf{x}, t) = \rho_f \quad (2.14)$$

$$\nabla \cdot \mathbf{B}(\mathbf{x}, t) = 0 \quad (2.15)$$

$$\nabla \times \mathbf{E}(\mathbf{x}, t) = -\frac{\partial \mathbf{B}(\mathbf{x}, t)}{\partial t} - \mathbf{K}^s(\mathbf{x}, t) \quad (2.16)$$

$$\nabla \times \mathbf{H}(\mathbf{x}, t) = \frac{\partial \mathbf{D}(\mathbf{x}, t)}{\partial t} + \mathbf{J}^c(\mathbf{x}, t) + \mathbf{J}^s(\mathbf{x}, t) \quad (2.17)$$

where $\mathbf{D}(\mathbf{x}, t)$ is the electric displacement, ρ_f is the volume density of free charge, $\mathbf{B}(\mathbf{x}, t)$ is the magnetic induction, $\mathbf{E}(\mathbf{x}, t)$ is the electric field, $\mathbf{H}(\mathbf{x}, t)$ is the magnetic field, $\mathbf{K}^s(\mathbf{x}, t)$ is the source volume density of magnetic current, $\mathbf{J}^s(\mathbf{x}, t)$ is the source volume density of electric current, $\mathbf{J}^c(\mathbf{x}, t)$ is the conduction current and by analogy $\frac{\partial \mathbf{D}(\mathbf{x}, t)}{\partial t}$ is called the displacement current (Slob 1994).

We assume that all media are linear, isotropic and homogeneous, and that their electrical properties do not vary over the time scales on which our electromagnetic investigations take place. Thus we write

$$\mu = \mu_0 = 4\pi \times 10^{-7} \text{H m}^{-1} \quad (2.18)$$

$$\mathbf{B}(\mathbf{x}, t) = \mu \mathbf{H}(\mathbf{x}, t) \quad (2.19)$$

$$\mathbf{D}(\mathbf{x}, t) = \epsilon \mathbf{E}(\mathbf{x}, t) \quad (2.20)$$

$$\mathbf{J}^c(\mathbf{x}, t) = \sigma \mathbf{E}(\mathbf{x}, t) \quad (2.21)$$

where ϵ is the dielectric permittivity and σ is the electrical conductivity. These assumptions are routine for exploration over volcanics, sedimentary and metamorphic rocks and target bodies in hydrogeological and oil and gas exploration.²

Substituting equation (2.19) in (2.16) yields

$$\nabla \times \mathbf{E}(\mathbf{x}, t) = -\mu \frac{\partial \mathbf{H}(\mathbf{x}, t)}{\partial t} - \mathbf{K}^s(\mathbf{x}, t). \quad (2.22)$$

Substituting equations (2.20) and (2.21) in (2.17) we obtain

$$\nabla \times \mathbf{H}(\mathbf{x}, t) = \epsilon \frac{\partial \mathbf{E}(\mathbf{x}, t)}{\partial t} + \sigma \mathbf{E}(\mathbf{x}, t) + \mathbf{J}^s(\mathbf{x}, t). \quad (2.23)$$

Taking the curl of (2.22) yields

$$\nabla \times \nabla \times \mathbf{E}(\mathbf{x}, t) = -\mu \frac{\partial \nabla \times \mathbf{H}(\mathbf{x}, t)}{\partial t} - \nabla \times \mathbf{K}^s(\mathbf{x}, t). \quad (2.24)$$

Substituting for $\nabla \times \mathbf{H}$ from (2.23) in (2.24) gives

$$\nabla \times \nabla \times \mathbf{E}(\mathbf{x}, t) + \mu\epsilon \frac{\partial^2 \mathbf{E}(\mathbf{x}, t)}{\partial t^2} + \mu\sigma \frac{\partial \mathbf{E}(\mathbf{x}, t)}{\partial t} = -\mu \frac{\partial \mathbf{J}^s(\mathbf{x}, t)}{\partial t} - \nabla \times \mathbf{K}^s(\mathbf{x}, t). \quad (2.25)$$

Similarly, taking the curl of (2.23) yields

$$\nabla \times \nabla \times \mathbf{H}(\mathbf{x}, t) = \epsilon \frac{\partial \nabla \times \mathbf{E}(\mathbf{x}, t)}{\partial t} + \sigma \nabla \times \mathbf{E}(\mathbf{x}, t) + \nabla \times \mathbf{J}^s(\mathbf{x}, t). \quad (2.26)$$

Substituting for $\nabla \times \mathbf{E}$ from (2.22) in (2.26) yields

$$\nabla \times \nabla \times \mathbf{H}(\mathbf{x}, t) + \mu\epsilon \frac{\partial^2 \mathbf{H}(\mathbf{x}, t)}{\partial t^2} + \mu\sigma \frac{\partial \mathbf{H}(\mathbf{x}, t)}{\partial t} = -\epsilon \frac{\partial \mathbf{K}^s(\mathbf{x}, t)}{\partial t} - \sigma \mathbf{K}^s(\mathbf{x}, t) + \nabla \times \mathbf{J}^s(\mathbf{x}, t). \quad (2.27)$$

The left hand side of equation (2.25) or (2.27) may be written as

$$\nabla \times \nabla \times \mathbf{F}(\mathbf{x}, t) + \mu\epsilon \frac{\partial^2 \mathbf{F}(\mathbf{x}, t)}{\partial t^2} + \mu\sigma \frac{\partial \mathbf{F}(\mathbf{x}, t)}{\partial t} \quad (2.28)$$

where $\mathbf{F}(\mathbf{x}, t)$ is now one of $\mathbf{E}(\mathbf{x}, t)$ or $\mathbf{H}(\mathbf{x}, t)$. The behaviour of this differential operator over the frequency range of interest to transient EM surveying can be analysed in the Fourier

²These assumptions are widely made because usually they are good approximations of the Earth we encounter. However it is important to be aware of anisotropy effects which can arise where fine layering is not resolved but results in an anisotropic bulk response.

domain. Taking the Fourier transform of (2.28) with respect to time gives

$$\nabla \times \nabla \times \tilde{\mathbf{F}}(\mathbf{x}, \omega) + i\omega\mu(i\omega\epsilon - \sigma)\tilde{\mathbf{F}}(\mathbf{x}, \omega) \quad (2.29)$$

In the Earth, the ratio σ/ϵ is unlikely to be below 10^8 S F^{-1} (Keller 1987), and so for frequencies below, say, 10^5 Hz it is reasonable to make the diffusive approximation and drop the term $\omega^2\mu\epsilon\tilde{\mathbf{F}}(\mathbf{x}, \omega)$ in (2.29). This is equivalent to dropping the term $\mu\epsilon\frac{\partial^2\mathbf{F}(\mathbf{x}, t)}{\partial t^2}$ in (2.28) or the displacement current term, $\frac{\partial\mathbf{D}(\mathbf{x}, t)}{\partial t}$, in (2.17).

Similarly the source term $-\epsilon\frac{\partial\mathbf{K}^s(\mathbf{x}, t)}{\partial t} - \sigma\mathbf{K}^s(\mathbf{x}, t)$ from Equation (2.27) has a Fourier transform

$$i\omega\epsilon\tilde{\mathbf{K}}^s(\mathbf{x}, \omega) - \sigma\tilde{\mathbf{K}}^s(\mathbf{x}, \omega) \quad (2.30)$$

and for the frequencies of interest it is reasonable to discard the term $i\omega\epsilon\tilde{\mathbf{K}}^s(\mathbf{x}, \omega)$.

After dropping these terms, equations (2.22), (2.23), (2.25) and (2.27) become

$$\nabla \times \mathbf{E}(\mathbf{x}, t) = -\mu\frac{\partial\mathbf{H}(\mathbf{x}, t)}{\partial t} - \mathbf{K}^s(\mathbf{x}, t) \quad (2.31)$$

$$\nabla \times \mathbf{H}(\mathbf{x}, t) = \sigma\mathbf{E}(\mathbf{x}, t) + \mathbf{J}^s(\mathbf{x}, t) \quad (2.32)$$

$$\nabla \times \nabla \times \mathbf{E}(\mathbf{x}, t) + \mu\sigma\frac{\partial\mathbf{E}(\mathbf{x}, t)}{\partial t} = -\mu\frac{\partial\mathbf{J}^s(\mathbf{x}, t)}{\partial t} - \nabla \times \mathbf{K}^s(\mathbf{x}, t) \quad (2.33)$$

$$\nabla \times \nabla \times \mathbf{H}(\mathbf{x}, t) + \mu\sigma\frac{\partial\mathbf{H}(\mathbf{x}, t)}{\partial t} = -\sigma\mathbf{K}^s(\mathbf{x}, t) + \nabla \times \mathbf{J}^s(\mathbf{x}, t). \quad (2.34)$$

Using the vector identity

$$\nabla \times \nabla \times \mathbf{F}(\mathbf{x}, t) = \nabla\nabla\cdot\mathbf{F}(\mathbf{x}, t) - \nabla^2\mathbf{F}(\mathbf{x}, t), \quad (2.35)$$

equations (2.33) and (2.34) become

$$\nabla^2\mathbf{E}(\mathbf{x}, t) - \mu\sigma\frac{\partial\mathbf{E}(\mathbf{x}, t)}{\partial t} = \mu\frac{\partial\mathbf{J}^s(\mathbf{x}, t)}{\partial t} + \nabla \times \mathbf{K}^s(\mathbf{x}, t) + \nabla\nabla\cdot\mathbf{E}(\mathbf{x}, t) \quad (2.36)$$

$$\nabla^2\mathbf{H}(\mathbf{x}, t) - \mu\sigma\frac{\partial\mathbf{H}(\mathbf{x}, t)}{\partial t} = \sigma\mathbf{K}^s(\mathbf{x}, t) - \nabla \times \mathbf{J}^s(\mathbf{x}, t) + \nabla\nabla\cdot\mathbf{H}(\mathbf{x}, t). \quad (2.37)$$

From equations (2.31) and (2.32) expressions can be derived for $\nabla\nabla\cdot\mathbf{E}(\mathbf{x}, t)$ and $\nabla\nabla\cdot\mathbf{H}(\mathbf{x}, t)$ in terms of the electric and magnetic sources. Taking the divergence of (2.31) gives

$$\nabla\cdot\nabla \times \mathbf{E}(\mathbf{x}, t) = -\mu\frac{\partial\nabla\cdot\mathbf{H}(\mathbf{x}, t)}{\partial t} - \nabla\cdot\mathbf{K}^s(\mathbf{x}, t). \quad (2.38)$$

Using the result that, for all twice differentiable functions \mathbf{E} , $\nabla\cdot\nabla \times \mathbf{E} \equiv 0$ gives

$$\mu\frac{\partial\nabla\cdot\mathbf{H}(\mathbf{x}, t)}{\partial t} = -\nabla\cdot\mathbf{K}^s(\mathbf{x}, t) \quad (2.39)$$

$$\nabla\cdot\mathbf{H}(\mathbf{x}, t) = -\frac{1}{\mu}\int_{\tau=0}^t \nabla\cdot\mathbf{K}^s(\mathbf{x}, \tau)d\tau. \quad (2.40)$$

Taking the divergence of (2.32) gives

$$\nabla \cdot \nabla \times \mathbf{H}(\mathbf{x}, t) = \sigma \nabla \cdot \mathbf{E}(\mathbf{x}, t) + \nabla \cdot \mathbf{J}^s(\mathbf{x}, t). \quad (2.41)$$

Using the result that, for all twice differentiable functions \mathbf{H} , $\nabla \cdot \nabla \times \mathbf{H} \equiv 0$ gives

$$\sigma \nabla \cdot \mathbf{E}(\mathbf{x}, t) = -\nabla \cdot \mathbf{J}^s(\mathbf{x}, t) \quad (2.42)$$

$$\nabla \cdot \mathbf{E}(\mathbf{x}, t) = -\frac{1}{\sigma} \nabla \cdot \mathbf{J}^s(\mathbf{x}, t). \quad (2.43)$$

Substituting (2.43) into (2.36) and (2.40) into (2.37) yields

$$\nabla^2 \mathbf{E}(\mathbf{x}, t) - \mu \sigma \frac{\partial \mathbf{E}(\mathbf{x}, t)}{\partial t} = \mu \frac{\partial \mathbf{J}^s(\mathbf{x}, t)}{\partial t} + \nabla \times \mathbf{K}^s(\mathbf{x}, t) - \frac{1}{\sigma} \nabla \nabla \cdot \mathbf{J}^s(\mathbf{x}, t) \quad (2.44)$$

$$\nabla^2 \mathbf{H}(\mathbf{x}, t) - \mu \sigma \frac{\partial \mathbf{H}(\mathbf{x}, t)}{\partial t} = \sigma \mathbf{K}^s(\mathbf{x}, t) - \nabla \times \mathbf{J}^s(\mathbf{x}, t) - \frac{1}{\mu} \int_0^t \nabla \nabla \cdot \mathbf{K}^s(\mathbf{x}, \tau) d\tau. \quad (2.45)$$

Equations (2.44) and (2.45) can be written as

$$\nabla^2 \mathbf{F}(\mathbf{x}, t) - \mu \sigma \frac{\partial \mathbf{F}(\mathbf{x}, t)}{\partial t} = \mathbf{S}(\mathbf{x}, t) \quad (2.46)$$

the vector diffusion equation in \mathbf{F} with source function $\mathbf{S}(\mathbf{x}, t)$. When \mathbf{F} represents the electric field

$$\mathbf{S}(\mathbf{x}, t) = \mu \frac{\partial \mathbf{J}^s(\mathbf{x}, t)}{\partial t} + \nabla \times \mathbf{K}^s(\mathbf{x}, t) - \frac{1}{\sigma} \nabla \nabla \cdot \mathbf{J}^s(\mathbf{x}, t); \quad (2.47)$$

when \mathbf{F} represents the magnetic field

$$\mathbf{S}(\mathbf{x}, t) = \sigma \mathbf{K}^s(\mathbf{x}, t) - \nabla \times \mathbf{J}^s(\mathbf{x}, t) - \frac{1}{\mu} \int_0^t \nabla \nabla \cdot \mathbf{K}^s(\mathbf{x}, \tau) d\tau. \quad (2.48)$$

The vector diffusion equation (2.46) is derived from the fundamental empirical relations for general media and general sources, by considering linear, isotropic and homogeneous media. It is also possible, and useful, to consider an anisotropic conductivity tensor (Yu & Edwards 1992). However this is beyond the scope of this study.

Box 2 James Clerk Maxwell

At Maxwell's centenary Einstein called Maxwell's contributions to physics "the most fruitful that physics has experienced since the time of Newton."

Maxwell was born in 1831 at number 14 India Street, Edinburgh. A member of the Scottish landed gentry, he never lacked the means for a comfortable life. He was not actually a Maxwell at all but belonged to the Clerk family, from Penicuik near Edinburgh. His father John Clerk had to adopt the surname Maxwell when he inherited an estate in "Maxwell territory" near Dumfries, and took up his residence there. Maxwell grew up at Glenlair and returned there throughout his career and again after his death in 1879 at the age of 48.

Despite his contributions to a remarkable variety of subjects it is the electromagnetic field that is Maxwell's crowning legacy.

Most of the work on his *Treatise on Electricity and Magnetism* was done at Glenlair during three years of relative seclusion after his withdrawal from academia in 1868 following a less than illustrious teaching career. He returned to the academic world in 1871 to become the first professor of experimental physics at Cambridge University and the first director of the subsequently famous Cavendish Laboratory.

Maxwell took Faraday's rudimentary qualitative ideas, put them into mathematical form and extended them into a complete theory with equations by which all interactions between electricity and magnetism could be expressed and understood. This was not merely a unification of things already known. The theory predicts the velocity at which electromagnetic radiation travels through space. Although this speed could not be directly measured it could be calculated. The result turned out to be the same as the measured speed of light, which was previously thought to be an unrelated phenomenon. Thus Maxwell's theory led directly to the discovery that light must be a form of electromagnetic radiation and ended centuries of controversy over the nature of light. "Great guns," Maxwell called it in a letter, with uncharacteristic lack of modesty.

Further Reading

J. C. Maxwell (1891) *A treatise on Electricity and Magnetism* Clarendon Press, UK. Republished by Dover, 1954

J. C. Maxwell edited by W. D. Niven (1890), *The Scientific Papers of James Clerk Maxwell*, Cambridge University Press.

Tanford, C. & Reynolds, J. (1992), *The Scientific Traveller*, Wiley.

Zhdanov, M. S. & Keller, G. V. (1994), *The Geoelectrical Methods in Geophysical Exploration*, number 31 in 'Methods in Geochemistry and Geophysics', Elsevier.



Figure 2.1: James Clerk Maxwell

2.2 Solution Using Irrotational and Solenoidal Components

2.2.1 The Completeness Theorem

It is useful to separate the elastic wavefield \mathbf{u} into its irrotational (longitudinal- or pressure-wave) component \mathbf{u}^p and solenoidal (transverse- or shear-wave) component \mathbf{u}^s . By definition

$$\begin{aligned}\mathbf{u} &= \mathbf{u}^p + \mathbf{u}^s \\ \nabla \times \mathbf{u}^p &= 0 \\ \nabla \cdot \mathbf{u}^s &= 0.\end{aligned}\tag{2.49}$$

Box 3 P-Wave and S-Wave Components

A little rearrangement of the elastic wave equation motivates the separation of the elastic wavefield \mathbf{u} into P- and S-wave components \mathbf{u}^p and \mathbf{u}^s . Beginning from Equation (2.13) and using the identity $\nabla \times \nabla \times \mathbf{u} = \nabla(\nabla \cdot \mathbf{u}) - \nabla^2 \mathbf{u}$

$$(\lambda + 2\mu)\nabla(\nabla \cdot \mathbf{u}) - \mu(\nabla(\nabla \cdot \mathbf{u}) - \nabla^2 \mathbf{u}) - \rho \frac{\partial^2 \mathbf{u}}{\partial t^2} = -\mathbf{f} - \lambda \nabla \text{trace}(\mathbf{H}) - 2\mu \nabla \mathbf{H} \tag{2.50}$$

$$\rho \alpha^2 \nabla(\nabla \cdot \mathbf{u}) - \rho \beta^2 \nabla \times \nabla \times \mathbf{u} - \rho \frac{\partial^2 \mathbf{u}}{\partial t^2} = \mathbf{f}^p + \mathbf{f}^s \tag{2.51}$$

$$\alpha^2 \nabla(\nabla \cdot (\mathbf{u}^p + \mathbf{u}^s)) - \beta^2 \nabla \times \nabla \times (\mathbf{u}^p + \mathbf{u}^s) - \frac{\partial^2 (\mathbf{u}^p + \mathbf{u}^s)}{\partial t^2} = \frac{1}{\rho} (\mathbf{f}^p + \mathbf{f}^s) \tag{2.52}$$

$$\alpha^2 \nabla(\nabla \cdot \mathbf{u}^p) - \beta^2 \nabla \times \nabla \times (\mathbf{u}^s) - \frac{\partial^2 \mathbf{u}^p}{\partial t^2} - \frac{\partial^2 \mathbf{u}^s}{\partial t^2} = \frac{1}{\rho} (\mathbf{f}^p + \mathbf{f}^s) \tag{2.53}$$

where $\alpha^2 = (\lambda + 2\mu)/\rho$, $\beta^2 = \mu/\rho$, $\text{trace}(\mathbf{H}) = h_{kk}$ is the trace of the source density of strain \mathbf{H} and \mathbf{f}^p and \mathbf{f}^s are the P and S components of the source force field. Taking insight from this we could define \mathbf{u}^p and \mathbf{u}^s by equations (2.49) and

$$\alpha^2 \nabla(\nabla \cdot \mathbf{u}^p) - \frac{\partial^2 \mathbf{u}^p}{\partial t^2} = \frac{1}{\rho} \mathbf{f}^p \tag{2.54}$$

$$-\beta^2 \nabla \times \nabla \times (\mathbf{u}^s) - \frac{\partial^2 \mathbf{u}^s}{\partial t^2} = \frac{1}{\rho} \mathbf{f}^s. \tag{2.55}$$

Using the identity $-\nabla \times \nabla \times \mathbf{u} = \nabla^2 \mathbf{u} - \nabla(\nabla \cdot \mathbf{u})$ and remembering that by definition $\nabla \cdot \mathbf{u}^s = 0$ we can re-write these as

$$\nabla(\nabla \cdot \mathbf{u}^p) - \frac{1}{\alpha^2} \frac{\partial^2 \mathbf{u}^p}{\partial t^2} = \mathbf{T}^p \tag{2.56}$$

$$\nabla^2 \mathbf{u}^s - \frac{1}{\beta^2} \frac{\partial^2 \mathbf{u}^s}{\partial t^2} = \mathbf{T}^s. \tag{2.57}$$

It is quite easy to see that if \mathbf{u}^p and \mathbf{u}^s satisfy (2.56) and (2.57) then they satisfy the elastic wave equation. However to find such \mathbf{u}^p and \mathbf{u}^s from (2.56) and (2.57) requires solution of two second order partial differential equations which are coupled at sources and interfaces through Equation (2.49). Substitution to remove this coupling results in a fourth-order system. The utility of the completeness theorem is that it provides a solution method which requires only un-coupled second order differential equations to be solved.

Every irrotational field can be expressed as the gradient of a scalar potential, and every solenoidal field has a vector potential. We seek such potentials ϕ and ψ such that

$$\begin{aligned} \mathbf{u}^p &= \nabla \phi \\ \mathbf{u}^s &= \nabla \times \psi \\ \nabla \cdot \psi &= 0. \end{aligned} \tag{2.58}$$

Given a suitable description of the initial conditions the completeness theorem for elastic media³ (Achenbach 1973, page 85, theorem 3.4.2) asserts that every solution of the elastic wave equation can be written in terms of irrotational and solenoidal components characterised by such potentials ϕ and ψ and that these potentials obey uncoupled second-order partial differential equations. The completeness theorem is useful because the individual potentials obey partial differential equations which are simpler than the partial differential equation obeyed by the elastic wavefield.⁴

If the displacement field \mathbf{u} satisfies the elastic wave equation

$$(\lambda + \mu)\nabla(\nabla \cdot \mathbf{u}) + \mu\nabla^2 \mathbf{u} - \rho \frac{\partial^2 \mathbf{u}}{\partial t^2} = \mathbf{T} \tag{2.59}$$

with source terms and initial conditions specified by

$$\mathbf{T} = \nabla \Phi + \nabla \times \Psi \tag{2.60}$$

$$\mathbf{u}(\mathbf{x}, 0) = \nabla A + \nabla \times \mathbf{Y} \tag{2.61}$$

$$\frac{\partial \mathbf{u}(\mathbf{x}, 0)}{\partial t} = \nabla C + \nabla \times \mathbf{Z} \tag{2.62}$$

$$\nabla \cdot \Psi = 0 \tag{2.63}$$

$$\nabla \cdot \mathbf{Z} = 0 \tag{2.64}$$

$$\nabla \cdot \mathbf{Y} = 0 \tag{2.65}$$

the completeness theorem for elastic media states that there exist potentials ϕ and ψ such that

$$\mathbf{u} = \nabla \phi + \nabla \times \psi \tag{2.66}$$

$$\nabla \cdot \psi = 0 \tag{2.67}$$

$$\nabla^2 \phi - \frac{1}{\alpha^2} \frac{\partial^2 \phi}{\partial t^2} = \frac{1}{\rho \alpha^2} \Phi \tag{2.68}$$

$$\nabla^2 \psi - \frac{1}{\beta^2} \frac{\partial^2 \psi}{\partial t^2} = \frac{1}{\rho \beta^2} \Psi \tag{2.69}$$

³The completeness theorem for elastic media is also sometimes called Lamé's theorem (Aki & Richards 1980, page 68, theorem 4.1.1).

⁴The essential difference between the Helmholtz theorem and the completeness theorem is that, while the Helmholtz decomposition provides a recipe for calculating the scalar and vector potentials from a given vector field (Aki & Richards 1980, Box 4.2, page 69), the completeness theorem allows a wavefield to be calculated through the use of scalar and vector potentials which obey given partial differential equations.

where $\alpha^2 = (\lambda + 2\mu)/\rho$ and $\beta^2 = \mu/\rho$. The completeness theorem may be proved by constructing ϕ and ψ as

$$\phi(\mathbf{x}, t) = A + tC + \int_0^t (t - \tau) \left[\frac{1}{\rho} \Phi(\mathbf{x}, \tau) + \alpha^2 \nabla \cdot \mathbf{u}(\mathbf{x}, \tau) \right] d\tau \quad (2.70)$$

$$\psi(\mathbf{x}, t) = \mathbf{Y} + t\mathbf{Z} + \int_0^t (t - \tau) \left[\frac{1}{\rho} \Psi(\mathbf{x}, \tau) - \beta^2 \nabla \times \mathbf{u}(\mathbf{x}, \tau) \right] d\tau \quad (2.71)$$

(Aki & Richards 1980, page 69).

2.2.2 Separation of the Diffusive Response into Irrotational and Solenoidal Components

Although it is common in exploration seismology to separate the wavefield \mathbf{u} into its irrotational (pressure- or P-wave) component \mathbf{u}^p and solenoidal (shear- or S-wave) component \mathbf{u}^s this is not usually done in electromagnetic surveying. Note that equations (2.33) and (2.34) are very similar to the elastic wave equation (2.13). While equation (2.57) is formally similar to (2.46) note that the source term in (2.57) is by definition solenoidal whereas this may not be true of equation (2.46).

In this section a general diffusive field⁵ \mathbf{F} is separated into its irrotational (longitudinal- or P-wave) component \mathbf{F}^p and solenoidal (transverse- or S-wave) component \mathbf{F}^s . The irrotational component is expressed as the gradient of a scalar potential, and the solenoidal component is expressed as the curl of a vector potential. It is then proven that these scalar and vector potentials obey un-coupled, second-order differential equations. This theorem is analogous to, and inspired by, the completeness theorem for elastic media. As with the completeness theorem for elastic media, its utility is that it provides a solution method which requires only un-coupled second order differential equations to be solved.

By definition

$$\begin{aligned} \mathbf{F} &= \mathbf{F}^p + \mathbf{F}^s \\ \nabla \times \mathbf{F}^p &= 0 \\ \nabla \cdot \mathbf{F}^s &= 0 \end{aligned} \quad (2.72)$$

Every irrotational field can be expressed as the gradient of a potential, and every solenoidal field has a vector potential. We seek such potentials ϕ and ψ such that

$$\mathbf{F}^p = \nabla \phi \quad (2.73)$$

⁵Physically realisable electromagnetic fields \mathbf{E} and \mathbf{H} are not merely solutions to the diffusion equation (2.46) they must in also satisfy Equations (2.14) and (refe:M2). If the diffusive field \mathbf{F} represents one of \mathbf{E} or \mathbf{H} then these additional constraints are manifested in the source term \mathbf{S} . The decomposition presented here holds for a general diffusive field, and is later applied to calculate the diffusive response for a directed point source term. This provides a useful intermediate mathematical construct but does not correspond to a physically realisable EM field.

$$\mathbf{F}^s = \nabla \times \psi \quad (2.74)$$

Theorem 2.1 A Completeness Theorem for Diffusive Media

If the field $\mathbf{F}(\mathbf{x}, t)$ satisfies

$$\nabla^2 \mathbf{F}(\mathbf{x}, t) - \frac{1}{c^2} \frac{\partial \mathbf{F}(\mathbf{x}, t)}{\partial t} = \mathbf{S}(\mathbf{x}, t) \quad (2.75)$$

with source terms and initial conditions specified by

$$\mathbf{S} = \nabla \Phi + \nabla \times \Psi \quad (2.76)$$

$$\mathbf{F}(\mathbf{x}, 0) = \nabla A + \nabla \times \mathbf{Y} \quad (2.77)$$

$$\nabla \cdot \Psi = 0 \quad (2.78)$$

$$\nabla \cdot \mathbf{Y} = 0 \quad (2.79)$$

then there exist potentials ϕ, ψ such that

$$\mathbf{F}(\mathbf{x}, t) = \nabla \phi + \nabla \times \psi \quad (2.80)$$

$$\nabla \cdot \psi = 0 \quad (2.81)$$

$$\nabla^2 \phi - \frac{1}{c^2} \frac{\partial \phi}{\partial t} = \Phi \quad (2.82)$$

$$\nabla^2 \psi - \frac{1}{c^2} \frac{\partial \psi}{\partial t} = \Psi. \quad (2.83)$$

Proof

Proof of Theorem 2.1 is by construction of the potentials ϕ and ψ . We define

$$\phi(\mathbf{x}, t) = A + c^2 \int_0^t [\nabla \cdot \mathbf{F}(\mathbf{x}, \tau) - \Phi(\mathbf{x}, \tau)] d\tau \quad (2.84)$$

$$\psi(\mathbf{x}, t) = \mathbf{Y} + c^2 \int_0^t [-\nabla \times \mathbf{F}(\mathbf{x}, \tau) - \Psi(\mathbf{x}, \tau)] d\tau \quad (2.85)$$

and now prove each of the properties (2.80), (2.81), (2.82) and (2.83) in turn.

Taking the gradient of (2.84) we have

$$\nabla \phi(\mathbf{x}, t) = \nabla c^2 \int_0^t [\nabla \cdot \mathbf{F}(\mathbf{x}, \tau) - \Phi(\mathbf{x}, \tau)] d\tau + \nabla A \quad (2.86)$$

$$= c^2 \int_0^t [\nabla(\nabla \cdot \mathbf{F}(\mathbf{x}, \tau)) - \nabla \Phi(\mathbf{x}, \tau)] d\tau + \nabla A \quad (2.87)$$

taking the curl of (2.85) we have

$$\nabla \times \psi(\mathbf{x}, t) = \nabla \times c^2 \int_0^t [-\nabla \times \mathbf{F}(\mathbf{x}, \tau) - \Psi(\mathbf{x}, \tau)] d\tau + \nabla \times \mathbf{Y} \quad (2.88)$$

$$= c^2 \int_0^t [-\nabla \times \nabla \times \mathbf{F}(\mathbf{x}, \tau) - \nabla \times \Psi(\mathbf{x}, \tau)] d\tau + \nabla \times \mathbf{Y} \quad (2.89)$$

hence

$$\begin{aligned} \nabla\phi(\mathbf{x}, t) + \nabla \times \psi(\mathbf{x}, t) &= c^2 \int_0^t [\nabla(\nabla \cdot \mathbf{F}(\mathbf{x}, \tau)) - \nabla\Phi(\mathbf{x}, \tau) - \nabla \times \nabla \times \mathbf{F}(\mathbf{x}, \tau) - \nabla \times \Psi(\mathbf{x}, \tau)] d\tau \\ &\quad + \nabla A + \nabla \times \mathbf{Y} \end{aligned} \quad (2.90)$$

$$= c^2 \int_0^t [\nabla^2 \mathbf{F}(\mathbf{x}, \tau) - \nabla\Phi(\mathbf{x}, \tau) - \nabla \times \Psi(\mathbf{x}, \tau)] d\tau + \nabla A + \nabla \times \mathbf{Y} \quad (2.91)$$

$$\begin{aligned} &= c^2 \int_0^t \left[\frac{1}{c^2} \frac{\partial \mathbf{F}(\mathbf{x}, \tau)}{\partial \tau} + \mathbf{S}(\mathbf{x}, \tau) - \nabla\Phi(\mathbf{x}, \tau) - \nabla \times \Psi(\mathbf{x}, \tau) \right] d\tau \\ &\quad + \nabla A + \nabla \times \mathbf{Y} \end{aligned} \quad (2.92)$$

$$= \int_0^t \frac{\partial \mathbf{F}(\mathbf{x}, \tau)}{\partial \tau} d\tau + \nabla A + \nabla \times \mathbf{Y} \quad (2.93)$$

$$= \mathbf{F}(\mathbf{x}, t) - \mathbf{F}(\mathbf{x}, 0) + \nabla A + \nabla \times \mathbf{Y} \quad (2.94)$$

$$= \mathbf{F}(\mathbf{x}, t) \quad (2.95)$$

this proves property (2.80).

Taking the divergence of equation (2.85)

$$\nabla \cdot \psi(\mathbf{x}, t) = \nabla \cdot c^2 \int_0^t [-\nabla \times \mathbf{F}(\mathbf{x}, \tau) - \Psi(\mathbf{x}, \tau)] d\tau + \nabla \cdot \mathbf{Y} \quad (2.96)$$

$$= c^2 \int_0^t [-\nabla \cdot \nabla \times \mathbf{F}(\mathbf{x}, \tau) - \nabla \cdot \Psi(\mathbf{x}, \tau)] d\tau + \nabla \cdot \mathbf{Y} \quad (2.97)$$

$$= c^2 \int_0^t [0 - 0] d\tau + 0 \quad (2.98)$$

$$= 0 \quad (2.99)$$

this proves property (2.81).

From (2.80), which is proven above, we can see that

$$\nabla\phi = \mathbf{F}(\mathbf{x}, t) - \nabla \times \psi. \quad (2.100)$$

Taking the divergence of this relation gives

$$\nabla \cdot (\nabla\phi) = \nabla \cdot (\mathbf{F}(\mathbf{x}, t) - \nabla \times \psi) \quad (2.101)$$

$$= \nabla \cdot \mathbf{F}(\mathbf{x}, t). \quad (2.102)$$

Taking the derivative of (2.84), the definition of ϕ , and bearing mind that A is a constant

$$\frac{\partial \phi(\mathbf{x}, t)}{\partial t} = \frac{\partial}{\partial t} \left\{ c^2 \int_0^t [\nabla \cdot \mathbf{F}(\mathbf{x}, \tau) - \Phi(\mathbf{x}, \tau)] d\tau \right\} + \frac{\partial A}{\partial t} \quad (2.103)$$

$$= c^2 [\nabla \cdot \mathbf{F}(\mathbf{x}, t) - \Phi(\mathbf{x}, t)] \quad (2.104)$$

$$\frac{1}{c^2} \frac{\partial \phi(\mathbf{x}, t)}{\partial t} = \nabla \cdot \mathbf{F}(\mathbf{x}, t) - \Phi(\mathbf{x}, t) \quad (2.105)$$

Property (2.82) is now easy to demonstrate using (2.102) and (2.105) to substitute into the left hand side.

$$\nabla^2 \phi - \frac{1}{c^2} \frac{\partial \phi}{\partial t} = \nabla \cdot \mathbf{F}(\mathbf{x}, t) - (\nabla \cdot \mathbf{F}(\mathbf{x}, t) - \Phi(\mathbf{x}, t)) \quad (2.106)$$

$$= \Phi(\mathbf{x}, t) \quad (2.107)$$

Taking the curl of (2.80), which is proven above,

$$\nabla \times \mathbf{F}(\mathbf{x}, t) = \nabla \times \nabla \phi(\mathbf{x}, t) + \nabla \times \nabla \times \psi \quad (2.108)$$

$$= 0 + \nabla(\nabla \cdot \psi) - \nabla^2 \psi \quad (2.109)$$

$$= -\nabla^2 \psi. \quad (2.110)$$

Taking the derivative of (2.85), the definition of ψ , and bearing in mind that \mathbf{Y} is a constant

$$\frac{\partial \psi(\mathbf{x}, t)}{\partial t} = \frac{\partial}{\partial t} c^2 \int_0^t [-\nabla \times \mathbf{F}(\mathbf{x}, \tau) - \Psi(\mathbf{x}, \tau)] d\tau + \frac{\partial \mathbf{Y}}{\partial t} \quad (2.111)$$

$$= c^2 [-\nabla \times \mathbf{F}(\mathbf{x}, t) - \Psi(\mathbf{x}, t)] \quad (2.112)$$

$$\frac{1}{c^2} \frac{\partial \psi(\mathbf{x}, t)}{\partial t} = -\nabla \times \mathbf{F}(\mathbf{x}, t) - \Psi(\mathbf{x}, t). \quad (2.113)$$

Property (2.83) is now quite easy to demonstrate using (2.107) and (2.113) to substitute into the left hand side.

$$\nabla^2 \psi - \frac{1}{c^2} \frac{\partial \psi(\mathbf{x}, t)}{\partial t} = -\nabla \times \mathbf{F}(\mathbf{x}, t) - (-\nabla \times \mathbf{F}(\mathbf{x}, t) - \Psi(\mathbf{x}, t)) \quad (2.114)$$

$$= \Psi(\mathbf{x}, t) \quad (2.115)$$

Box 4 Representation and Calculation of The Electromagnetic Field Using Potentials

The calculation of analytical expressions for the electromagnetic field can be eased by representing the electric and magnetic fields in terms of potentials. Several representations are possible including the Schelkunoff potentials which employ two vector and two scalar potentials (Ward & Hohmann 1987, Schelkunoff 1943), the Debye potentials which employ two scalar potentials (Strack 1992) and in this thesis \mathbf{F} , the electric or magnetic field, is divided into its irrotational and solenoidal components and represented using a scalar and vector potential

$$\mathbf{F} = \nabla\phi + \nabla \times \psi \quad (2.116)$$

$$\nabla \cdot \psi = 0. \quad (2.117)$$

The standard representation employing a scalar and vector potential is

$$\mathbf{B} = \nabla \times \mathbf{A} \quad (2.118)$$

$$\mathbf{E} = -\frac{\partial \mathbf{A}}{\partial t} - \nabla \Phi \quad (2.119)$$

$$\nabla \cdot \mathbf{A} = -\mu\sigma\Phi \quad (2.120)$$

(Weaver 1994, Morse & Feshbach 1953). These potentials can in turn be represented using the electric Hertz vector $\mathbf{\Pi}$ and the magnetic Hertz vector $\mathbf{\Gamma}$, defined in uniform regions as

$$\Phi = -\nabla \cdot \mathbf{\Pi} \quad (2.121)$$

$$\mathbf{A} = \mu\sigma\mathbf{\Pi} + \nabla \times \mathbf{\Gamma} \quad (2.122)$$

(Weaver 1994). In terms of the Hertz vectors the electric and magnetic fields are

$$\mathbf{E} = -\mu\sigma\frac{\partial \mathbf{\Pi}}{\partial t} - \nabla \times \frac{\partial \mathbf{\Gamma}}{\partial t} + \nabla \{\nabla \cdot \mathbf{\Pi}\} \quad (2.123)$$

$$\mathbf{B} = \mu\sigma\nabla \times \mathbf{\Pi} + \nabla \times \nabla \times \mathbf{\Gamma} \quad (2.124)$$

Considering the source terms for the electric and magnetic fields given by Equations (2.47) and (2.48) and comparing these with Equations (2.123) and (2.124) we recognise that the electric and magnetic Hertz vectors are closely related to the solution of the vector diffusion equation (2.46) with source terms corresponding to, respectively, the volume density of electric source current and magnetic dipole moment.

Chapter 3 develops methods for solving the the vector diffusion equation and these are applied in Chapter 4 to find the solutions for a directed point source term.

Further Reading

Morse, P. M. and Feshbach H. (1953) *Methods of Theoretical Physics*, McGraw-Hill.

Schelkunoff, S. A. (1943), *Electromagnetic Waves*, Van Nostrand.

Strack, K. M. (1992), *Exploration with Deep Transient Electromagnetics*, Elsevier.

Ward, S. H. & Hohmann, G. W. (1987), *Electromagnetic theory for geophysical applications*, in M. N. Nabighian, ed., 'Electromagnetic Methods in Applied Geophysics', Investigations in Geophysics, SEG, pp. 131–311. Volume I, Theory.

Weaver, J. T. (1994), *Mathematical methods for geo-electromagnetic induction*, Wiley.

2.3 Conclusions

The propagation of mechanical disturbances in a homogeneous, isotropic and perfectly elastic solid is described by the elastic wave equation

$$(\lambda + \mu)\nabla(\nabla\cdot\mathbf{u}) + \mu\nabla^2\mathbf{u} - \varrho\frac{\partial^2\mathbf{u}}{\partial t^2} = \mathbf{f} - \lambda\nabla\text{trace}(\mathbf{H}) - 2\mu\nabla\mathbf{H} \quad (2.125)$$

where λ and μ are Lamé coefficients, \mathbf{u} is the particle displacement, ϱ is the density of the solid, \mathbf{f} is the volume source density of volume force and $\text{trace}(\mathbf{H})$ is the trace of the source density of strain \mathbf{H} .

The diffusion-dominated response of a linear, homogeneous and isotropic imperfect conductor is described by the vector diffusion equation

$$\nabla^2\mathbf{F}(\mathbf{x}, t) - \mu\sigma\frac{\partial\mathbf{F}(\mathbf{x}, t)}{\partial t} = \mathbf{S}(\mathbf{x}, t) \quad (2.126)$$

where $\mathbf{F}(\mathbf{x}, t)$ is one of either the electric field $\mathbf{E}(\mathbf{x}, t)$ or magnetic field $\mathbf{H}(\mathbf{x}, t)$, μ is the magnetic permeability, σ is the conductivity and $\mathbf{S}(\mathbf{x}, t)$ is a source term appropriate to either the electric or magnetic field. The special form of physically realisable diffusive electromagnetic fields (i.e. that they are diffusive responses which satisfy all of Maxwell's equations) are manifested in constraints on the form of the source term \mathbf{S} .

The elastic wavefield \mathbf{u} can be divided into irrotational (P-wave) and solenoidal (S-wave) components characterised by potentials ϕ and ψ such that

$$\mathbf{u} = \nabla\phi + \nabla\times\psi. \quad (2.127)$$

The completeness theorem for elastic media asserts that every solution of the elastic wave equation can be written in this way and gives a prescription for calculating the potentials ϕ and ψ from source terms.

A general diffusive field can also be separated into irrotational and solenoidal components. A completeness theorem for diffusive media, analogous to the completeness theorem for elastic media, is presented here. As with the completeness theorem for elastic media, its utility is that it provides a solution method which requires only un-coupled second-order differential equations to be solved.

The completeness theorem is later applied to calculate the diffusive response for a directed point source term. This useful intermediate mathematical construct is closely related to the Hertz vector, but does not correspond to a physically realisable EM field.

Chapter 3

The Diffusive Response and its Equivalent Wavefield

The equivalent wavefield concept relates diffusive propagation to an equivalent non-diffusive, wave propagation, provided equivalent source and boundary conditions are satisfied. The equivalent wavefield concept is applied here to relate diffusive electromagnetic propagation to an equivalent wavefield. This equivalent wavefield is a concept not a physically occurring phenomenon.

The properties of the equivalent medium, equivalent sources, equivalent receivers and equivalent boundary conditions are determined by their electromagnetic counterparts. In this case the velocity of the equivalent wavefield is proportional to the square root of the resistivity of the diffusive electromagnetic medium.

Knowledge of the equivalent wavefield allows calculation of the corresponding diffusive field. This approach may seem circuitous, however the solution of the wave equation for appropriate media, sources and boundary conditions, may be simpler than the direct solution of the diffusion equation. In addition the study of the differences and equivalences between wave propagation and diffusion gives insights into both processes.

3.1 The Equivalent Wavefield Concept

The equivalent wavefield concept relates diffusive propagation to an equivalent non-diffusive, wave propagation, provided equivalent source and boundary conditions are satisfied. The equivalent wavefield concept is applied here to relate diffusive electromagnetic propagation to an equivalent wavefield.

The Q transform is a prescription for calculating a diffusive response from its equivalent wavefield. To motivate the derivation of the Q transform and give a specific example of the Q transform in action, we consider the response to a directed impulsive point source term.

In Figures 3.1a and 3.1b, and similar figures which follow, time is increasing down the page and offset from the source is increasing across the page from left to right. Figures 3.1a and 3.1b depict respectively the response to a directed impulsive point source term in propagative and diffusive media; these are an impulse travelling with constant velocity, and a pulse whose profile gradually changes, dispersing and broadening with increasing time.

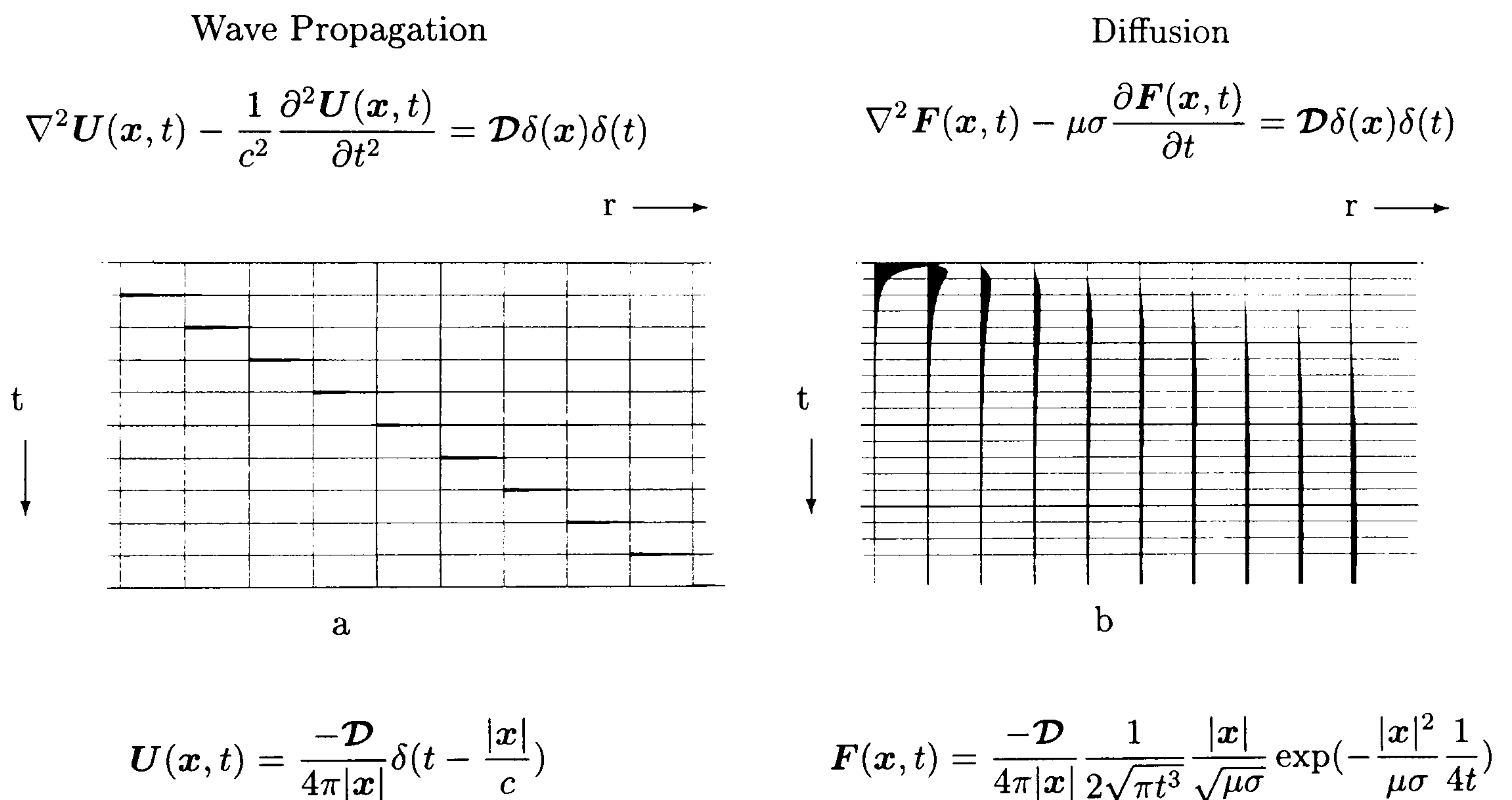


Figure 3.1: Response to a directed impulsive point source term in propagative and diffusive media.

After taking a Laplace transform with respect to time the responses in propagative and diffusive media are

$$\hat{U}(\mathbf{x}, p) = \frac{-\mathcal{D}}{4\pi r} \exp(-\frac{r}{c} p) \quad \hat{\mathbf{F}}(\mathbf{x}, s) = \frac{-\mathcal{D}}{4\pi r} \exp(-r\sqrt{\mu\sigma} s^2) \quad (3.1)$$

where p and s are the Laplace transform parameters for the wave and diffusive domains respectively, $r = |\mathbf{x}|$, \mathbf{F} is the diffusive field and \mathbf{U} is the equivalent wavefield. The diffusive response can be converted into the propagative response simply by writing $\mu\sigma = c^{-2}$, $s = p^2$ and $\hat{\mathbf{F}}(\mathbf{x}, s) = \hat{U}(\mathbf{x}, p)$.

This result is more general. In the Laplace transform domain the (source-free) wave and

diffusion equations are respectively

$$(\nabla^2 - \frac{p^2}{c^2})\hat{U}(\mathbf{x}, p) = 0 \quad (\nabla^2 - s\mu\sigma)\hat{\mathbf{F}}(\mathbf{x}, s) = 0. \quad (3.2)$$

To convert the diffusion equation into the wave equation we simply write $s = p^2$, $\hat{\mathbf{F}}(\mathbf{x}, s) = \hat{U}(\mathbf{x}, p)$ and $\mu\sigma = c^{-2}$. This gives the Q transform in the Laplace transform domain

$$\hat{\mathbf{F}}(\mathbf{x}, p^2) = \hat{U}(\mathbf{x}, p). \quad (3.3)$$

The time domain form of the Q transform is easily calculated by taking the inverse Laplace transform of equation 3.3 to yield

$$\mathbf{F}(\mathbf{x}, t) = \frac{1}{2\sqrt{\pi t^3}} \int_0^\infty q \exp(-\frac{q^2}{4t}) U(\mathbf{x}, q) dq, \quad (3.4)$$

which is known as the Q transform (Lee, Liu & Morrison 1989) or wave transform (Oliver 1994).

Note that the equivalent wavefield is a concept not a physically occurring phenomenon. While the velocity of a physical wavefield will have units of m/s the equivalent velocity $c = 1/\sqrt{\mu\sigma}$ has units of m/ \sqrt{s} .

Box 5 Calculating the Diffusive field of an Equivalent Wavefield

Given an analytic expression for an equivalent wavefield component $U(q)$ a simple recipe may be followed to find the equivalent diffusive field $F(t)$ without calculating the integral

$$F(t) = \frac{1}{2\sqrt{\pi t^3}} \int_0^\infty q \exp(-\frac{q^2}{4t}) U(q) dq.$$

Given the equivalent wavefield $U(q)$

1. calculate its Laplace transform $\hat{U}(p)$,
2. set $\hat{F}(s) = \hat{U}(\sqrt{s})$,
3. calculate the inverse Laplace transform to yield $F(t)$.

Although this recipe is simple, its execution requires the calculation of an inverse Laplace transform which is not always trivial.

3.1.1 How the Q Transform Works

Diffusive responses may usefully be expressed as a sum of exponentially decaying components. Taking the Laplace transform of one such component we obtain

$$\mathcal{L}\{\exp(-at)\}(s) = \frac{1}{s+a}, \quad a > 0. \quad (3.5)$$

Setting $s = p^2$ and taking the inverse Laplace transform from the transform variable p to

the time-like variable q yields

$$\mathcal{L}^{-1} \left[\frac{1}{p^2 + a} \right] (q) = \frac{\sin(\sqrt{a}q)}{\sqrt{a}}. \quad (3.6)$$

Thus the Q transform relates a decaying exponential and a sine wave. A list of some time domain functions and their equivalents in the q domain is presented in Table 0.2.

Box 6 The History of the Q Transform

It is perhaps unclear how to assign credit for the first derivation of the Q transform. Certainly it appears that more than one group may have independently derived equivalent results.

(Bragg & Dettman 1968*a*, Bragg & Dettman 1968*b*) present an early statement of the transform in a generalised form in a short communication to the American Mathematical Society. Almost concurrently (Filippi & Frisch 1969*a*, Filippi & Frisch 1969*b*) present their results on the other side of the Atlantic. Soon after these short, abstract, mathematical notes an equivalent result appears, albeit in the frequency domain, with application to inversion of electromagnetic induction data (Weidelt 1972, equation 5.1).

The running then seems to have been taken up by mathematicians in Eastern Europe (Lavrent'ev, Romanov & Shishatskii 1980, Filatov 1984). The Q transform seems to disappear from the Western literature until taken up in a series of papers by Ki Ha Lee and co-authors. These demonstrated its usefulness both in forward modelling (Lee *et al.* 1989) and inversion (Lee 1988, Lee & Xie 1993). This work should not be confused with the 'electromagnetic migration' work of Seunghee Lee (Lee *et al.* 1987) and (Zhdanov & Frenkel 1988). Work continues on Q transform inversion of EM data in the frequency domain (Levy, Oldenburg & Wang 1988, Gibert & Virieux 1991, Gibert, Tournier & Virieux 1994, Tournier & Gibert 1995) and time domain (Gershenson 1993, Becker, Lee & Wang 1994, Wilson 1994, Slob, Habashy & Torres-Verdin 1995, Becker, Das & Lee 1997, Gershenson 1997).

The Q transform is now becoming more widely known and publicised (De Hoop 1992, De Hoop 1996*b*, De Hoop 1996*a*) and is attracting interest in diverse fields which deal with diffusion problems, including non-destructive testing of metal components (Zorgati, Duchene, Lesselier & Pons 1991, Zorgati, Lesselier, Duchene & Pons 1992), transmission tomography of thermal waves (Mandelis 1991), the investigation of hydrocarbon reservoirs through pressure pulse transients (Oliver 1994), detection of water-borne metallic hazards (Gershenson 1993, Gershenson 1997) and transmission characteristics of fractal media (Hargreaves 1996).

3.1.2 A More Rigorous Derivation

This section provides a more rigorous derivation of the Q transform, which also takes account of source terms. The approach taken is a special case of the much wider derivation in Appendix B, but is carried out in full to allow this section to be read independently.

Considering the obvious similarities between the vector diffusion equation (2.46)

$$\nabla^2 \mathbf{F}(\mathbf{x}, t) - \mu\sigma \frac{\partial \mathbf{F}(\mathbf{x}, t)}{\partial t} = \mathbf{S}(\mathbf{x}, t) \quad (3.7)$$

and the vector wave equation

$$\nabla^2 \mathbf{U}(\mathbf{x}, q) - \frac{1}{c^2} \frac{\partial^2 \mathbf{U}(\mathbf{x}, q)}{\partial q^2} = \mathbf{T}(\mathbf{x}, q), \quad (3.8)$$

we set up our initial value problems as follows

$$\begin{aligned}
\nabla^2 \mathbf{F}(\mathbf{x}, t) - \mu\sigma \frac{\partial \mathbf{F}(\mathbf{x}, t)}{\partial t} &= \mathbf{S}(\mathbf{x}, t), \quad \mathbf{x} \in \mathcal{V}, t > 0 \\
\mathbf{F}(\mathbf{x}, 0) &= \boldsymbol{\alpha}(\mathbf{x}), \quad \mathbf{x} \in \mathcal{V} \\
\mathbf{F}(\mathbf{x}, t) &= \mathbf{f}(\mathbf{x}, t), \quad \mathbf{x} \in \partial\mathcal{V}, t > 0
\end{aligned} \tag{3.9}$$

and

$$\begin{aligned}
\nabla^2 U(\mathbf{x}, q) - \frac{1}{c^2} \frac{\partial^2 U(\mathbf{x}, q)}{\partial q^2} &= \mathbf{T}(\mathbf{x}, q), \quad \mathbf{x} \in \mathcal{V}, q > 0 \\
U(\mathbf{x}, 0) &= 0 \quad \mathbf{x} \in \mathcal{V} \\
\frac{\partial U(\mathbf{x}, 0)}{\partial q} &= \boldsymbol{\alpha}(\mathbf{x}), \quad \mathbf{x} \in \mathcal{V} \\
U(\mathbf{x}, q) &= u(\mathbf{x}, q), \quad \mathbf{x} \in \partial\mathcal{V}, q > 0
\end{aligned} \tag{3.10}$$

In these equations $\mathbf{F}(\mathbf{x}, t)$ is a diffusive field, and $\mathbf{S}(\mathbf{x}, t)$ is a source term representing, in our case, either a current or magnetic dipole source. Similarly $U(\mathbf{x}, q)$ is a wavefield with $\mathbf{T}(\mathbf{x}, q)$ as source term. The independent variable q in equation (3.10) is a time-like variable. The equations are postulated to hold in some homogeneous, isotropic region \mathcal{V} with boundary $\partial\mathcal{V}$.

Taking the Laplace transform of problems (3.9) and (3.10) with respect to t and q with transform parameters s and p respectively we obtain

$$\begin{aligned}
\nabla^2 \hat{\mathbf{F}}(\mathbf{x}, s) - s\mu\sigma \hat{\mathbf{F}}(\mathbf{x}, s) &= \hat{\mathbf{S}}(\mathbf{x}, s) - \boldsymbol{\alpha}(\mathbf{x}), \quad \mathbf{x} \in \mathcal{V} \\
\hat{\mathbf{F}}(\mathbf{x}, s) &= \hat{\mathbf{f}}(\mathbf{x}, s), \quad \mathbf{x} \in \partial\mathcal{V}
\end{aligned} \tag{3.11}$$

and

$$\begin{aligned}
\nabla^2 \hat{U}(\mathbf{x}, p) - \frac{p^2}{c^2} \hat{U}(\mathbf{x}, p) &= \hat{\mathbf{T}}(\mathbf{x}, p) - \boldsymbol{\alpha}(\mathbf{x}), \quad \mathbf{x} \in \mathcal{V} \\
\hat{U}(\mathbf{x}, p) &= \hat{u}(\mathbf{x}, p), \quad \mathbf{x} \in \partial\mathcal{V}
\end{aligned} \tag{3.12}$$

We now require that $c^{-2} = \mu\sigma$, where c is the velocity term in equation (3.8), and make the substitution¹ $p = \sqrt{s}$ in (3.11) and the definition

$$\hat{\mathbf{R}}(\mathbf{x}, s) \equiv \hat{\mathbf{F}}(\mathbf{x}, s) - \hat{U}(\mathbf{x}, \sqrt{s}) \tag{3.13}$$

¹Since p is a Laplace transform parameter, we require $p > 0$, or at the very least $\text{Re}(p) > 0$. This requirement selects the positive square root of s . Happily, this choice ensures that valid, physically realistic solutions are obtained.

then by subtracting equations (3.11) from (3.12) we see that $\hat{\mathbf{R}}(\mathbf{x}, s)$ obeys

$$\begin{aligned}\nabla^2 \hat{\mathbf{R}}(\mathbf{x}, s) - s/c^2 \hat{\mathbf{R}}(\mathbf{x}, s) &= \hat{\mathbf{S}}(\mathbf{x}, s) - \hat{\mathbf{T}}(\mathbf{x}, \sqrt{s}) \quad \mathbf{x} \in \mathcal{V} \\ \hat{\mathbf{R}}(\mathbf{x}, s) &= \hat{\mathbf{f}}(\mathbf{x}, s) - \hat{\mathbf{u}}(\mathbf{x}, \sqrt{s}), \quad \mathbf{x} \in \partial\mathcal{V}.\end{aligned}\tag{3.14}$$

Let us require that the boundary, and source terms in (3.14) match, i.e.

$$\hat{\mathbf{f}}(\mathbf{x}, q) - \hat{\mathbf{u}}(\mathbf{x}, \sqrt{s}) = 0\tag{3.15}$$

and

$$\hat{\mathbf{S}}(\mathbf{x}, q) - \hat{\mathbf{T}}(\mathbf{x}, \sqrt{s}) = 0\tag{3.16}$$

so that all terms on the right hand side of equations (3.14) are identically zero. Then, we may cite a uniqueness theorem and declare that $\hat{\mathbf{R}}(\mathbf{x}, s) \equiv 0$ must be the only solution and in this case

$$\hat{\mathbf{F}}(\mathbf{x}, s) = \hat{\mathbf{U}}(\mathbf{x}, \sqrt{s}).\tag{3.17}$$

By the definition of the Laplace transform (0.7) this implies that

$$\hat{\mathbf{F}}(\mathbf{x}, s) = \int_0^\infty \mathbf{U}(\mathbf{x}, q) \exp(-\sqrt{s}q) dq.\tag{3.18}$$

an equation which has been studied for some time (Weidelt 1972, equation 5.1).

Using the result that for real $q > 0$

$$\mathcal{L} \left[\frac{q}{2\sqrt{\pi t^3}} \exp\left(-\frac{q^2}{4t}\right) \right] = \exp(-\sqrt{s}q)\tag{3.19}$$

(Erdélyi 1954, equation (1), page 245) we take the inverse Laplace transform of equation (3.18) and obtain our result

$$\mathbf{F}(\mathbf{x}, t) = \frac{1}{2\sqrt{\pi t^3}} \int_0^\infty q \exp\left(-\frac{q^2}{4t}\right) \mathbf{U}(\mathbf{x}, q) dq.\tag{3.20}$$

This result has been derived here for a homogeneous, isotropic region. De Hoop (1996*a*) establishes the Q transform between a diffusive electromagnetic field in an arbitrarily inhomogeneous and anisotropic medium and an equivalent non-diffusive electromagnetic field propagating in an equivalent medium. Considering individual electric or magnetic fields, a generalised form of the Q transform is derived between the responses to point-transmitter excitations for either electric- or magnetic-current sources. In this case the resistivity of the diffusive medium is related to the permittivity of the equivalent lossless medium, while the permeabilities of the two are the same.

Box 7 Calculating the Equivalent Wavefield of a Diffusive Field

Given an analytic expression for the strength of a diffusive field component $F(t)$ at a particular point in space; a simple recipe may be followed to find the equivalent wavefield. Given the diffusive field $F(t)$

1. calculate its Laplace transform $\hat{F}(s)$,
2. set $\hat{U}(p) = \hat{F}(p^2)$,
3. calculate the inverse Laplace transform from transform variable p to the time like variable q to yield $U(q)$.

Although this recipe is simple, its execution requires the calculation of an inverse Laplace transform which is not always trivial.

3.1.3 Correspondence of Sources

Recall equation (3.16) which stated that for source functions to match we require

$$\hat{S}(\mathbf{x}, q) = \hat{T}(\mathbf{x}, \sqrt{s}), \quad (3.21)$$

which by the definition of the Laplace transform (0.7) implies that

$$\hat{S}(\mathbf{x}, s) = \int_0^\infty T(\mathbf{x}, q) \exp(-\sqrt{s}q) dq. \quad (3.22)$$

If $S(\mathbf{x}, t) = Q(\mathbf{x})\delta(t - 0^+)$ then the Laplace transform of $S(\mathbf{x}, t)$ with respect to t and with transform parameter s is $\hat{S}(\mathbf{x}, s) = Q(\mathbf{x})$. The crucial point here is that $\hat{S}(\mathbf{x}, s)$ is independent of s . Substituting $\hat{S}(\mathbf{x}, s)$ in (3.22) we obtain

$$Q(\mathbf{x}) = \int_0^\infty \exp(-\sqrt{s}q) T(\mathbf{x}, q) dq, \quad (3.23)$$

which implies

$$T(\mathbf{x}, q) = Q(\mathbf{x})\delta(q - 0^+) \quad (3.24)$$

since otherwise the right hand side of equation (3.23) cannot be independent of s .

3.1.4 The Effect of the Choice of the Time Origin

Let $u(q)$ be the equivalent wavefield corresponding to a diffusive response $f(t)$, and define $v(q)$ by

$$v(q) = \begin{cases} u(q - a) & q > a \\ 0 & q < a \end{cases} \quad (3.25)$$

where $a > 0$. The diffusive response $g(t)$ of the delayed equivalent wavefield $v(q)$ is calculated by applying the recipe outlined in Box 5.

The Laplace transform of $v(q)$ is

$$\hat{v}(s) = \exp(-as)\hat{u}(s) \quad (3.26)$$

(Erdélyi 1954, Equation (4), page 129). By definition

$$\hat{g}(s) = \hat{v}(\sqrt{s}) \quad (3.27)$$

$$= \exp(-a\sqrt{s})\hat{u}(\sqrt{s}) \quad (3.28)$$

$$= \exp(-a\sqrt{s})\hat{f}(s) \quad (3.29)$$

where $u(q)$ is the equivalent wavefield of $f(t)$. Using the results

$$\mathcal{L}^{-1}[\hat{u}_1(s)\hat{u}_2(s)](t) = \int_0^t u_1(\tau)u_2(t-\tau) d\tau \quad (3.30)$$

(Erdélyi 1954, Equation (20), page 131)

$$\mathcal{L}^{-1}[\exp(-a\sqrt{s})](\tau) = \frac{a}{2\sqrt{\pi}}\tau^{-3/2}\exp(-\frac{a^2}{4\tau}) \quad (3.31)$$

(Erdélyi 1954, Equation (28), page 146)

gives

$$g(t) = \int_0^t \frac{a}{2\sqrt{\pi}}\tau^{-3/2}\exp(-\frac{a^2}{4\tau})f(t-\tau) d\tau. \quad (3.32)$$

Hence a simple shift of the time origin in the equivalent wavefield domain results in a more complex change in the corresponding diffusive response.

3.2 Conclusions

The equivalent wavefield concept relates diffusive propagation to an equivalent non-diffusive, wave propagation, provided equivalent source and boundary conditions are satisfied. The equivalent wavefield concept is applied here to relate diffusive electromagnetic propagation to an equivalent wavefield. This equivalent wavefield is a concept not a physically occurring phenomenon.

In this case the velocity of the equivalent wavefield is proportional to the square root of the resistivity of the diffusive electromagnetic medium.

Knowledge of the equivalent wavefield \mathbf{U} allows calculation of the corresponding diffusive electromagnetic field \mathbf{F} using the Q transform

$$\mathbf{F}(\mathbf{x}, t) = \frac{1}{2\sqrt{\pi t^3}} \int_0^\infty q \exp(-\frac{q^2}{4t}) \mathbf{U}(\mathbf{x}, q) dq \quad (3.33)$$

where q is the time-like variable, with dimensions \sqrt{s} , in the equivalent wave domain. The equivalent sources, equivalent receivers and equivalent boundary conditions are similarly linked to their EM counterparts by the Q transform.

The Q transform is equivalent to a non-linear warping of the Laplace transform variable

$$\hat{\mathbf{F}}(\mathbf{x}, p^2) = \hat{\mathbf{U}}(\mathbf{x}, p) \quad (3.34)$$

and can also be thought of as a mapping between decaying exponentials and sine waves.

A simple shift of the time origin in the equivalent wavefield domain results in a more complex change in corresponding diffusive response. Specifically, if $u(q)$ is the equivalent wavefield corresponding to a diffusive response $f(t)$, and $v(q)$ is defined by

$$v(q) = \begin{cases} u(q - a) & q > a \\ 0 & q < a \end{cases} \quad (3.35)$$

where $a > 0$ then the diffusive response $g(t)$ of the delayed equivalent wavefield $v(q)$ is

$$g(t) = \int_0^t \frac{a}{2\sqrt{\pi}} \tau^{-3/2} \exp(-\frac{a^2}{4\tau}) f(t - \tau) d\tau. \quad (3.36)$$

Chapter 4

Point Sources in Infinite Media

Chapter 2 developed the completeness theorem for diffusive media, which states that the diffusive response may be divided into irrotational and solenoidal components each characterised by a potential which itself is the solution of a diffusion equation. In this chapter the equivalent wavefield concept is used to find diffusive responses by first calculating the potentials and components of the equivalent wavefield response.

Initially the response to a point source term is calculated. The response for physically realistic sources is then calculated by combining this response with the source description. Using a moment tensor and a dipole moment to represent electromagnetic dipole sources allows comparison with seismic sources. For example, the equivalent wavefield of the magnetic field generated by an electric current dipole in a whole space is generated by a point source of torque, generating solenoidal waves only.

4.1 EM Responses to Point Sources in Infinite Media

Section 2.1.2 developed Maxwell's equations, which describe the diffusion of electromagnetic (EM) energy through an imperfect conductor such as the Earth. The differential equations which describe electric and magnetic fields in linear, isotropic, homogeneous regions differ only in the source terms. The different source terms are given by Equations (2.47) and (2.48). In these equations derivatives of the source volume density of electric current \mathbf{J}^s and the source volume density of magnetic current \mathbf{K}^s are taken with respect to space and/or time. Consequently even a simple source current density leads to a complicated source term.

This section begins by calculating the response to a directed impulsive point source term. The response to more general sources is then calculated by combining this with the appropriate source description.

4.1.1 Response to a Directed Point Source Term

Starting from the vector diffusion equation in uniform media, this section calculates the diffusive and equivalent wavefield responses to a directed impulsive point source term. The directed impulsive point source term does *not* correspond to a physically realisable electromagnetic source. Hence these responses are only intermediate results; building blocks from which the responses for physically realistic sources are calculated in later sections.

The novel method of calculation employed here divides the diffusive field into irrotational and solenoidal components, and uses the method of Theorem 2.1 to specify differential equations in potentials for each component. These equations are solved using the equivalent wavefield concept, to yield the irrotational and solenoidal components of the equivalent wavefield. From these the equivalent wavefield, and finally the diffusive response are easily calculated. At times it is easier to employ subscript notation and the summation convention — see Box 1.

We seek to solve the vector diffusion equation in \mathbf{F} for a directed point source term aligned in the \mathcal{D} direction and located at the origin of an infinite, homogeneous, isotropic medium of equivalent velocity c . That is, we seek to solve

$$\nabla^2 \mathbf{F}(\mathbf{x}, t) - \frac{1}{c^2} \frac{\partial \mathbf{F}(\mathbf{x}, t)}{\partial t} = \mathbf{S}(\mathbf{x}, t) \quad (4.1)$$

with source function $\mathbf{S}(\mathbf{x}, t) = \mathcal{D}\delta(x_1)\delta(x_2)\delta(x_3)I(t) = \mathcal{D}\delta(\mathbf{x})I(t)$.

Following the method of Theorem 2.1, the first step in the calculation is to construct Helmholtz potentials Φ and Ψ such that

$$\mathcal{D}\delta(\mathbf{x}) = \nabla\Phi + \nabla \times \Psi \quad (4.2)$$

$$\nabla \cdot \Psi = 0. \quad (4.3)$$

To construct Φ and Ψ it is enough to solve the vector Poisson equation $\nabla^2 W(\mathbf{x}) = \mathcal{D}\delta(\mathbf{x})$, since then we can choose potentials $\Phi = \nabla \cdot W$ and $\Psi = -\nabla \times W$ (Aki & Richards 1980, Box 4.2). The solution for the vector Poisson equation is

$$W(\mathbf{x}) = - \iiint \frac{\mathcal{D}\delta(\boldsymbol{\eta})}{4\pi|\mathbf{x} - \boldsymbol{\eta}|} d\boldsymbol{\eta}. \quad (4.4)$$

Following this recipe to find Φ and Ψ

$$W(\mathbf{x}) = -\frac{\mathcal{D}}{4\pi} \iiint \frac{\delta(\boldsymbol{\eta})}{|\mathbf{x} - \boldsymbol{\eta}|} d\boldsymbol{\eta} \quad (4.5)$$

$$= -\frac{\mathcal{D}}{4\pi|\mathbf{x}|} \quad (4.6)$$

$$= -\frac{\mathcal{D}}{4\pi r} \quad (4.7)$$

where $r = |\mathbf{x}|$ and then

$$\Phi = \nabla \cdot W \quad (4.8)$$

$$= \nabla \cdot \left(-\frac{\mathcal{D}}{4\pi r}\right) \quad (4.9)$$

$$= \frac{1}{4\pi r^2} \boldsymbol{\gamma} \cdot \mathcal{D} \quad (4.10)$$

$$\Psi = -\nabla \times W \quad (4.11)$$

$$= \frac{1}{4\pi r^2} \boldsymbol{\gamma} \times \mathcal{D} \quad (4.12)$$

where $\boldsymbol{\gamma} = \mathbf{x}/r$.

The second step in the calculation is to solve for potentials ϕ and ψ . In the case that we are solving for a diffusive field the equations to be solved are

$$\nabla^2 \phi - \frac{1}{c^2} \frac{\partial \phi}{\partial t} = \Phi I(t) \quad (4.13)$$

$$\nabla^2 \psi - \frac{1}{c^2} \frac{\partial \psi}{\partial t} = \Psi I(t) \quad (4.14)$$

where $I(t)$ is the source current time profile.

In the case that we are solving for the equivalent wavefield the equations to be solved are

$$\nabla^2 \phi - \frac{1}{c^2} \frac{\partial^2 \phi}{\partial q^2} = \Phi X(q) \quad (4.15)$$

$$\nabla^2 \psi - \frac{1}{c^2} \frac{\partial^2 \psi}{\partial q^2} = \Psi X(q) \quad (4.16)$$

where $X(q)$ is the equivalent wavefield source profile.

Considering this second case and calculating $\phi(\mathbf{x}, q)$ the response to a source term $\delta(\mathbf{x})X(q)$

is

$$\mathbf{g}(\mathbf{x}, q) = \frac{-1}{4\pi r} X(q - r/c). \quad (4.17)$$

(Aki & Richards 1980, Equation 4.4). The solution of Equation (4.15) is the spatial convolution of \mathbf{g} , defined in Equation (4.17) above, with the spatial directivity of the source term in Equation (4.15)

$$\phi(\mathbf{x}, q) = \mathbf{g}(\mathbf{x}, q) * \Phi(\mathbf{x}) X(q) \quad (4.18)$$

$$= \mathbf{g}(\mathbf{x}, q) * \frac{1}{4\pi r^2} \gamma \cdot \mathcal{D} \quad (4.19)$$

$$= \iiint \frac{-1}{4\pi r} X(q - r/c) \frac{1}{4\pi r^2} \gamma \cdot \mathcal{D} dV \quad (4.20)$$

$$= \frac{-1}{(4\pi)^2} \iiint X(q - r/c) \frac{1}{r^3} \gamma \cdot \mathcal{D} dV \quad (4.21)$$

The integral can be simplified by integrating over the volume V via a system of concentric shells S , each centred on the origin and with radius $r = c\tau$.

$$\phi(\mathbf{x}, q) = \frac{-1}{(4\pi)^2} \iiint X(q - r/c) \frac{1}{r^3} \gamma \cdot \mathcal{D} dV \quad (4.22)$$

$$= \frac{-1}{(4\pi)^2} \iiint X(q - r/c) \frac{1}{r^3} \gamma \cdot \mathcal{D} dS dr \quad (4.23)$$

$$= \frac{-1}{(4\pi)^2} \int_{\tau=0}^{\infty} \iint_{r=c\tau} X(q - \tau) \frac{1}{r} \frac{1}{r^2} \gamma \cdot \mathcal{D} dS c d\tau \quad (4.24)$$

$$= \frac{-1}{(4\pi)^2} \int_{\tau=0}^{\infty} \frac{X(q - \tau)}{\tau} \left(\iint_{r=c\tau} \frac{1}{r^2} \gamma \cdot \mathcal{D} dS \right) d\tau \quad (4.25)$$

Using the result

$$\iint_{r=c\tau} \frac{1}{r^2} \gamma_i dS = \mathcal{H}(r/c - \tau) 4\pi c^2 \tau^2 \frac{1}{r^2} \gamma_i \quad (4.26)$$

(Aki & Richards 1980, Box 4.3) we have

$$\phi(\mathbf{x}, q) = \frac{-1}{(4\pi)^2} \int_{\tau=0}^{\infty} \frac{X(q - \tau)}{\tau} \left(\iint_{r=c\tau} \frac{1}{r^2} \gamma \cdot \mathcal{D} dS \right) d\tau \quad (4.27)$$

$$= \frac{-1}{(4\pi)^2} \int_{\tau=0}^{\infty} \frac{X(q - \tau)}{\tau} \left(\mathcal{H}(r/c - \tau) 4\pi c^2 \tau^2 \frac{1}{r^2} \gamma \cdot \mathcal{D} \right) d\tau \quad (4.28)$$

$$= \frac{-1}{(4\pi)^2} 4\pi c^2 \frac{1}{r^2} \gamma \cdot \mathcal{D} \int_{\tau=0}^{\infty} X(q - \tau) \tau \mathcal{H}(r/c - \tau) d\tau \quad (4.29)$$

$$= \frac{-c^2}{4\pi r^2} \gamma \cdot \mathcal{D} \int_{\tau=0}^{\infty} X(q - \tau) \tau \mathcal{H}(r/c - \tau) d\tau \quad (4.30)$$

After following a similar calculation for ψ we conclude

$$\phi = \frac{-c^2}{4\pi r^2} \gamma \cdot \mathcal{D} \int_{\tau=0}^{\infty} X(q - \tau) \tau \mathcal{H}(r/c - \tau) d\tau \quad (4.31)$$

$$\psi = \frac{c^2}{4\pi r^2} \gamma \times \mathcal{D} \int_{\tau=0}^{\infty} X(q - \tau) \tau \mathcal{H}(r/c - \tau) d\tau \quad (4.32)$$

compare with Equations (4.21), (4.22) (Aki & Richards 1980).

The third step in the calculation is to form $\mathbf{U} = \nabla\phi + \nabla \times \boldsymbol{\psi}$. A result which is useful in this step is that

$$\begin{aligned} & \frac{\partial}{\partial x_i} \left[\frac{\gamma_j}{4\pi r^2} \int_{\tau=0}^{\infty} X(q-\tau) \tau \mathcal{H}(r/c-\tau) d\tau \right] \\ &= \frac{\partial}{\partial x_i} \left[\frac{\gamma_j}{4\pi r^2} \right] \int_{\tau=0}^{\infty} X(q-\tau) \tau \mathcal{H}(r/c-\tau) d\tau \\ & \quad + \frac{\gamma_j}{4\pi r^2} \frac{\partial}{\partial x_i} \left[\int_{\tau=0}^{\infty} X(q-\tau) \tau \mathcal{H}(r/c-\tau) d\tau \right] \end{aligned} \quad (4.33)$$

$$\begin{aligned} &= \frac{1}{4\pi r^3} (\delta_{ij} - 3\gamma_i \gamma_j) \int_{\tau=0}^{\infty} X(q-\tau) \tau \mathcal{H}(r/c-\tau) d\tau \\ & \quad + \frac{\gamma_i \gamma_j}{4\pi c^2 r} X(q-r/c) \end{aligned} \quad (4.34)$$

Using this result we can now calculate $\nabla\phi$ and $\nabla \times \boldsymbol{\psi}$.

$$\nabla\phi = \nabla \left[\frac{-c^2}{4\pi r^2} \boldsymbol{\gamma} \cdot \boldsymbol{\mathcal{D}} \int_{\tau=0}^{\infty} X(q-\tau) \tau \mathcal{H}(r/c-\tau) d\tau \right] \quad (4.35)$$

$$= \mathbf{e}_i \frac{\partial}{\partial x_i} \left[\frac{-c^2}{4\pi r^2} \gamma_j \mathcal{D}_j \int_{\tau=0}^{\infty} X(q-\tau) \tau \mathcal{H}(r/c-\tau) d\tau \right] \quad (4.36)$$

$$\begin{aligned} &= \frac{-c^2}{4\pi r^3} \mathbf{e}_i \mathcal{D}_j (\delta_{ij} - 3\gamma_i \gamma_j) \int_{\tau=0}^{\infty} X(q-\tau) \tau \mathcal{H}(r/c-\tau) d\tau \\ & \quad - \frac{1}{4\pi r} \mathbf{e}_i \mathcal{D}_j \gamma_i \gamma_j X(q-r/c) \end{aligned} \quad (4.37)$$

$$\begin{aligned} &= \frac{-c^2}{4\pi r^3} (\boldsymbol{\mathcal{D}} - 3(\boldsymbol{\gamma} \cdot \boldsymbol{\mathcal{D}}) \boldsymbol{\gamma}) \int_{\tau=0}^{\infty} X(q-\tau) \tau \mathcal{H}(r/c-\tau) d\tau \\ & \quad - \frac{1}{4\pi r} (\boldsymbol{\gamma} \cdot \boldsymbol{\mathcal{D}}) \boldsymbol{\gamma} X(q-r/c) \end{aligned} \quad (4.38)$$

$$\nabla \times \boldsymbol{\psi} = \nabla \times \left[\frac{c^2}{4\pi r^2} \boldsymbol{\gamma} \times \boldsymbol{\mathcal{D}} \int_{\tau=0}^{\infty} X(q-\tau) \tau \mathcal{H}(r/c-\tau) d\tau \right] \quad (4.39)$$

$$\begin{aligned} &= \boldsymbol{\mathcal{D}} \left(\nabla \cdot \left[\frac{-c^2}{4\pi r^2} \boldsymbol{\gamma} \int_{\tau=0}^{\infty} X(q-\tau) \tau \mathcal{H}(r/c-\tau) d\tau \right] \right) \\ & \quad + (\boldsymbol{\mathcal{D}} \cdot \nabla) \left[\frac{c^2}{4\pi r^2} \boldsymbol{\gamma} \int_{\tau=0}^{\infty} X(q-\tau) \tau \mathcal{H}(r/c-\tau) d\tau \right] \end{aligned} \quad (4.40)$$

(using the result that $\nabla \times (\mathbf{A} \times \mathbf{B}) = -\mathbf{B}(\nabla \cdot \mathbf{A}) + (\mathbf{B} \cdot \nabla) \mathbf{A}$ for a constant \mathbf{B})

$$\begin{aligned} &= \boldsymbol{\mathcal{D}} \frac{\partial}{\partial x_j} \left[\frac{-c^2}{4\pi r^2} \gamma_j \int_{\tau=0}^{\infty} X(q-\tau) \tau \mathcal{H}(r/c-\tau) d\tau \right] \\ & \quad + \mathcal{D}_j \frac{\partial}{\partial x_j} \left[\frac{c^2}{4\pi r^2} \gamma_i \mathbf{e}_i \int_{\tau=0}^{\infty} X(q-\tau) \tau \mathcal{H}(r/c-\tau) d\tau \right] \\ &= \boldsymbol{\mathcal{D}} \frac{-c^2}{4\pi r^3} (\delta_{jj} - 3\gamma_j \gamma_j) \int_{\tau=0}^{\infty} X(q-\tau) \tau \mathcal{H}(r/c-\tau) d\tau \\ & \quad - \boldsymbol{\mathcal{D}} \frac{1}{4\pi r} \gamma_j \gamma_j X(q-r/c) \\ & \quad + \mathcal{D}_j \mathbf{e}_i \frac{c^2}{4\pi r^3} (\delta_{ij} - 3\gamma_i \gamma_j) \int_{\tau=0}^{\infty} X(q-\tau) \tau \mathcal{H}(r/c-\tau) d\tau \end{aligned} \quad (4.41)$$

$$-\frac{1}{4\pi r} \mathcal{D}_j \mathbf{e}_i \gamma_i \gamma_j X(q - r/c) \quad (4.42)$$

$$\begin{aligned} = & -\mathcal{D} \frac{1}{4\pi r} X(q - r/c) \\ & + \frac{c^2}{4\pi r^3} (\mathcal{D} - 3(\gamma \cdot \mathcal{D}) \gamma) \int_{\tau=0}^{\infty} X(q - \tau) \tau \mathcal{H}(r/c - \tau) d\tau \\ & + \frac{1}{4\pi r} (\gamma \cdot \mathcal{D}) \gamma X(q - r/c) \end{aligned} \quad (4.43)$$

$$(4.44)$$

Combining these results we conclude that

$$\mathbf{U} = \nabla \phi + \nabla \times \psi \quad (4.45)$$

$$= \frac{-\mathcal{D}}{4\pi r} X(q - r/c) \quad (4.46)$$

compare with Equation (4.23)(Aki & Richards 1980).¹ This completes the calculation of the equivalent wavefield.

The diffusive response can be calculated from the equivalent wavefield, using the Q transform

$$\mathbf{F}(\mathbf{x}, t) = \frac{1}{2\sqrt{\pi t^3}} \int_0^{\infty} q \exp(-\frac{q^2}{4t}) \mathbf{U}(\mathbf{x}, q) dq \quad (4.47)$$

$$= \frac{-\mathcal{D}}{4\pi r} \frac{1}{2\sqrt{\pi t^3}} \int_0^{\infty} q \exp(-\frac{q^2}{4t}) X(q - r/c) dq. \quad (4.48)$$

4.1.2 A Shorter Derivation

We seek to solve the vector diffusion equation in \mathbf{F} for a directed point source term aligned in the \mathcal{D} direction and located at the origin of an infinite, homogeneous, isotropic medium of equivalent velocity c . That is, we seek to solve

$$\nabla^2 \mathbf{F}(\mathbf{x}, t) - \frac{1}{c^2} \frac{\partial \mathbf{F}(\mathbf{x}, t)}{\partial t} = \mathcal{D} \delta(\mathbf{x}) I(t) \quad (4.49)$$

where $I(t)$ is the source current time profile.

Following the method of Section 3.1, the first step in the calculation is to find the equivalent wavefield $\mathbf{U}(\mathbf{x}, q)$ which satisfies

$$\nabla^2 \mathbf{U}(\mathbf{x}, q) - \frac{1}{c^2} \frac{\partial^2 \mathbf{U}(\mathbf{x}, q)}{\partial q^2} = \mathcal{D} \delta(\mathbf{x}) X(q) \quad (4.50)$$

where the equivalent wavefield source profile $X(q)$ is related to the source current time profile by the Q transform.

¹In isotropic media both the irrotational and solenoidal components diffuse at the same rate. Hence the massive cancellation observed in Equation (4.46). In contrast the irrotational (P-wave) and solenoidal (S-Wave) components of the elastic wavefield do not have the same velocity.

The solution of Equation (4.50) is

$$U(\mathbf{x}, q) = \frac{-\mathcal{D}}{4\pi r} X(q - r/c). \quad (4.51)$$

(Aki & Richards 1980, Equation 4.4) and from this the diffusive response can be calculated using the Q transform to be

$$F(\mathbf{x}, t) = \frac{-\mathcal{D}}{4\pi r} \frac{1}{2\sqrt{\pi t^3}} \int_0^\infty q \exp(-\frac{q^2}{4t}) X(q - r/c) dq. \quad (4.52)$$

4.1.3 Representation of EM Sources

This section develops a concise notation for the representation of sources, which eases the calculation of the equivalent wavefield, and hence the diffusive EM field. Beginning by returning to a directed point source term, the resulting equivalent wavefield is expressed in terms of a source function and a tensor.² More complicated sources are then represented in terms of a source tensor.

We introduce $\mathcal{G}(\mathbf{x}, q)$, a second order tensor such that the equivalent wavefield response $U(\mathbf{x}, q)$ to a directed point source term $\mathcal{D}\delta(\mathbf{x})\delta(q)$ is

$$U_i = D_j \mathcal{G}_{ij}. \quad (4.53)$$

Section 4.1.1 calculated that the equivalent wavefield response to a source term $\mathcal{D}\delta(\mathbf{x})X(q)$ is

$$U(\mathbf{x}, q) = \frac{-\mathcal{D}}{4\pi r} X(q - r/c). \quad (4.54)$$

Hence we have the result that

$$\mathcal{G}_{ij} = \frac{-1}{4\pi r} \delta_{ij} \delta(q - r/c). \quad (4.55)$$

We can see that the equivalent wavefield response to a source function $\mathbf{T} = \mathcal{D}X(q)\delta(\mathbf{x})$ is

$$U_i = T_j * \mathcal{G}_{ij} \quad (4.56)$$

where $*$ denotes convolution in space and time. Since we assume a linear response from the physical system under consideration, the response for extended sources can be calculated by a convolution of the extended source density with $\mathcal{G}(\mathbf{x}, q)$ the response to a directed point source term.

Source terms for the electric and magnetic fields are given by Equations (2.47) and (2.48). In these equations derivatives of the source volume density of electric current \mathbf{J}^s and the source volume density of magnetic current \mathbf{K}^s are taken with respect to space and/or time.

²To avoid confusion between the response to a directed point source term, an electric current dipole, and a magnetic dipole, this tensor will not be referred to as a Green's tensor.

For an electric current dipole or magnetic current dipole source, terms appear in Equations (2.47) and (2.48) which have the form

$$\mathbf{S}(\mathbf{x}, t) = -\nabla \times (\mathcal{D}\delta(\mathbf{x})I(t)). \quad (4.57)$$

The equivalent source for the equivalent wavefield is

$$\mathbf{T}(\mathbf{x}, q) = -\nabla \times (\mathcal{D}\delta(\mathbf{x})X(q)) \quad (4.58)$$

where $X(q)$ and $I(t)$ are related by the Q transform (3.4).

The equivalent wavefield response to source terms including spatial derivatives of a directed point source can be calculated by taking spatial derivatives of $\mathbf{U}(\mathbf{x}, q)$, the response to a source term $\mathcal{D}\delta(\mathbf{x})X(q)$.

$$\mathbf{U}(\mathbf{x}, q) = \frac{-\mathcal{D}}{4\pi r} X(q - r/c) \quad (4.59)$$

$$-\nabla \times (\mathbf{U}(\mathbf{x}, q)) = -\epsilon_{ijk} \mathbf{e}_i \partial_j U_k \quad (4.60)$$

$$= \epsilon_{ijk} \mathbf{e}_i \partial_j \left(\frac{D_k}{4\pi r} X(q - r/c) \right) \quad (4.61)$$

$$= \epsilon_{ijk} \mathbf{e}_i \frac{D_k}{4\pi} \left(\frac{-\gamma_j}{r^2} X(q - r/c) + \frac{1}{r} \frac{-\gamma_j}{c} X'(q - r/c) \right) \quad (4.62)$$

$$= \epsilon_{ijk} \mathbf{e}_i \frac{-\gamma_j D_k}{4\pi r} \left(\frac{1}{r} X(q - r/c) + \frac{1}{c} X'(q - r/c) \right) \quad (4.63)$$

$$= \frac{-1}{4\pi r} \boldsymbol{\gamma} \times \mathcal{D} \left(\frac{1}{r} X(q - r/c) + \frac{1}{c} X'(q - r/c) \right). \quad (4.64)$$

We now introduce a moment tensor representation of the equivalent wavefield source term $-\nabla \times (\mathcal{D}\delta(\mathbf{x})X(q))$. We define this moment tensor \mathcal{M} by

$$-\epsilon_{ijk} \partial_j U_k = \mathcal{M}_{jk} X * \frac{\partial \mathcal{G}_{ij}}{\partial x_k}. \quad (4.65)$$

Using the result that

$$\frac{\partial \mathcal{G}_{ij}}{\partial x_k} = \frac{\partial}{\partial x_k} \left(\frac{-1}{4\pi r} \delta_{ij} \delta(q - r/c) \right) \quad (4.66)$$

$$= \frac{1}{4\pi r} \delta_{ij} \gamma_k \left(\frac{1}{r} \delta(q - r/c) + \frac{1}{c} \delta'(q - r/c) \right), \quad (4.67)$$

it is easy to verify that

$$\mathcal{M}_{jk} = -\epsilon_{jnk} D_n \delta(\mathbf{x}). \quad (4.68)$$

For an electric current dipole or magnetic current dipole source, terms appear in Equations (2.47) and (2.48) which have the form

$$\mathbf{S}(\mathbf{x}, t) = -\nabla \nabla \cdot (\mathcal{D}\delta(\mathbf{x})I(t)). \quad (4.69)$$

The equivalent source for the equivalent wavefield is

$$\mathbf{T}(\mathbf{x}, q) = -\nabla\nabla \cdot (\mathcal{D}\delta(\mathbf{x})X(q)), \quad (4.70)$$

where $X(q)$ and $I(t)$ are related by the Q transform (3.4).

The equivalent wavefield response to source terms including spatial derivatives of a directed point source can be calculated by taking spatial derivatives of $\mathbf{U}(\mathbf{x}, q)$, the response to a source term $\mathcal{D}\delta(\mathbf{x})X(q)$.

$$\mathbf{U}(\mathbf{x}, q) = \frac{-\mathcal{D}}{4\pi r} X(q - r/c) \quad (4.71)$$

$$-\nabla\nabla \cdot (\mathbf{U}(\mathbf{x}, q)) = -\mathbf{e}_i \partial_i \partial_j U_j \quad (4.72)$$

$$= -\mathbf{e}_i \partial_i \partial_j \left(\frac{-1}{4\pi r} \mathbf{D}_j X(q - r/c) \right) \quad (4.73)$$

$$= -\mathbf{e}_i \partial_i \left[\frac{1}{4\pi r} \gamma_j \mathbf{D}_j \left(\frac{1}{r} X(q - r/c) + \frac{1}{c} X'(q - r/c) \right) \right] \quad (4.74)$$

$$= \mathbf{e}_i \frac{-1}{4\pi r} \mathbf{D}_j \left[\frac{1}{r} (\delta_{ij} - 3\gamma_i \gamma_j) \left(\frac{1}{r} X(q - r/c) + \frac{1}{c} X'(q - r/c) \right) - \frac{\gamma_i \gamma_j}{c^2} X''(q - r/c) \right]. \quad (4.75)$$

Using this result it is easy to verify that

$$-\partial_i \partial_j U_j = (-\mathbf{D}_j X) * \frac{\partial^2 \mathcal{G}_{ik}}{\partial x_k \partial x_j} \quad (4.76)$$

Hence the response to a source term $\nabla\nabla \cdot (\mathcal{D}\delta(\mathbf{x})I(t))$ can be represented using the equivalent wavefield response to a directed point source term and the dipole moment, without need of an additional source representation tensor.

4.1.4 Magnetic Field of a Transient Electric Current dipole

This section calculates the magnetic field response to a switch-on electric current dipole source in an infinite, homogeneous medium of resistivity ρ . The method of solution is through the equivalent wavefield. The first step is to calculate the equivalent source, next the equivalent wavefield response to this source is derived and finally the diffusive response is calculated from the equivalent wavefield.

For an electric current dipole located at the origin aligned in the \mathcal{D} direction with source current profile $I(t)$ the source volume density of electric current is $\mathbf{J}^s = \mathcal{D}\delta(\mathbf{x})I(t)$. From Equation (2.48) the magnetic field due to a source volume density of electric current \mathbf{J}^s has a source term $-\nabla \times \mathbf{J}^s(\mathbf{x}, t)$. Hence the equivalent wavefield has a source term

$$\mathbf{T}(\mathbf{x}, q) = -\nabla \times (\mathcal{D}\delta(\mathbf{x})X(q)) \quad (4.77)$$

where $X(q)$ and $I(t)$ are related by the Q transform (3.4).

Section 4.1.3 demonstrated that this source term has an equivalent moment tensor $\mathcal{M}_{jk} = -\epsilon_{jnk}D_n\delta(\mathbf{x})$ and an equivalent wavefield response

$$\mathbf{e}_i(\mathcal{M}_{jk}X) * \frac{\partial \mathcal{G}_{ij}}{\partial x_k} = \epsilon_{ijk}\mathbf{e}_i \frac{-1}{4\pi r} \gamma_j D_k \left(\frac{1}{r}X(q-r/c) + \frac{1}{c}X'(q-r/c) \right) \quad (4.78)$$

$$= \frac{-1}{4\pi r} \gamma \times \mathcal{D} \left(\frac{1}{r}X(q-r/c) + \frac{1}{c}X'(q-r/c) \right). \quad (4.79)$$

For a switch-on source current profile in the time domain $I(t) = \mathcal{H}(t)$ and the equivalent source time profile is $X(q) = q\mathcal{H}(q)$ (see Table 0.2). Since $X(q) = q\mathcal{H}(q)$, $X'(q) = \mathcal{H}(q)$ and the response in the equivalent wavefield domain is

$$\frac{-1}{4\pi r} \gamma \times \mathcal{D} \left(\frac{1}{r}(q-r/c)\mathcal{H}(q-r/c) + \frac{1}{c}\mathcal{H}(q-r/c) \right) \quad (4.80)$$

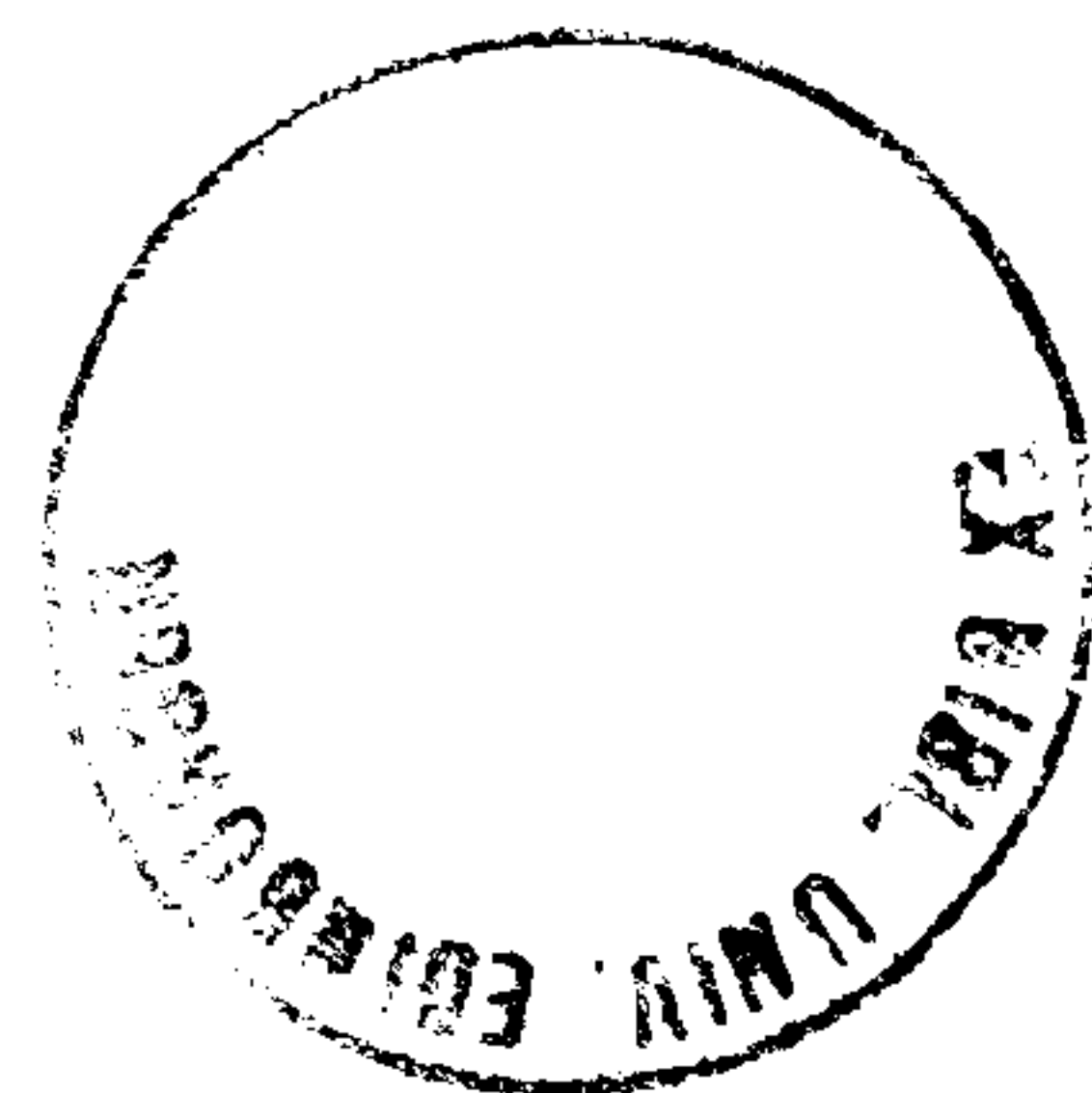
$$= \frac{-1}{4\pi r} \gamma \times \mathcal{D} \frac{q}{r} \mathcal{H}(q-r/c) \quad (4.81)$$

Given this analytic expression for the equivalent wavefield we follow the recipe outlined in Box 5 to calculate the diffusive response. Using the results that

$$\mathcal{L}_{q \rightarrow p} [\mathcal{H}(q-a)] = \frac{1}{p} \exp(-ap) \quad (4.82)$$

(Erdélyi 1954, Equation (1), page 241)

$$\mathcal{L}_{q \rightarrow p} [qU(q)] = -\frac{\partial \hat{U}(p)}{\partial p} \quad (4.83)$$



(Erdélyi 1954, Equation (6), page 129) we calculate that

$$U(q) = q\mathcal{H}(q - r/c) \quad (4.84)$$

$$\hat{U}(p) = -\frac{\partial}{\partial p} \left(\frac{1}{p} \exp(-pr/c) \right) \quad (4.85)$$

$$= \left(\frac{r}{cp} + \frac{1}{p^2} \right) \exp(-pr/c) \quad (4.86)$$

$$\hat{F}(p) = \hat{U}(\sqrt{p}) = \left(\frac{r}{c\sqrt{p}} + \frac{1}{p} \right) \exp(-\sqrt{p}r/c). \quad (4.87)$$

From (Erdélyi 1954, Equation (3), page 245) for $a > 0$

$$\mathcal{L}_{p \rightarrow t}^{-1} \left[\frac{1}{p} \exp(-a\sqrt{p}) \right] = \operatorname{erfc}\left(\frac{a}{2\sqrt{t}}\right). \quad (4.88)$$

From (Erdélyi 1954, Equation (6), page 246) for $a > 0$

$$\mathcal{L}_{p \rightarrow t}^{-1} \left[\frac{a}{\sqrt{p}} \exp(-a\sqrt{p}) \right] = \frac{a}{\sqrt{\pi t}} \exp\left(-\frac{a^2}{4t}\right). \quad (4.89)$$

Hence

$$F(t) = \operatorname{erfc}\left(\frac{r}{c2\sqrt{t}}\right) + \frac{r}{c\sqrt{\pi t}} \exp\left(-\frac{r^2}{c^2 4t}\right). \quad (4.90)$$

and we conclude that the magnetic field response to a switch-on electric current dipole in an infinite, homogeneous medium of resistivity ρ is

$$\mathbf{H}(\mathbf{x}, t) = \frac{-1}{4\pi r^2} \boldsymbol{\gamma} \times \mathcal{D} \left[\operatorname{erfc}\left(\frac{r}{c2\sqrt{t}}\right) + \frac{r}{c\sqrt{\pi t}} \exp\left(-\frac{r^2}{c^2 4t}\right) \right] \quad (4.91)$$

where $c^2 = \rho/\mu$, which agrees with (Slob 1994, Equation (3.14), page 35).³

4.1.5 Electric Field of a Transient Electric Current dipole

This section calculates the electric field response to a switch-on electric current dipole source in an infinite, homogeneous medium of resistivity ρ . The method of solution is through the equivalent wavefield. The first step is to calculate the equivalent source, next the equivalent wavefield response to this source is derived and finally the diffusive response is calculated from the equivalent wavefield.

From Equation (2.47) the electric field due to a source volume density of electric current \mathbf{J}^s has source terms

$$\mathbf{S}(\mathbf{x}, t) = \mu \frac{\partial \mathbf{J}^s(\mathbf{x}, t)}{\partial t} - \rho \nabla \nabla \cdot \mathbf{J}^s(\mathbf{x}, t). \quad (4.92)$$

For an electric current dipole located at the origin aligned in the \mathcal{D} direction with source current profile $I(t)$ the source volume density of electric current is $\mathbf{J}^s = \mathcal{D}\delta(\mathbf{x})I(t)$. For a switch-

³The typographical error in (Ward & Hohmann 1987, Equation (2.51), page 175), can be confirmed by comparison with (Ward & Hohmann 1987, Equation (2.42), page 174).

on source current profile in the time domain $I(t) = \mathcal{H}(t)$ and $I'(t) = \delta(t)$. The equivalent source time profile for a Heaviside step-on function is $q\mathcal{H}(q)$ and the equivalent source time profile for an impulse at zero time is $\delta(q)$.

Hence the equivalent wavefield has a source function

$$\mathbf{T}(\mathbf{x}, q) = \mu \mathcal{D} \delta(\mathbf{x}) \delta(q) - \rho \nabla \nabla \cdot (\mathcal{D} \delta(\mathbf{x}) q \mathcal{H}(q)) \quad (4.93)$$

$$= \mathbf{T}1(\mathbf{x}, q) + \mathbf{T}2(\mathbf{x}, q) \quad (4.94)$$

where

$$\mathbf{T}1(\mathbf{x}, q) = \mu \mathcal{D} \delta(\mathbf{x}) \delta(q) \quad (4.95)$$

$$\mathbf{T}2(\mathbf{x}, q) = -\rho \nabla \nabla \cdot (\mathcal{D} \delta(\mathbf{x}) q \mathcal{H}(q)) \quad (4.96)$$

Section 4.1.3 demonstrated that source term $\mathbf{T}1$ has an equivalent wavefield response

$$U1(\mathbf{x}, q) = \frac{-\mu}{4\pi r} \mathcal{D} \delta(q - r/c) \quad (4.97)$$

$$= \frac{-\rho}{4\pi r} \frac{1}{c^2} \mathcal{D} \delta(q - r/c) \quad (4.98)$$

Section 4.1.3 demonstrated that source term $\mathbf{T}2$ has an equivalent wavefield response

$$U2(\mathbf{x}, q) = \mathbf{e}_i (\rho \mathcal{D}_j q \mathcal{H}(q)) * \frac{\partial^2 \mathcal{G}_{ik}}{\partial x_k \partial x_j} \quad (4.99)$$

$$= \frac{-\rho}{4\pi r} \left[\frac{1}{r} (\mathcal{D} - 3\gamma(\gamma \cdot \mathcal{D})) \left(\frac{1}{r} (q - r/c) \mathcal{H}(q - r/c) + \frac{1}{c} \mathcal{H}(q - r/c) \right) - \frac{\gamma(\gamma \cdot \mathcal{D})}{c^2} \delta(q - r/c) \right] \quad (4.100)$$

$$= \frac{-\rho}{4\pi r} \left[\frac{1}{r} (\mathcal{D} - 3\gamma(\gamma \cdot \mathcal{D})) \frac{q}{r} \mathcal{H}(q - r/c) - \frac{\gamma(\gamma \cdot \mathcal{D})}{c^2} \delta(q - r/c) \right] \quad (4.101)$$

Hence the equivalent wavefield arising from terms $\mathbf{T}1 + \mathbf{T}2$ is

$$U(\mathbf{x}, q) = \frac{-\rho}{4\pi r} \frac{1}{c^2} \mathcal{D} \delta(q - r/c) + \frac{-\rho}{4\pi r} \left[\frac{1}{r} (\mathcal{D} - 3\gamma(\gamma \cdot \mathcal{D})) \frac{q}{r} \mathcal{H}(q - r/c) - \frac{\gamma(\gamma \cdot \mathcal{D})}{c^2} \delta(q - r/c) \right] \quad (4.102)$$

$$= \frac{-\rho}{4\pi r} \mathcal{D} \left[\frac{1}{r^2} q \mathcal{H}(q - r/c) + \frac{1}{c^2} \delta(q - r/c) \right] + \frac{\rho}{4\pi r} \gamma(\gamma \cdot \mathcal{D}) \left[\frac{3}{r^2} q \mathcal{H}(q - r/c) + \frac{1}{c^2} \delta(q - r/c) \right] \quad (4.103)$$

Given this analytic expression for the equivalent wavefield we can calculate the diffusive field. Using the results (4.90) and (3.4) we can write that the diffusive response corresponding to an equivalent wavefield of

$$U(q) = \frac{n}{r^2} q \mathcal{H}(q - r/c) + \frac{1}{c^2} \delta(q - r/c) \quad (4.104)$$

is

$$F(t) = \frac{n}{r^2} \left(\operatorname{erfc}\left(\frac{r}{c2\sqrt{t}}\right) + \frac{r}{c\sqrt{\pi t}} \exp\left(-\frac{r^2}{c^2 4t}\right) \right) + \frac{1}{c^2} \frac{1}{2\sqrt{\pi t^3}} \frac{r}{c} \exp\left(-\frac{r^2}{c^2 4t}\right) \quad (4.105)$$

$$= \frac{n}{r^2} \operatorname{erfc}\left(\frac{r}{c2\sqrt{t}}\right) + \frac{1}{r^2} \left(n + \frac{r^2}{c^2 2t} \right) \frac{r}{c\sqrt{\pi t}} \exp\left(-\frac{r^2}{c^2 4t}\right) \quad (4.106)$$

Hence we conclude that the electric field response to a switch-on electric current dipole in an infinite, homogeneous medium of resistivity ρ is

$$\begin{aligned} \mathbf{E}(\mathbf{x}, t) = & \frac{-\rho}{4\pi r^3} \mathcal{D} \left[\operatorname{erfc}\left(\frac{r}{c2\sqrt{t}}\right) + \left(1 + \frac{r^2}{c^2 2t}\right) \frac{r}{c\sqrt{\pi t}} \exp\left(-\frac{r^2}{c^2 4t}\right) \right] \\ & + \frac{\rho}{4\pi r^3} \gamma(\gamma \cdot \mathcal{D}) \left[3\operatorname{erfc}\left(\frac{r}{c2\sqrt{t}}\right) + \left(3 + \frac{r^2}{c^2 2t}\right) \frac{r}{c\sqrt{\pi t}} \exp\left(-\frac{r^2}{c^2 4t}\right) \right] \end{aligned} \quad (4.107)$$

where $c^2 = \rho/\mu$, which agrees with (Ward & Hohmann 1987, Equation (2.50), page 175)

4.2 Comparison of EM Sources and Seismic Sources

In the calculation of the magnetic field of a transient electric dipole, a source volume density of electric current of $\mathbf{J}^s = \mathcal{D}\delta(\mathbf{x})I(t)$ results in an equivalent wavefield source term $-\nabla \times (\mathcal{D}\delta(\mathbf{x})X(q))$.

In the calculation of the electric field of a transient magnetic dipole, a source volume density of magnetic current of $\mathbf{K}^s = \mathcal{D}\delta(\mathbf{x})I(t)$ results in an equivalent wavefield source term $\nabla \times (\mathcal{D}\delta(\mathbf{x})X(q))$.

If the dipole moment is directed along the \mathbf{e}_1 direction, that is, if $\mathcal{D} = D_1\mathbf{e}_1$ then

$$-\nabla \times (\mathcal{D}\delta(\mathbf{x})X(q)) \quad (4.108)$$

$$= -\nabla \times (D_1\mathbf{e}_1\delta(\mathbf{x})X(q)) \quad (4.109)$$

$$= D_1X(q)(\mathbf{e}_3\partial_2(\delta(\mathbf{x})) - \mathbf{e}_2\partial_3(\delta(\mathbf{x}))) \quad (4.110)$$

a source expression which takes the *difference* of two couples. More generally, these source terms have an antisymmetric equivalent moment tensor, $\mathcal{M}_{jk} = -\epsilon_{jnk}D_n\delta(\mathbf{x})$.

This source term is equivalent to a seismic torque source, which would generate solenoidal (shear) waves only. Liu, Crampin & Queen (1991) and Cole (1997) report the use of a downhole orbital source (DHOS) which generates horizontally polarised shear-wave radiation. This source is proprietary technology of Conoco and little further information is available, however it is reasonable to suggest that this is the analogous seismic source.

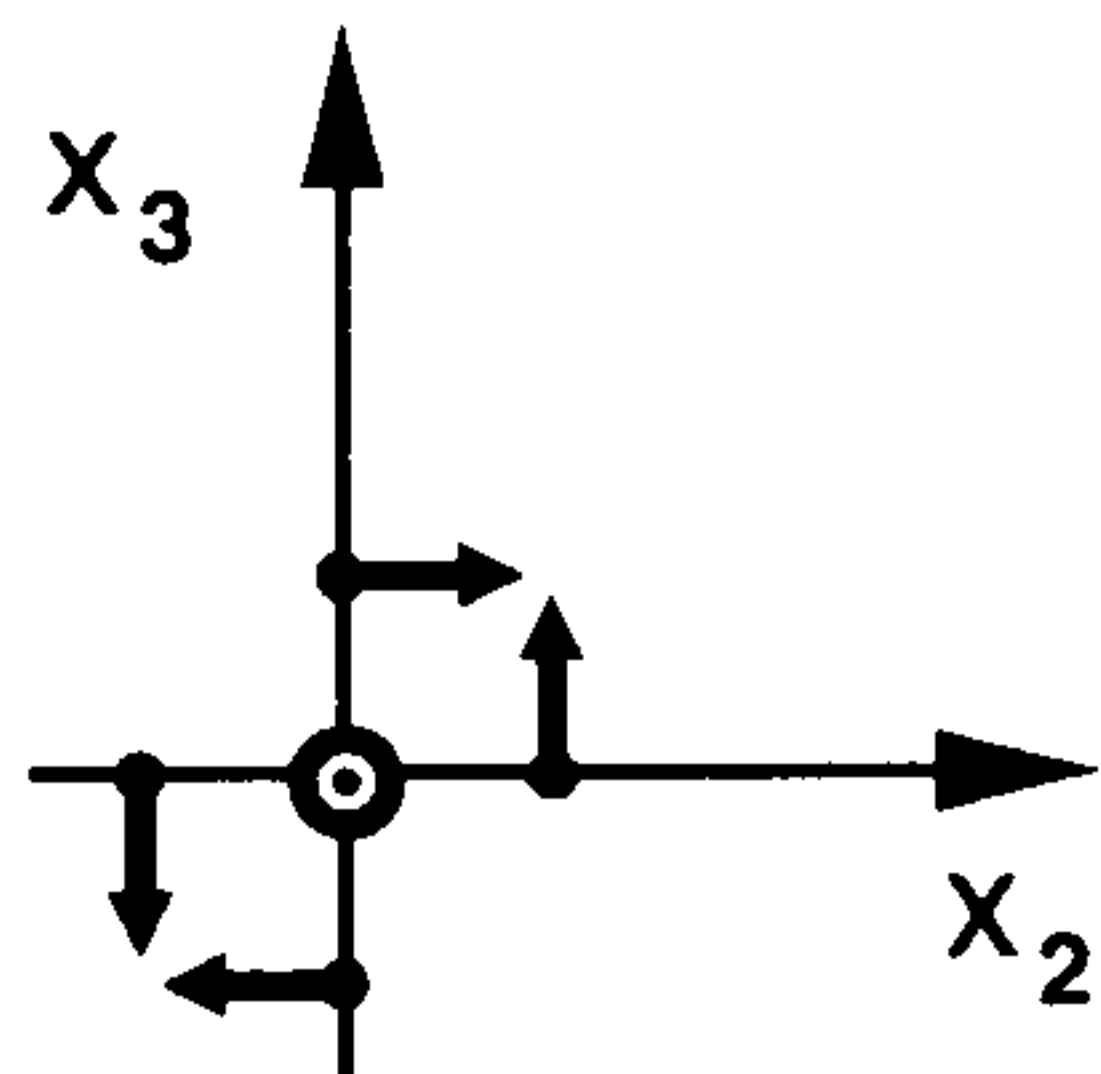


Figure 4.4: Graphical representation of a double-couple source.

In earthquake seismology a double-couple source term is often effective in producing a mathematical model with a radiation pattern which matches observations. The double-couple source is the sum of two couples (see Box 8) for example the sum of couple (2,3) and couple (3,2) — see Figure 4.4. The moment tensor representing such a source is symmetric, with a zero diagonal. Because the two couples are summed, the double-couple source has zero net force and zero net torque.

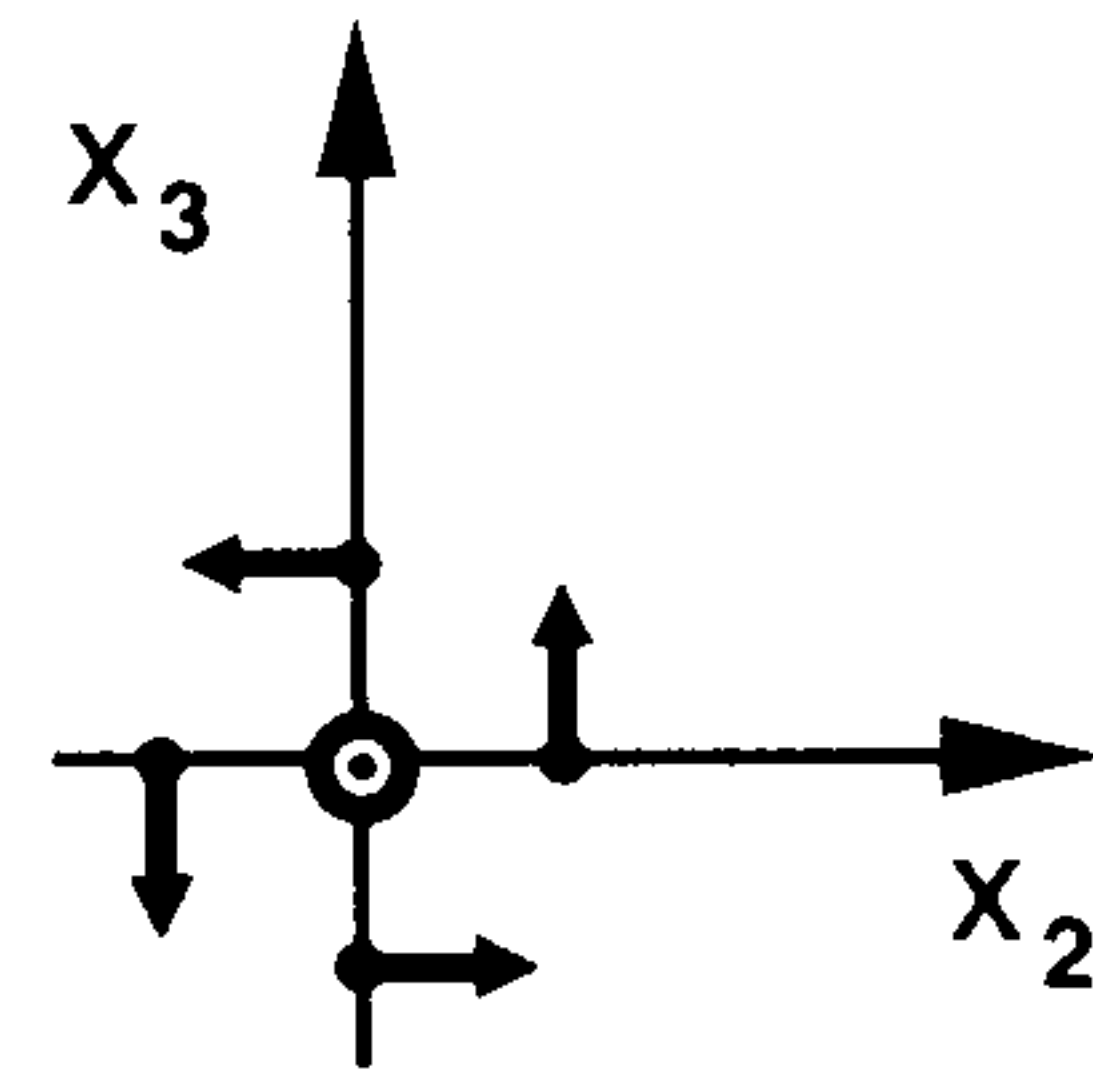


Figure 4.5: Graphical representation of the two couples arising from the curl of a point dipole source.

In this figure the dipole moment is directed along the x_1 axis, which points out of the page. The familiar “right hand rule” of EM induction can easily be read from this figure.

Box 8 The Single Couple

Dirac delta functions are used in the mathematical modelling of physical sources for both elastic wave propagation and electromagnetic propagation. Consequently Dirac delta functions, and derivatives of Dirac delta functions, appear in source terms in the governing equations.

The usual mathematical definition of the Dirac delta function $\delta(x)$ is that for all continuous functions $f(x)$, the integral $\int_{-\infty}^{\infty} \delta(x - a)f(x)dx = f(a)$. In this sense the Dirac delta function is only well defined when it appears under a suitable integral. A useful graphical representation of a Dirac delta function is presented in Figure 4.1.

By extension, derivatives of the Dirac delta function require to appear under an integral to be well defined. One perspective is to consider that the requirement for these integrations is understood and they are implicit but unspoken in our notation.

A point source in 3-dimensional space may be compactly represented using the 3D Dirac delta function

$$\delta(\mathbf{x}) = \delta(x_1)\delta(x_2)\delta(x_3).$$

Taking the partial derivative with respect to one spatial variable of a 3D Dirac delta function results in a couple. Figure 4.2 presents a useful graphical representation of the (3,2) couple $\mathbf{e}_3\partial_2\delta(\mathbf{x})$. A right-handed coordinate system is used and in this figure the x_1 axis points out of the page.

In 3-dimensional space there are nine possible different couples, which are schematically represented in Figure 4.3 (after Figure 3.7, page 51, Aki & Richards 1980).

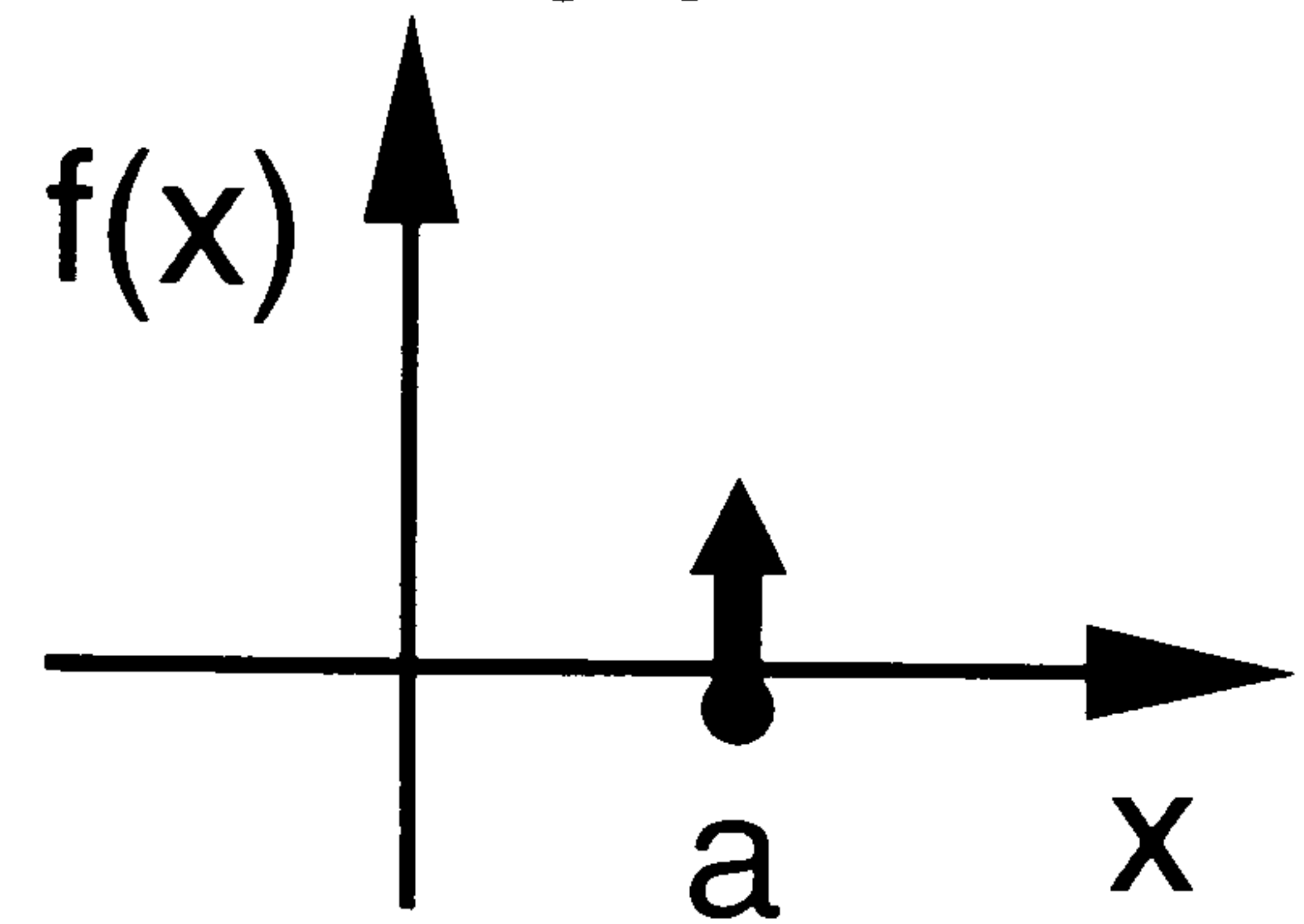


Figure 4.1: Graphical representation of a Dirac delta function.

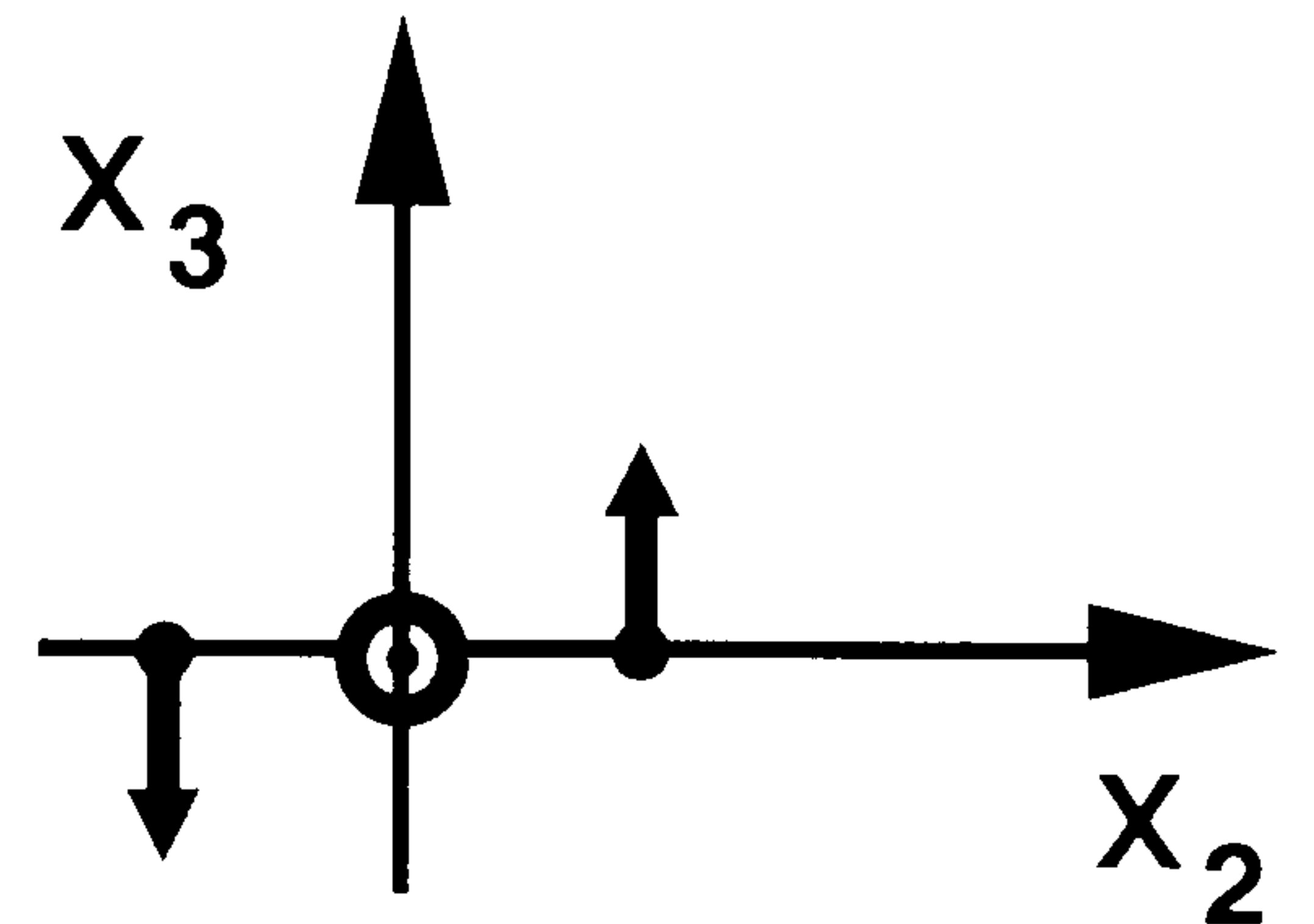


Figure 4.2: Graphical representation of a couple in 3D space.

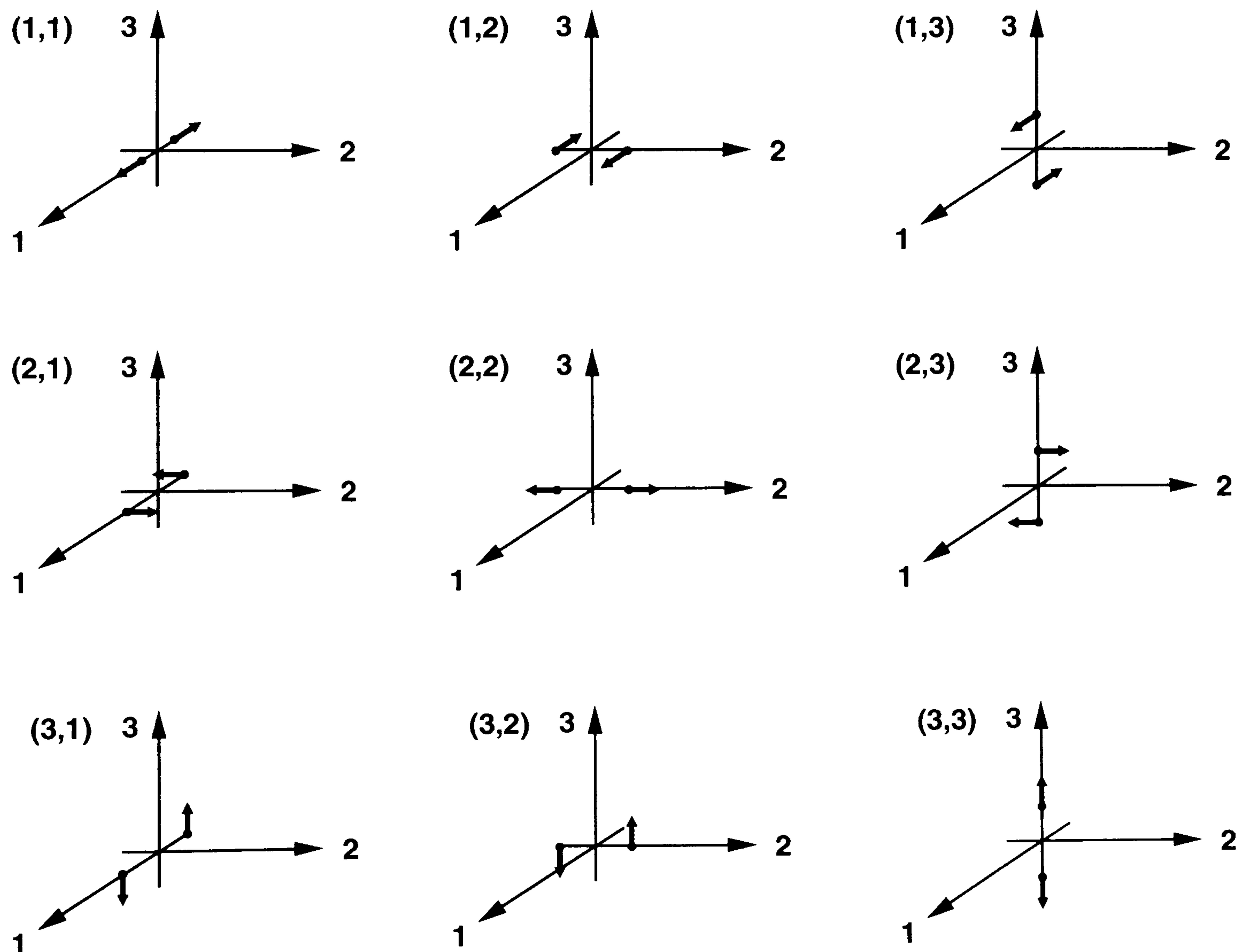


Figure 4.3: The nine possible couples in 3 dimensional space.

4.3 Conclusions

The response to a directed impulsive point source term can be calculated for the diffusive field, or its equivalent wavefield, using the appropriate completeness theorems. However, it is easier to calculate the equivalent wavefield response

$$\mathcal{G}_{ij} = \frac{-1}{4\pi r} \delta_{ij} \delta(q - r/c). \quad (4.111)$$

first, and then calculate the diffusive response by applying the Q transform.

The response to more general sources can be calculated by combining the response to a directed point source term with the appropriate source description. EM source terms involve derivatives with respect to space and/or time of the source volume density of electric current \mathbf{J}^s and the source volume density of magnetic current \mathbf{K}^s , and differ between the electric and magnetic fields. Consequently even a simple source current density leads to a complicated source term. However both the electric and magnetic fields of an electric current dipole can be compactly expressed as the convolution of the dipole moment \mathcal{D} and a moment tensor \mathcal{M}_{jk} with the diffusive response to a directed impulsive point source term.

It is easier to combine the source description with the equivalent wavefield response to a directed point source term, to calculate the equivalent wavefield and then the diffusive EM field, rather than work directly from the diffusive response. This is because the mathematical form of the diffusive response to a directed point source term is more complicated than that for the equivalent wavefield and this complication increases when higher spatial derivatives are required.

The magnetic field generated by an electric current dipole has a source term described by an anti-symmetric moment tensor. This source term is equivalent to a seismic torque source, which would generate solenoidal (shear) waves only. The electric field generated by an electric current dipole has a source term described by two components, one of which is equivalent to a seismic directed point force.

Chapter 5

Sources at the Surface of a Uniform Half-Space

The transient electromagnetic field of a grounded horizontal electric current dipole source located at the surface of a uniform half-space is known for receivers located at the surface of the half-space. Given the analytic expression for this diffusive response the equivalent wavefield at the surface of the halfspace can be calculated analytically. This calculation involves the analytic calculation of forward and inverse Laplace transforms.

The equivalent wavefield can be calculated for a variety of different source current profiles. The EM response to a transmitter with an electric current profile which is an impulse at zero time can be calculated by taking the derivative with respect to time of the switch-off response and multiplying by -1. Because the Q transform is non-linear in time, this procedure cannot be applied to calculate the equivalent wavefield for an impulsive current profile from the equivalent wavefield for a switch-off current profile.

5.1 Horizontal Electric Current Dipole at the Surface of a Uniform Half-Space

Few analytical expressions have been published describing the time domain behaviour of the field of a finite source over finite media. The transient electromagnetic field of a grounded horizontal electric current dipole source located at the surface of a uniform half-space is known for receivers located at the surface of the half-space.

Consider an electric current transmitter bipole centred on the origin with the current in the transmitter wire flowing in the \mathcal{D} direction. The source moment $|\mathcal{D}|$, is the product of current flowing and the length of the bipole. A dipole source is a mathematical construction and is the limiting case of a bipole which shrinks to infinitesimally short length while at the same time the source moment is kept constant.

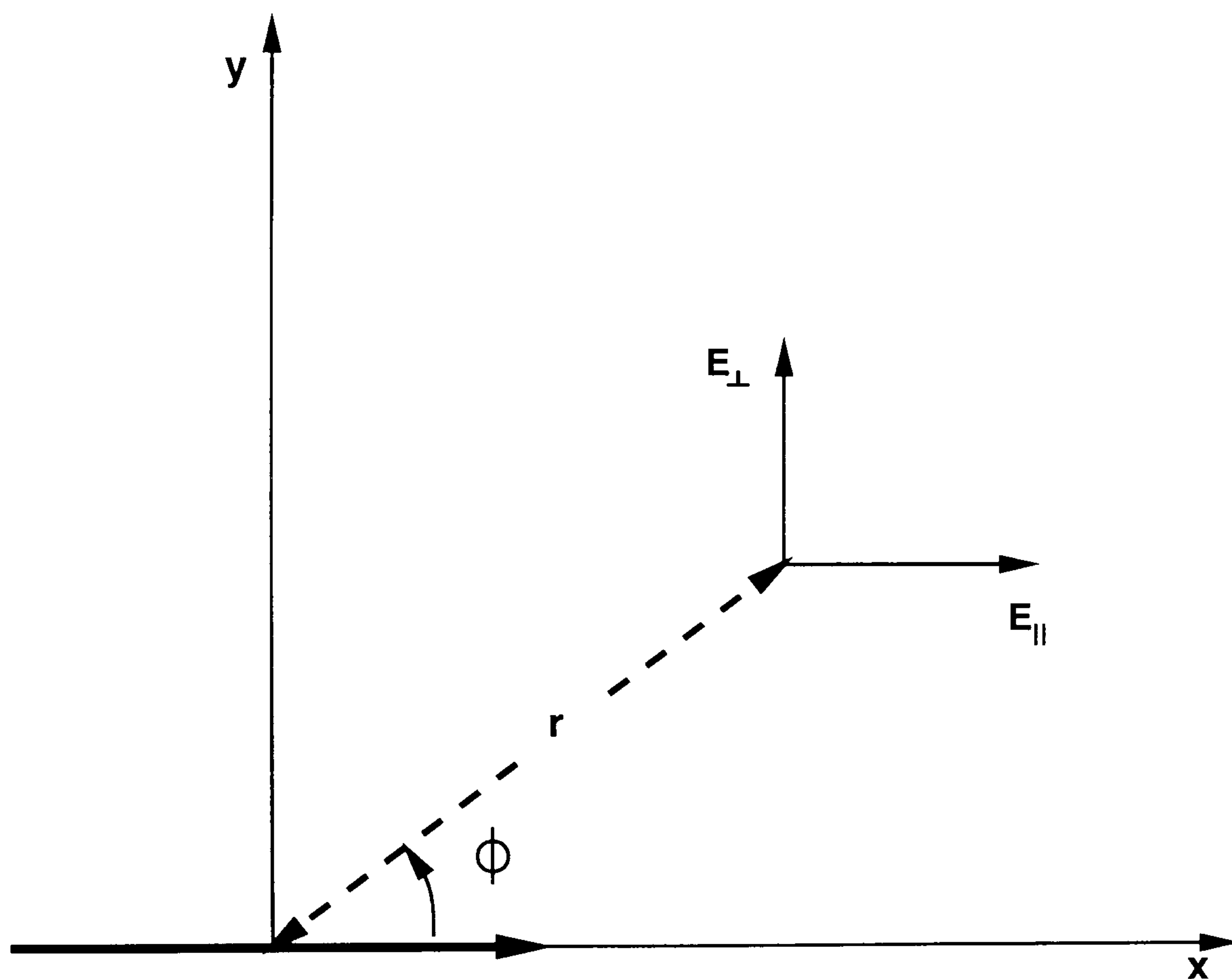


Figure 5.1: Configuration of a grounded dipole source.

The horizontal component of the electric field **parallel** to the transmitter orientation is denoted $E_{||}$ and the horizontal component of the electric field **orthogonal** to the transmitter orientation is denoted E_{\perp} . The rate of change with respect to time of the vertical component of the magnetic field is denoted dH_z/dt .

5.1.1 EM Response for a Switch-off Transmitter Current Profile

For a horizontal electric current dipole source and a *switch off* transmitter current profile, that is, a transmitter current which is constant for negative times and zero for positive times Weir

(1980) gives

$$\mathbf{E}_{\perp}(t > 0) = 0 \quad (5.1)$$

$$\mathbf{E}_{\parallel}(r, \phi, t < 0) = -\frac{\mathcal{D}}{2\pi\sigma r^3}(1 - 3\cos^2\phi), \quad (5.2)$$

$$\mathbf{E}_{\parallel}(r, \phi, t > 0) = \frac{\mathcal{D}}{2\pi\sigma r^3}\left(\operatorname{erf}\left(\frac{r}{c2\sqrt{t}}\right) - \frac{2}{\sqrt{\pi}}\frac{r}{c2\sqrt{t}}\exp\left(-\frac{r^2}{c^24t}\right)\right) \quad (5.3)$$

$$= \frac{\mathcal{D}}{2\pi\sigma r^3}(F1(t) - F2(t)) \quad (5.4)$$

where

$$F1(t) = \operatorname{erf}\left(\frac{r}{c2\sqrt{t}}\right) \quad (5.5)$$

$$F2(t) = \frac{2}{\sqrt{\pi}}\frac{r}{c2\sqrt{t}}\exp\left(-\frac{r^2}{c^24t}\right) \quad (5.6)$$

\mathcal{D} is the moment of the dipole

$$c^2 = (\mu\sigma)^{-1} \quad (5.7)$$

and

erf is the error function.

5.1.2 Equivalent Wavefield for a Switch-off Transmitter Current Profile

Given the analytic expression (5.4) for the diffusive response we follow the recipe outlined in Box 7 to calculate the equivalent wavefield \mathbf{U}_{\parallel} .

Taking the first term

$$F(t) = F1(t) = \operatorname{erf}\left(\frac{r}{c2\sqrt{t}}\right) \quad (5.8)$$

$$\hat{F}(s) = \frac{1}{s}(1 - \exp(-\frac{r}{c}\sqrt{s})) \quad (5.9)$$

(Erdélyi 1954, Equation (6), page 176)

$$\hat{U}(p) = \hat{F}(p^2) = \frac{1}{p^2}(1 - \exp(-\frac{r}{c}p)) \quad (5.10)$$

From (Erdélyi 1954, Equation (2), page 241) for $a > 0$.

$$\mathcal{L}_{p \rightarrow q}^{-1} \left[\frac{1}{p}(1 - \exp(-ap)) \right] = \begin{cases} 1 & 0 < q < a \\ 0 & q > a \end{cases} \quad (5.11)$$

$$= \mathcal{H}(a - q). \quad (5.12)$$

From (Erdélyi 1954, Equation (10), page 130)

$$\mathcal{L}_{p \rightarrow q}^{-1} \left[\frac{1}{p} \hat{u}(p) \right] = \int_0^q u(v) dv. \quad (5.13)$$

Hence

$$U1(q) = \mathcal{L}_{p \rightarrow q}^{-1} \left[\frac{1}{p^2} (1 - \exp(-\frac{r}{c}p)) \right] = \int_0^q \mathcal{H}(\frac{r}{c} - v) dv \quad (5.14)$$

$$= \begin{cases} q & 0 < q < r/c \\ r/c & q \geq r/c \end{cases} \quad (5.15)$$

$$= q\mathcal{H}(\frac{r}{c} - q) + \frac{r}{c}\mathcal{H}(q - \frac{r}{c}) \quad (5.16)$$

where it is understood throughout the above that $q > 0$.

Taking the second term

$$F(t) = F2(t) = \frac{2}{\sqrt{\pi}} \frac{r}{c2\sqrt{t}} \exp(-\frac{r^2}{c^2 4t}) \quad (5.17)$$

$$\hat{F}(s) = \frac{r}{c\sqrt{s}} \exp(-\frac{r}{c}\sqrt{s}) \quad (5.18)$$

(Erdélyi 1954, Equation (27), page 146)

$$\hat{U}(p) = \hat{F}(p^2) = \frac{r}{cp} \exp(-\frac{r}{c}p) \quad (5.19)$$

$$U2(q) = \mathcal{L}_{p \rightarrow q}^{-1} [\hat{U}(p)] \quad (5.20)$$

$$= \mathcal{L}_{p \rightarrow q}^{-1} \left[\frac{r}{cp} \exp(-\frac{r}{c}p) \right] \quad (5.21)$$

$$= \frac{r}{c} \mathcal{H}(q - r/c) \quad (5.22)$$

(Erdélyi 1954, Equation (1), page 241)

Combining these two results yields

$$U_{\parallel}(r, q) = \frac{\mathcal{D}}{2\pi\sigma r^3} (U1(q) - U2(q)) \quad (5.23)$$

$$= \frac{\mathcal{D}}{2\pi\sigma r^3} \left(q\mathcal{H}(\frac{r}{c} - q) + \frac{r}{c}\mathcal{H}(q - r/c) - \frac{r}{c}\mathcal{H}(q - r/c) \right) \quad (5.24)$$

$$= \frac{\mathcal{D}}{2\pi\sigma r^3} q\mathcal{H}(\frac{r}{c} - q) \quad (5.25)$$

for $q > 0$.

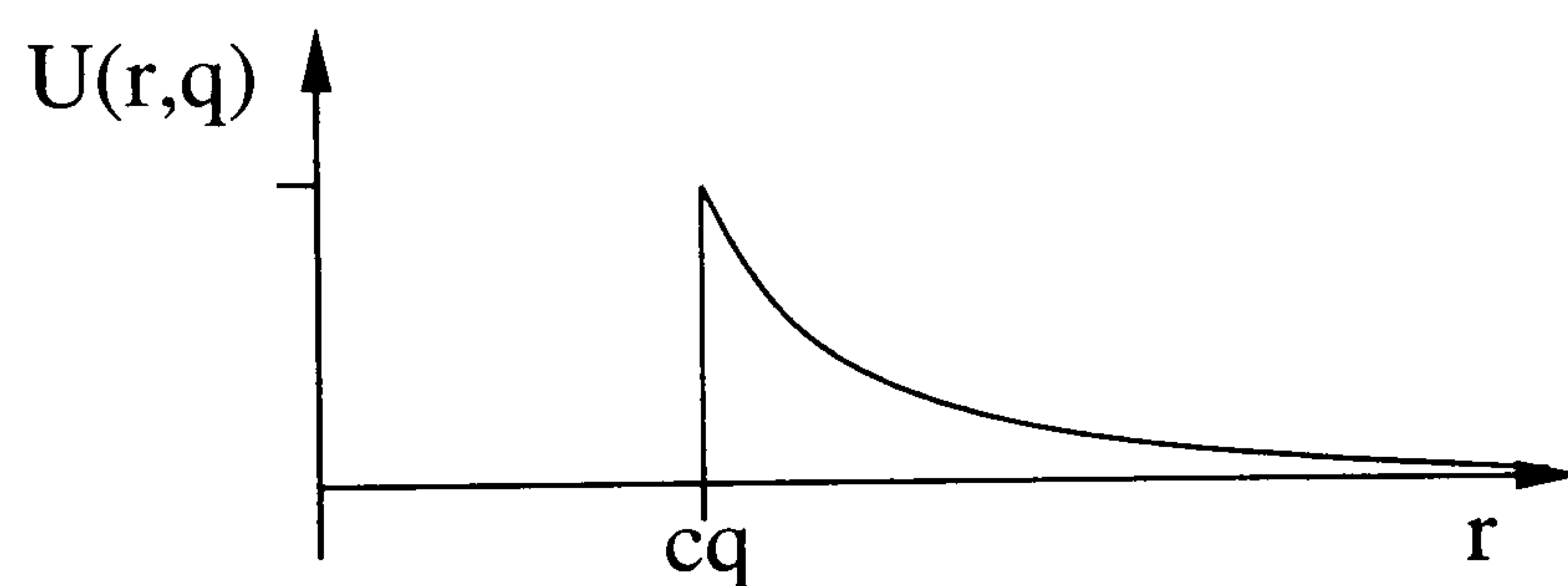
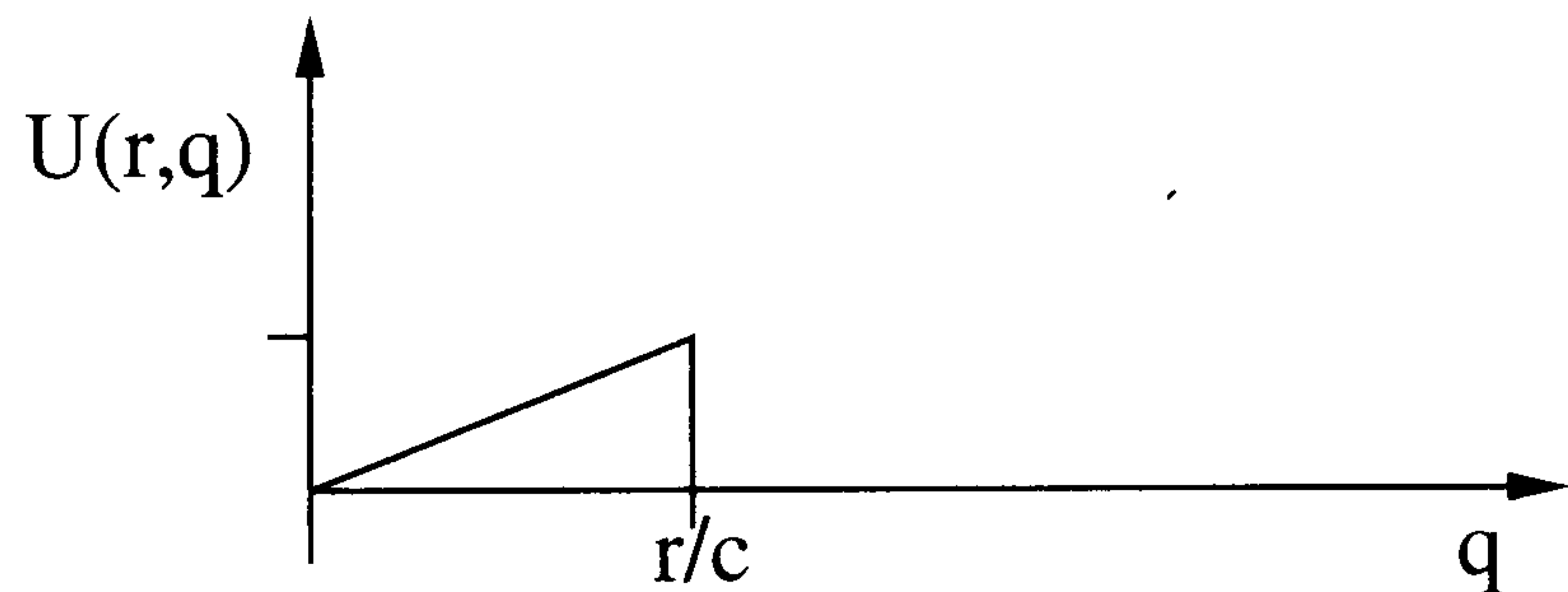
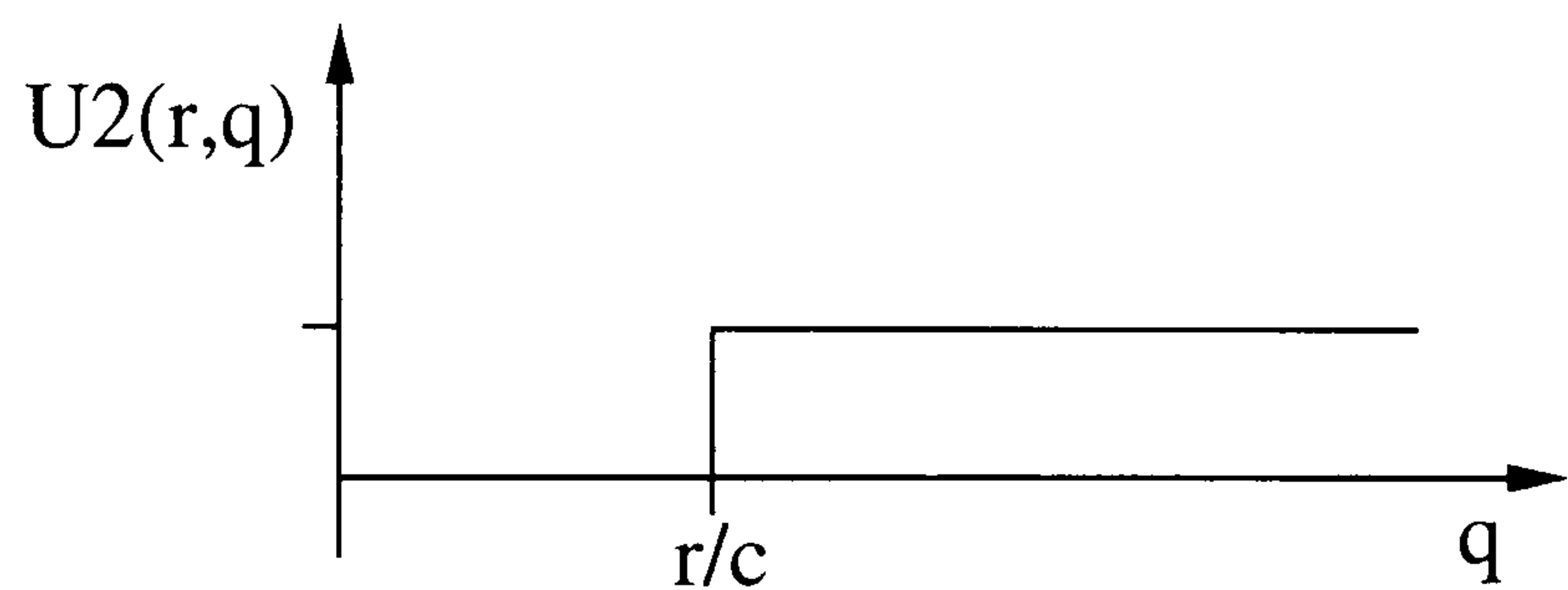
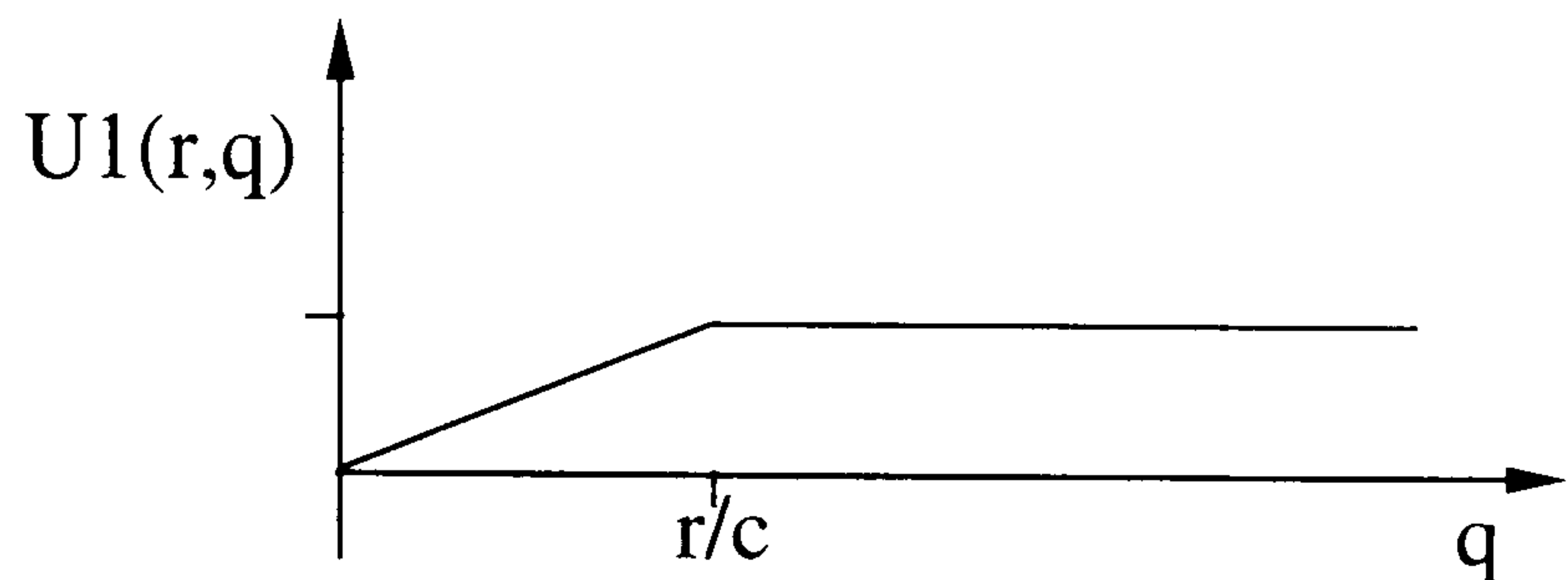
Figure 5.2: The equivalent wavefield of a grounded dipole source.

For the response to a switch-off source profile the equivalent wavefield $U(q)$ arises from the difference of two terms,

$$\frac{\mathcal{D}}{2\pi\sigma r^3}(U1(q) - U2(q)).$$

This results in a “triangle” waveform. **N.B.** this result was derived from the analytical formula for the electric field on the interface between two media. Hence this result only holds on this interface and cannot be used to give the equivalent wavefield in other regions.

At $q > 0$ the wavefield is zero inside the circle $r = cq$. The maximum amplitude at a given $q > 0$ is $\frac{\mathcal{D}}{2\pi\sigma c^3 q^2}$, and occurs on this circle.



5.1.3 EM Response and Equivalent Wavefield for an Impulsive Transmitter Current Profile

The response to a transmitter with an electric current profile which is an impulse at zero time can be calculated by taking the derivative with respect to time of the switch-off response and multiplying by -1.

$$-\frac{\partial}{\partial t} \mathbf{E}_{\parallel}(r, \phi, t > 0) \quad (5.26)$$

$$= -\frac{\partial}{\partial t} \frac{\mathcal{D}}{2\pi\sigma r^3} \left(\operatorname{erf}\left(\frac{r}{c2\sqrt{t}}\right) - \frac{2}{\sqrt{\pi}} \frac{r}{c2\sqrt{t}} \exp\left(-\frac{r^2}{c^2 4t}\right) \right) \quad (5.27)$$

$$= -\frac{\mathcal{D}}{2\pi\sigma r^3} \exp\left(-\frac{r^2}{c^2 4t}\right) \left(\frac{2}{\sqrt{\pi}} \frac{r}{2c} \frac{-1}{2} t^{-3/2} - \frac{2}{\sqrt{\pi}} \frac{r}{2c} \frac{-1}{2} t^{-3/2} - \frac{2}{\sqrt{\pi}} \frac{r}{2c\sqrt{t}} \frac{r^2}{4c^2} t^{-2} \right) \quad (5.28)$$

$$= -\frac{\mathcal{D}}{2\pi\sigma r^3} \exp\left(-\frac{r^2}{c^2 4t}\right) \frac{2}{\sqrt{\pi}} \frac{r}{2c} t^{-3/2} \left(-\frac{1}{2} + \frac{1}{2} - \frac{r^2}{4c^2} t^{-1} \right) \quad (5.29)$$

$$= \frac{\mathcal{D}}{2\pi\sigma r^3} \exp\left(-\frac{r^2}{c^2 4t}\right) \frac{2}{\sqrt{\pi}} \frac{r^3}{8c^3} t^{-5/2} \quad (5.30)$$

Given this analytic expression for the diffusive response we follow the recipe outlined in Box 7 to calculate the equivalent wavefield.

Combining the results

$$\mathcal{L} \left[t^{-3/2} \exp\left(-\frac{a^2}{4t}\right) \right] = \frac{2}{a} \sqrt{\pi} \exp(-a\sqrt{s}) \quad (5.31)$$

(Erdélyi 1954, Equation (28), page 146) for $a > 0$

$$\mathcal{L} \left[\left(\frac{a^2}{4} - \frac{t}{2} \right) t^{-5/2} \exp\left(-\frac{a^2}{4t}\right) \right] = \sqrt{s} \sqrt{\pi} \exp(-a\sqrt{s}) \quad (5.32)$$

(Erdélyi 1954, Equation (5), page 246) for $a > 0$

gives

$$\mathbf{F}(t) = \frac{\mathcal{D}}{2\pi\sigma r^3} \exp\left(-\frac{r^2}{c^2 4t}\right) \frac{2}{\sqrt{\pi}} \frac{r^3}{8c^3} t^{-5/2} \quad (5.33)$$

$$\hat{\mathbf{F}}(s) = \frac{\mathcal{D}}{2\pi\sigma r^3} \left(\frac{r}{c} \sqrt{s} + 1 \right) \exp\left(-\frac{r}{c} \sqrt{s}\right) \quad (5.34)$$

$$\hat{\mathbf{U}}(p) = \hat{\mathbf{F}}(p^2) = \frac{\mathcal{D}}{2\pi\sigma r^3} \left(\frac{r}{c} p + 1 \right) \exp\left(-\frac{r}{c} p\right) \quad (5.35)$$

$$\mathbf{U}_{\parallel}(r, q) = \frac{\mathcal{D}}{2\pi\sigma r^3} \left[\frac{r}{c} \delta'(q - r/c) + \delta(q - r/c) \right] \quad r/c > 0. \quad (5.36)$$

Note that this equivalent wavefield is a highly discontinuous function.

This calculation demonstrates that, while the Q transform is linear with respect to space derivatives, it is not linear with respect to the time derivative.

5.2 Conclusions

The transient electromagnetic field parallel to a grounded horizontal electric current dipole source located at the surface of a uniform half-space and with a switch-off transmitter current profile is

$$\mathbf{E}_{\parallel}(r, \phi, t > 0) = \frac{\mathcal{D}}{2\pi\sigma r^3} \left(\operatorname{erf}\left(\frac{r}{c2\sqrt{t}}\right) - \frac{2}{\sqrt{\pi}} \frac{r}{c2\sqrt{t}} \exp\left(-\frac{r^2}{c^2 4t}\right) \right) \quad (5.37)$$

and for an impulsive transmitter current profile is

$$-\frac{\partial}{\partial t} \mathbf{E}_{\parallel}(r, \phi, t > 0) = \frac{\mathcal{D}}{2\pi\sigma r^3} \exp\left(-\frac{r^2}{c^2 4t}\right) \frac{2}{\sqrt{\pi}} \frac{r^3}{8c^3} t^{-5/2} \quad (5.38)$$

Given these analytic expressions for the diffusive response the equivalent wavefield can be calculated analytically by taking a Laplace transform with respect time with transform parameter p , warping the Laplace domain so that energy at parameter value p is mapped to \sqrt{p} and then taking an inverse Laplace transform from p to the time-like variable q .

This process yields, for the equivalent wavefield of the switch-off source current profile

$$\mathbf{U}_{\parallel}(r, q) = \frac{\mathcal{D}}{2\pi\sigma r^3} q \mathcal{H}\left(\frac{r}{c} - q\right) \quad q > 0. \quad (5.39)$$

and for the equivalent wavefield of the impulse source current profile

$$\mathbf{U}_{\parallel}(r, q) = \frac{\mathcal{D}}{2\pi\sigma r^3} \left[\frac{r}{c} \delta'(q - r/c) + \delta(q - r/c) \right] \quad r/c > 0. \quad (5.40)$$

This demonstrates that, while the Q transform is linear with respect to space derivatives, it is not linear with respect to the time derivative.

Chapter 6

Multichannel Transient Electromagnetic Acquisition and Pre-processing with TEAMEX

The long offset transient electromagnetic (LOTEM) method is designed to penetrate to depths which are of interest in mineral and hydrocarbon exploration and to detect both resistive and conductive targets. LOTEM surveys employ a grounded electric bipole source at the Earth's surface and a number of surface receivers measuring both electric and magnetic fields. In the LOTEM method the distance between transmitter and receiver is approximately equal to or greater than the exploration depth.

The TEAMEX multichannel transient electromagnetic (MTEM) acquisition system enables LOTEM acquisition with simultaneous recording from one source into many receivers. The large dynamic range of the TEAMEX receiver unit allows data to be recorded at much nearer offsets than was previously possible. In addition this technology greatly speeds the data acquisition process. This allows many more transmitter locations to be occupied than was previously possible and results in a dramatic increase in the spatial density of data collected.

Transient electromagnetic surveys have traditionally collected relatively small amounts of data upon which great effort was lavished in order to extract the maximum possible amount of information from each data point. In the main, previously developed data pre-processing techniques remain useful and viable. However, efficient processing of increased data volumes requires new software for efficient storage, display and processing of the data. Applying automated processing procedures has the potential for misleading distortion of the signal.

6.1 The TEAMEX MTEM Acquisition System

The TEAMEX system for multichannel transient electromagnetic sounding was developed by DMT, based on their successful seismic exploration system SEAMEX. Many TEAMEX receiver units can be linked together in a spread, enabling simultaneous recording from one source into many receivers.

The system is designed to record the time domain response to a transient electromagnetic source. A horizontal electric current bipole transmitter carrying a *bipolar* current waveform is commonly employed, switching alternately between positive and negative current — see

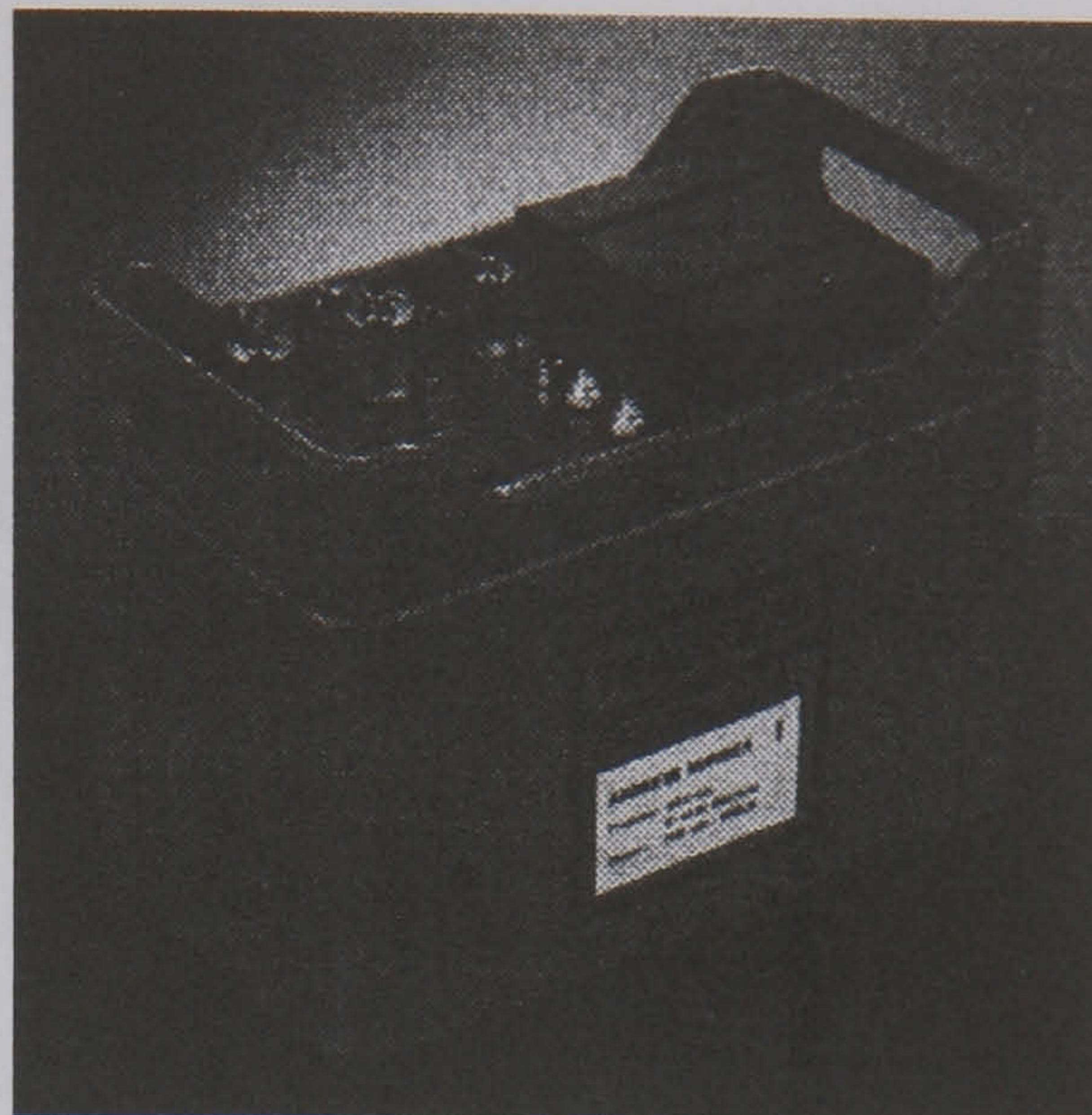


Figure 6.1: A TEAMEX receiver unit.

Figure 6.3 and (Strack 1992). The interval between switching must be long enough for the transient EM response to reach a constant level before next the next polarity switch.

Receivers of both the electric dipole or induction coil type can be used. Each TEAMEX receiver unit converts two analogue channels into digital format for transmission to a central PC which controls the action of the entire spread. Transients may be digitised with a sample interval of 0.25, 0.5, 1, 2, 4, 8 or 16 ms. Each recorded transient may contain 2048 or 4096 samples.

The TEAMEX receiver units do not record all the time. Each receiver unit records transients on two channels in a time interval which captures a specified number of samples before and after the switching of the current polarity. After recording and digitisation the transient signals are then sent back to a controlling PC-compatible workstation.

In practice, the time taken to transmit the digitised signals along the PCM line from the remote units to the central controlling PC is likely to determine the minimum interval between switches of the transmitter current polarity and hence the number of transients which can be recorded in a given time. The time required to transmit the digitised signals depends upon the number of samples recorded, number of receiver units employed and bandwidth achieved through the PCM digital transmission line. Wet weather and long distances from the remote units to the receiver line controller exaggerates capacitative loss in the PCM line which in turn limits the achievable bandwidth.

6.1.1 Acquisition Configuration

The dynamic range of the transient signal decreases with distance from the transmitter. The increased dynamic range of the new TEAMEX receiver unit allows data to be recorded at much nearer offsets than was previously possible (Strack 1992, Chapter 5, page 140). In addition, the centralised digital control and transmission of the receiver spread greatly speeds the data acquisition process. This allows many more transmitter locations to be occupied than was

previously possible and results in a dramatic increase in the volume of data that can be collected.

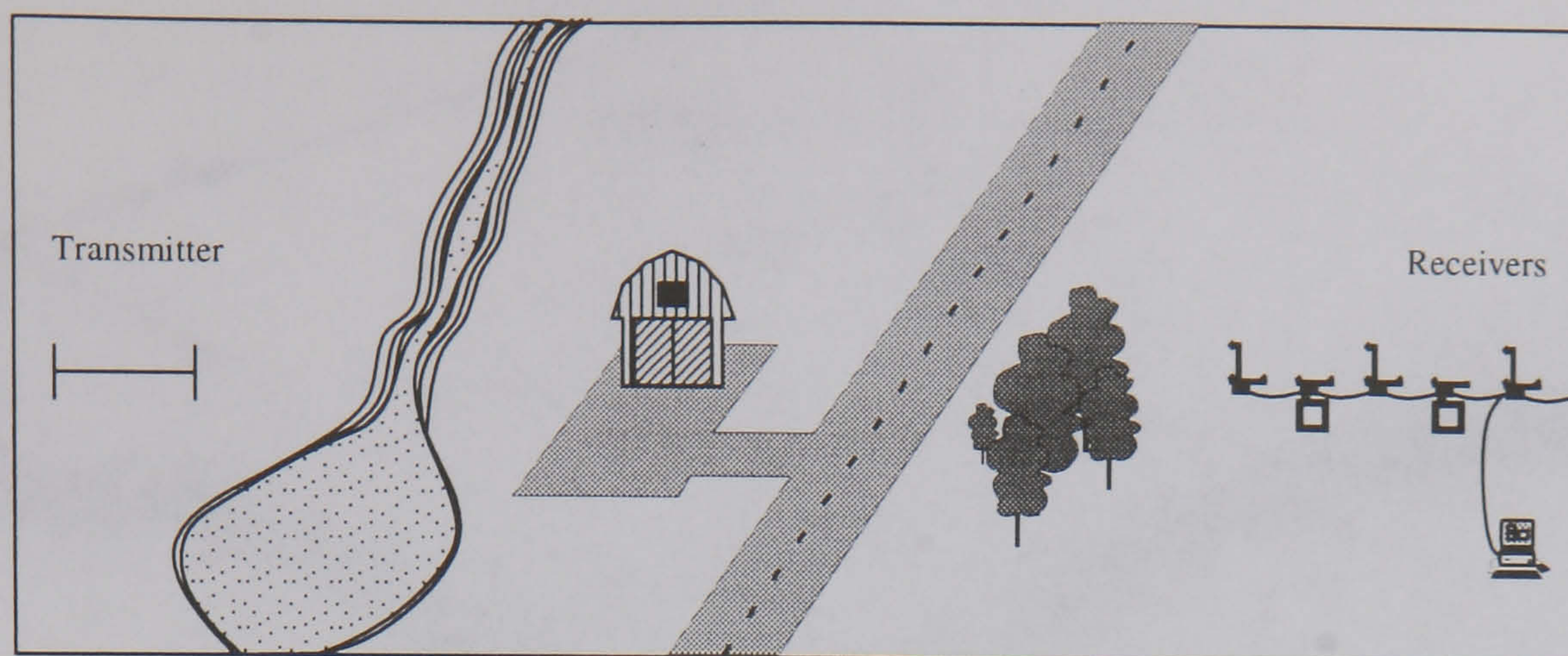


Figure 6.2: Synchronisation between the transmitter and receiver systems is necessary, not only because the receiver units do not record continuously, but also because the onset time is not always clear from the data. Using clocks to synchronise the transmitter and receiver systems removes the necessity for a physical connection or line-of-sight between the transmitter and receiver crews. This means that there is not a need for long cable runs or telemetry repeater stations when there are large distances or obstacles between transmitter and receiver crews.

For large multichannel surveys a regular acquisition geometry, as pictured in Figure 6.3, simplifies field work, survey design and processing.¹ Using a grounded line current source as transmitter, two orthogonal transmitter orientations are “shot” into each receiver spread. Both in-line and broadside transmitters are used with a bipolar transmitter current wave form. Each TEAMEX receiver unit records two channels. When a grounded current bipole source is used it is usual to measure the horizontal electric field parallel to the transmitter and one additional component, which is alternately the horizontal electric field perpendicular to the transmitter and the rate of change of the vertical component of the magnetic field.² This acquisition geometry is a development of that described by Strack (1992, figure 5.14, page 139).

For convenient reference, and compatibility with previous work, the measured electric field components are always named with reference to the transmitter orientation employed when they were recorded. The horizontal component of the field **parallel** to the transmitter orientation is always denoted E_x , regardless of any external coordinate system. Similarly the horizontal component of the electric field **orthogonal** to the transmitter orientation is always denoted E_y . The rate of change with respect to time of the vertical component of the magnetic field is denoted dH_z/dt .

¹When only a small number of sources and receivers are employed it is reasonable to select their exact positioning according to field conditions and this has been common practice.

²It is convenient to measure the rate of change of the vertical component of the magnetic field, partly because this can be achieved by using a simple horizontal loop of cable as a transponder and partly because for a grounded current source the natural-field noise in the magnetic field is greater in the horizontal direction than in the vertical direction (Gunderson, Newman & Hohmann 1986).

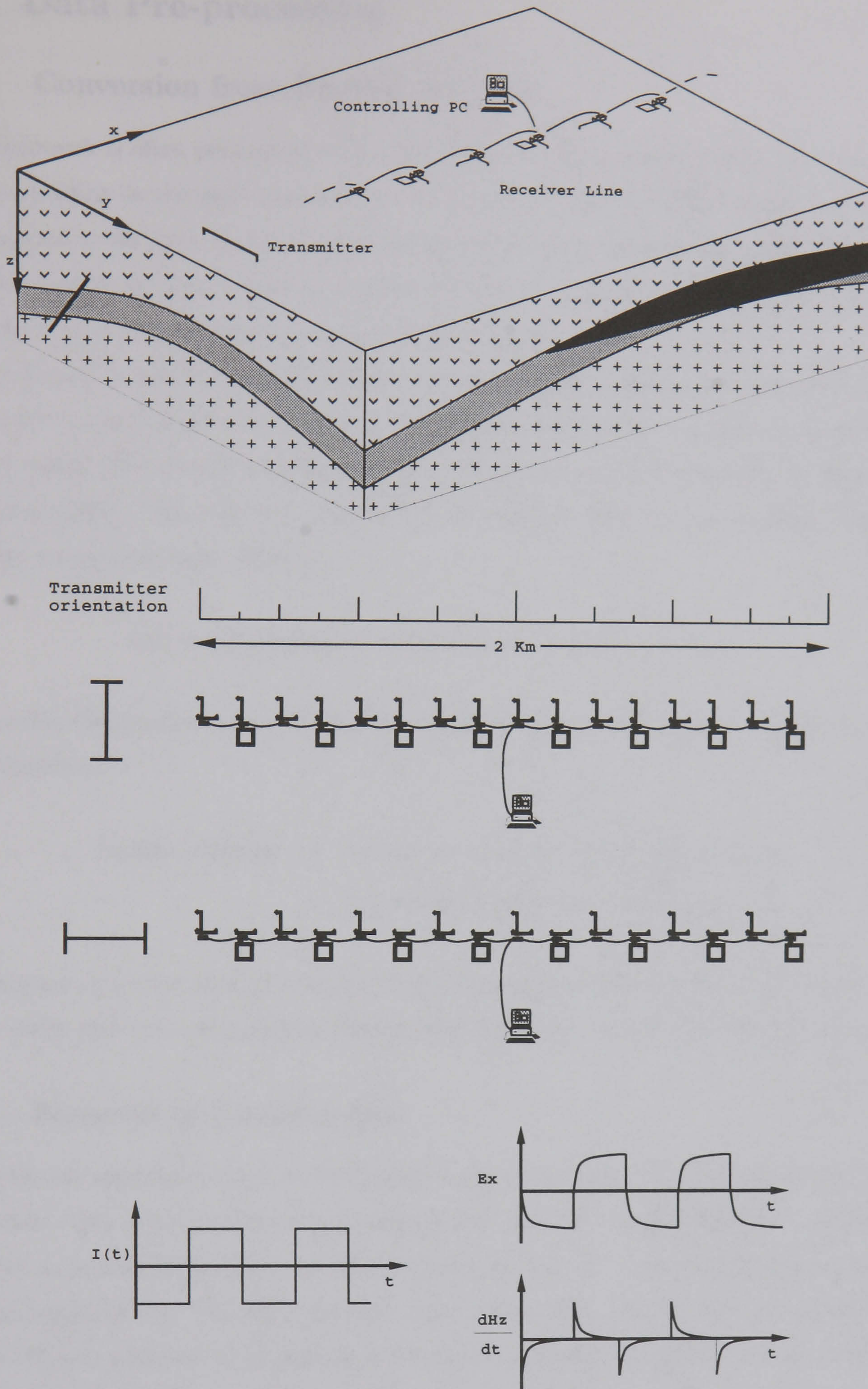


Figure 6.3: Surface to surface MTEM data acquisition configuration. Top: The transmitter and receivers are laid out along a line over the target (after Strack 1992, figure 5.14, page 139). Middle: Each TEAMEX receiver unit measures E_x , the horizontal component of the electric field parallel to the transmitter orientation, and one additional component, which is alternately the horizontal component of the electric field perpendicular to the transmitter orientation and the rate of change with respect to time of the vertical component of the magnetic field, denoted dH_z/dt . Bottom: A bipolar transmitter current wave form $I(t)$ induces transient electromagnetic signals whose decays reveal the subsurface resistivity structure.

6.2 Data Pre-processing

6.2.1 Conversion from Bipolar Response

TEM fieldwork is often performed with a bipolar transmitter current profile, since this gives a constant loading on the generator and switching systems. However TEM signals are more usually analysed in the form of the response to a *switch-on* or *switch-off* transmitter current profile. Transients recorded using a bipolar transmitter current waveform are commonly converted to a switch-on or switch-off response during pre-processing.

A switch-on transmitter current profile is zero for negative times and constant for positive times while the switch-off transmitter current profile is constant for negative times and zero for positive times. The switch-on response is also sometimes known as the step-on response (Yu & Edwards 1992). The switch-on and switch-off responses differ by the constant value of the late-time asymptotic level. That is

$$\text{switch-off response} = \text{late time level} - \text{switch-on response.} \quad (6.1)$$

Consider the situation where the bipolar current is flipping from negative to positive polarity. The response is

$$\text{bipolar response} = \text{switch-on response} - \text{switch-off response} \quad (6.2)$$

$$= 2 \times \text{switch-on response} - \text{late time level.} \quad (6.3)$$

The constant late time level is removed during bias removal (see Section 6.2.2 below) and so we can safely take the pre-processed bipolar response to be twice the switch-on response.

6.2.2 Removal of Residual Bias

Transients are recorded every time the bipolar current waveform is switched from one polarity to another. The interval between switching is such that the signal from the transmitter has settled to a constant level before the next transient is recorded. Immediately prior to recording the next transient the TEAMEX receiver units try to back off this background signal level or *bias*. This is achieved by averaging the signal to estimate the DC level and subtracting it from the signal. In addition to the bipolar waveform of the transmitter, bias can also result from self-potential generated between electrodes, or magnetotelluric signals originating from fluctuations in the Earth's natural magnetic field.³ Because of these unpredictable signals it is likely that some residual bias will remain.

Each transient contains a certain number of samples the initial few hundred of which are recorded *pre-trigger*. That is they are recorded *before* the current polarity is switched. These

³In fact the magnetotelluric signal is likely to be larger in amplitude than the signal from the transmitter.

pre-trigger samples allow accurate identification and backing off of any residual bias not corrected by the receiver unit. Failure to remove residual bias can result in significant misinterpretation of the data (Strack 1992, Chapter 5, page 143).

6.2.3 Reduction of Random Noise by Vertical Stacking

In order to improve the signal-to-noise ratio many transients are recorded for one transmitter-receiver configuration and then *vertically* stacked. Given an adequate number of relatively clean transients, a simple averaging procedure is remarkably effective in improving the signal to noise ratio. There are also a number of algorithms which try to improve upon this brute force approach. *Selective stacking* procedures attempt to identify and remove individual uncharacteristic samples (outliers) due to noise bursts in an otherwise acceptable transient (Strack 1992). Helwig, Hanstein & Hördt (1995) employ cluster analysis to identify and discount uncharacteristic transients, which are likely to be noisy or distorted. Due to the volume of data to be processed these procedures are automated to the greatest extent possible.

6.2.4 Reduction of Organised Noise

EM measurements collected in inhabited regions are typically contaminated with a significant amount of noise from power sources. Generally this noise is concentrated in a few narrow frequency bands; the base frequency of the power supply, and higher harmonics.

Notch filters may be applied to reduce this noise energy. However this approach introduces distortion of the signal, particularly around the onset, resulting in great difficulties during interpretation.

An alternative approach is the *lockin* filter. This is typically used to attenuate periodic noise associated with the base frequency of the power supply, which is commonly the most powerful single periodic noise energy. Given the frequency of this noise, the procedure estimates its phase by fitting a sine waveform to the pre-trigger samples. Then assuming that the noise is frequency- and phase-stable over the duration of the transient, this sine waveform is extrapolated and subtracted from the transient.

Helwig *et al.* (1995) report a refinement of the method, which refines the estimate of the frequency of the noise, as well as its phase. This gives improved results but at much greater computational cost.

If the phase of periodic noise varies from transient to transient in a random fashion then vertical stacking can have some effect in reducing this noise energy. In this way vertical stacking can assist in reduction of residual periodic noise remaining after filtering. However vertical stacking can also mask distortions introduced by periodic noise reduction filters.

6.3 Noise Environments

The frequency content of the transient EM signal varies significantly, and in a systematic way, over the duration of the response. This means that the transient EM signal is *non-stationary*. For this reason it can be suggested that it is not possible to define sensibly a single signal-to-noise ratio for a transient EM signal.

For example, it is possible to obtain a very accurate estimate of the asymptotic late-time (DC) signal level by using both vertical stacking and averaging in time. In contrast, at the very early times the signal is changing fastest and the scope for using the temporal coherence of the signal is at a minimum.

It is perhaps more useful to discuss the uncertainty in the signal level at a particular time, which can be derived during vertical stacking by considering the distribution of samples about the mean. When performing feasibility studies it is important to consider the achievable uncertainty over the time range used for interpretation.

6.4 Distortions of the Signal

6.4.1 Low-pass Filtering

It is a general principle in data acquisition to employ a bandpass filter to restrict the frequencies recorded to the range of interest. If no filters are employed then noise from uninteresting frequency ranges will unnecessarily be recorded and energy from frequencies above the Nyquist will be aliased and appear as spurious energy in the signal.

In TEM surveying the late time (DC) response is usually of interest and so a low-pass filter is commonly employed. Application of a low-pass filter can be discussed either in terms of multiplying the Fourier power spectrum of the signal with the Fourier-domain filter response function, or equivalently, convolution of the signal with the time-domain filter response function. Usually filter design takes place in the Fourier domain.

It is important when designing a low-pass filter to bear in mind the distortion of the TEM signal which will occur when it is applied. A given Fourier-domain filter response function determines the time-domain filter response. Generally speaking, the wider the time-domain filter response, and the greater the blurring and distortion of the signal.

The width of the filter response in the time domain is related to the steepness of the decay of the filter response in the Fourier domain. The faster the decay, the wider the response and the greater the distortion. As a consequence TEM acquisition systems typically employ a low-pass filter with an unusually low rate of decay.

6.4.2 Clock Drift

During acquisition with the TEAMEX system synchronisation between the transmitter and receiver systems is usually achieved using clocks. Inevitably these clocks do not remain perfectly in step throughout acquisition: there is some *drift* between them. This drift causes the receiver and transmitter systems to move gradually out of synchronisation, resulting in a gradual change in the onset time in the recorded transients. When the raw traces are vertically stacked to reduce noise levels the signal becomes slightly smeared (see Section 6.2.3 for an explanation of vertical stacking). The degree of smearing of the signal is determined by the amount of drift between the receiver and transmitter clocks. For this reason it is important that the drift between the clocks is negligible over time intervals on which a particular acquisition configuration is occupied.

6.4.3 Transmitter Waveform Instability

The objective of the transmitter system is to inject into the Earth a bipolar current with the maximum possible dipole moment. Usually this is achieved by connecting a standard electrical power generator to a switch-box which controls the source current profile. The length of the transmitter bipole is generally fixed by survey considerations, leaving only the current amplitude to be maximised. Selection of a safe current amplitude is the task of the transmitter operator.

It is not possible to realise a perfect square wave. In practice the quality of the “square wave” produced by the transmitter system degrades as the current amplitude approaches the capacity of the switch-box, and/or the injected power approaches the capacity of the generator. In general a slightly different transmitter waveform is realised for differing current amplitudes and power inputs. The transmitter operator must select a suitable power input which can be sustained at a stable level without unfortunate degradation of the bipolar waveform or damage to generator or switch-box.

The effective ground resistivity encountered by the transmitter crew can vary widely over relatively short distances. Once in operation heat builds up in the switch-box and generator. This causes changes in performance. On arrival at a transmitter site the transmitter operator must quickly assess what power can be sustained, based upon the behaviour of a newly installed, cold, system.

Instrumentation of the transmitter installation is usually minimal. Commonly a reading of nominal current amplitude is provided by a gauge on the switch-box. This reading is recorded at the start of acquisition from a particular configuration, and sometimes at completion of acquisition if there has been a significant change. If the transmitter performance declines dramatically it is necessary to stop acquisition, re-evaluate, and begin again.

6.4.4 Near Surface Heterogeneities

Lateral variations in the resistivity of the near surface can arise for many reasons including weathering of the near surface and different surface cover. It is widely known that such near-surface heterogeneities can strongly distort magnetotelluric responses. Controlled source EM methods also suffer from such distortion (Newman 1989, Strack 1992, Qian 1994).

Typically an acquisition configuration is optimised to resolve deeper features and is not well suited to resolve the very near surface. A useful analogy can be drawn with the experience of viewing the world through bottom of a drinking glass. It is quite possible to deduce that the distorting layer is there but difficult to focus at the same time on the bottom of the glass, and the world which is viewed through it.

Qian (1994) analyses the effect of a small local surface heterogeneity over an otherwise 1D Earth using a thin-sheet integral equation formulation. Considering a grounded electric current dipole transmitter Qian (1994) demonstrates that the greatest effect arises when the heterogeneity is directly under either the transmitter or receiver. When the heterogeneity is under the transmitter the effect is to change the effective dipole moment of the transmitter. This effect is well known in magnetotellurics as *static shift* and is sometimes called *transmitter overprint* in controlled source methods. When the heterogeneity is under the receiver the electric field is again strongly affected, as would be expected from reciprocity of the source and receiver. However the magnetic field is less strongly distorted, resulting in measurements which are more difficult to interpret.

6.4.5 Induced Polarisation

In the theory of TEM propagation and interpretation, it is often assumed that subsurface resistivity is invariant with frequency and capacitive effects are neglected. This may not be a good approximation to the EM response in areas of significant subsurface metallic mineralisation or near to conducting objects such as pipelines and wire fences.

When the subsurface contains significant metallic minerals, electric current from a TEM source causes electrochemical reactions. Ions are exchanged at the surface of contact between the minerals and the electrolytes dissolved in the fluid filling the pore spaces. This electrochemical exchange creates a voltage which opposes the current flow through the material. When the externally applied current is turned off, the electrochemical voltages at the metallic grain surfaces are dissipated, but not instantaneously (Dobrin, & Savit 1988). Because the build-up and decay of these opposing voltages is not instantaneous, this effect decreases with the frequency of the source current. This effect is called induced polarisation (IP) and has been widely used in the exploration for minerals (Sumner 1985).

Cultural conductors such as buried cables and pipelines are commonly encountered in EM exploration programs (Nekut & Eaton 1990, Qian & Boerner 1995) and can produce IP effects

similar to subsurface mineralisation. Flis, Newman & Hohman (1989) demonstrate how IP effects can distort TEM responses to result in sign reversals. These sign reversals cannot be explained or interpreted using a theory which only allows a frequency-independent resistivity and neglects capacitative effects.

6.4.6 Pulsed Cathodic Protection

Pipelines, well casings and other steel structures corrode when buried in soil. The cathodic protection technique causes DC electrical current to flow from the soil to the surface of the structure and has been used to mitigate corrosion for many years.

Typically, the negative lead from a rectifier is connected to the structure, and the positive lead to a bed of expendable anode rods. The resulting DC current mitigates corrosion by electrochemically reducing corrosive oxygen molecules and hydrogen ions present in the soil adjacent to the surface of the structure. This protective reaction occurs within microseconds of the application of the cathodic current. Before the corrosion reactions can begin again, further molecules and ions must diffuse to the surface of the structure from the surrounding soil.

The diffusion process is orders of magnitude slower than the reduction process. The throw, or distance down the pipeline or well casing increases with current magnitude. With Pulsed Cathodic Protection (PCP), the corrosive molecules and ions are electrochemically reduced with current pulses of short duration but high magnitude. The short duration PCP pulses are separated by relatively long intervals, consequently the PCP voltage is applied less than 10% of the total time.

PCP systems produce a characteristic signal which should be clearly visible on MTEM data collected nearby. If at all possible, the cathodic protection of structures near the field area should be switched off during acquisition of a TEM survey.

6.5 Measurement and Compensation for the System Response

Controlled source geophysics operates by measuring the Earth's response to an external source and then estimating subsurface parameters from this response. In order to extract this information it is necessary to have a good estimate of the source signal. Perhaps the most obvious approach to obtaining a good estimate of the source is to measure it (Ziolkowski 1987).

In LOTEM surveying it is normal practice during initial field system tests to measure the EM fields a few metres from the transmitter. This is performed with routine receiver units and controller. Since the EM field amplitude is much higher than at usual acquisition offsets the dimensions of the receiver bipoles and/or receiver coils employed are greatly reduced. However the acquisition settings (sample interval etc) are as for normal operation.

In this measurement regime the EM field effectively retains the source profile injected by the transmitter system. Since the measured data includes the response of the receiver system, as well as the transmitter, it is called the system response.

It is not usual to measure the system response throughout a LOTEM survey. It would be quite possible to deploy an additional TEAMEX receiver unit at the transmitter to measure continually the system response. In the case that there is not a connection between receiver and transmitter installations (this is the usual case — see Section 6.1.1) this would require a dedicated PCM digital transmission line and PC-compatible. Since this recording would be operating independently from the main data capture unit it would be very difficult to identify with complete certainty the system response corresponding to a particular transient.

Compensation for the system response is required during interpretation. Most quantitative interpretation is model-based and operates by iterative forward modelling to match synthetics to the measured data. In such a situation the synthetics can be convolved with the system response before comparison with the data. An alternative approach is to deconvolve the system response to recover (a band limited measurement of) the impulse response of the Earth, which can then be interpreted (Ziolkowski, Hobbs, Chisholm, Wilson, Sharrock, Rüter, Hördt, Neubauer, Vozoff, Helwig & Andrieux 1996).

6.6 Experience from an Early Time-Lapse Multichannel Survey with TEAMEX

Two MTEM surveys were acquired at a gas storage facility which uses a natural underground reservoir in the Paris basin. The goal of this time-lapse surveying was to determine if differences between the two surveys could be interpreted to monitor changes in the gas “bubble” as the operator, Gaz de France, injected and recovered gas reserves.

The acquisition was performed by Compagnie Générale de Géophysique and their sub-contractors, including

HarbourDom Consulting GmbH, using a horizontal electric current bipole source and TEAMEX receiver units. The same densely-spaced pattern of sources and receivers was used in both surveys. The first survey employed a total of 64 receiver channels and 57 transmitter stations, concentrated along a profile over the gas reservoir (Wilson, Ziolkowski, Hobbs & Sharrock 1995), giving exceptionally dense spatial data coverage for a LOTEM survey. Accurate surveying of the field area, and semi-permanent installation of electrodes, ensured that the second survey returned to the same source and receiver locations.

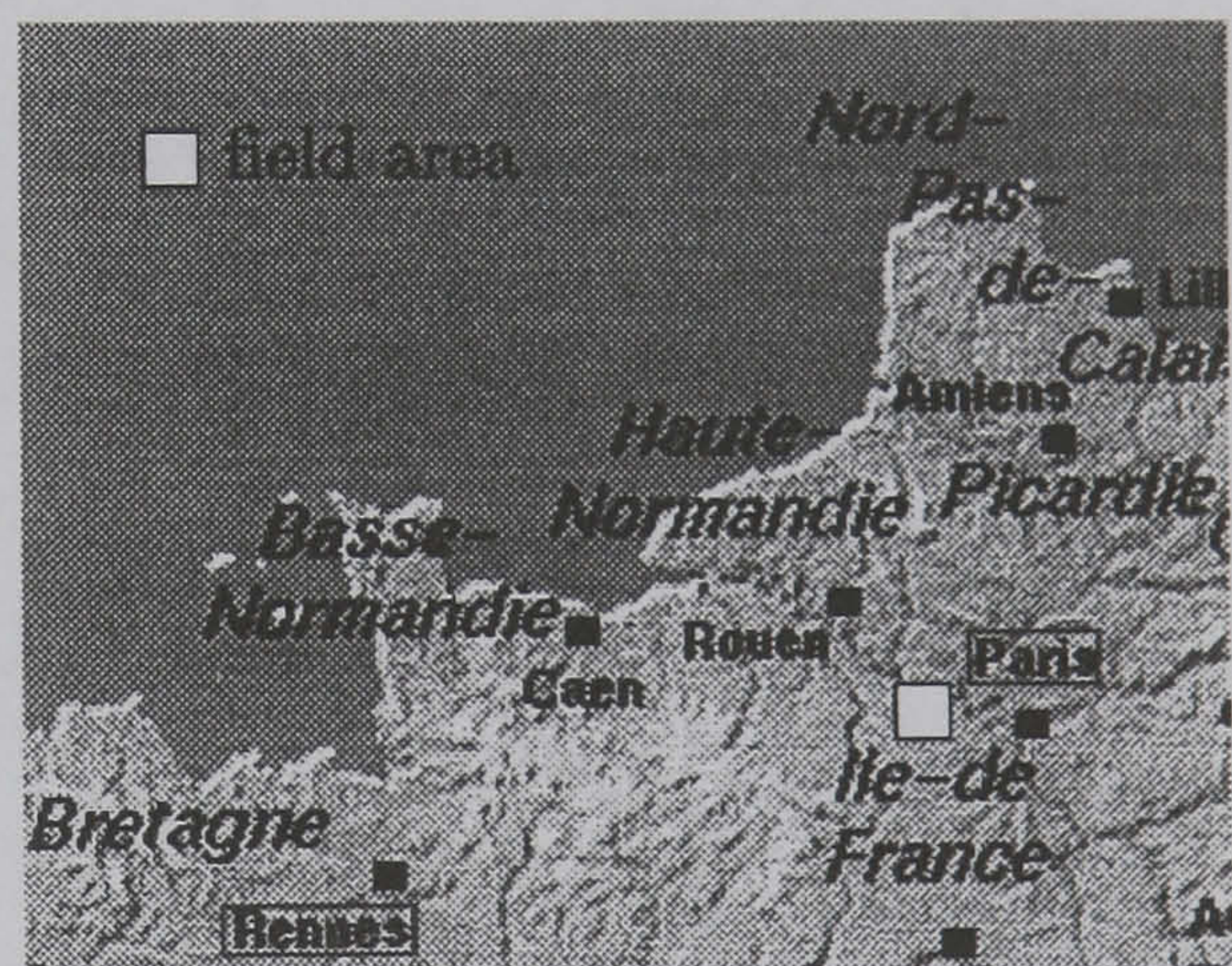


Figure 6.4: Location of field area.

Each TEAMEX receiver unit recorded two transients every time the bipolar current waveform was switched. Each transient contains 2048 samples at a sampling rate of 1 ms. Of these approximately 384 are pre-trigger samples, which allow accurate identification and backing off of remaining bias and also record valuable information on background noise characteristics.

Figure 6.5 displays in the form of a common source gather the in-line Ex component recorded from transmitter 19 at several receiver locations.

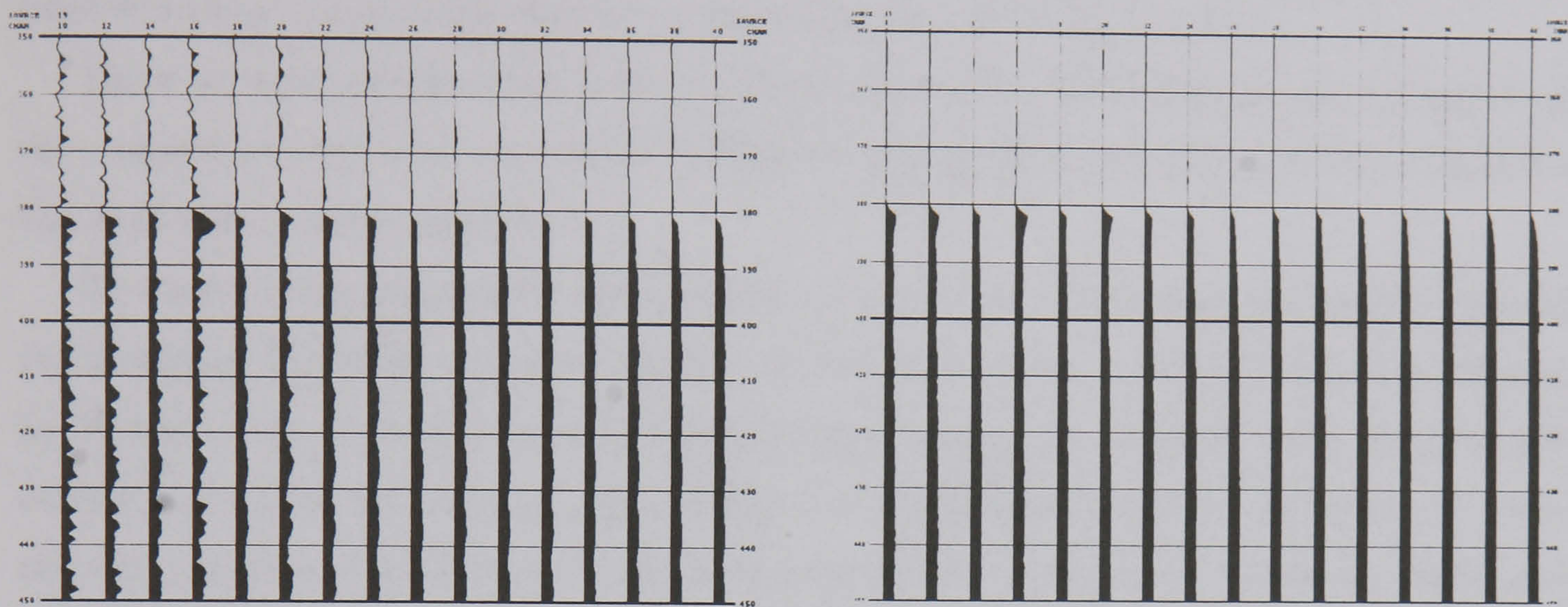


Figure 6.5: Common source gather of E field components in-line with transmitter 19, presented in the style of a seismic common source gather. In each figure offset from the transmitter increases from right to left in intervals of 125 m, starting from 1 km. Time increases from top to bottom in intervals of 1 ms while timing lines are set at 10 ms intervals. On each trace is apparent a number of pre-trigger samples followed by onset of the pulse from the transmitter. Left: the first raw trace recorded at each receiver. Right: the result of vertical stacking of all the traces at each receiver, demonstrating a greatly improved signal-to-noise ratio.

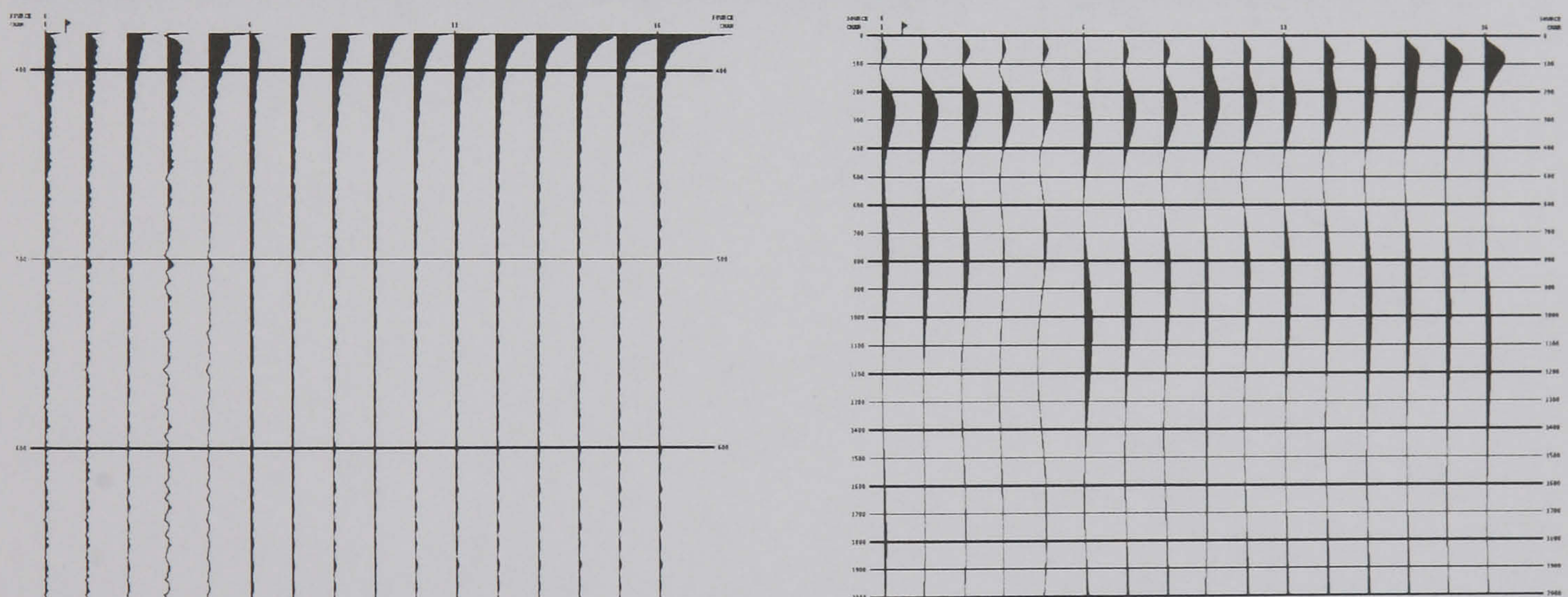


Figure 6.6: Common source gather of E field components in-line with transmitter 19 after processing. In each figure offset from the transmitter increases from right to left in intervals of 125 m, starting from 1 km. Left: The last 200 samples of the trace have been used to estimate the late-time DC level of the signal. The trace is then subtracted from the DC level in order to convert from the switch-on response, which is recorded in the field, to the switch-off response, which is more advantageous for processing. Right: Preliminary calculation of the equivalent wavefield using Q transform inversion by singular value decomposition (see Section 7.3). The equivalent wavefield is plotted against the time-like variable q which has units of \sqrt{s} . q increases down the page with timing lines at $1 \sqrt{s}$ intervals.

The number of pre-trigger samples was intended to be fixed but is observed to vary from

transmitter to transmitter. Zooming in on the onset of the arrival allows the interpreter to estimate the actual number of pre-trigger samples, and compensate in later processing. For transmitter 19, the zero time is picked as sample 381.

Analysis of noise content concludes that the principal periodic noise is cultural 50 Hz background from power supplies and is not phase-stable between transients. Since the noise is not phase stable between transmitter switchings a simple averaging of an adequate number of relatively clean transients is effective in improving the signal-to-noise ratio.

These surveys have demonstrated the effectiveness of the TEAMEX acquisition system and the viability of large-scale time-lapse MTEM surveying. However interpretation of data from this field area remains unfinished.

Geological noise, topography and the presence of pipelines mean that, as would be expected, the measured data does not match exactly the response to the reservoir which was estimated by 3D modelling. Principal among these distorting factors are about 40 wells, and associated surface pipes used for injection, production and monitoring of gas in the reservoir. While the EM response of pipelines is broadly understood the quantitative evaluation and removal of pipeline effects in EM surveys remains an area of active research (Qian & Boerner 1995). Certainly it would be a very non-routine task to interpret and eliminate the effects of 40 wells and the conclusivity of the results might still be held in question.

However it can be hoped that these distorting features will all remain the same during the second survey. Taking the difference between the data collected in the two surveys will then eliminate effects from pipelines and uncover the response to changes in the reservoir.

6.7 Conclusions

The TEAMEX system for multichannel transient electromagnetic sounding was developed by DMT, based on their successful seismic exploration system SEAMEX. Many TEAMEX receiver units can be linked together in a spread, enabling simultaneous recording from one source into many receivers. The large dynamic range of the TEAMEX receiver unit allows data to be recorded at much nearer offsets than was previously possible. In addition this technology greatly speeds the data acquisition process. This allows many more transmitter locations to be occupied than was previously possible and results in a dramatic increase in the spatial density of data collected.

The system is designed to be used in the time domain with a transient electromagnetic source. Synchronisation between the transmitter and receiver systems can be achieved using clocks. In a typical acquisition both in-line and broadside transmitters are used with a bipolar transmitter current wave form. Data pre-processing includes conversion from a bipolar response to a switch-on response, removal of residual bias, reduction of random noise by vertical stacking, filtering of periodic noise and noise bursts.

Distortion is inevitably introduced by filtering employed in the acquisition system and during noise reduction. This distortion can be measured or estimated. Additional distortion is introduced during vertical stacking of transients for example as a result of instability of the transmitter waveform or drift between the clocks controlling the transmitter and receiver systems. It is important that possible sources of distortion are understood and accounted for during interpretation.

Chapter 7

Diffusive to Propagative Mapping

Seismic energy propagates through the Earth as, to a good approximation, a non-dispersive wave motion. Seismic signals can often be interpreted very effectively using procedures which analyse the time seismic pulses take to travel to and from a reflecting target. Electromagnetic energy propagates through air as a wave motion, but its movement through the Earth is diffusive. Because of the imperfect conduction of the Earth the different frequencies in an electromagnetic pulse move at different speeds and are attenuated at different rates causing the shape of the pulse to change over time. This diffusive nature limits resolution, nullifies the concept of a travel time and makes interpretation of diffusive EM data more difficult than for the seismic reflection method. Because of the absence of an alternative interpretation procedure, for example based upon travel-times, iterative forward modelling continues to be the mainstay of many EM processing and interpretation schemes despite high computational cost and well understood difficulties of the approach.

The equivalent wavefield concept relates diffusive propagation to an equivalent non-diffusive, wave propagation, provided equivalent source and boundary conditions are satisfied. The equivalent wavefield concept is applied here to relate diffusive electromagnetic propagation to an equivalent wavefield.

The Q transform is a prescription for calculating a diffusive response from its equivalent wavefield. The Q transform may be inverted to calculate an equivalent wavefield from diffusive transients. Following Tournier & Gibert (1995) we call this process diffusive to propagative mapping (DPM). Given a suitable equivalent wavefield, data processing and interpretation techniques inspired by the seismic method may be applied to the equivalent wavefield to recover the equivalent velocity $c(\mathbf{x})$. For EM data a conductivity profile $\sigma(\mathbf{x})$ may then be calculated using the relationship $\mu\sigma(\mathbf{x}) = c(\mathbf{x})^{-2}$ (Lee & Xie 1993).

7.1 Diffusive to Propagative Mapping (DPM) as an Ill-posed Inverse Problem

Section 3.1 derived the Q transform and explained how it may be used as a prescription to calculate the diffusive field corresponding to a wavefield. This might be the case if it was desired to model a diffusive process by first computing the equivalent wavefield. This approach has been taken by a number of authors (Lee *et al.* 1989, Oliver 1994). This chapter concentrates on inverting the Q transform to achieve diffusive to propagative mapping.

Section 3.1 explains that the action of the Q transform can be understood as being equivalent to the following steps

1. a forward Laplace transform of the input signal,
2. a non-linear warping of the Laplace transform variable and
3. an inverse Laplace transform.

Formally, this action of the Q transform can be inverted by reversing this process. Unfortunately the inverse Laplace transform is troublesome to calculate numerically and so it is not usually convenient to calculate the equivalent wavefield through the Laplace transform domain.

We seek to derive a formula directly prescribing the equivalent wavefield $\mathbf{U}(\mathbf{x}, q)$ in terms of the diffusive field $\mathbf{F}(\mathbf{x}, t)$. Following along the lines of the derivation in section 3.1 and starting from $\hat{\mathbf{F}}(\mathbf{x}, p^2) = \hat{\mathbf{U}}(\mathbf{x}, p)$ we may write

$$\hat{\mathbf{U}}(\mathbf{x}, p) = \int_0^\infty \mathbf{F}(\mathbf{x}, t) \exp(-p^2 t) dt, \quad (7.1)$$

however it is not possible to continue further along this route since the inverse Laplace transform of $\exp(-p^2 t)$ with respect to transform variable p does not exist.

The difficulty of calculating a numerical or analytical inverse Laplace transform arises not because of inadequate development of the technology or theory of the inverse Laplace transform, but because diffusive to propagative mapping is fundamentally an *ill-posed* problem. If we desire to compute the equivalent wavefield of a diffusive field some other approach must be found. Inspiration and understanding of such techniques can be obtained from an analysis of the Q transform in terms of inversion theory.

A Fredholm integral equation of the first kind is an equation of the form

$$f(t) = \int_a^b K(t, q) u(q) dq \quad (7.2)$$

(Kress 1989). A kernel $K(t, q)$ may be expanded in terms of its nonzero singular values ν_i , and

left and right singular functions \mathbf{u}_i and \mathbf{v}_i as

$$K(t, q) = \sum_{i=1}^{\infty} \nu_i \mathbf{u}_i(t) \mathbf{v}_i(q). \quad (7.3)$$

Picard's theorem (Kress 1989, theorem 15.18, page 234) states that (7.2) is solvable only if

$$\sum_{i=1}^{\infty} \frac{1}{\nu_i^2} |(f, \mathbf{u}_i)|^2 < \infty \quad (7.4)$$

where (f, \mathbf{u}_i) denotes the scalar product of f and \mathbf{u}_i and $|a|$ denotes the modulus of a . In this case the solution is

$$u = \sum_{i=1}^{\infty} \frac{1}{\nu_i} (f, \mathbf{u}_i) \mathbf{v}_i. \quad (7.5)$$

When considered as a formulation for calculating the q -domain equivalent wavefield from the time-domain diffusive electromagnetic field, the Q transform

$$\mathbf{F}(\mathbf{x}, t) = \frac{1}{2\sqrt{\pi t^3}} \int_0^{\infty} q \exp(-\frac{q^2}{4t}) \mathbf{U}(\mathbf{x}, q) dq, \quad (7.6)$$

is an example of a Fredholm integral equation of the first kind with a kernel

$$K(t, q) = \frac{q}{2\sqrt{\pi t^3}} \exp(-\frac{q^2}{4t}). \quad (7.7)$$

Following Hofmann (1986, definition 2.42) we can use the rate of decay of the singular values ν_i to characterise the degree of ill-posedness of a problem. If there exists a positive real number ν such that the singular values satisfy $\nu_i = \mathcal{O}(i^{-\nu})$ then ν is called the degree of ill-posedness, and the problem is characterised as mildly or moderately ill posed if $\nu \leq 1$, or $\nu > 1$ respectively. However if the singular values decay exponentially so that there is no such ν then the problem is termed severely ill-posed. Oliver (1994) analyses the Q transform in terms of a singular value decomposition (B.17) and concludes that inversion of the Q transform is severely ill-posed by the categorisation of Hofmann (1986).

Inversion of the Q transform is therefore a particularly extreme example of a wider class of problems which are inherently ill-posed. This should not be surprising since there are deep differences between the wave equation and the diffusion equation. Perhaps the most important single difference is that the wave equation is symmetric with respect to time, while the diffusion equation is asymmetric. If $U(\mathbf{x}, t)$ is a solution of the scalar wave equation, then $U(\mathbf{x}, -t)$ is also a solution. In contrast, if $F(\mathbf{x}, t)$ is a solution of the scalar diffusion equation, then $F(\mathbf{x}, -t)$ is not a solution. The direction of time is significant, then in physical processes described by the diffusion equation. In electromagnetic imaging of the Earth its significance is that local inhomogeneities in an electric or magnetic field will be smoothed away as time increases. Given this behaviour it is easy to see why trying to extrapolate from later times to earlier times is

an inherently ill-posed process as noted by other authors working in the field of reverse-time electromagnetic migration (Lee *et al.* 1987).

As demonstrated in section 2.1.2 the conduction current dominates the displacement current for electromagnetic phenomena in the Earth, in the frequency range of interest. Conduction generates heat and increases entropy — a process which is irreversible. As was emphasised in the derivations of section 2.1.1 the wave equation (2.13) describes the propagation of small displacements in a perfectly elastic solid; a highly idealised approximation to a physical system. Under the wave equation energy is not dissipated, entropy does not increase, and so the process can be reversed.

This property arises because we have used Hooke’s law of elasticity and a lossless equation of motion so that all media rebound perfectly and without loss of energy to frictional or viscous forces. This is in contrast to real life where Hooke’s law is an approximation and, for example, when a dynamite charge is used as a seismic source some region near the source is pushed beyond the elastic limit and changed forever. The wave equation is a quite remarkable system then, quite unlike our everyday experience where entropy must increase and, for example, we cannot reverse the arrow of time and “un-scramble eggs”.

By making this connection between the physics of the wave and diffusion problems we understand why inversion of the Q transform is inherently ill-posed. Further, this understanding should temper our expectations when inverting the Q transform. It is precisely because reflection seismology may, within certain limits, be adequately described by the wave equation that it achieves resolution. Inverting the Q transform cannot be expected to produce an equivalent wavefield transient which has magically been given high resolution at late times. This is simply not possible. The underlying resolvability of any particular feature is limited by the diffusion process and cannot be enhanced.

However, the Q transform may help in the interpretation of diffusive transients. A well-developed and well-understood methodology for interpretation of multichannel transients exists for seismic exploration, whereas none currently exists for multichannel LOTEM exploration. By converting LOTEM transients to equivalent wavefield transients interpretation of multichannel surveys may become significantly easier.

There is no suggestion that diffusive to propagative mapping (DPM) can somehow lend electromagnetic surveying the high resolution enjoyed by seismic methods; fundamental limitations on resolution will remain.¹ However, the equivalent wavefield may be significantly easier to interpret than the original diffusive data.

¹In the earliest days of hydrocarbon surveying with EM methods it was claimed that the EM signals measured at the surface were caused by reflections of the electromagnetic waves from subsurface layers in a manner entirely analogous to reflection seismology. As might be expected the method gained a lot of interest in oil exploration but failed to deliver results. It was not until the 1950’s that work at the Socony Mobil laboratory demonstrated that EM propagation is fundamentally different from seismic propagation and that analogies between seismic and EM propagation should not be drawn hastily (Yost 1952, Yost, Caldwell, Beor, McChere & Skomal 1952, Orsinger & Nostrand 1954, Keller 1968, Strack 1992).

7.2 Diffusive to Propagative Mapping (DPM) by Deconvolution of the Q Transform in Logarithmic Time

Section 3.1 introduces the equivalent wavefield concept and derives the form of the Q transform in the frequency and time domains. In the time domain the Q transform is

$$\mathbf{F}(\mathbf{x}, t) = \frac{1}{2\sqrt{\pi t^3}} \int_0^\infty q \exp\left(-\frac{q^2}{4t}\right) \mathbf{U}(\mathbf{x}, q) dq. \quad (7.8)$$

As expected the action of the transform is to smooth out a pulse as it travels. Inversion of the Q transform involves the recovery of the impulse from the smooth diffusive transient. Because the action of the forward transform is to smooth out any sharp irregularities, the action of the inverse transform is to amplify any irregularities. This causes Q transform inversion, or diffusive to propagative mapping (DPM) to be an ill-posed problem; a small perturbation of the input, such as the addition of some random noise, is amplified causing a dramatic change in the output. Thus small errors in the measured data can produce large changes in the solution. In order to obtain a useful processing system some constraints must be applied to regularise the inversion, so that stable, but approximate, results are obtained.

By moving to a logarithmic sampling in both time and the time-like variable q the Q transform may be re-formulated as a convolution (Gershenson 1993). In effect, moving to logarithmic time sampling parameterises the inversion; the regularisation which is being imposed by this scheme is such that uniform resolution is achieved in logarithmic q . Deconvolution, the inversion of convolution equations, is a subject much studied in exploration seismology. One advantage of formulating the Q transform as a convolution is that it allows the inversion to be performed using standard deconvolution techniques. This deconvolution method is also computationally more efficient than some previous approaches, such as discretising the Q transform as a matrix equation and applying regularised inversion. In addition DPM by deconvolution has been demonstrated to give superior results to other techniques using known wave/diffusion pairs, synthetic diffusive transients and field data (Gershenson 1993).

7.2.1 Formulation of the Q Transform as a Convolution in Logarithmic Time

Re-arranging the Q transform (7.8) yields

$$2\sqrt{\pi t} \mathbf{F}(\mathbf{x}, t) = \frac{1}{t} \int_0^\infty q \exp\left(-\frac{q^2}{4t}\right) \mathbf{U}(\mathbf{x}, q) dq. \quad (7.9)$$

Substituting $q = \exp(u)$ and $t = \frac{1}{4} \exp(2v)$ gives

$$\sqrt{\pi} \exp(v) \mathbf{F}\left(\mathbf{x}, \frac{1}{4} \exp(2v)\right)$$

$$= \int_{-\infty}^{+\infty} 4 \exp(2(u-v)) \exp(-\exp(2(u-v))) U(\mathbf{x}, \exp(u)) du \quad (7.10)$$

$$\text{or} \quad (7.11)$$

$$\mathbf{G}(v) = \int_{-\infty}^{+\infty} W(v-u) \mathbf{R}(u) du \quad (7.12)$$

$$= W(v) * \mathbf{R}(v) \quad (7.13)$$

where $*$ represents the convolution operation and

$$\mathbf{G}(\mathbf{x}, v) = \sqrt{\pi} \exp(v) \mathbf{F}(\mathbf{x}, \frac{1}{4} \exp(2v)) \quad (7.14)$$

$$\mathbf{R}(\mathbf{x}, v) = \mathbf{U}(\mathbf{x}, \exp(v)) \quad (7.15)$$

$$W(v) = 4 \exp(-2v) \exp(-\exp(-2v)). \quad (7.16)$$

This is a convolution equation, which may be inverted by finding the inverse filter $M(v)$ such that

$$M(v) * W(v) = \delta(v) \quad (7.17)$$

where $\delta(v)$ is the Dirac delta function, and hence

$$\mathbf{R}(v) = M(v) * \mathbf{G}(v) \quad (7.18)$$

Inverting $t = \frac{1}{4} \exp(2v)$ gives

$$v = \frac{1}{2} \ln(4t) \quad (7.19)$$

$$= \ln(2\sqrt{t}) \quad (7.20)$$

and substituting (7.20) in $q = \exp(v)$ yields

$$q = 2\sqrt{t}. \quad (7.21)$$

Note that using this definition of v it is safe to use ‘early times’ and ‘late times’ to refer to, respectively, low values and high values of any of t , v and q .

At first glance the calculation of $\mathbf{G}(v)$ from the measured transient $\mathbf{F}(t)$ may seem dangerously unstable since late time values, and any uncertainties associated with them, are amplified due to the $\sqrt{\pi} \exp(v)$ term in equation (7.14). However field data captured using the TEAMEX acquisition system are regularly spaced in time, which implies from equation (7.20) that $\mathbf{G}(v)$ is increasingly densely sampled as v increases. This increasing data density can be used to ensure a stable calculation of $\mathbf{G}(v)$ at late times.

A second concern is that the range of t values measured in the field range from 0 upwards and, as can be seen from equation (7.20) v tends to $-\infty$ as t tends to zero so that the equivalent wavefield cannot be recovered at $q = 0$. However values can be found for q as close to zero

as is desired, although in this case v becomes large and negative implying that a small sample interval in t is needed.

7.2.2 Analytical Demonstration of the Convolutional Relationship

Given a known pair of equivalent responses a simple recipe may be followed to demonstrate analytically that a diffusive response $\mathbf{F}(t)$ is related to its equivalent wavefield $\mathbf{U}(q)$ via convolution in log time. Given the diffusive response $\mathbf{F}(t)$ and its equivalent wavefield $\mathbf{U}(q)$

1. calculate $\mathbf{R}(v) = \mathbf{U}(\exp(v))$,
2. calculate $\mathbf{G}(v) = \sqrt{\pi} \exp(v) \mathbf{F}(\frac{1}{4} \exp(2v))$,
3. demonstrate that $\mathbf{G}(v) = W(v) * \mathbf{R}(v)$.

The diffusive response $\mathbf{F}(t) = \frac{1}{2\sqrt{\pi t^3}} q_0 \exp(-\frac{q_0^2}{4t})$, $t > 0$, $q_0 > 0$, has an equivalent wavefield $\mathbf{U}(q) = \delta(q - q_0)$, $q > 0$. From this

$$\mathbf{R}(v) = \mathbf{U}(\exp(v)) = \delta(\exp(v) - q_0) = \delta(\exp(v) - \exp(v_0)) \quad (7.22)$$

$$\mathbf{G}(v) = \sqrt{\pi} \exp(v) \mathbf{F}(\frac{1}{4} \exp(2v)) \quad (7.23)$$

$$= \sqrt{\pi} \exp(v) \frac{1}{2\sqrt{\pi}} \frac{8}{\exp(3v)} q_0 \exp(-\frac{q_0^2}{\exp(2v)}) \quad (7.24)$$

$$= 4 \exp(-2v) q_0 \exp(-\exp(-2(v - v_0))) \quad (7.25)$$

where v_0 is defined by $q_0 = \exp(v_0)$ and as above $q = \exp(v)$ and $t = \frac{1}{4} \exp(2v)$. Then

$$W(v) * \mathbf{R}(v) = \int_{-\infty}^{+\infty} W(v - u) \mathbf{R}(u) du \quad (7.26)$$

$$= \int_{-\infty}^{+\infty} W(v - u) \delta(\exp(u) - \exp(v_0)) du. \quad (7.27)$$

Substituting $q = \exp(u)$ gives

$$W(v) * \mathbf{R}(v) = \int_0^{+\infty} W(v - \ln(q)) \delta(q - q_0) \frac{1}{q} dq \quad (7.28)$$

$$= W(v - \ln(q_0)) \frac{1}{q_0} \quad (7.29)$$

$$= W(v - v_0) \frac{1}{q_0} \quad (7.30)$$

$$= 4 \exp(-2(v - v_0)) \exp(-\exp(-2(v - v_0))) \frac{1}{q_0} \quad (7.31)$$

$$= 4 \exp(-2v) q_0^2 \exp(-\exp(-2(v - v_0))) \frac{1}{q_0} \quad (7.32)$$

$$= 4 \exp(-2v) q_0 \exp(-\exp(-2(v - v_0))) \quad (7.33)$$

$$= \mathbf{G}(v).$$

This calculation demonstrates analytically that the diffusive response $F(t) = \frac{1}{2\sqrt{\pi t^3}} q_0 \exp(-\frac{q_0^2}{4t})$, $t > 0$, $q_0 > 0$, is related to its equivalent wavefield $U(q)$ via a convolution equation in the log time domain.

7.2.3 Calculating a Deconvolution Filter in the Frequency Domain

This section demonstrates how a suitable deconvolution filter $M(v)$ may be calculated. Returning to equation (7.17), $M(v) * W(v) = \delta(v)$, the convolution theorem is used to write

$$\tilde{M}(\omega)\tilde{W}(\omega) = 1 \quad (7.34)$$

where $\tilde{M}(\omega)$, $\tilde{W}(\omega)$ and 1 are the Fourier transforms of $M(v)$, $W(v)$ and $\delta(v)$ respectively. Formally

$$\tilde{M}(\omega) = \frac{1}{\tilde{W}(\omega)} \quad (7.35)$$

but $\tilde{W}(\omega)$ may be zero at some values of ω . Multiplying above and below by $\tilde{W}^*(\omega)$, the complex conjugate of $\tilde{W}(\omega)$, and adding a (small) constant \wp to the denominator gives

$$\tilde{M}(\omega) \simeq \frac{\tilde{W}^*(\omega)}{|\tilde{W}(\omega)|^2 + \wp}. \quad (7.36)$$

The effect of adding the term \wp into equation (7.36) is to ignore frequency components with magnitudes much below $\sqrt{\wp}$. In order to see this consider the magnitude of a particular frequency component. If the magnitude of the component in W is r then the magnitude in the inverse M is $r/(r^2 + \wp)$ which peaks at $r = \sqrt{\wp}$ and then decays quickly to zero as $r \rightarrow 0^+$ — see Figure 7.1.

The addition of \wp is equivalent to the addition of white noise to the input filter W . In order to see this, first follow Robinson & Treitel (1980, page 143) and define the cross correlation of two time series a_t and b_t as

$$\Phi_{ab}(k) = \sum_t a_t b_{t+k}. \quad (7.37)$$

Then, loosely, by the convolution theorem

$$|\tilde{W}(\omega)|^2 = \tilde{W}(\omega)\tilde{W}^*(\omega) \quad (7.38)$$

$$\leftrightarrow W(t) * W^*(t) \quad (7.39)$$

$$= \Phi_{ab}(k) \quad (7.40)$$

where $a_t = W(-t)$ and $b_t = W^*(t)$ and \leftrightarrow indicates a Fourier transform pair. If now $c_t = a_t + n_t$

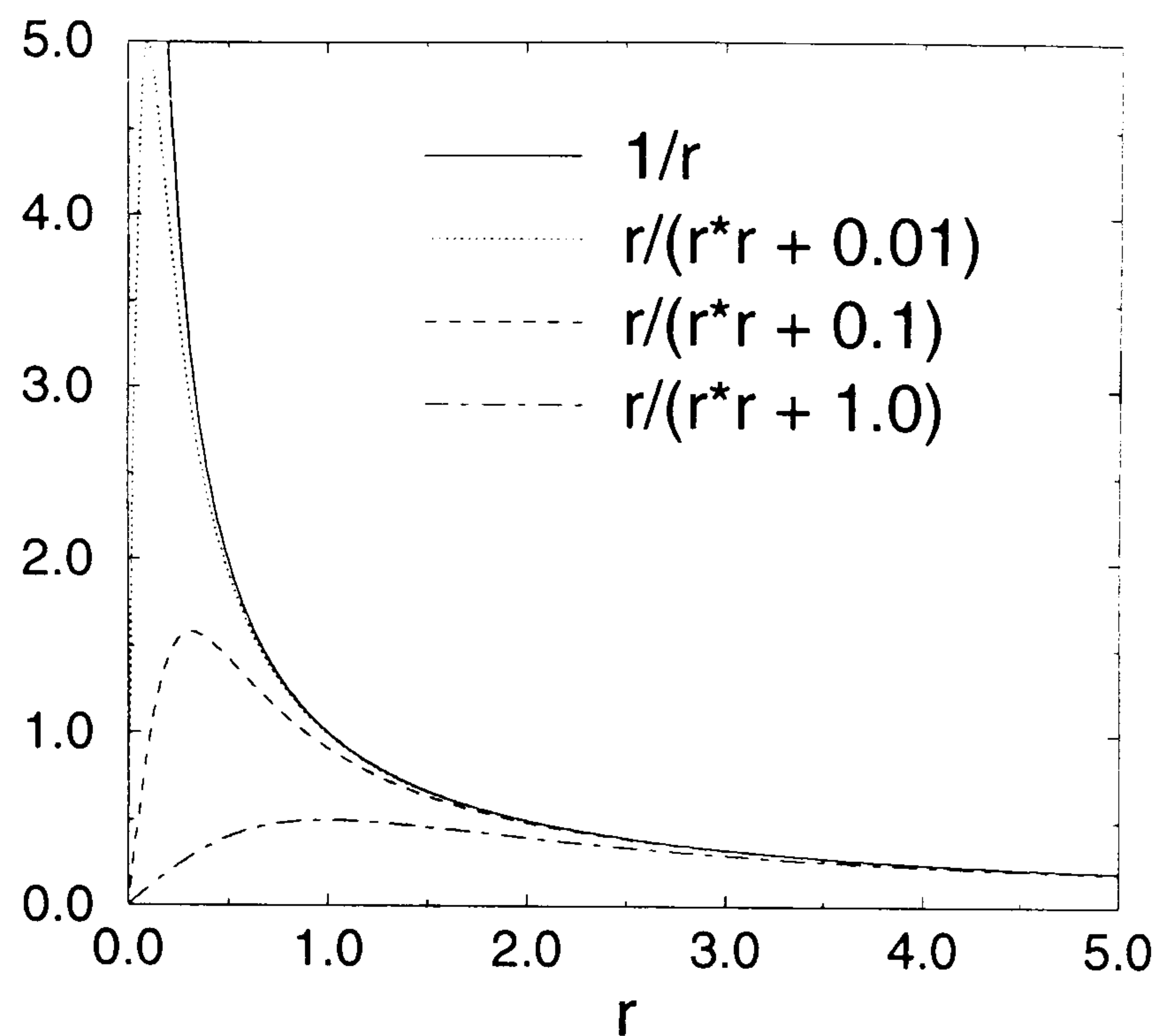


Figure 7.1: Magnitude of frequency components in inverse filter calculated through Fourier domain as a function of the magnitude of the same frequency component in the forward filter.

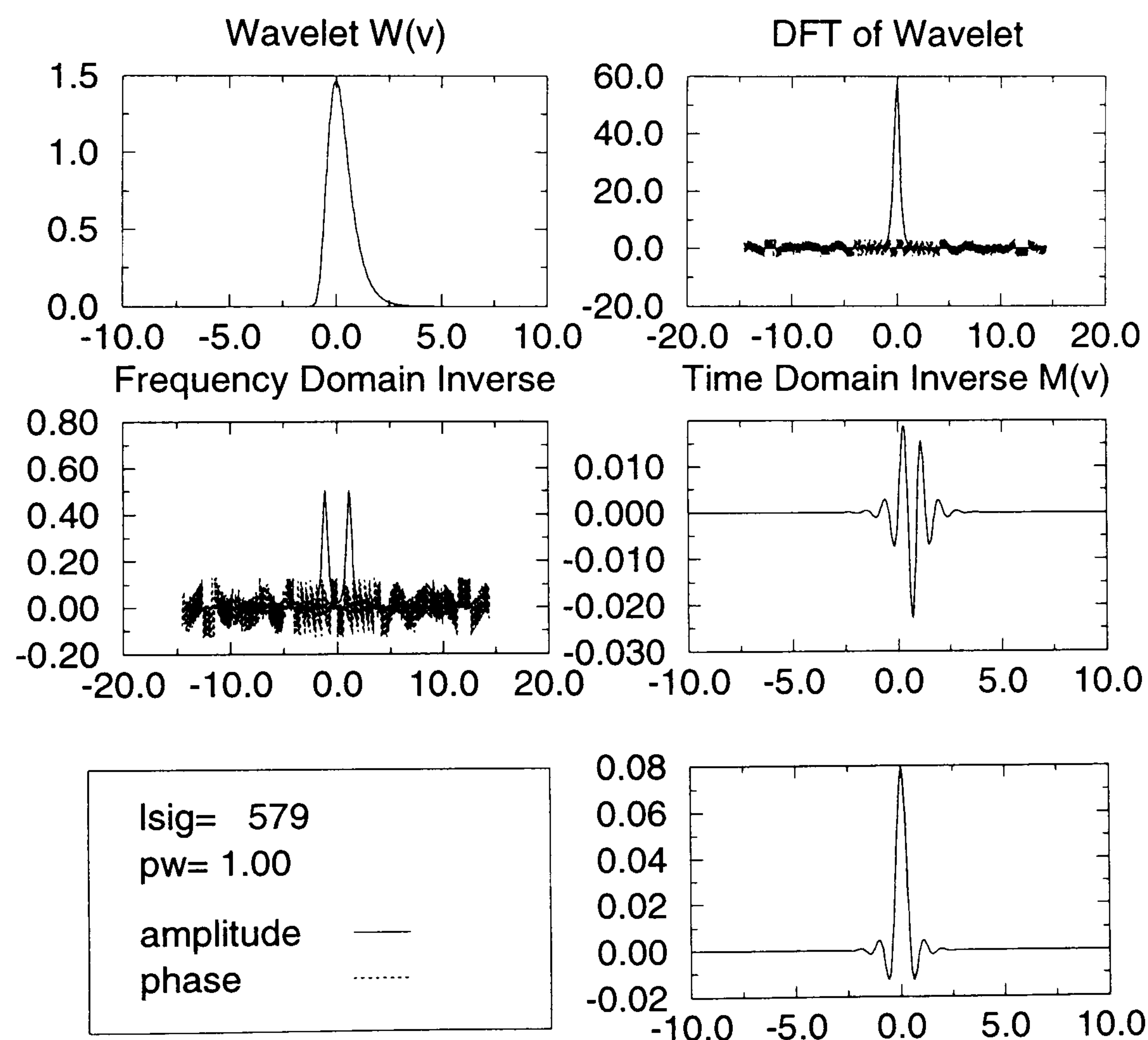


Figure 7.2: Calculation of inverse filter for $W(v)$ via the Fourier domain. $W(v)$ is evaluated using a sampling interval of $\delta v = 0.138155$ which gives adequate, but not excessive, sampling. An inverse filter is then calculated through the Fourier domain using equation (7.36). Inverse filters with higher sampling rates may then be found by interpolation of this filter.

and $d_t = a_t + n_t$ where n_t is ‘white noise’ then

$$\Phi_{cd}(k) = \sum_t c_t d_{t+k} \quad (7.41)$$

$$= \sum_t (a_t + n_t)(b_{t+k} + n_{t+k}) \quad (7.42)$$

$$= \Phi_{ab}(k) + \Phi_{an}(k) + \Phi_{nb}(k) + \Phi_{nn}(k) \quad (7.43)$$

$$= \Phi_{ab}(k) + P\delta(k) \quad (7.44)$$

since it is assumed that the filter $W(t)$ is uncorrelated with the white noise n_t and, by definition, the autocorrelation of white noise is zero except at zero lag. Taking the Fourier transform of (7.44) gives

$$|\tilde{W}'(\omega)|^2 = |\tilde{W}(\omega)|^2 + P \quad (7.45)$$

where P is the power of the white noise (Ziolkowski 1993).

7.2.4 The Effects of DPM Regularisation on Recovered Waveforms

It must be remembered that in numerical calculation we obtain an estimate $\langle \mathbf{R} \rangle$ of \mathbf{R} by numerical deconvolution. In practice it is not possible to obtain a perfect deconvolution operator M , however a computable approximation $\langle M \rangle$ may be obtained using the methods outlined in section 7.2.3. The effectiveness of the approximate deconvolution operator $\langle M \rangle$ may be usefully investigated by considering the resolving kernel \mathbf{K} which is defined by

$$\mathbf{K} = \langle M \rangle * W. \quad (7.46)$$

$\langle M \rangle$ is related to the perfect deconvolution operator by $\langle M \rangle = \mathbf{K} * M$. In order to see this observe that

$$(\mathbf{K} * M) * W = \mathbf{K} * (M * W) \quad (\text{by the associative property of convolution}) \quad (7.47)$$

$$= \mathbf{K} \quad (\text{by the definition of } W) \quad (7.48)$$

$$= \langle M \rangle * W \quad (\text{by the definition of } \mathbf{K}) \quad (7.49)$$

$$0 = (\langle M \rangle - (\mathbf{K} * M)) * W. \quad (7.50)$$

Hence $\langle M \rangle - \mathbf{K} * M$ lies in the null space of W . Since W is general

$$\langle M \rangle = \mathbf{K} * M. \quad (7.51)$$

This implies that

$$\langle \mathbf{R} \rangle = \langle M \rangle * G \quad (7.52)$$

$$= (\mathbf{K} * \mathbf{M}) * \mathbf{G} \quad (7.53)$$

$$= \mathbf{K} * (\mathbf{M} * \mathbf{G}) \quad (7.54)$$

$$= \mathbf{K} * \mathbf{R}. \quad (7.55)$$

This analysis demonstrates that DPM by numerical deconvolution in log time does not yield the exact $\mathbf{R}(v)$ but instead an approximation $\langle \mathbf{R} \rangle = \mathbf{K} * \mathbf{R}$. This means that DPM by numerical deconvolution in log time does not yield the exact equivalent wavefield $\mathbf{U}(q)$ but instead an approximation

$$\langle \mathbf{U} \rangle (q) = \langle \mathbf{R} \rangle (\ln(q)). \quad (7.56)$$

7.2.5 Demonstration of Numerical DPM by Deconvolution in Log Time

Given a known pair of equivalent responses a simple recipe may be followed to demonstrate numerical diffusive to propagative mapping by deconvolution in log time. Given the diffusive response $\mathbf{F}(t)$

1. calculate $\mathbf{G}(v) = \sqrt{\pi} \exp(v) \mathbf{F}(\frac{1}{4} \exp(2v))$,
2. solve the convolution equation $\mathbf{G}(v) = \mathbf{W}(v) * \mathbf{R}(v)$ for $\mathbf{R}(v)$ given $\mathbf{G}(v)$,
3. calculate $\mathbf{U}(q) = \mathbf{R}(\ln(v))$ and compare with the analytically calculated equivalent wavefield.

Figure 7.3 shows each step in the process when applied to the diffusive response

$$\mathbf{F}(r, t) = \frac{1}{2\sqrt{\pi t^3}} \frac{r}{c} \exp\left(-\frac{r^2}{4c^2 t}\right)$$

at 10 equispaced values of r/c . The calculation of $\mathbf{R}(v)$ from $\mathbf{G}(v)$ is achieved by convolving $\mathbf{G}(v)$ with a deconvolution filter calculated through the frequency domain — see Section 7.2.3 and Figure 7.2. The ill-posedness of the problem means that the analytic result for the “true” equivalent wavefield, an impulse at $q = r/c$, cannot be perfectly recovered (Slob *et al.* 1995). However the smoothed version which is recovered can still be easily interpreted. The maximum value on each trace in the equivalent wavefield falls on a line with constant slope in the (r, q) domain. Comparing this slope with the values of r/c used to calculate the input $\mathbf{F}(r, t)$ confirms that the correct equivalent velocity c is interpreted from the slope of this line.

7.2.6 Self-Similar Scaling of the Equivalent Wavefield

Section 5.1.2 calculates that the equivalent wavefield response for a grounded horizontal electric current dipole source at the surface of a uniform half-space with a switch-off transmitter current

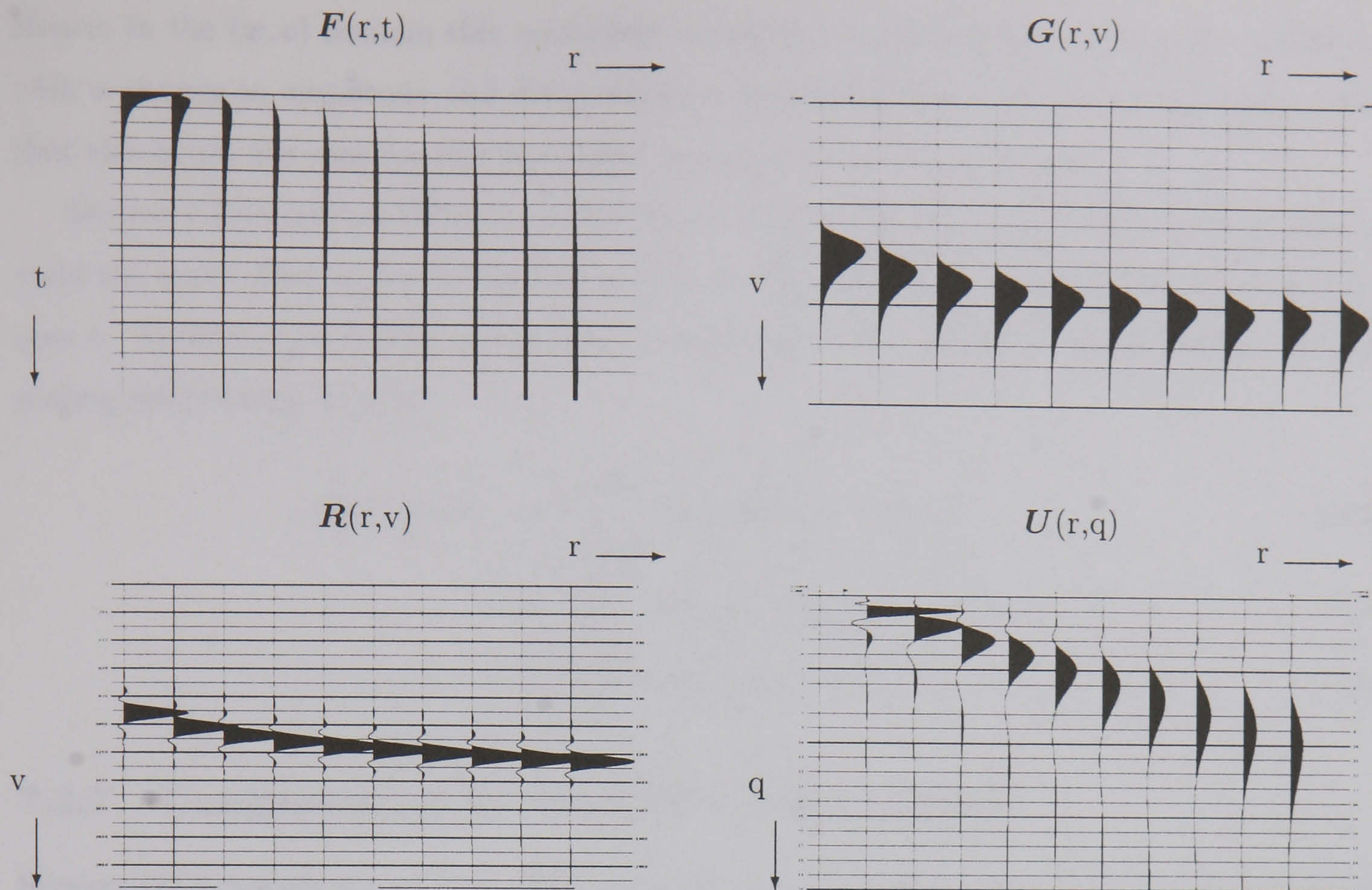


Figure 7.3: Numerical demonstration of diffusive to propagative mapping (DPM) by deconvolution in log time. Top left: The diffusive field $\mathbf{F}(r, t) = \frac{1}{2\sqrt{\pi t^3}} \frac{r}{c} \exp(-\frac{r^2}{4c^2 t})$ is calculated for ten equispaced values of r . Top right: $\mathbf{G}(r, v) = \sqrt{\pi} \exp(v) \mathbf{F}(r, \frac{1}{4} \exp(2v))$. Bottom left: $\mathbf{R}(r, v)$ is calculated from $\mathbf{G}(r, v)$, in this case by convolving $\mathbf{G}(r, v)$ with a deconvolution filter. Notice that the numerically recovered $\mathbf{R}(r, v)$ has a wavelet which is the resolving kernel of the deconvolution filter, which is symmetric about its peak value. Bottom right: The extremum values of the traces in the numerically recovered equivalent wavefield lie on a straight line, whose slope is related to the equivalent velocity c .

profile is

$$U_{\parallel}(\mathbf{x}, q) = \frac{\mathcal{D}}{2\pi\sigma r^3} q \mathcal{H}(\frac{r}{c} - q) \quad (7.57)$$

where $r = |\mathbf{x}|$ and \mathbf{x} lies on the surface of the uniform half-space.

This wavefield obeys a simple scaling relationship

$$U(a\mathbf{x}, q) = 1/a^2 U(\mathbf{x}, q/a). \quad (7.58)$$

Applying this scaling relationship to Equation (7.15), the definition of $\mathbf{R}(\mathbf{x}, v)$, yields a similar scaling relationship for $\mathbf{R}(\mathbf{x}, v)$

$$\mathbf{R}(a\mathbf{x}, v) = \mathbf{U}(a\mathbf{x}, \exp(v)) \quad (7.59)$$

$$= 1/a^2 \mathbf{U}(\mathbf{x}, \exp(v)/a) \quad (7.60)$$

$$= 1/a^2 \mathbf{U}(\mathbf{x}, \exp(v - \ln(a))) \quad (7.61)$$

$$= 1/a^2 \mathbf{R}(\mathbf{x}, v - \ln(a)). \quad (7.62)$$

Hence, in the (x, v) domain this equivalent wavefield retains the same elemental wavelet in v with a change in amplitude and delay which is dependent upon offset from the source. Note that this is not the case for this equivalent wavefield in the (x, q) domain.²

Section 7.2.4 analyses DPM by numerical deconvolution in log time to show that it does not yield the exact $\mathbf{R}(x, v)$ but instead an approximation $\langle \mathbf{R} \rangle = \mathbf{K} * \mathbf{R}$ where the convolution is over v . Applying the scaling relationship of \mathbf{R} (7.62) to the definition of $\langle \mathbf{R} \rangle$ yields the same scaling relationship for $\langle \mathbf{R} \rangle$

$$\langle \mathbf{R} \rangle(ax, v) = \int_{-\infty}^{\infty} \mathbf{K}(u) \mathbf{R}(ax, v - u) du \quad (7.63)$$

$$= \int_{-\infty}^{\infty} \mathbf{K}(u) 1/a^2 \mathbf{R}(x, v - u - \ln(a)) du \quad (7.64)$$

$$= 1/a^2 \langle \mathbf{R} \rangle(x, v - \ln(a)). \quad (7.65)$$

7.2.7 Compensating for Waveform Regularisation

Section 7.2.4 demonstrated that DPM by numerical deconvolution in log time does not yield the exact equivalent wavefield, but instead a numerical approximation. Understanding the behaviour of this process and the features of the resulting numerical approximation to the equivalent wavefield, is an important step towards establishing a procedure for interpretation of equivalent wavefields calculated numerically from synthetic responses and field data whose precise analytic formulation is unknown.

Equation (7.55) allows the numerically recovered equivalent wavefield to be predicted from the analytical equivalent wavefield. In this section the equivalent wavefield of a horizontal electric current dipole source at the surface of a 10 Ωm halfspace is calculated analytically and then compared with the numerically recovered approximation predicted by Equation (7.55). The horizontal electric current dipole transmitter is located at the origin and the horizontal electric field receivers aligned collinear with the transmitter. Figure 7.4 presents synthetic switch-on TEM responses for receivers at offsets from 125 m to 3375 m, calculated using the MODALL program for LOTEM modelling (Strack 1992).

Figure 7.5 compares the analytically calculated waveform with the estimate of the numerically recovered wavefield $\langle \mathbf{U} \rangle$. The analytic expression for the equivalent wavefield of a horizontal electric current dipole over a half space at a given offset r has a peak value at $q = r/c$. For this deconvolution operator the peak value of the predicted recovered waveform occurs at a q value very near to $1/\sqrt{2}$ of the distance from $q = 0$ to the peak of the analytical waveform at $q = r/c$. These observations indicate that the waveform recovered from DPM by numerical deconvolution in log time is related to the analytical result, but smoothed so that the peak value is nearer the centre of the analytical waveform.

²A very elegant analysis of scaling relationships for pulses propagating in dispersive media, including both diffusive and weakly attenuative propagation, is presented by Bickel (1993).

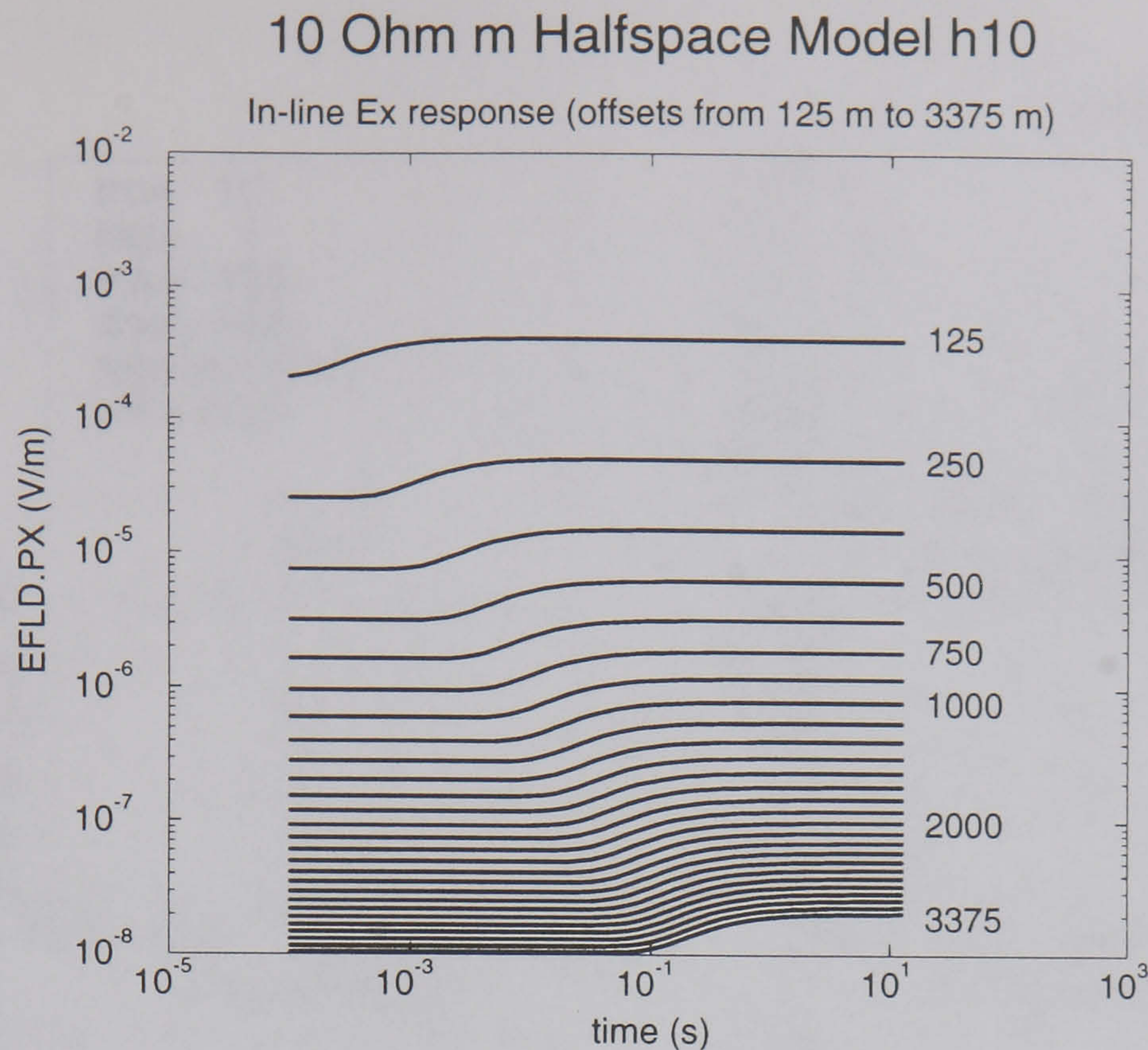


Figure 7.4: The switch-on response for the in-line Ex component for model h10, at receiver offsets from 125 m to 3375 m in intervals of 125 m. Presentation on a log-log plot such as this figure accentuates the pattern of the variation in signal amplitude and shape as a function of offset from the transmitter. At the earliest and latest times the signal asymptotes to a constant. Interesting information about the Earth's response is captured within an intermediary time interval. This interval becomes later in time, and the amplitude of the response decreases, with increasing offset from transmitter to receiver.

In Figure 7.6 the equivalent waveform predicted to be recovered from DPM by numerical deconvolution in log time is calculated for a series of receivers over a 10 Ωm halfspace. The horizontal electric current dipole transmitter is located at the origin and the collinear electric field receivers spaced at 125 m. Figure 7.6 (top) presents the equivalent wavefield calculated from the analytic expression for $\langle \mathbf{R} \rangle(\mathbf{x}, v)$ using Equation (7.55).

Section 7.2.6 calculates the scaling relationship for $\langle \mathbf{R} \rangle(\mathbf{x}, v)$ obtained through DPM by numerical deconvolution in log time. For this equivalent wavefield $\mathbf{R}(\mathbf{x}, v)$ has the same elemental wavelet in v at all receiver offsets (with a change in amplitude and delay which is dependent upon offset r from the source) Hence $\langle \mathbf{R} \rangle(\mathbf{x}, v)$ also contains a single elemental wavelet. Hence the peak value of $\langle \mathbf{R} \rangle$ is moved nearer to the centre of the waveform by the same amount Δv for all offsets \mathbf{x} .

Recalling that $q = \exp(v)$, in the (\mathbf{x}, v) domain the analytic expression for this equivalent wavefield has peak values at $v = \ln(r/c)$. The numerically recovered equivalent wavefield has peak values at $v = \ln(r/c) - \Delta v$ in the (\mathbf{x}, v) domain and at $q = \exp(-\Delta v)r/c$ in the (\mathbf{x}, q) domain. Hence the peak values of the numerically recovered equivalent wavefield lie on a straight line whose slope is modified by the regularisation of the recovered waveform.

In Figure 7.6 (bottom) the extremum on each trace is marked with an impulse. These

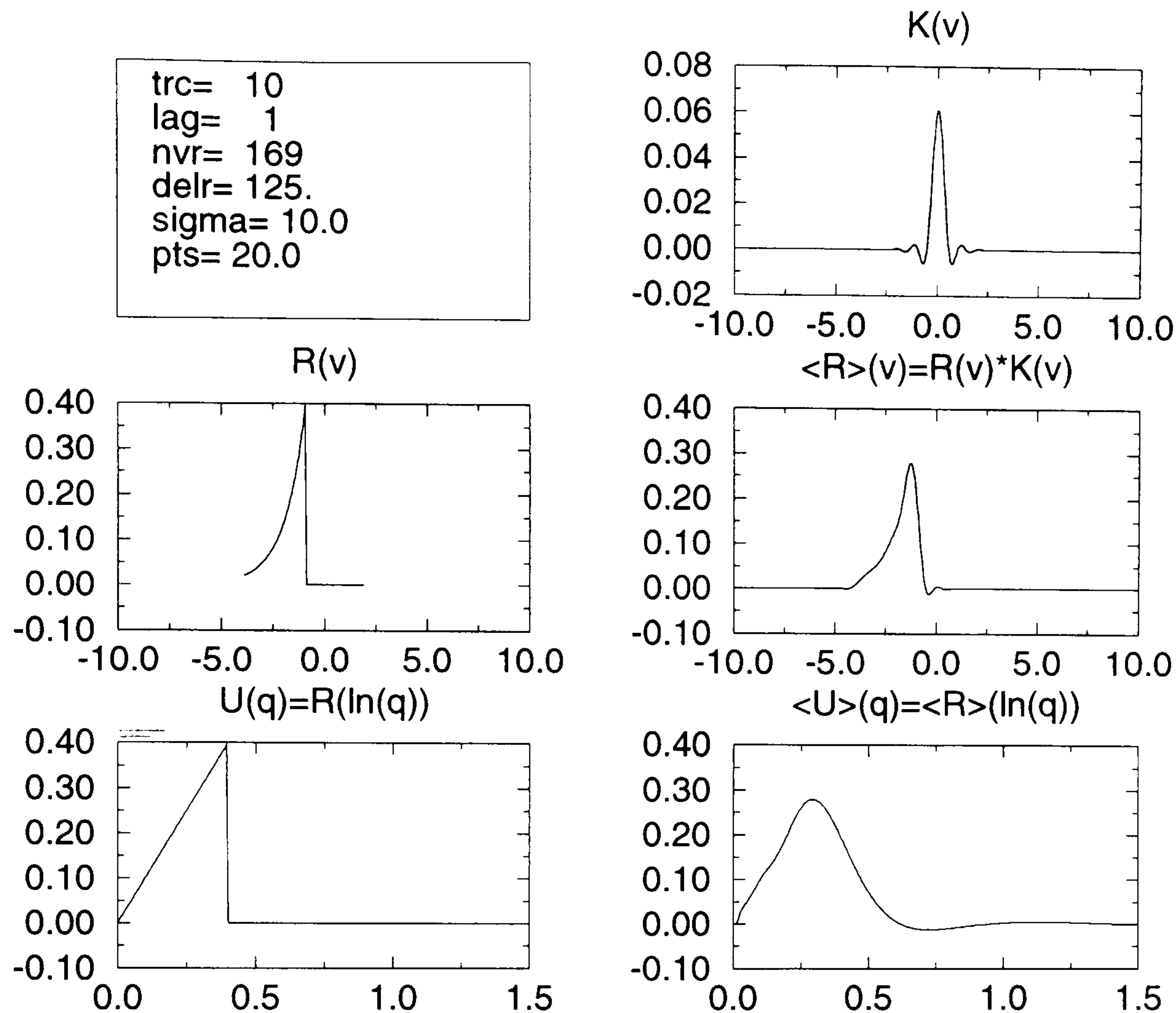


Figure 7.5: Comparison of the equivalent wavefield calculated analytically and the equivalent wavefield predicted to be recovered from DPM by numerical deconvolution in log time. DPM by numerical deconvolution in log time does not yield the exact $\mathbf{R}(v)$ but instead an approximation $\langle \mathbf{R} \rangle = \mathbf{K} * \mathbf{R}$. This means that DPM by numerical deconvolution in log time does not yield the exact equivalent wavefield $\mathbf{U}(q)$ but instead an approximation $\langle \mathbf{U} \rangle(q) = \langle \mathbf{R} \rangle(\ln(q))$.

extrema lie on or near a straight line through the origin. Treating this as a direct arrival from the source to the receiver, and interpreting the slope of this arrival using $q = r/c$ yields an equivalent velocity c which differs from the equivalent velocity of a 10 Ωm halfspace by a factor of approximately $\sqrt{2}$. As outlined above, this results from smoothing of the recovered waveform which pulls the peak amplitude towards the centre of the waveform.

This analysis predicts that DPM by numerical deconvolution in log time applied to the diffusive response of a horizontal electric dipole over a uniform halfspace recovers an equivalent wavefield whose waveforms are smoothed so that the peak values fall on a straight line whose slope is different from that of the analytically calculated equivalent wavefield. The exact relationship between the recovered slope and the equivalent velocity is dependent upon the deconvolution filter which is used; in this case the arrival appears to be slower by a factor of $\sqrt{2}$. This corresponds to a systematic underestimate of resistivity by a factor of 2. In the next section DPM by numerical deconvolution in log time is applied to the diffusive response of a horizontal electric dipole over a uniform halfspace and this prediction is tested.

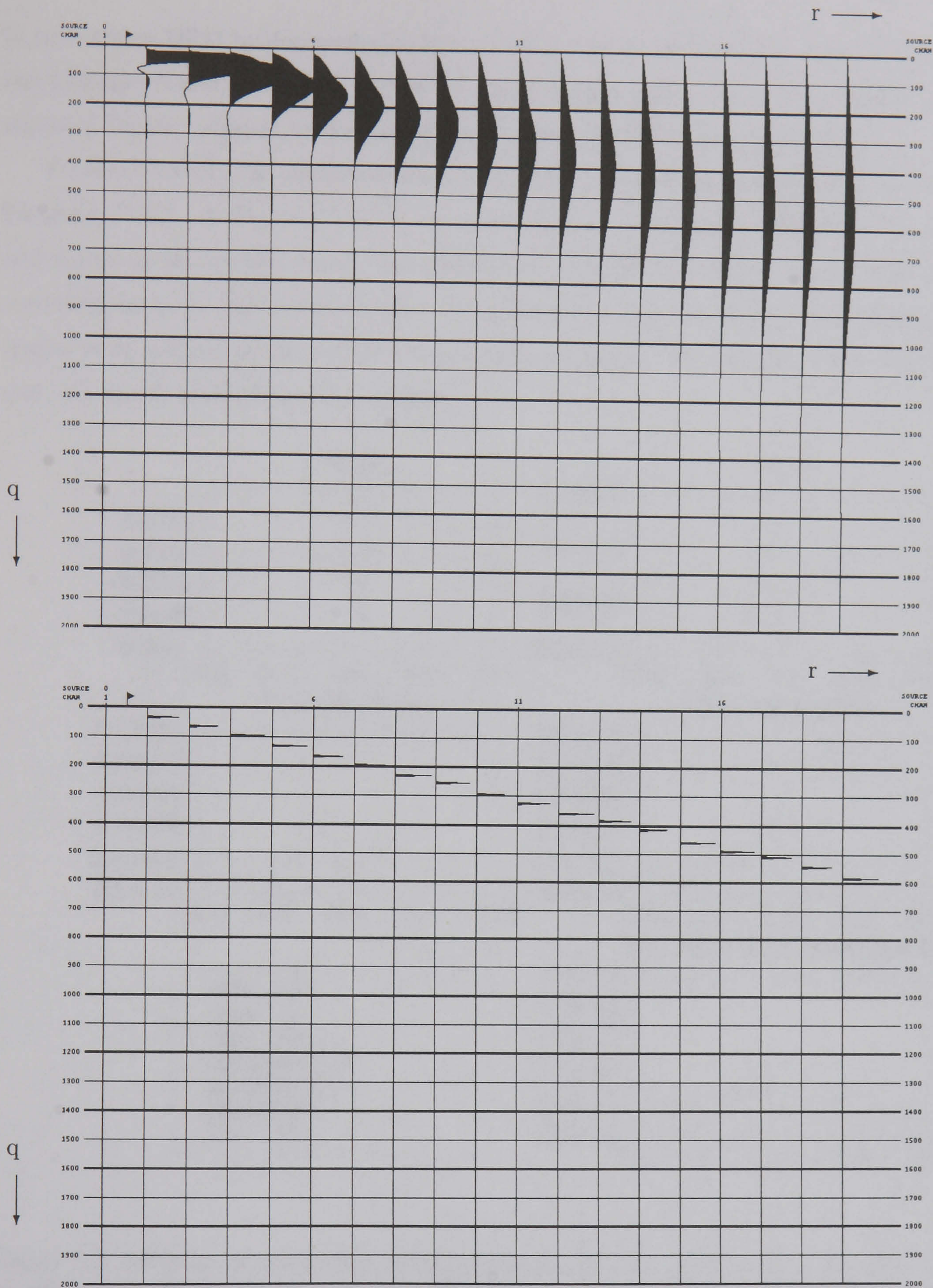


Figure 7.6: Top: The equivalent waveform predicted to be recovered from DPM by numerical deconvolution in log time, calculated for receivers over the h10 (10 Ω m halfspace) model. The time-like variable q increases down the page with timing lines every $0.1 \sqrt{s}$. Offset from the transmitter increases across the page starting from 0 m in intervals of 125 m. Bottom: Extrema have been marked on each trace.

7.2.8 DPM by Deconvolution in Log Time of 10 Ω m Half Space Synthetics

In this section DPM by deconvolution in log time is applied to synthetics calculated for the 10 Ω m halfspace Earth model h10. Figure 7.7 displays each stage of the process for the synthetic transient for the collinear Ex component at an offset of 1125 m from the source.

The function $G(v)$ is calculated directly from the values of the synthetic $F(t)$ according to Equation (7.14). In Figure 7.7 $G(v)$ does not decay to 0 at the smallest values of v (which correspond to the earliest times), but remains at a fraction of its peak value. When $G(v)$ is convolved with the deconvolution filter $M(v)$ there is a response to this discontinuity, which results in an artifact in the calculated equivalent wavefield. Tapering and smoothing of $G(v)$ does not significantly reduce this artifact.

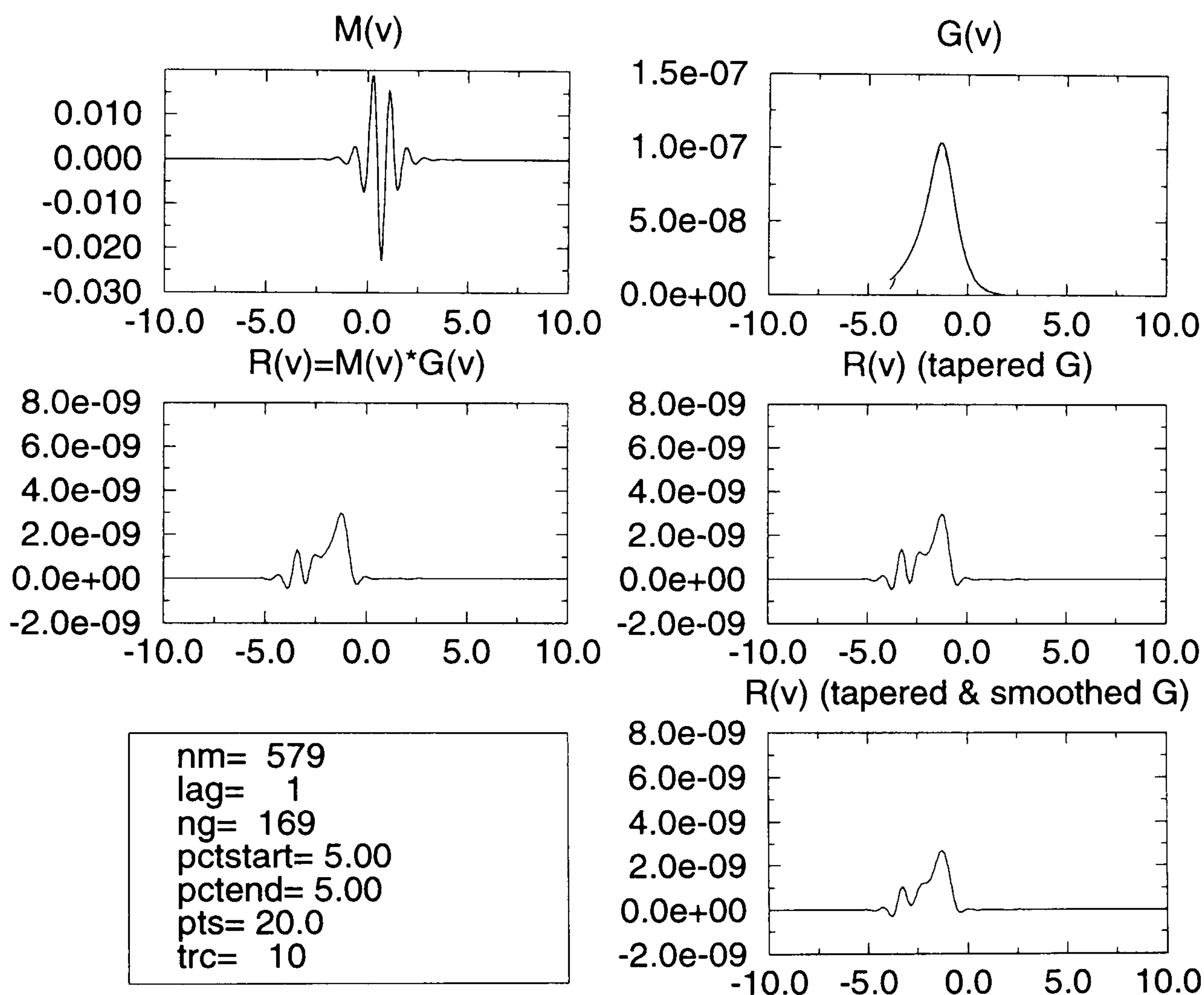


Figure 7.7: DPM by deconvolution in log time applied to the collinear Ex component at 1125 m offset from the source for a 10 Ω m halfspace model. The synthetic is calculated for times in the range $[10^{-4}, 10^1]$ s. The synthetic has not been calculated for sufficiently early times to capture the rise from zero of the function $G(v)$. This results in an extraneous response at early times.

This artifact could be avoided by calculating synthetics at earlier times, enabling $G(v)$ to be calculated at earlier v . When processing field data it is not possible to simply re-run the field work to obtain earlier times. A procedure must be found which can accommodate this

lack of early times.³

An alternative to calculating synthetics at earlier times is to extrapolate. In general extrapolation is a dangerous and unstable process. However, we know that the synthetic response asymptotes to a constant at early and late times. If the synthetic is calculated over a time interval which captures the early-time asymptotic value then it is reasonable to extrapolate by assuming the response takes this value at earlier times.⁴

In fact a slightly different extrapolation procedure is implemented. In order to extrapolate to earlier times (smaller v) a value v_0 corresponding to a suitably early time is selected, $G(v_0)$ is set to zero, and values of $G(v)$ between this early value of v and the first data point are calculated by spline interpolation. Extrapolation to late times is handled similarly.

DPM by deconvolution in log time is applied to synthetics for halfspace model h10 to determine the effectiveness of this procedure. The function $G(v)$ is extrapolated to decay smoothly with smaller v (earlier times). Figure 7.8 displays each stage of the process for the synthetic transient for the collinear Ex component at an offset 1125 m from the transmitter. Artifacts due to a lack of early times are clearly reduced in comparison with Figure 7.7.

Figure 7.9 (top) displays the equivalent wavefield for each receiver. In this and similar figures the time-like variable q increases down the page and offset from the transmitter increases across the page from left to right in intervals of 125 m starting from 0 m. In Figure 7.9 (bottom) the location of the extremum on each trace of the numerically calculated equivalent wavefield displayed in Figure 7.9 (top) is marked with an impulse. The slope of this arrival can be estimated by assuming it passes through the origin in the (r, q) domain, picking the time of the extremum q_i on the trace at offset r_i and then calculating the equivalent velocity c using $c = q_i/r_i$. A lower bound on the uncertainty in this estimate of equivalent velocity can be established from the uncertainty in the extremum pick q_i , which is $\pm 1/2$ the sample interval in q . Alternatively a line-fitting procedure could be employed to find the best fit to a selection of traces and provide an estimate of uncertainty.

Picking on the trace at 1125 m offset from the source, the extremum is at 0.28 ± 0.0025 m/ \sqrt{s} . The slope of this arrival corresponds to an equivalent velocity $c = 4018 \pm 36$ m/ \sqrt{s} . Compensating for systematic error resulting from distortion of the waveform during regularisation, as analysed in Section 7.2.7, gives an estimated equivalent wavefield velocity of 2841 ± 26 m/ \sqrt{s} . Calculating resistivity using $\rho = \mu c^2$ yields an estimate of 10.1 ± 0.18 Ωm .

³This problem is likely to be encountered whenever deconvolutional formulations of DPM are applied to field data. Gershenson (1993) employs a very similar formulation for theoretical analysis and treatment of synthetics but in order to avoid problems with field data reformulates the deconvolution as a matrix equation over the time range of the data and calculates an inverse using singular value decomposition (SVD) (Gershenson 1994).

⁴The TEAMEX acquisition system samples signals at a constant rate. When recording data in the field a sampling rate and time series length must be chosen. It can be difficult to find a sampling rate which enables the TEM response to be adequately sampled over the whole of the interesting time interval. This is because, first, the signal characteristics would more effectively be captured by a logarithmic distribution of the same number of sample points and, second, the interesting time interval varies with offset. The optimum sampling rate is higher for receivers near to the source, than for those far from the source. Inevitably a compromise must be selected.

If the time interval over which data are available does not fully capture the significant time interval for a particular receiver then this method of extrapolation is not reasonable.

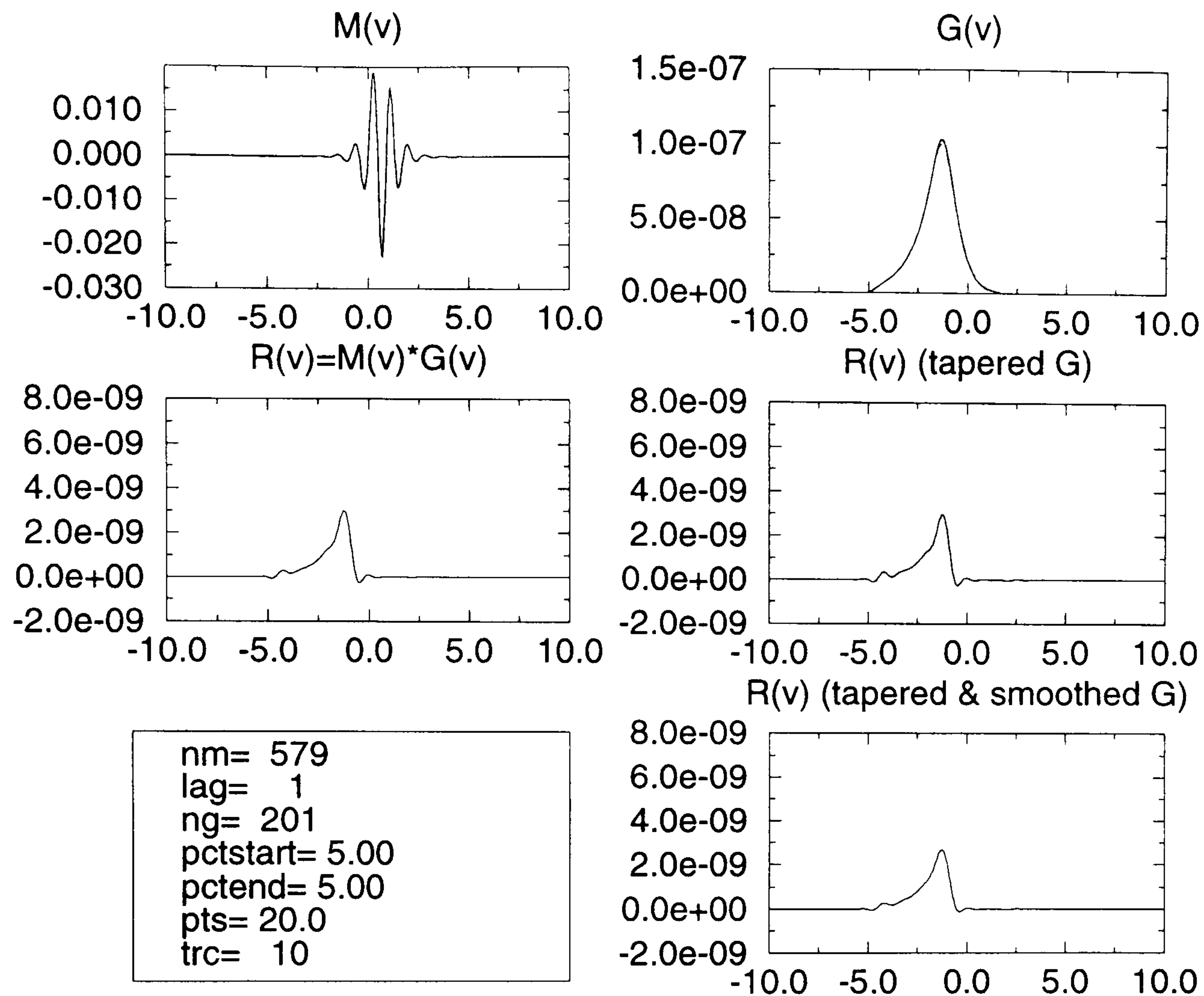


Figure 7.8: DPM by deconvolution in log time applied to the collinear Ex component at 1125 m offset from the source for a 10 Ωm halfspace model. The synthetic is calculated for times in the range $[10^{-4}, 10^1]$ s. Extrapolation is used to extend the range of the function $G(v)$ to allow it to rise smoothly from zero.

This demonstrates that numerical DPM of synthetic MTEM responses calculated for a horizontal electric current dipole over a halfspace Earth model produces an equivalent wavefield which is well understood. Further, for this simple model, the equivalent wavefield can be interpreted without the use of iterative forward modelling.

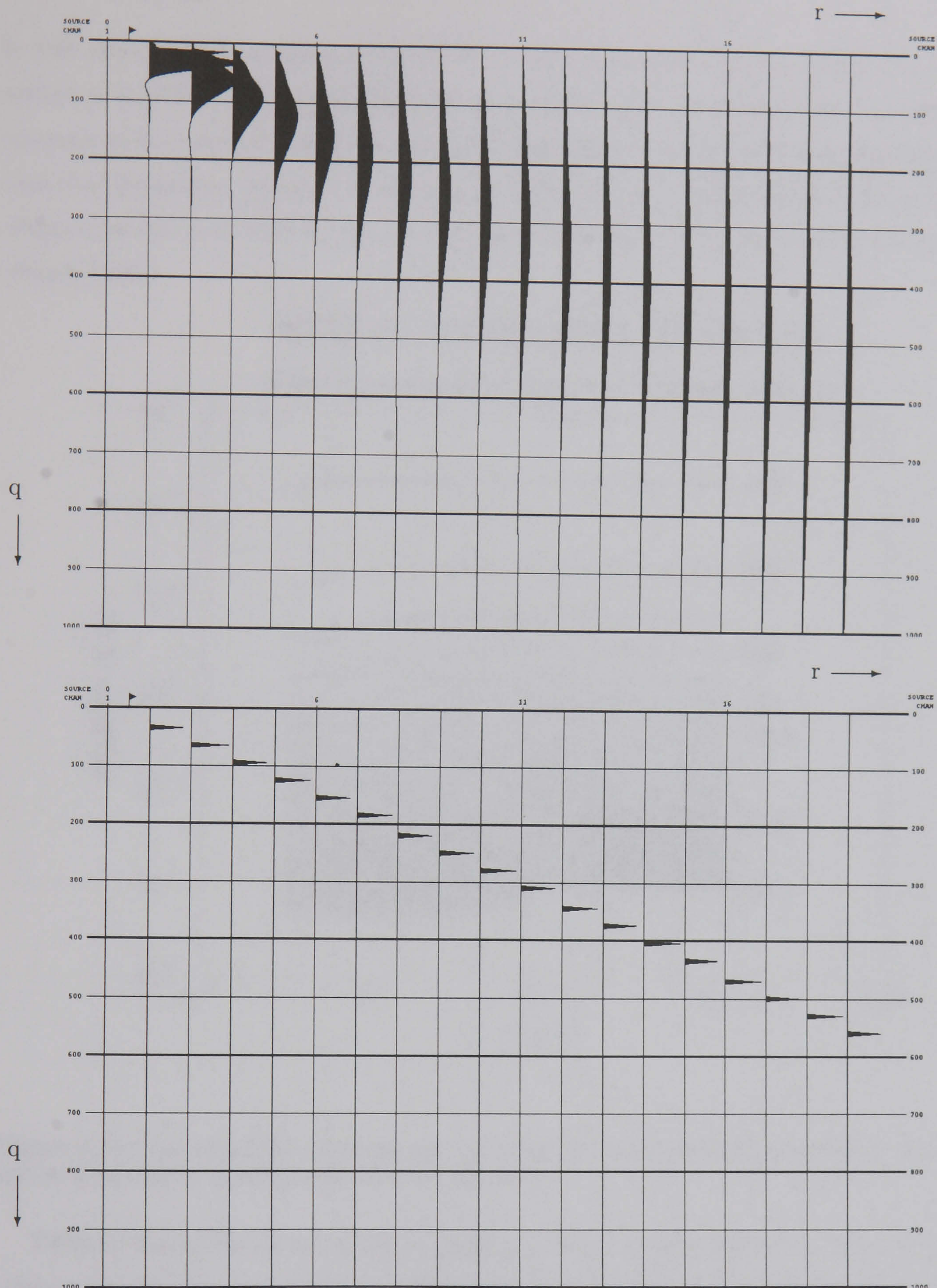


Figure 7.9: Top: Equivalent wavefield calculated using DPM by deconvolution in log time for the h10 (10 Ω m halfspace) model. The time-like variable q increases down the page with timing lines every $0.1 \sqrt{s}$. Offset from the transmitter increases across the page starting from 0 m in intervals of 125 m. The synthetic is calculated for times in the range $[10^{-4}, 10^1]$ s. Extrapolation is used to extend the range of the function $G(v)$ to allow it to rise smoothly from zero. Bottom: Extrema have been marked on each trace.

7.2.9 DPM by Deconvolution in Log Time of 50 Ω m Half Space Synthetics

In this section the equivalent wavefield of a horizontal electric current dipole source at the surface of a 50 Ω m halfspace is calculated numerically. The horizontal electric current dipole transmitter is located at the origin and the horizontal electric field receivers aligned collinear with the transmitter. Figure 7.10 presents synthetic switch-on TEM responses for receivers at offsets from 125 m to 3375 m, calculated using the MODALL program for LOTEM modelling (Strack 1992).

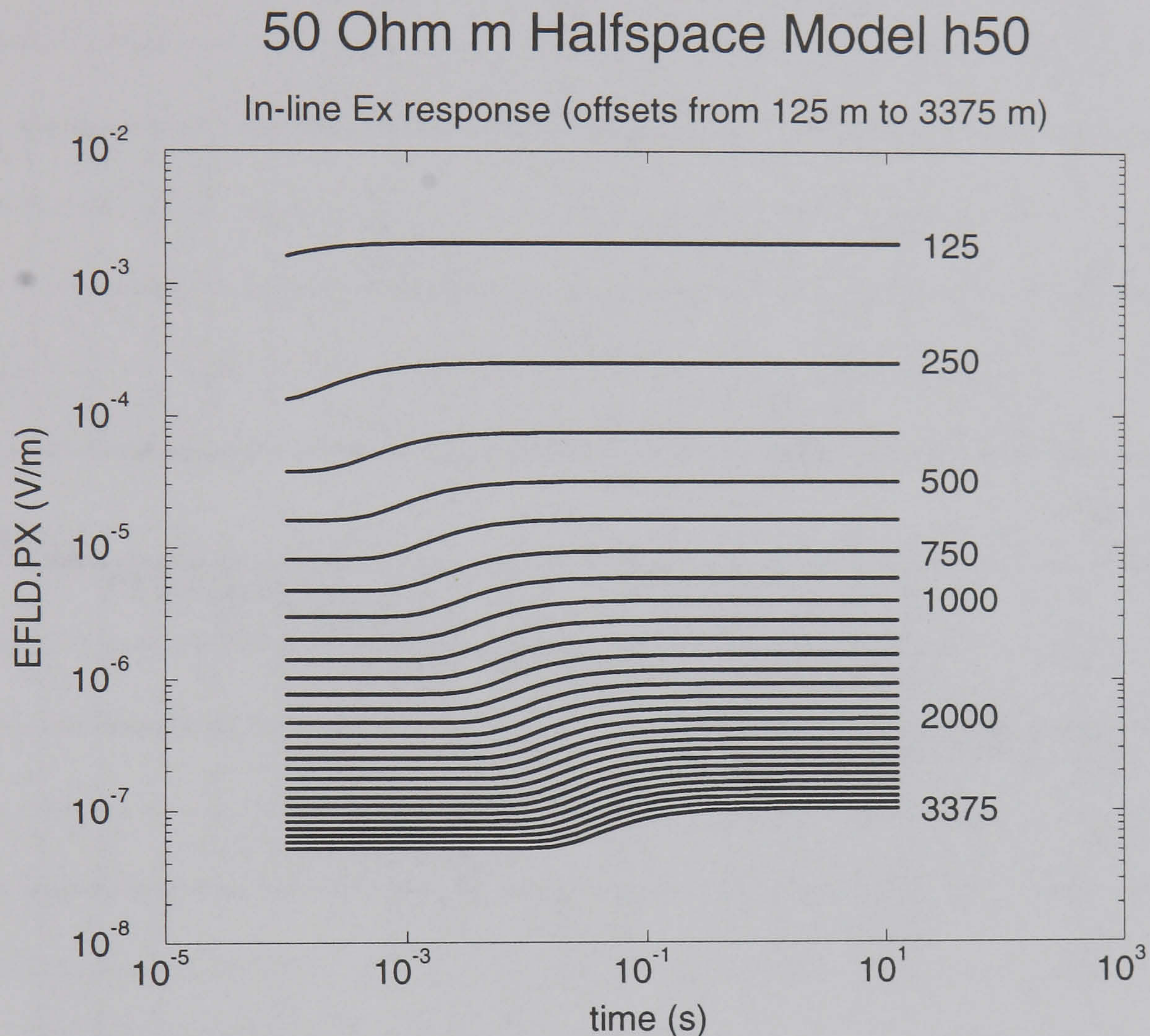


Figure 7.10: The switch-on response for the in-line Ex component for model h50, at receiver offsets from 125 m to 3375 m in intervals of 125 m.

DPM by deconvolution in log time is applied to these synthetic transients. Figure 7.11 (top) presents the resulting equivalent wavefield and in Figure 7.11 (bottom) the extremum on each trace is marked with an impulse. Picking on the trace at 1125 m offset from the source, the extremum is at 0.125 ± 0.0025 m/ \sqrt{s} . The slope of this arrival corresponds to an equivalent velocity $c = 9000 \pm 184$ m/ \sqrt{s} . Compensating for systematic error resulting from distortion of the waveform during regularisation, as analysed in Section 7.2.7, gives an estimated equivalent wavefield velocity of 6364 ± 130 m/ \sqrt{s} . Calculating the resistivity using $\rho = \mu c^2$ yields a resistivity estimate of 50.9 ± 2 Ω m.

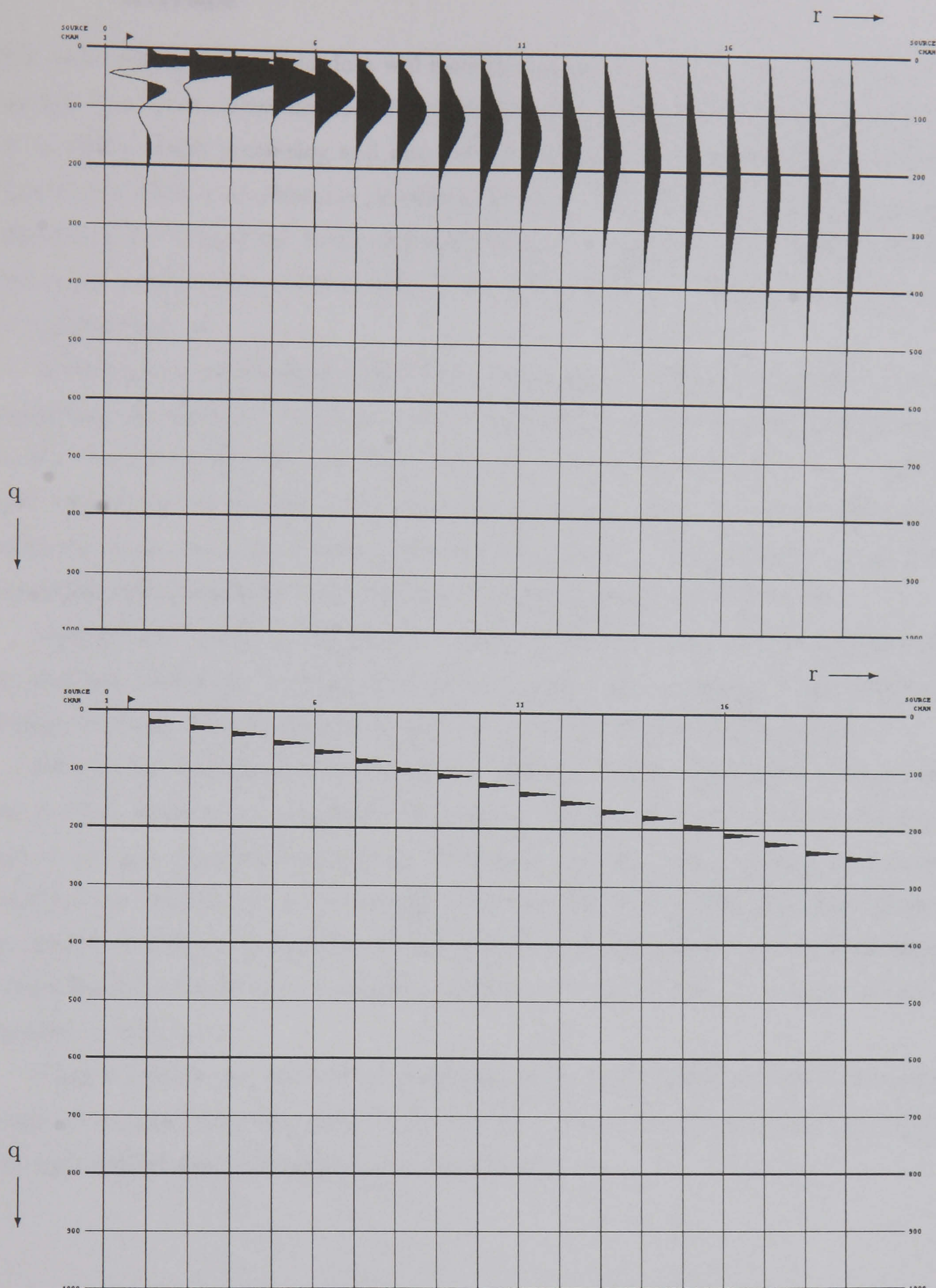


Figure 7.11: Top: Equivalent wavefield calculated using DPM by deconvolution in log time for a 50 Ω m halfspace model. The time-like variable q increases down the page with timing lines every $0.1 \sqrt{s}$. Offset from the transmitter increases across the page starting from 0 m in intervals of 125 m. The synthetic is calculated for times in the range $[10^{-4}, 10^1]$ s. Extrapolation is used to extend the range of the function $G(v)$ to allow it to rise smoothly from zero. Bottom: Extrema have been marked on each trace.

7.2.10 DPM by Deconvolution in Log Time in the Presence of Several Arrivals

It is to be expected that field data will have an equivalent wavefield containing more than one arrival. The correct identification of several arrivals is recognised as a difficult problem (Slob *et al.* 1995). Some processing and interpretation techniques such as travel time tomography (Lee & Xie 1993) and refraction processing (Dobrin *et al.* 1988) only require information on the time of the first arrival. Even when only seeking a single arrival time it is still important to have some understanding of how other arrivals may distort the results of processing and lead to biased estimates.

In order to test the robustness of DPM by deconvolution in log time a synthetic was created containing two arrivals. This was achieved by adding a second pulse of propagating energy to the synthetic of Figure 3.1b which was used previously. In Figure 3.1b the pulse has a unit velocity and on the first trace is arriving after a unit delay. The second additional pulse originates later, but travels faster. Hence at near offsets it appears later in time, but with increasing offset it quickly catches up and overtakes to become the first arrival.

Figures 7.12, 7.13 and 7.14 present the results of DPM by deconvolution in log time followed by marking of extrema. In Figure 7.12 the new pulse travels at twice the unit velocity and in Figures 7.13 and 7.14 it travels three and four times the unit velocity respectively.

Rather than marking only the location of the single largest extrema the n largest extrema are marked, where n is a user selected parameter. This is easily achieved by creating a sorted list of extrema. Starting from the first sample in the trace, local extrema (local maxima or minima) are identified by zero crossings of the first derivative. Each local extrema is added to the list. If the list becomes over-full it is sorted and the smallest extremum discarded. On return the list contains up to n extrema. In Figures 7.12, 7.13 and 7.14 two extrema have been marked on each trace.

When the pulses are well separated this simple procedure produces good results and arrival times which quite accurately reflect the true values. When the pulses are poorly separated they are not resolved and misleading results are obtained.

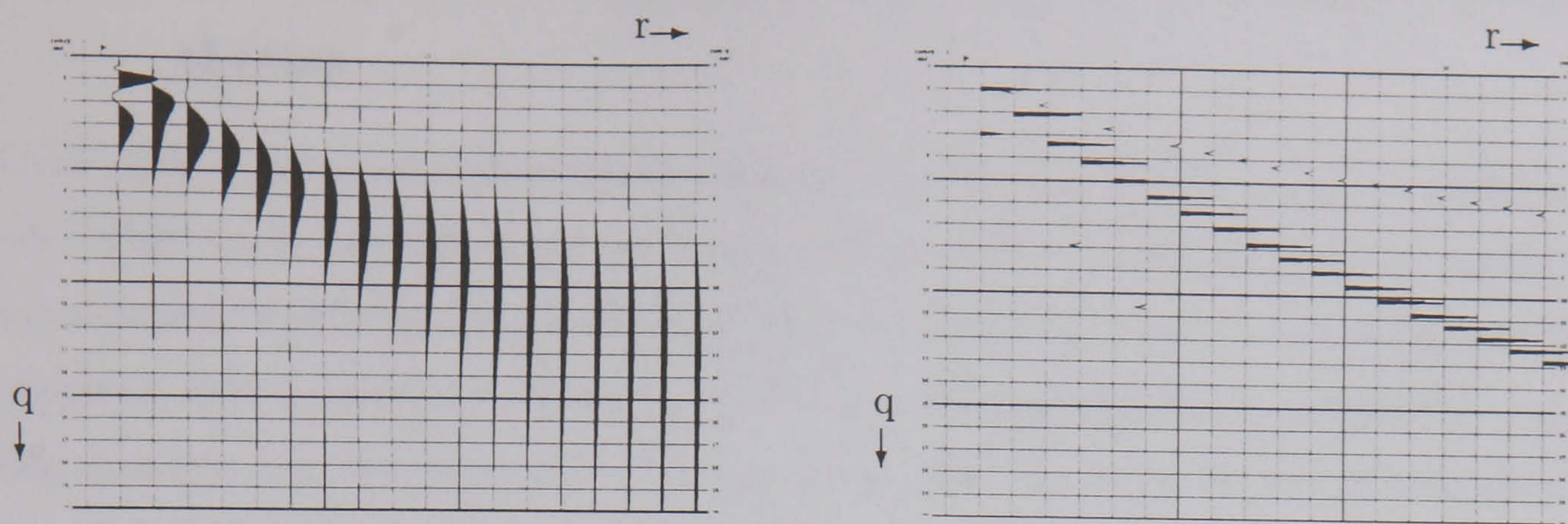


Figure 7.12: Top: equivalent wavefield calculated by DPM by deconvolution in log time of a synthetic containing two pulses, one travelling twice as fast as the other. Bottom: the two largest local extrema on each trace have been marked, and their relative amplitude and sign have been retained. Because the pulses are poorly separated they are not resolved and misleading results are obtained.

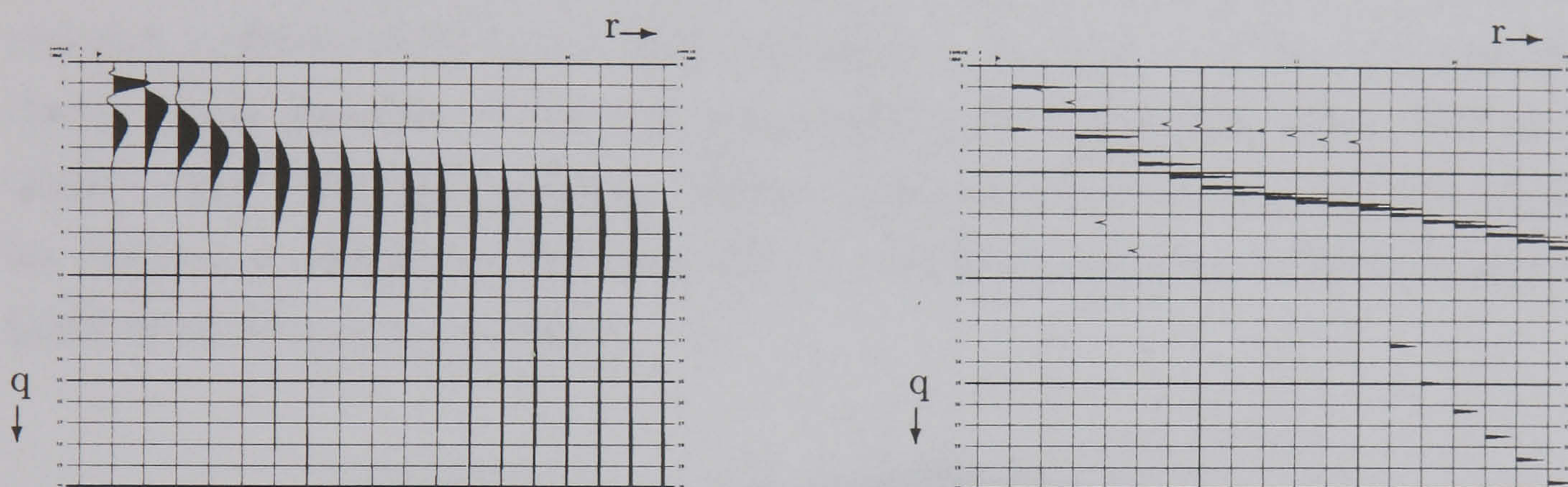


Figure 7.13: Top: equivalent wavefield calculated by DPM by deconvolution in log time of a synthetic containing two pulses, one travelling three times as fast as the other. Bottom: the two largest local extrema on each trace have been marked, and their relative amplitude and sign have been retained. The pulses are moderately well separated and an interpretable set of arrival times is obtained.

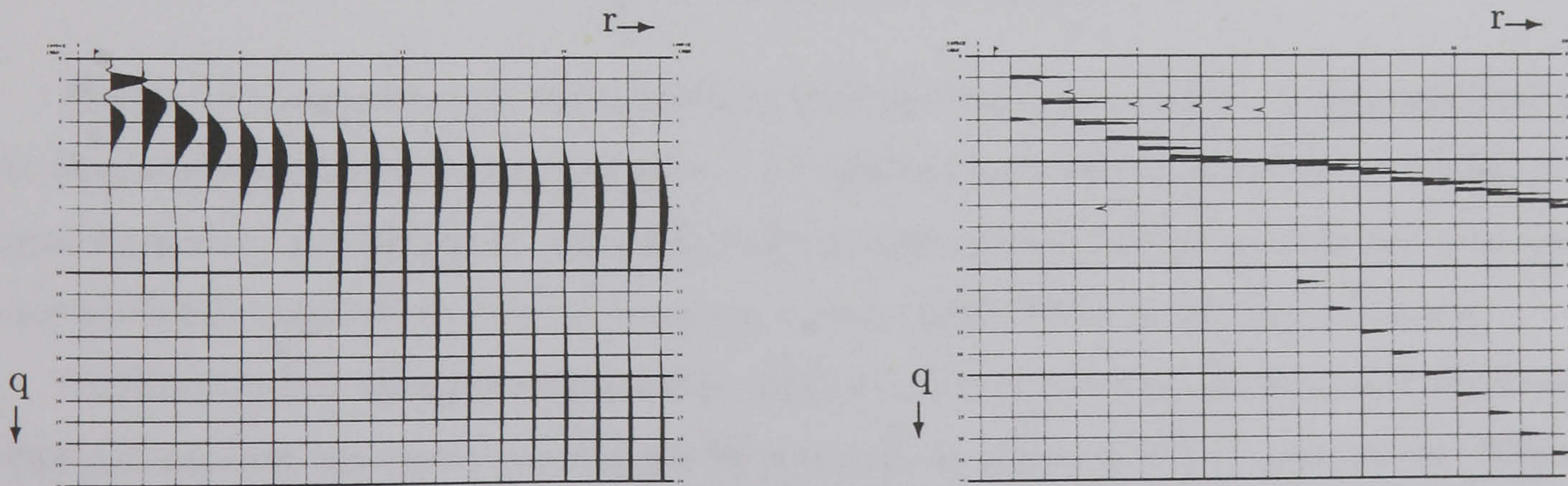


Figure 7.14: Top: equivalent wavefield calculated by DPM by deconvolution in log time of a synthetic containing two pulses, one travelling four times as fast as the other. Bottom: the two largest local extrema on each trace have been marked, and their relative amplitude and sign have been retained. The pulses are well separated and an easily interpretable set of arrival times is obtained.

7.2.11 DPM by Deconvolution in Log Time of 1D Layered Earth Synthetics

In this section diffusive to propagative mapping by deconvolution in log time is applied to synthetic TEM responses calculated for layered Earth models. Synthetics are calculated using a source-receiver configuration, transmitter current profile and receiver recording interval comparable to field acquisition. Where possible the resulting equivalent wavefield is interpreted using concepts from the refraction seismic method. This enables preliminary evaluation of data processing and interpretation methods.

Q-Type Layered Earth Model ilq1

In this section the equivalent wavefield of a horizontal electric current dipole source over a Q-type layered Earth model is calculated numerically. A Q-type layered Earth model has a resistive layer over a more conductive basement. Model ilq1 places a single layer 310 m in thickness and with resistivity 50 Ωm over a 10 Ωm basement — see figure 7.15. The horizontal electric current dipole transmitter is located at the origin and the horizontal electric field receivers aligned collinear with the transmitter. Figure 7.16 presents synthetic switch-on TEM responses for receivers at offsets from 125 m to 2250 m, calculated using the MODALL program for LOTEM modelling (Strack 1992).

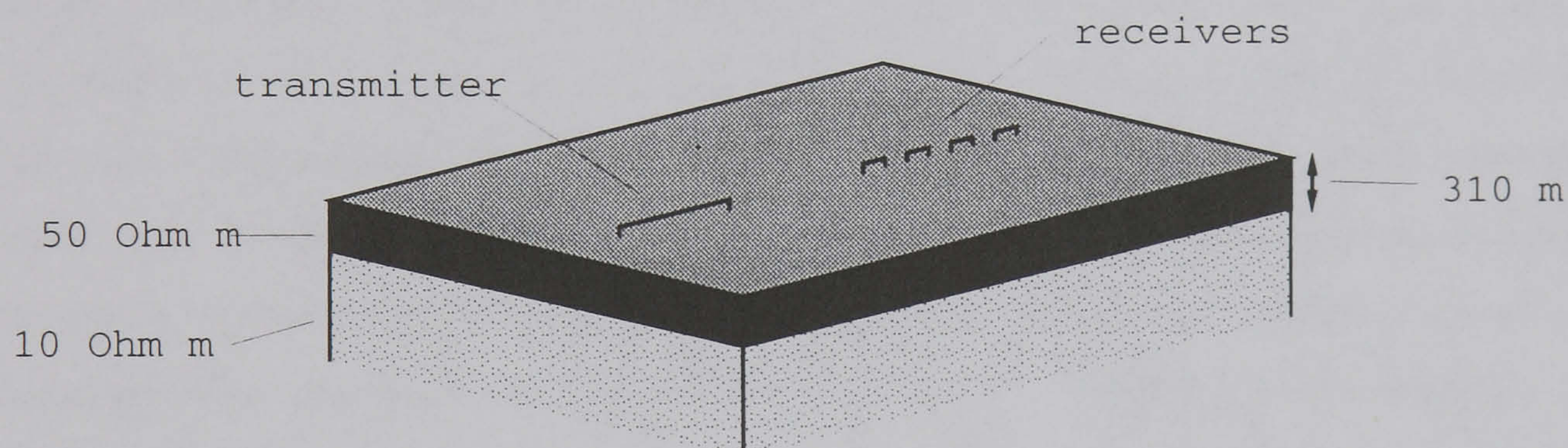


Figure 7.15: Earth Model ilq1

Figure 7.17 (top) displays the equivalent wavefield for each receiver, calculated using DPM by deconvolution in log time. In Figure 7.17 (bottom) the two largest local extrema on each trace have been marked, and their relative amplitude and sign have been retained. Two arrivals can be clearly seen which may be interpreted using concepts from seismic refraction.

Considering first the near-offset traces. Figure 7.16 indicates that the time interval employed does not capture the transient response for receivers at offsets of 125 m and 250 m. Picking on the trace at 500 m offset from the source, the extremum is at $0.055 \pm 0.0025 \text{ m}/\sqrt{s}$. The slope of this arrival corresponds to an equivalent velocity $c = 9091 \pm 433 \text{ m}/\sqrt{s}$. Compensating for systematic error resulting from distortion of the waveform during regularisation, as analysed in Section 7.2.7, gives an estimated equivalent wavefield velocity of $6428 \pm 306 \text{ m}/\sqrt{s}$. Calculating the resistivity using $\rho = \mu c^2$ yields a resistivity estimate of $51 \pm 5 \Omega\text{m}$. Picking on the trace at

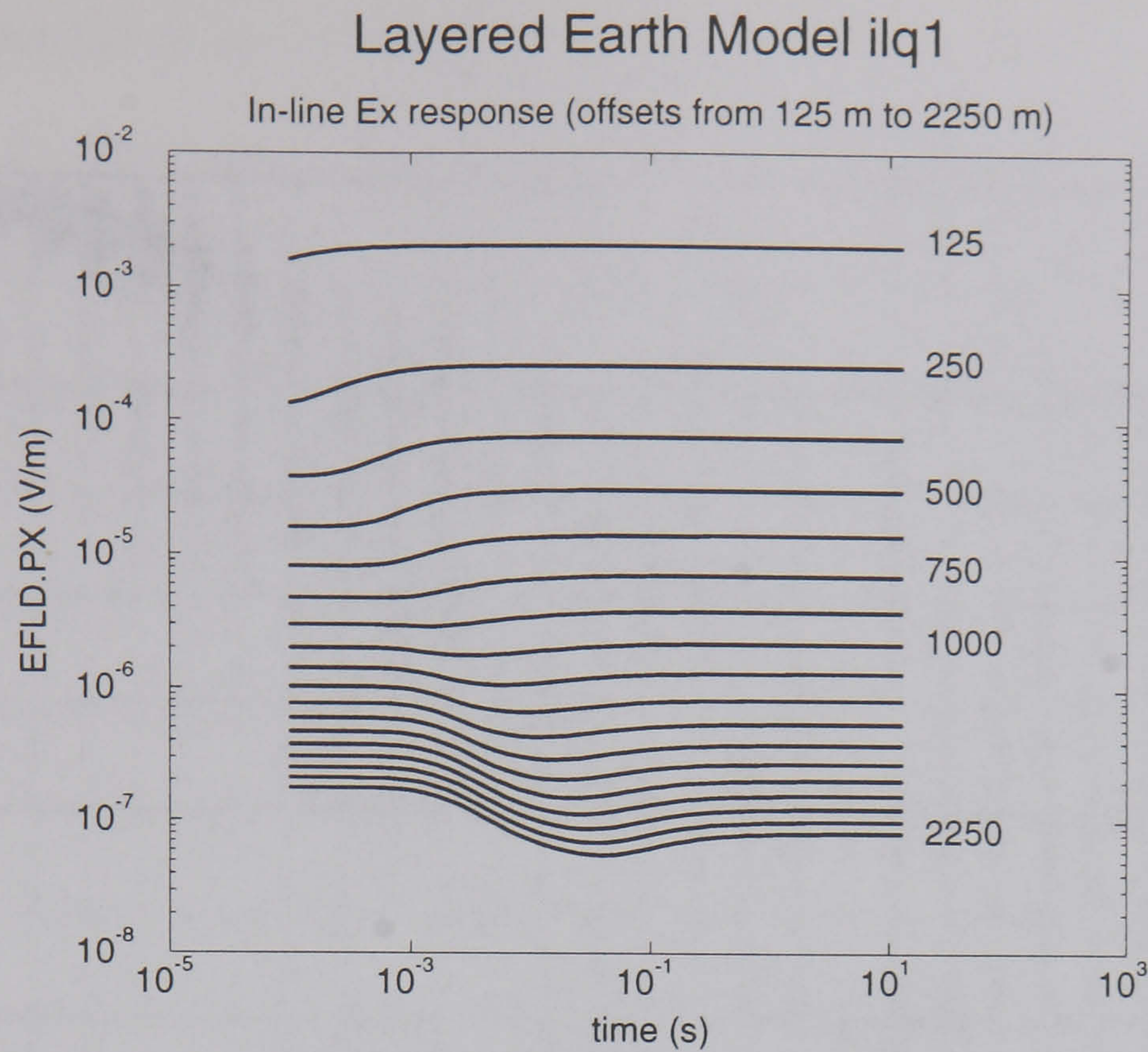


Figure 7.16: The switch-on response for the in-line Ex component for layered Earth model ilq1, a single layer 310 m in thickness and with resistivity $50 \Omega\text{m}$ over a $10 \Omega\text{m}$ basement. Receiver offset increases from 125 m to 2250 m in intervals of 125 m.

625 m offset from the source, yields a resistivity estimate of $50.1 \pm 4 \Omega\text{m}$.

Selecting the second, slower arrival which is dominant at longer offsets and picking on traces at offsets of 1625 m and 3375 m the extrema are at $0.405 \pm 0.0025 \text{ m}/\sqrt{\text{s}}$ and $0.840 \pm 0.0025 \text{ m}/\sqrt{\text{s}}$ respectively. The slope of the arrival between these two picks corresponds to an equivalent velocity $c = 4023 \pm 33 \text{ m}/\sqrt{\text{s}}$. Compensating for systematic error resulting from distortion of the waveform during regularisation, as analysed in Section 7.2.7, gives an estimated equivalent wavefield velocity of $2844 \pm 33 \text{ m}/\sqrt{\text{s}}$. Calculating the resistivity using $\rho = \mu c^2$ yields a resistivity estimate of $10.1 \pm 0.2 \Omega\text{m}$. This compares well to the resistivity of the lower halfspace.

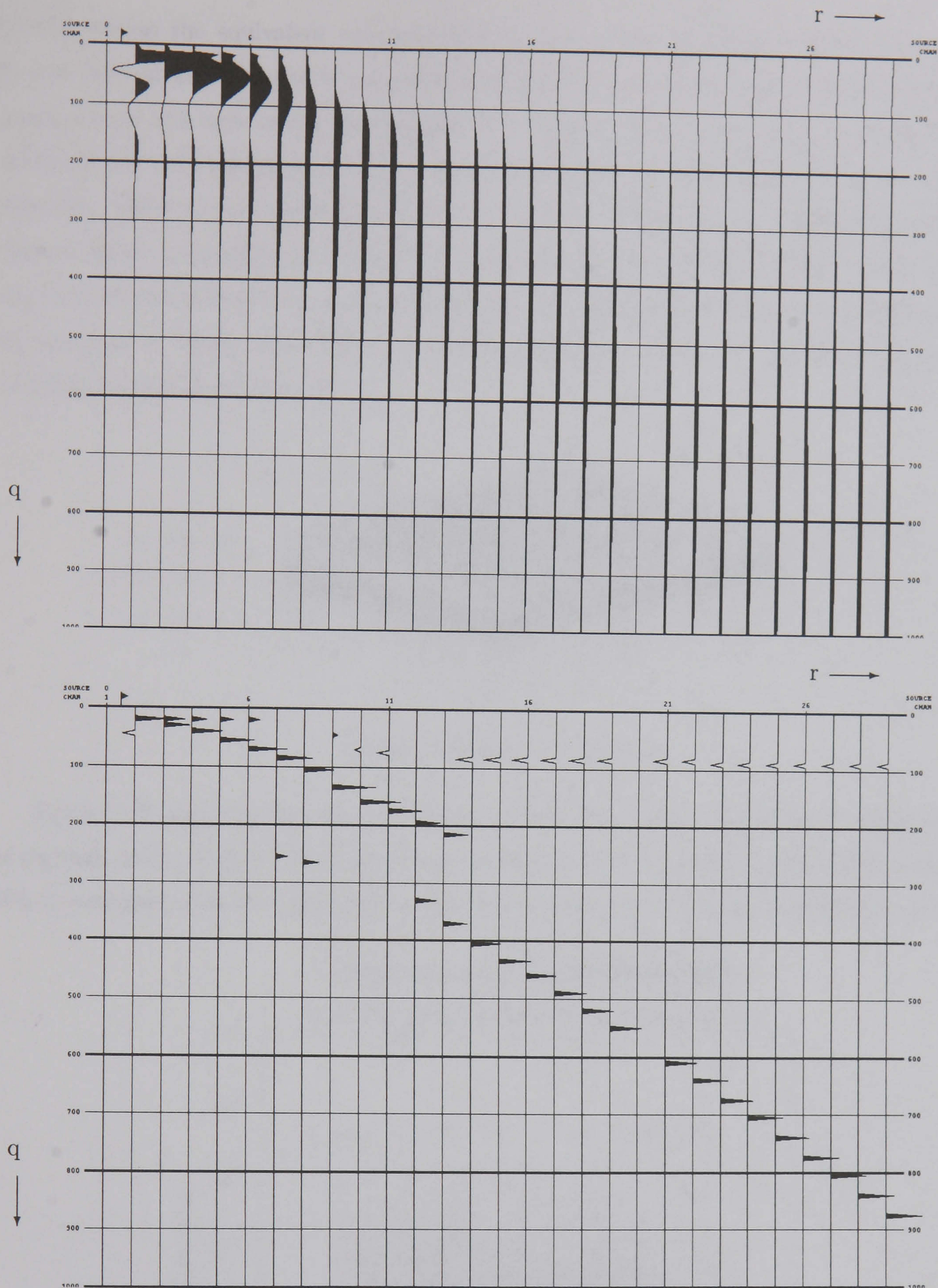


Figure 7.17: Top: Equivalent wavefield calculated using DPM by deconvolution in log time for a Q-type model with a single layer 310 m in thickness and with resistivity $50 \Omega\text{m}$ over a $10 \Omega\text{m}$ half space (model ilq1). The time-like variable q increases down the page with timing lines every $0.1 \sqrt{s}$. Offset from the transmitter increases across the page starting from 0 m in intervals of 125 m. The synthetic is calculated for times in the range $[10^{-4}, 10^1]$ s. Extrapolation is used to extend the range of the function $G(v)$ to allow it to rise smoothly from zero. Bottom: the two largest local extrema on each trace have been marked, and their relative amplitude and sign have been retained.

K-Type Layered Earth Model k44

In this section the equivalent wavefield of a horizontal electric current dipole source over a K-type layered Earth model is calculated numerically. A K-type layered Earth model has a resistive layer in a more conductive background. Model k44 places an uppermost layer 700 m in thickness and with resistivity $10 \Omega\text{m}$, over a second layer 700 m in thickness and of resistivity $1000 \Omega\text{m}$, which in turn covers a $10 \Omega\text{m}$ half space — see Figure 7.18. The horizontal electric current dipole transmitter is located at the origin and the horizontal electric field receivers aligned collinear with the transmitter. Figure 7.19 presents synthetic switch-on TEM responses for receivers at offsets from 250 m to 4625 m, calculated using the MODALL program for LOTEM modelling (Strack 1992).

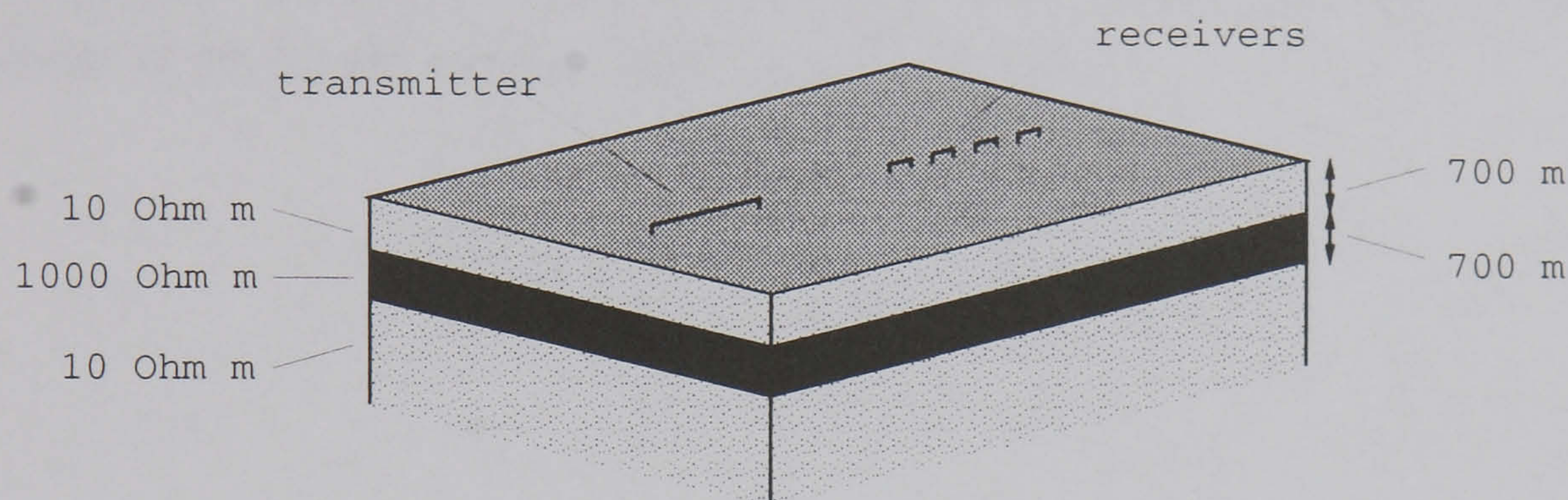


Figure 7.18: Earth Model k44

Figure 7.20 (top) presents the equivalent wavefield calculated using DPM by deconvolution in log time, and in Figure 7.20 (bottom) the extremum on each trace is marked with an impulse. When compared with the equivalent wavefield calculated over this range of offsets for a $10 \Omega\text{m}$

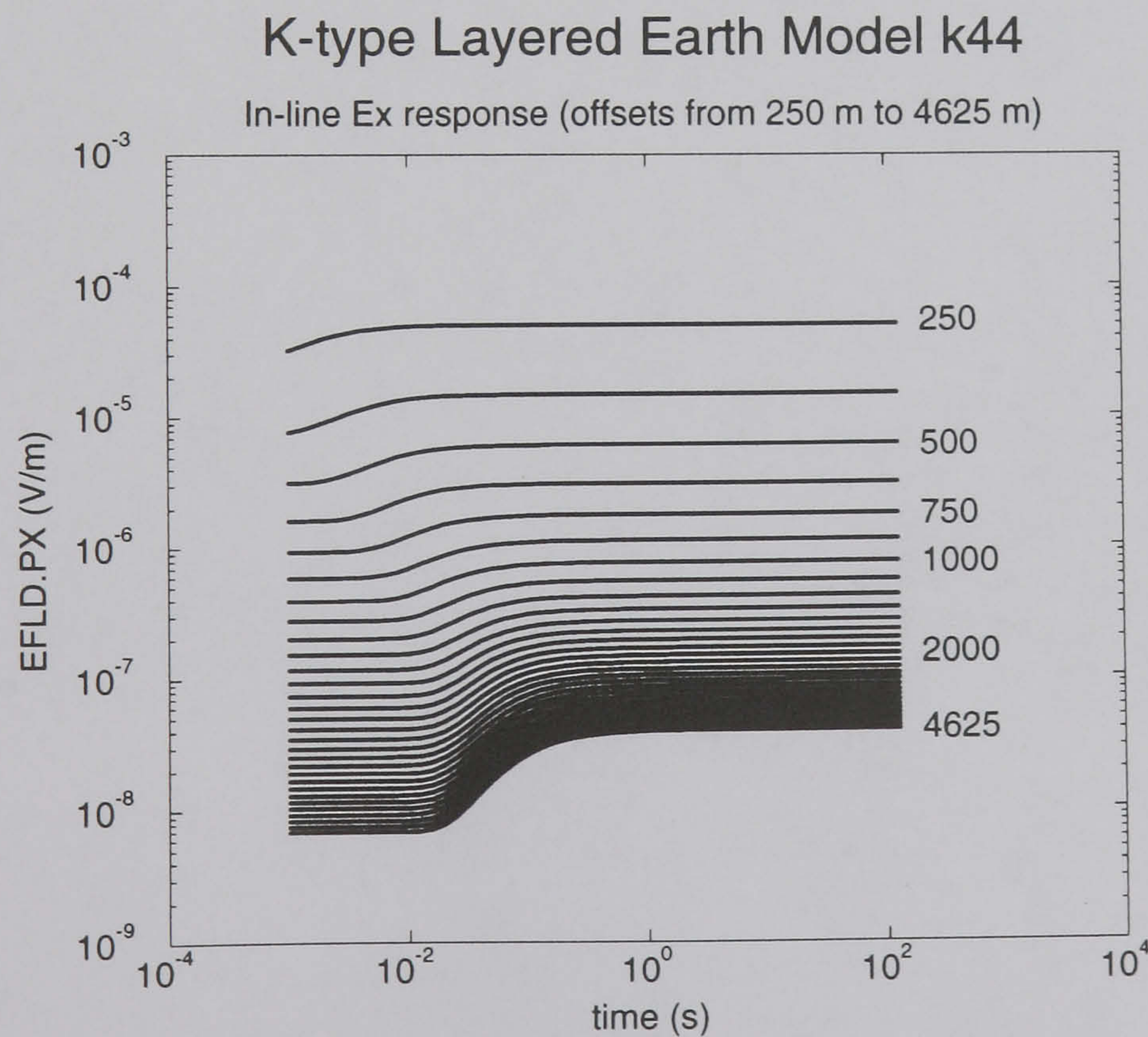


Figure 7.19: The switch-on response for the in-line Ex component for model k44, at receiver offsets from 250 m to 4625 m in intervals of 125 m.

halfspace Earth model (Figure 7.21) it is clear that the pattern of the arrivals, although the same at shorter offsets, is different at longer offsets.

At short offsets the extrema on each trace lie on the same straight line as for the equivalent wavefield calculated for the 10 Ωm half space model. At longer offsets an earlier, faster, arrival is evident. This energy is interpreted as a refracted arrival.

Picking on traces at offsets of 2500 m and 4375 m the extrema are at 0.385 ± 0.0025 m/ $\sqrt{\text{s}}$ and 0.43 ± 0.0025 m/ $\sqrt{\text{s}}$ respectively. The slope of the arrival between these two picks corresponds to an equivalent velocity $c = 41667 \pm 5208$ m/ $\sqrt{\text{s}}$. Compensating for systematic error resulting from distortion of the waveform during regularisation, as analysed in Section 7.2.7, gives an estimated equivalent wavefield velocity of 29462 ± 3682 m/ $\sqrt{\text{s}}$. Calculating the resistivity using $\rho = \mu c^2$ yields a resistivity estimate of 1090 ± 290 Ωm . This compares well to the resistivity of the middle, resistive layer in the k44 model.

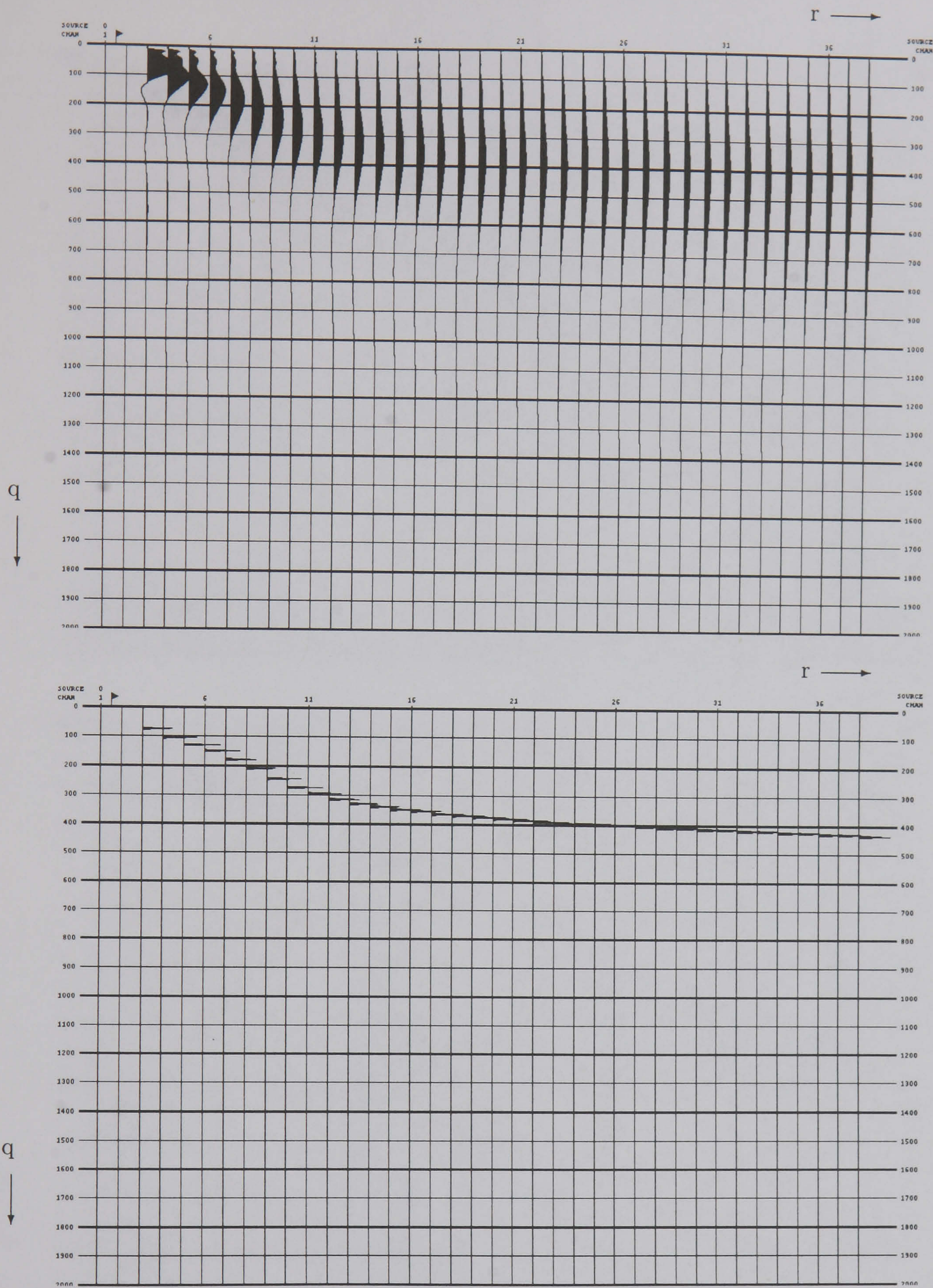


Figure 7.20: Top: Equivalent wavefield calculated using DPM by deconvolution in log time for the k44 K-type layered Earth model. The time-like variable q increases down the page and offset from the transmitter increases across the page starting from 0 m in intervals of 125 m. The synthetic is calculated for times in the range $[10^{-3}, 10^2]$ s. Extrapolation is used to extend the range of the function $G(v)$ to allow it to rise smoothly from zero. Bottom: Extrema have been marked on each trace.

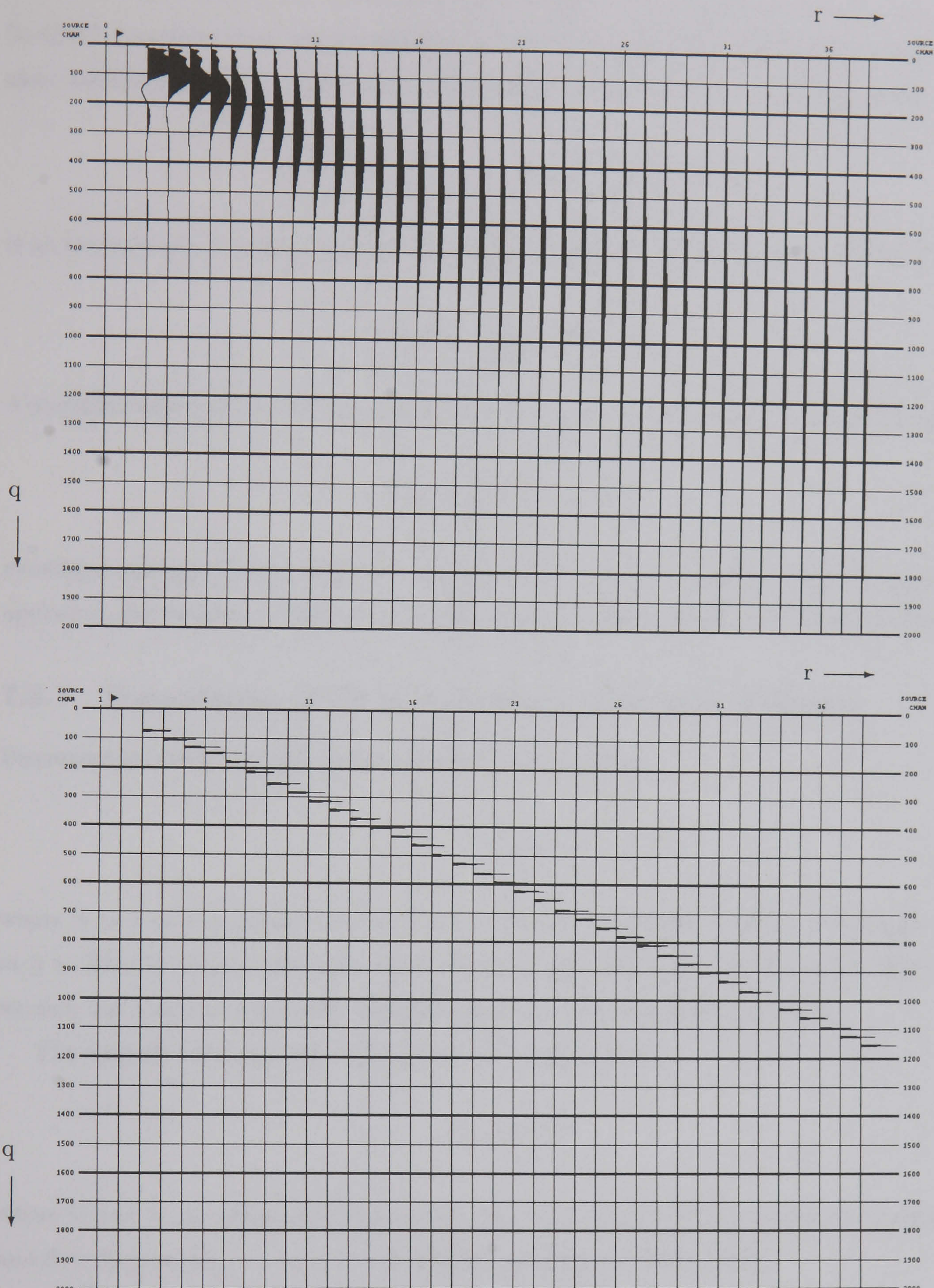


Figure 7.21: Top: Equivalent wavefield calculated using DPM by deconvolution in log time for the h44 (10 Ω m halfspace) Earth model. The time-like variable q increases down the page and offset from the transmitter increases across the page from 0 m in intervals of 125 m. Bottom: Extrema have been marked on each trace.

7.3 Diffusive to Propagative Mapping (DPM) by Singular Value Decomposition of the Q Transform

Section 7.1 explains that, when considered as a formulation for calculating the q -domain equivalent wavefield from the time-domain diffusive electromagnetic field, the Q transform

$$\mathbf{F}(\mathbf{x}, t) = \frac{1}{2\sqrt{\pi t^3}} \int_0^\infty q \exp\left(-\frac{q^2}{4t}\right) \mathbf{U}(\mathbf{x}, q) dq, \quad (7.66)$$

is an example of a Fredholm integral equation of the first kind (Kress 1989) with kernel

$$K(t, q) = \frac{q}{2\sqrt{\pi t^3}} \exp\left(-\frac{q^2}{4t}\right). \quad (7.67)$$

A standard technique for the numerical solution of such problems is to discretise the integral

$$f(t) = \int_a^b K(t, q) u(q) dq \quad (7.68)$$

yielding a system of linear equations which are then inverted. In this section this approach is applied to the problem of diffusive to propagative mapping and tested on synthetic data.

7.3.1 Formulation of DPM as a Matrix Inversion Problem

Discretisation of the integral equation (7.68) yields a system

$$\mathbf{F} = \mathbf{A}\mathbf{U} \quad (7.69)$$

where \mathbf{A} is a $m \times n$ matrix (m rows by n columns). In Equation (7.69) it is usual to have $m \geq n$. That is, the system is over-determined. In the context of DPM (Q transform inversion) we seek less than one equivalent wavefield data point per transient observation.

The singular value decomposition (SVD) of a matrix \mathbf{A} is

$$\mathbf{A} = \mathbf{U}\mathbf{S}\mathbf{V}^T, \quad (7.70)$$

where \mathbf{U} and \mathbf{V} are orthonormal matrices, $\mathbf{V}_1 \geq \mathbf{V}_2 \geq \dots \geq \mathbf{V}_n > 0$ are the singular values of \mathbf{A} and $\mathbf{S} = \text{diag}(\mathbf{V}_1, \mathbf{V}_2, \dots, \mathbf{V}_n, 0, 0, \dots)$. For the discretised system (7.69)

$$\mathbf{U} = \sum_{i=1}^n \frac{1}{\mathbf{V}_i} (\mathbf{F}, \mathbf{u}_i) \mathbf{v}_i. \quad (7.71)$$

where \mathbf{u}_i and \mathbf{v}_i , the left and right singular vectors of \mathbf{A} , are the columns of \mathbf{U} and \mathbf{V} .

Amplification of infinitesimal high-frequency noise in the data by a naive inversion scheme will result in wild fluctuation of the output. Therefore it is not surprising that inversion of the

system (7.69) is found to be an ill-posed problem. Such ill-posedness is a feature of a problem not of a particular inversion algorithm. Any algorithm which attempts to address the problem must at some point address the ill-posedness.

If the discretised system (7.69) is a faithful representation of the original then \mathbf{v}_i will be close to ν_i , and \mathbf{u}_i and \mathbf{v}_i will be sampled versions of \mathbf{u}_i and \mathbf{v}_i . That is, the better the discretized system models the integral equation, the more closely the ill-conditioning of the matrix system will resemble the ill-posedness of the original equation (Hansen 1992).

Some approach must be found which will prevent high frequency components associated with small singular values from rendering the solution meaningless. Such techniques are often called regularisation methods. The underlying idea of regularisation is to replace an ill-posed problem with a neighbouring well-posed problem. Typically regularisation techniques seek to minimise $\|\mathbf{A}\mathbf{U} - \mathbf{F}\|_2$ subject to some criteria which singles out a solution which is in some sense close to the desired, but unknown, true solution of (7.69).

In the time domain the Q transform is

$$\mathbf{F}(\mathbf{x}, t) = \frac{1}{2\sqrt{\pi t^3}} \int_0^\infty q \exp(-\frac{q^2}{4t}) \mathbf{U}(\mathbf{x}, q) dq. \quad (7.72)$$

Following Lee & Xie (1993) we apply the trapezoidal rule

$$\int_{x_1}^{x_n} f(x) dx = h(\frac{1}{2}f_1 + f_2 + f_3 + \dots + f_{n-1} + \frac{1}{2}f_n) + O\left(\frac{(x_n - x_1)f''}{n^2}\right) \quad (7.73)$$

to obtain a discretised version

$$\begin{aligned} \mathbf{F}_i &= \frac{1}{2\sqrt{\pi t_i^3}} \left(\frac{\Delta q}{2} q_1 e^{-\frac{q_1^2}{4t_i}} \mathbf{U}_1 + \Delta q \sum_{j=2}^{n-1} q_j e^{-\frac{q_j^2}{4t_i}} \mathbf{U}_j + \frac{\Delta q}{2} q_n e^{-\frac{q_n^2}{4t_i}} \mathbf{U}_n \right) \\ q_j &= (j-1)\Delta q \quad j = 1 \dots n \end{aligned} \quad (7.74)$$

where \mathbf{F}_i are our m transient values, observed at times t_i , and $\mathbf{U}_j = \mathbf{U}(\mathbf{x}, q_j) \quad j = 1 \dots n$ is the sampled version of the equivalent wavefield we seek.

Alternatively, setting $q = e^v$ in (7.72) we obtain

$$\mathbf{F}(\mathbf{x}, t) = \frac{1}{2\sqrt{\pi t^3}} \int_{-\infty}^\infty q^2 e^{-\frac{q^2}{4t}} \mathbf{U}(\mathbf{x}, q) dv. \quad (7.75)$$

which may be discretised as

$$\begin{aligned} \mathbf{F}_i &= \frac{1}{2\sqrt{\pi t_i^3}} \left(\frac{\Delta v}{2} q_1^2 e^{-\frac{q_1^2}{4t_i}} \mathbf{U}_1 + \Delta v \sum_{j=2}^{n-1} q_j^2 e^{-\frac{q_j^2}{4t_i}} \mathbf{U}_j + \frac{\Delta v}{2} q_n^2 e^{-\frac{q_n^2}{4t_i}} \mathbf{U}_n \right) \\ q_j &= \exp(v_0 + (j-1)\Delta v) \quad j = 1 \dots n \end{aligned} \quad (7.76)$$

a new discretisation with $\mathbf{U}_j = \mathbf{U}(\mathbf{x}, q_j) \quad j = 1 \dots n$ a uniform sampling in $\log q$ of the

equivalent wavefield we seek. Equations 7.74 and (7.76) may both be written as a matrix equation (7.69).

In order to investigate the effect on numerical stability, an option is introduced into the numerical formulation of Equation (7.69) to multiply both sides by t^p for some (possibly fractional) power p

$$t^p \mathbf{F}(\mathbf{x}, t) = \frac{1}{2\sqrt{\pi t^{3-p}}} \int_{-\infty}^{\infty} q^2 e^{-\frac{q^2}{4t}} \mathbf{U}(\mathbf{x}, q) dv. \quad (7.77)$$

After multiplying both sides by t^p with $p = 0.5$ Equation (7.77) is exactly equivalent to Equation (7.10). This means that, for $p = 0.5$, the matrix equation obtained by discretising Equation (7.77) is equivalent to performing the deconvolution operation expressed in Equation (7.18). Nevertheless this will be referred to as DPM by singular value decomposition, in order to avoid confusion between deconvolution using a spiking filter in logarithmic time, as applied in Section 7.2.

7.3.2 Demonstration of DPM by Singular Value Decomposition

In this section diffusive to propagative mapping (DPM) by singular value decomposition is applied to a diffusive field with a known equivalent wavefield. As in Section 7.2.5 a diffusive field is chosen for which the equivalent wavefield is an impulse propagating from the origin at unit velocity.

Figure 7.22 shows each stage in the process for the response at one offset. Figure 7.23 presents the equivalent wavefield in the style of a seismic common-source gather.

The ill-conditioning of the problem means that the analytic result for the “true” equivalent wavefield, an impulse propagating with constant velocity, cannot be perfectly recovered (Slob *et al.* 1995). By marking the location of the extremum (maximum absolute amplitude either negative or positive) on each trace in the equivalent wavefield we can easily see that the pulse is travelling outward from the source at a constant velocity which can be estimated from the slope of the line along which these maxima lie. Comparing this velocity with that used to calculate the synthetics confirms that the correct velocity is interpreted.

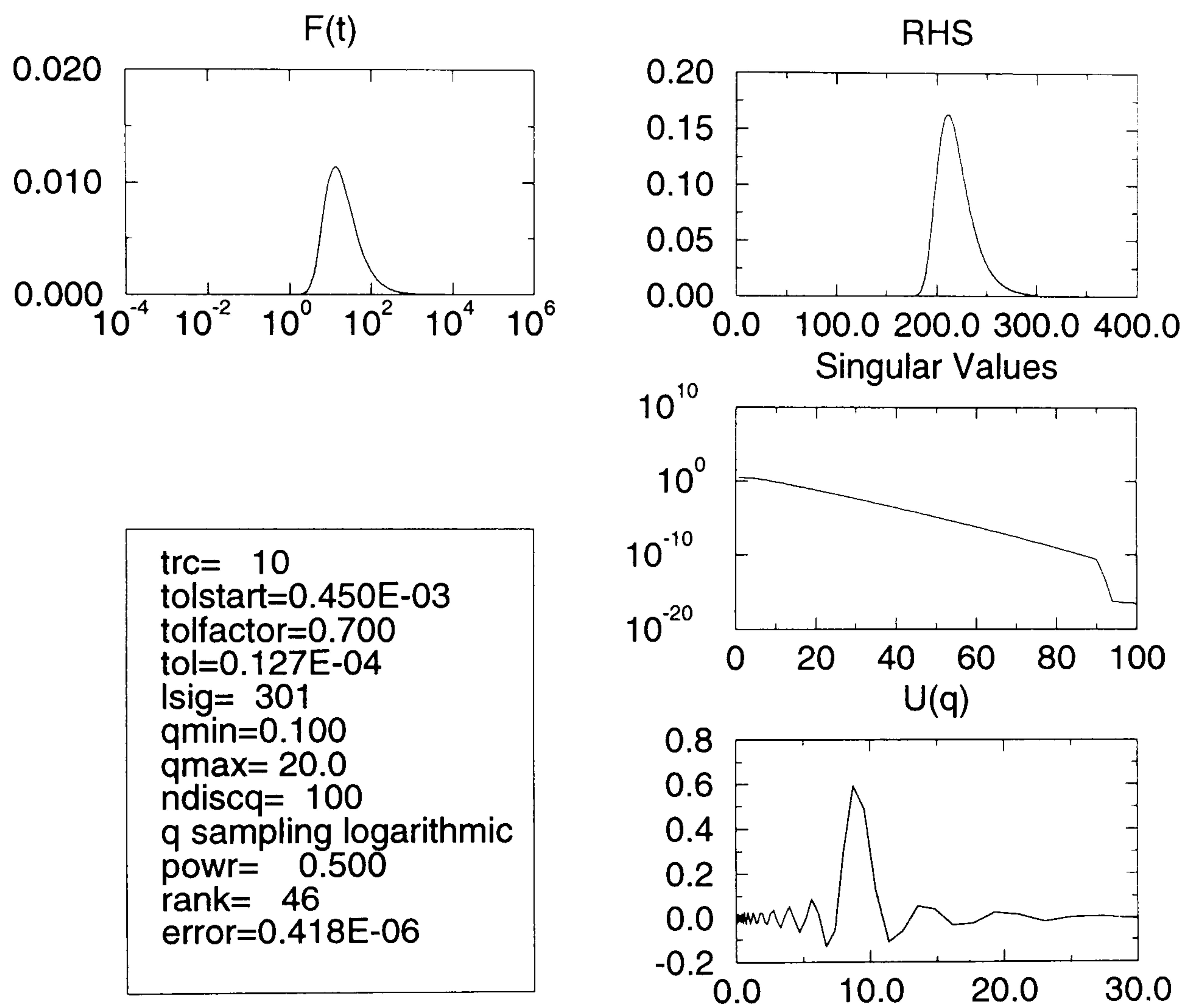


Figure 7.22: DPM by singular value decomposition applied to the response at a single offset. Top left: the synthetic response, $F(t)$, plotted against log time. Top right: the right hand side of the matrix system. This is $2\sqrt{(\pi)t_i^p F_i}$ and for this example $p = 0.5$. Middle right: the singular values of the matrix system. Bottom right: the numerically recovered equivalent wavefield, plotted as a function of the time-like variable q .

7.3.3 DPM by Singular Value Decomposition

Synthetic

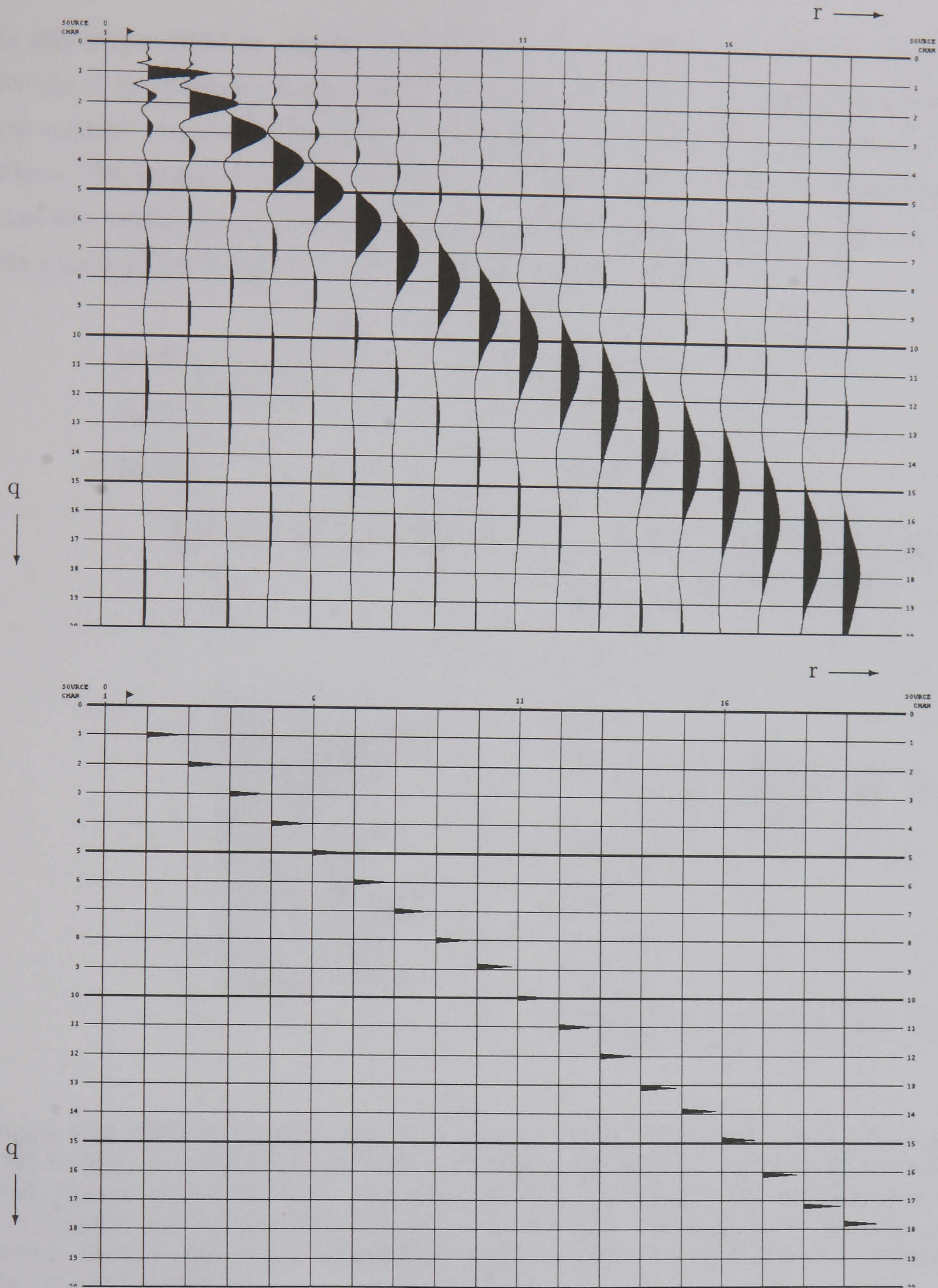


Figure 7.23: Top: Equivalent wavefield calculated by DPM by singular value decomposition of a synthetic containing one pulse, travelling at unit velocity. Offset from the origin increases across the page starting from 0 in unit intervals. The time-like variable q increases down the page with timing lines at unit intervals. Bottom: The extremum on each trace is marked, from which the arrival can quite easily be interpreted to have a unit velocity.

7.3.3 DPM by Singular Value Decomposition of 10 Ω m Half Space Synthetics

In this section DPM by singular value decomposition is applied to synthetics calculated for the 10 Ω m halfspace Earth model h10. Figure 7.24 displays each stage of the process for the synthetic transient for the collinear Ex component at an offset of 1125 m from the source. Figure 7.25 displays the equivalent wavefield for each receiver. In this and similar figures the time-like variable q increases down the page and offset from the transmitter increases across the page from left to right in intervals of 125 m starting from 0 m.

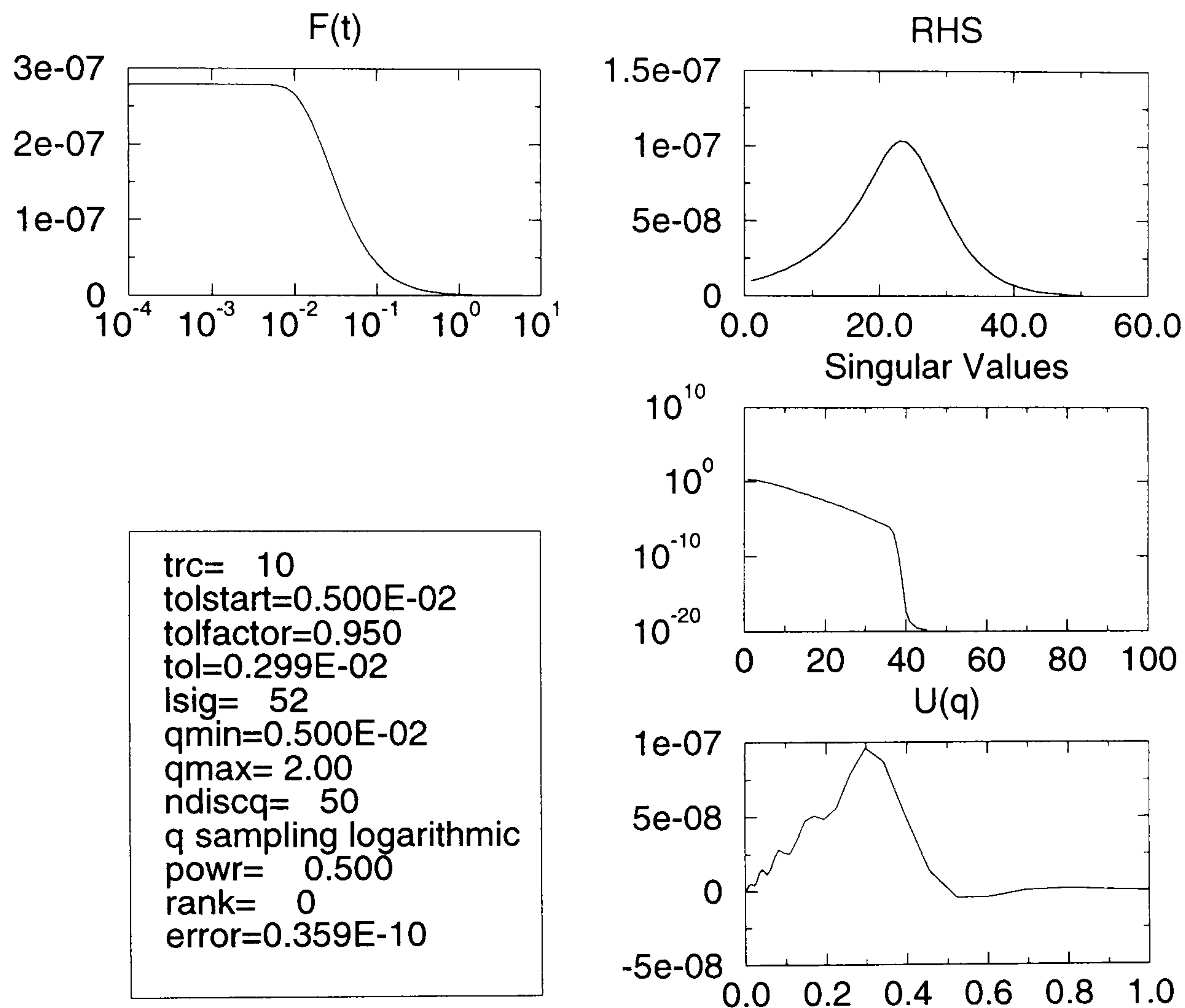


Figure 7.24: DPM by singular value decomposition applied to the collinear Ex component at 1125 m offset from the source for a 10 Ω m halfspace model. Top left: the synthetic response, $F(t)$, plotted against log time. Top right: the right hand side of the matrix system. This is $2\sqrt{(\pi)}t_i^p F_i$ and for this example $p = 0.5$. Middle right: the singular values of the matrix system. Bottom right: the numerically recovered equivalent wavefield, plotted as a function of the time-like variable q .

In Figure 7.25 (bottom) the location of the extremum on each trace of the numerically calculated equivalent wavefield displayed in Figure 7.25 (top) is marked with an impulse. The slope of this arrival can be estimated by assuming it passes through the origin in the (r, q) domain, picking the time of the extremum q_i on the trace at offset r_i and then calculating the equivalent velocity c using $c = q_i/r_i$. A lower bound on the uncertainty in this estimate of equivalent velocity can be established from the uncertainty in the extremum pick q_i , which is

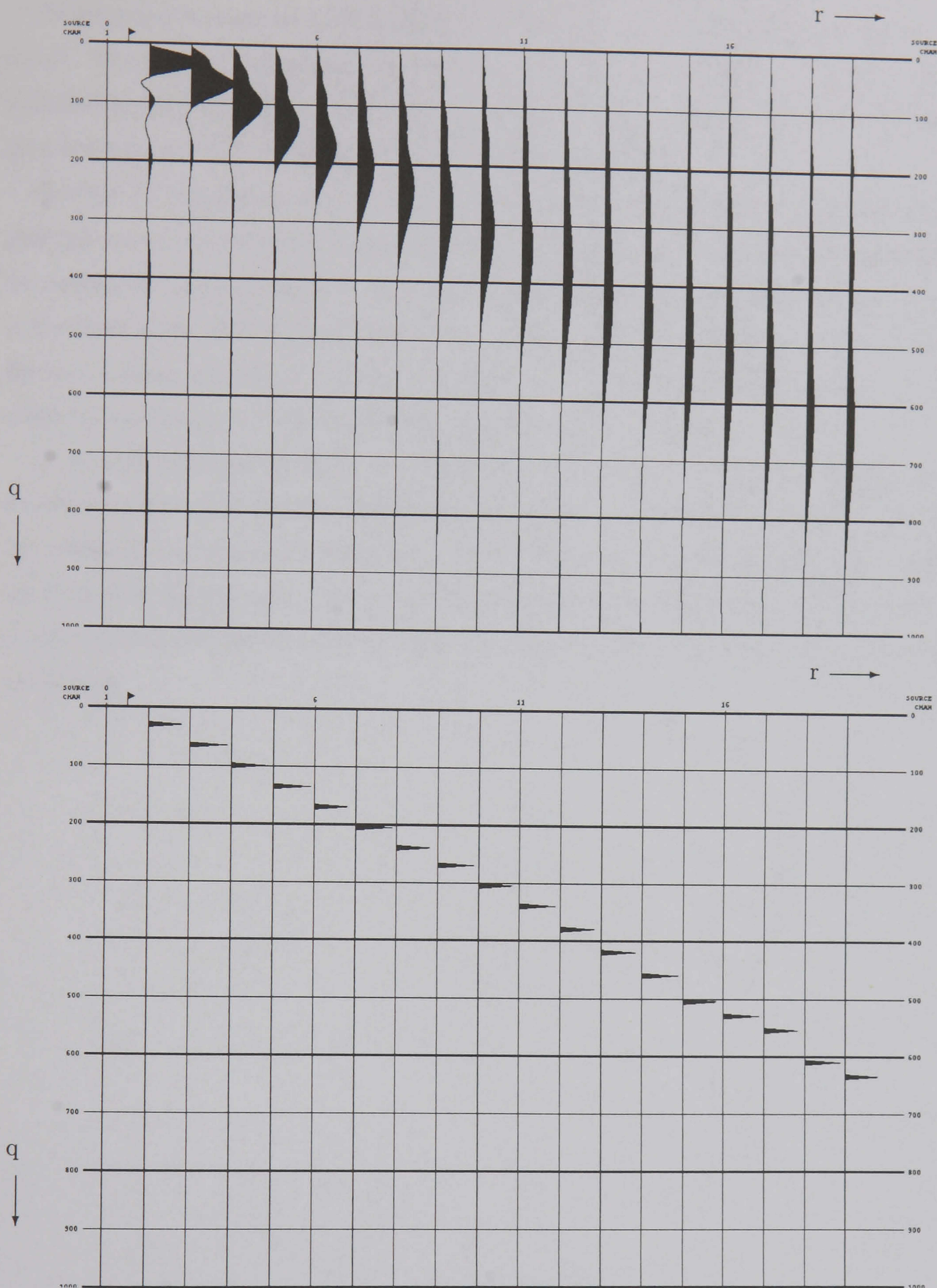


Figure 7.25: Top: Equivalent wavefield calculated using DPM by singular value decomposition for the h10 (10 Ω m halfspace) model. The time-like variable q increases down the page with timing lines every $0.1 \sqrt{s}$. Offset from the transmitter increases across the page starting from 0 m in intervals of 125 m. The synthetic is calculated for times in the range $[10^{-4}, 10^1]$ s. Bottom: Extrema have been marked on each trace.

$\pm 1/2$ the sample interval in q . Alternatively a line-fitting procedure could be employed to find the best fit to a selection of traces and provide an estimate of uncertainty.

Picking on the trace at 1125 m offset from the source, the extremum is at 0.305 ± 0.0025 m/ \sqrt{s} . The slope of this arrival corresponds to an equivalent velocity $c = 3688 \pm 329$ m/ \sqrt{s} . Calculating the resistivity using $\rho = \mu c^2$ yields a resistivity estimate of 17.1 ± 3.2 Ωm . This does not compare well with the halfspace resistivity of 10 Ωm .

Section 7.2.4 demonstrated that DPM by numerical deconvolution in log time does not yield the exact equivalent wavefield, but instead a numerical approximation. In Section 7.2.7 the equivalent wavefield which is recovered using DPM by numerical deconvolution in log time is predicted from the analytical equivalent wavefield and compared to the numerical results. Because a good agreement is found this justifies a calibration procedure which enables the halfspace resistivity to be estimated from the equivalent wavefield.

It is expected that for DPM by singular value decomposition the numerically recovered waveform is also related to the analytical result, but smoothed so that the peak value is nearer the centre of the analytical waveform. An analysis of the relationship is more difficult to calculate than for the case of DPM by deconvolution in log time. While it is possible to find a calibration factor based on known wave-diffusion pairs, it is not possible to justify it without an analysis.

7.4 Conclusions

The Q transform

$$\mathbf{F}(\mathbf{x}, t) = \frac{1}{2\sqrt{\pi t^3}} \int_0^\infty q \exp\left(-\frac{q^2}{4t}\right) \mathbf{U}(\mathbf{x}, q) dq \quad (7.78)$$

is a prescription for calculating a diffusive response $\mathbf{F}(\mathbf{x}, t)$ from its equivalent wavefield $\mathbf{U}(\mathbf{x}, q)$. The Q transform may be inverted to calculate an equivalent wavefield from diffusive transients. Following Tournier & Gibert (1995) we call this process diffusive to propagative mapping (DPM).

When considered as an inversion problem the Q transform is an example of a wider class of problems which are well known to be ill-posed. Such ill-posedness is a feature of a problem not a particular inversion algorithm. Any algorithm which attempts to address the problem must at some point address the ill-posedness. Otherwise the slightest perturbation in the diffusive data \mathbf{F} will be amplified during inversion to give an estimate of the equivalent wavefield \mathbf{U} which is meaningless. Regularisation techniques recognise ill-posedness and attempt to select an answer which is stable, and in some sense as close as possible to the “true” solution.

By moving to a logarithmic sampling in both time and the time-like variable q the Q transform may be re-formulated as a convolution. Standard deconvolution techniques can then be applied to recover the equivalent wavefield. Regularisation imposed by this scheme results from stabilisation employed during deconvolution and the uniform sampling in logarithmic q . This regularisation affects the shape of the recovered equivalent waveform. This regularisation of the recovered waveform can be analysed and understood using known correspondences between diffusive and propagative waveforms; principally it results in smoothing of the numerically recovered equivalent wavefield, relative to the analytic result. This introduces a systematic error which can be analysed and corrected. Application of DPM by deconvolution in log time to synthetic responses for simple layered Earth models yields equivalent wavefields which, after compensation for waveform regularisation, can be interpreted to recover the half space resistivity using simple travel-time concepts.

Discretisation of the Q transform integral yields a system of linear equations which can be inverted to determine the equivalent wavefield from the diffusive EM field. Again the ill-posedness of the problem must be dealt with. A truncated singular value decomposition method is used to regularise the inversion. As with DPM by deconvolution in log time, waveform regularisation is again observed, but no analysis equivalent to that performed for DPM by deconvolution in log time has yet been undertaken.

Chapter 8

Conclusions

Recent adaptation of technology from multichannel seismic acquisition systems has delivered multichannel transient electromagnetic (MTEM) acquisition systems. These have the capacity to investigate both resistive and conductive targets at depths of interest in hydrocarbon exploration and production. EM explorationists are now presented with systems capable of collecting an unprecedented abundance of data and require a supporting methodology for designing, acquiring, processing and interpreting such surveys.

The equivalent wavefield concept relates diffusive electromagnetic propagation to non-diffusive propagation, provided equivalent source and boundary conditions are satisfied. This well-known concept is a special case of a more general theorem, proven here, relating the solutions of two systems of partial differential equations that have the same spatial, but different temporal derivatives. Motivated by a desire to generate novel analysis, processing and interpretation methods this thesis investigates the use of the equivalent wavefield concept in the analysis of multichannel transient electromagnetic responses, for some configurations of interest to EM surveying.

Using the equivalent wavefield concept, and results from wave theory, the response to a directed impulsive point source is calculated for uniform, isotropic media. The response for physically realistic sources is then calculated by combination with the source description. A moment tensor and a dipole moment are used to represent the electric current dipole source, which is commonly used in field data acquisition. This representation also allows comparison with seismic sources. For example, the equivalent wavefield of the magnetic field generated by an electric current dipole in a whole space is generated by a point source of torque, generating shear waves only. In general, electromagnetic fields have an irrotational component that is equivalent to P-wave propagation, and a solenoidal component that is equivalent to S-wave propagation.

The Q transform is a prescription for calculating a diffusive response from its equivalent wavefield. For the case considered here the conductivity $\sigma(\mathbf{x})$ of a diffusive electromagnetic

medium is related to the velocity $c(\mathbf{x})$ of the equivalent wavefield by $\mu\sigma(\mathbf{x}) = c(\mathbf{x})^{-2}$.

The equivalent wavefield of a grounded horizontal electric current dipole source located at the surface of a uniform half-space is calculated analytically for receivers located at the surface of the half-space. Considered as a function of the time-like variable q , this has a triangular waveform with origin at the switch-off time, a peak at the arrival time and is zero thereafter. The arrival time is r/c where r is offset from the transmitter. When plotted as a common source gather, with offset of the receiver from the transmitter vs q , the peak of the equivalent wavefield (the “arrival”) lies on a straight line whose slope depends on the equivalent velocity c , and hence the half-space conductivity, and which intersects the 0 offset axis at the 0 q origin.

This result motivates the development of a method for interpreting diffusive data based upon estimating the slopes and intersects of straight lines in common source gathers of the equivalent wavefield. Such a method would require first to recover the equivalent wavefield from the diffusive data, then to interpret the equivalent wavefield to estimate the equivalent velocity $c(\mathbf{x})$, from which a conductivity estimate can be directly calculated.

The action of the Q transform is to transform from an equivalent wavefield, which may contain discontinuities, to a diffusive field which is smooth. That is, it smoothes out irregularities. In reversing this action a small perturbation in the diffusive data, possibly caused by noise, is amplified greatly in the output equivalent wavefield. In this sense inverting the Q transform (also called diffusive to propagative mapping – DPM) is an inherently ill-posed problem (Oliver 1994).

Regularisation methods aim to modify ill-posed problems to find a nearby problem which is close to the original, but stable in the presence of noise. In this thesis it is demonstrated that the Q transform may be re-written as a convolution equation in logarithmic time. This is an original result derived independently but first published by Gershenson (1993). This formulation allows standard deconvolution techniques to be applied. More generally, discretising the Q transform yields a matrix equation, which can then be tackled using regularised matrix inversion techniques. In both cases the regularisation introduced to stabilise the solution method causes the numerically recovered equivalent wavefield to be a smoothed version of the “true” solution. This introduces a systematic error, or bias, in the estimate of equivalent velocity.

If a spiking filter is used to implement deconvolution in log time, then the resulting smoothing, or regularisation, of the numerically recovered wavefield can be analysed. When this analysis is combined with a known, analytically calculated, equivalent wavefield the regularisation of the numerically recovered equivalent wavefield can be predicted. This analysis is applied to the equivalent wavefield of a grounded horizontal electric current dipole source located at the surface of a uniform half-space for receivers located at the surface of the half-space. The predicted regularised equivalent waveform is in good agreement with that obtained numerically. This understanding of the systematic error introduced by regularisation enables calibration of DPM by numerical deconvolution in log time.

Numerical modelling studies using layered Earth models are used to investigate the feasibility of using multichannel, long-offset TEM surveys to detect and monitor hydrocarbon reservoirs. These studies indicate that when drawing an analogy between long-offset TEM surveying and the seismic method it is more appropriate to consider wide-angle, refraction seismic than near-offset, reflection seismic surveying.

Using the calibrated numerical calculation of DPM by deconvolution in log time, synthetic responses from simple layered Earth models are mapped to the equivalent wavefield domain and plotted as common source gathers. That is, the equivalent wavefield is plotted in a “wiggle trace” style as a function of the source-receiver-offset and q . Arrivals on these plots are interpreted using concepts from seismic refraction.

It is to be expected that field data will have an equivalent wavefield containing more than one arrival. The correct identification of several arrivals is recognised as a difficult problem (Slob *et al.* 1995). Some results have been shown here for the equivalent waveform above a half space. Assuming that these also hold for layered media, they have been applied to synthetics and found to enable useful interpretation of numerically recovered equivalent wavefields where more than one arrival is evident. It has been necessary to make this assumption because an analytic expression for the TEM response above a layered Earth is not known in the space-time domain.

Arrivals dominant at short offsets and intercepting the origin of the offset axis and the q axis are interpreted as the direct wave, travelling through the surface layer from the source to the receiver. Arrivals becoming dominant at longer offsets are interpreted to be from deeper layers. In the case of resistive layers, which have a high equivalent wavefield velocity, arrivals are observed which intercept the 0-offset axis at $q > 0$. These are interpreted as refracted arrivals.

Analysis of the equivalent wavefield in the q domain is helpful in producing novel analysis of multichannel transient electromagnetic responses and in giving insight through an analogy with seismic propagation. However it is not clear that the best way to apply the equivalent wavefield concept to processing and interpretation of field data is through DPM followed by interpretation of the equivalent wavefield in the q domain.

In this thesis the equivalent wavefield velocity is estimated from the slope of arrivals in the q domain, and from this resistivity is calculated directly. This approach exploits, indeed requires, multi-channel acquisition. As a possible basis for an interpretation method it is noteworthy for its simplicity and minimal computational expense, and because it does not employ an apparent resistivity transform, or iterative forward modelling.

A disadvantage of this approach is that, because the interpretation is performed on the equivalent wavefield in the q domain, it requires effective DPM. DPM is acknowledged to be a difficult problem. The DPM and interpretation methods presented here are simplistic, their sensitivity in the presence of noise has not been examined, nor have they been demonstrated

on field data.

A drawback of interpretation in the q domain is that the “wavelet” on each trace in a common source gather is expected to vary with offset. In the presence of noise it may be difficult to locate the precise position of the peak on each trace in the equivalent wavefield, and difficult in a common source gather of traces because of the trace-to-trace variation in the shape of the wavelet.

This thesis demonstrates a scaling relationship for the equivalent wavefield of a horizontal electric current dipole at the surface of a half space. To be specific, when plotted as a function of v , where $v = \ln(q)$, this equivalent wavefield has the same elemental wavelet at all receiver offsets (with a variation in amplitude and delay which is dependent upon offset from the source). This constant elemental wavelet is clear in Figure 7.3 as is the mapping between an arrival falling on the straight line $q = r/c$ and the line $v = \ln(r) - \ln(c)$ where, as before, r is offset and c is the equivalent wavefield velocity.

A constant elemental wavelet gives an advantage to interpreting the equivalent wavefield in the v domain, as opposed to the q domain. Arrival time as a function of offset could be estimated by normalised cross-correlation of the equivalent wavefield in the v domain. Resistivity would then be estimated from this function. This approach would be similar to the analysis used to find stacking velocities from reflection seismic data (Hatton, Worthington & Makin 1986, Section 3.3.6).

A scaling relationship also holds for $\mathbf{G}(\mathbf{x}, v)$, an intermediate quantity calculated directly from the diffusive data during DPM by deconvolution in log time. It may be possible to apply the analysis direct to $\mathbf{G}(\mathbf{x}, v)$, without concluding the DPM procedure. This would provide a interpretation procedure of minimal computational expense.

Bibliography

- Achenbach, J. D. (1973), *Wave propagation in elastic solids*, North-Holland.
- Adams, J. C. (1989), 'MUDPACK - multigrid portable fortran software for the efficient solution of linear elliptic partial-differential equations', *Applied Mathematics and Computation* **34**(2), 113–146.
- Aki & Richards (1980), *Quantitative seismology*, W. H. Freeman and Co.
- Alumbaugh, D., Becker, A., Deszcz-Pan, M., Lee, K. H., Morrison, H. F., Nichols, E. & Wilt, M. (1994), Cross borehole electromagnetic tomography, in 'SAGEEP Electromagnetic Workshop: Bridging the Gap Between Research and Practice'.
- Alumbaugh, D. L. & Morrison, H. F. (1995a), 'Monitoring subsurface changes over time with cross-well electromagnetic tomography', *Geophysical Prospecting* **43**(7), 873–902.
- Alumbaugh, D. L. & Morrison, H. F. (1995b), 'Theoretical and practical considerations for cross-well electromagnetic tomography assuming a cylindrical geometry', *Geophysics* **60**(3), 846–870.
- Becker, A., Das, K. K. & Lee, K. H. (1997), Validation of the EM wave field transform, in '59th EAGE Conference'. Abstract number F003.
- Becker, A., Lee, K. H. & Wang, Z. (1994), System design for acquisition of precise electromagnetic data, in '56th EAGE Conference'. Abstract number 1028.
- Bickel, S. H. (1993), 'Similarity and the inverse q filter: The pareto-levy stretch', *Geophysics* **58**(11), 1629–1633.
- Bradshaw, A. & Schleicher, K. (1980), 'Electrical conductivity of sea water', *IEEE J. Ocean. Eng.* **OE-5**, 50–62.
- Bragg, L. R. & Dettman, J. W. (1968a), 'Related partial differential equations and their applications', *SIAM journal on Applied Mathematics* **16**(3), 459–467.
- Bragg, L. R. & Dettman, J. W. (1968b), 'Related problems in partial differential equations', *Bull. Amer. Math. Soc.* **74**, 375–378.
- Bruce, R. A. A., Chapple, S., MacDonald, N. B., Trew, A. S. & Trewin, S. (1995), 'CHIMP and PUL: Support for portable parallel computing', *Journal of Future Generation Computer Systems*.
- Buselli, G. & O'Neill, B. (1977), 'SIROTEM: a new portable instrument for multichannel transient electromagnetic measurements', *Exploration Geophysics* **88**, 82–87.
- Butler, D. B. & Knight, R. J. (1995), 'The effect of steam quality on the electrical behavior of steam- flooded sands - a laboratory study', *Geophysics* **60**(4), 998–1006.
- Chang, S. K. & Anderson, B. (1984), 'Simulation of induction logging by the finite-element method', *Geophysics* **49**(11), 1943–1958.
- Cheesman, S. J., Edwards, R. N. & Law, L. K. (1990), 'A test of a short-base-line sea-floor transient electromagnetic system', *Geophysical Journal International* **103**(2), 431–437.

- Cole, J. H. (1997), 'The orbital vibrator, a new tool for characterising interwell reservoir space.', *Geophysics: The Leading Edge of Exploration* **10**(4), 21–27.
- Constable, S. C., Cox, C. S. & Chave, A. D. (1986), Offshore electromagnetic surveying techniques, in '56th Meeting, SEG', pp. 81–82. Abstract number EM3.1.
- Constable, S. C., Cox, C. S. & Chave, A. D. (1987), 'Offshore electromagnetic surveying techniques', *Geophysics* **52**(3), 385–385. Abstract from paper EM3.1 of the SEG annual meeting.
- Cooper, N. J. & Swift, R. (1994), 'The application of tem to cyprus-type massive sulfide exploration in cyprus', *Geophysics* **59**(2), 202–214.
- Côte, P., Degauque, P., Lagabrielle, R. & Levent, N. (1995), 'Detection of underground cavities with monofrequency electromagnetic tomography between boreholes in the frequency range 100 mhz to 1 ghz', *Geophysical Prospecting* **43**, 1083–1107.
- Cox, C. S., Constable, S. C., Chave, A. D. & Webb, S. C. (1986), 'Controlled-source electromagnetic sounding of the oceanic lithosphere', *Nature* **320**(6057), 52–54.
- Daily, W. & Ramirez, A. (1995), 'Electrical-resistance tomography during in-situ trichloroethylene remediation at the Savanna river site', *Journal of Applied Geophysics* **33**(4), 239–249.
- De Hoop, A. T. (1992), Transient electromagnetic and seismic prospecting – an analysis of their similarities, in '54th Meeting, EAGE', pp. 422–423. Abstract number GO12.
- De Hoop, A. T. (1996a), 'A general correspondence principle for time-domain electromagnetic wave and diffusion fields', *Geophysical Journal International* **127**(3), 757–761.
- De Hoop, A. T. (1996b), 'Transient electromagnetic vs. seismic prospecting – a correspondence principle', *Geophysical Prospecting* **44**, 987–995.
- Dobrin, M. B., & Savit, C. H. (1988), *Introduction to Geophysical Prospecting*, McGraw-Hill. ISBN 0-07-100404-1.
- Dongarra, J., Meuera, H. & Stromaier, E. (1995), 'Top500 supercomputer sites', <http://parallel.rz.uni-mannheim.de/top500.html>.
- Eadie, T. (1981), 'Detection of hydrocarbon accumulations by surface electrical methods: a feasibility study', *Research in Applied Geophysics*.
- Eaton, P. A. (1989), '3D electromagnetic inversion using integral-equations', *Geophysical Prospecting* **37**(4), 407–426.
- Edwards, R. N. & Cheesman, S. J. (1987), 'Two-dimensional modeling of a towed transient magnetic dipole-dipole sea-floor EM system', *Journal of Geophysics* **61**(2), 110–121.
- Erdélyi, A. (1954), *Tables of Integral Transforms*, McGraw-Hill. Vols No I and II.
- Evans, R., Cairns, G. & Edwards, R. (1993), 'A transient electromagnetic investigation of the TAG hydrothermal mound', *EOS* **74**, 99.
- Filatov, V. V. (1984), 'Construction of focusing transformations of transient electromagnetic fields', *Geol. i Geofiz. (Soviet Geology and Geophysics)* **25**(5), 89–95.
- Filipo, W. A. S., Eaton, P. A. & Hohmann, G. W. (1985), 'The transient EM response of a prism in a conductive half-space', *Geophysics* **50**(2), 272–272.
- Filippi, P. & Frisch, U. (1969a), 'Relation entre l'équation de la chaleur et l'équation des ondes de Helmholtz', *Comptes Rendus Acad. Sci.* **268**(A), 804–807.
- Filippi, P. & Frisch, U. (1969b), 'Relation entre l'équation de la chaleur et l'équation des ondes', in 'Deuxieme Colloque sur le traitement du signal et ses applications', pp. 159–174. In French.

- Flis, M. F., Newman, G. A. & Hohman, G. W. (1989), 'Induced-polarization effects in time-domain electromagnetic measurements.', *Geophysics* **54**, 514–523.
- Flynn, M. J. (1972), 'Some Computer Organisations and Their Effectiveness', *IEEE Transactions on Computers* **C-21**(9), 948–960.
- Gershenson, M. (1993), Simple interpretation of time-domain electromagnetic sounding using similarities between wave and diffusion propagation, in 'SEG Annual International Meeting 93', pp. 1342–1345. Extended Abstract number SS2.34.
- Gershenson, M. (1994), Electromagnetic sounding for seismologists with case history, in '64th SEG Annual International Meeting', pp. 354 – 356. expanded abstract number EM1.3.
- Gershenson, M. (1997), 'Simple interpretation of time-domain electromagnetic sounding using similarities between wave and diffusion propagation', *Geophysics* **62**(3), 763–774.
- Gibert, D. & Virieux, J. (1991), 'Electromagnetic imaging and simulated annealing', *Journal of Geophysical Research-Solid Earth And Planets* **96**(NB5), 8057–8067.
- Gibert, D., Tournerie, B. & Virieux, J. (1994), 'High-resolution electromagnetic imaging of the conductive earth interior', *Inverse problems*. In press.
- Goldman, M. M. & Stoyer, C. H. (1983), 'Finite-difference calculations of the transient field of an axially-symmetric earth for vertical magnetic dipole excitation', *Geophysics* **48**(7), 953–963.
- Goldman, M., Tabarovsky, L. & Rabinovich, M. (1994), 'On the influence of 3-D structures in the interpretation of transient electromagnetic sounding data', *Geophysics* **59**(6), 889–901.
- Gunderson, B. M., Newman, G. A. & Hohmann, G. W. (1986), '3-dimensional transient electromagnetic responses for a grounded source', *Geophysics* **51**(11), 2117–2130.
- Hansen, P. C. (1992), 'Numerical tools for analysis and solution of Fredholm integral equations', *Inverse Problems* **8**(6), 849–872.
- Hargreaves, N. D. (1996), Some geophysical consequences of fractal scaling, in '58th Meeting, EAEG'. Abstract number X025.
- Hatton, L., Worthington, W. M. & Makin, J. (1986), *Seismic Data Processing, theory and practice*, Blackwell Scientific Publications.
- Helwig, S., Hanstein, T. & Hördt, A. (1995), Cluster analysis and digital filtering of TEM, in '57th Meeting, EAEG'. Abstract number D050.
- Herzen, R. V., Francis, T. & Becker, K. (1983), 'Insitu large-scale electrical-resistivity of ocean crust, hole-504b', *Initial Reports of the Deep Sea Drilling Project* **69**(MAY), 237–244.
- Hobbs, B. A. (1992), 'Terminology and symbols for use in studies of electromagnetic induction in the earth', *Surveys in Geophysics* **13**, 489–515.
- Hofmann, B. (1986), *Regularization for Applied Inverse and Ill-Posed Problems*, Teubner.
- Hördt, A., Druskin, V. L., Knizhnerman, L. A. & Strack, K. M. (1992), 'Interpretation of 3-D effects in long-offset transient electromagnetic (LOTEM) soundings in the Munsterland area Germany', *Geophysics* **57**(9), 1127–1137.
- Hördt, A., Vozoff, K. & Neubauer, F. M. (1995), Multichannel transient electromagnetics for underground gas storage monitoring, in '57th Meeting, EAEG'. Abstract number D051.
- Jones, A. G. (1987), 'MT and reflection: an essential combination', *Geophys. J. Roy. Astr. Soc.* **89**, 7–18.
- Journal of Geomagnetism and Geoelectricity (1993), *Special Issue on EM Induction in the Earth*, Vol. 45, Terra Scientific Publishing Co. 9.

- Jupp, D. L. B. & Vozoff, K. (1975), 'Stable iterative methods for the inversion of geophysical data', *Geophysical Journal Roy. Astr. Soc.* **42**, 957–976.
- Kaufman, A. A. & Keller, G. V. (1983), *Frequency and transient soundings*, Elsevier.
- Keller, G. V. (1968), 'Electrical prospecting for oil', *Quarterly of the Colorado School of Mines*.
- Keller, G. V. (1987), Rock and mineral properties, in M. N. Nabighian, ed., 'Electromagnetic Methods in Applied Geophysics', Investigations in Geophysics, SEG, pp. 13–51. Volume I, Theory.
- Knight, J. H. & Raiche, A. P. (1982), 'Transient electromagnetic calculations using the gaver-stehfest inverse laplace transform method', *Geophysics* **47**(1), 47–50.
- Kress, R. (1989), *Linear Integral Equations*, Springer-Verlag.
- Lavrent'ev, M. M., Romanov, V. G. & Shishatskii, S. P. (1980), 'Ill-posed problems of mathematical physics and analysis', *Nauka*.
- Lee, K. H. (1988), A new approach to interpreting electromagnetic-sounding data, Technical report, Lawrence Berkeley Laboratory. Annual report 1988, LBL-26362.
- Lee, K. H. & Xie, G. Q. (1993), 'A new approach to imaging with low-frequency electromagnetic fields', *Geophysics* **58**(6), 780–796.
- Lee, K. H., Liu, G. & Morrison, H. F. (1989), 'A new approach to modeling the electromagnetic response of conductive media', *Geophysics* **54**(9), 1180–1192.
- Lee, K. H., Xie, G., Hoversten, G. M. & Pellerin, L. (1995), Electromagnetic imaging for environmental site characterization, in 'International Symposium on Three-Dimensional Electromagnetics'.
- Lee, S., McMechan, G. A. & Aiken, C. L. V. (1987), 'Phase-field imaging: the electromagnetic equivalent of seismic migration', *Geophysics* **52**(5), 678–693.
- Levy, S., Oldenburg, D. & Wang, J. (1988), 'Subsurface imaging using magnetotelluric data', *Geophysics* **53**, 104–117.
- Lines, L. R. & Treitel, S. (1984), 'Tutorial, a review of least-squares inversion and its application to geophysical problems', *Geophysical Prospecting* **32**, 159–186.
- Liu, E., Crampin, S. & Queen, J. H. (1991), 'Fracture detection using crosshole surveys and reverse vertical seismic profiles at the Conoco borehole test facility, Oklahoma', *Geophysical Journal International* **107**(3), 449–463.
- Liu, Q. H. (1993), 'Electromagnetic-field generated by an off-axis source in a cylindrically layered medium with an arbitrary number of horizontal discontinuities', *Geophysics* **58**(5), 616–625.
- Mandelis, A. (1991), 'Theory of photothermal wave diffraction tomography via spatial Laplace spectral decomposition', *J. Phys. A: Math. Gen.* **24**, 2485–2505.
- Nagy, Z. (1992), Advances in the integrated interpretation of seismics with magnetotellurics (illustrated by practical examples from the Pannonian basin in Hungary), in '54th Meeting, EAEG', pp. 420–421. Abstract number GO11.
- Nekut, A. G. (1994), 'Electromagnetic ray-trace tomography', *Geophysics* **59**(3), 371–377.
- Nekut, A. G. (1995), 'Crosswell electromagnetic tomography in steel-cased wells', *Geophysics* **60**(3), 912–920.
- Nekut, A. G. & Eaton, P. A. (1990), Effect of pipelines on EM soundings, in '60th SEG Annual International Meeting', pp. 491–494. expanded abstracts.

- Nelson, P. H. & Johnston, D. (1994), 'Geophysical and geochemical logs from a copper-oxide deposit, Santa-Cruz project, Casa-Grande, Arizona', *Geophysics* **59**(12), 1827–1838.
- Newman, G. & Alumbaugh, D. (1996), 3-D electromagnetic modeling and inversion on massively parallel computers, *in* 'Three-Dimensional Electromagnetics', SEG. Preprint.
- Newman, G. A. (1989), 'Deep transient electromagnetic soundings with a grounded source over near-surface conductors', *Geophysical Journal International* **98**(3), 587–601.
- Newman, G. A. & Alumbaugh, D. L. (1995), 3D massively parallel electromagnetic inversion, *in* 'International Symposium on Three-Dimensional Electromagnetics', pp. 287–296.
- Newman, G. A. & Hohmann, G. W. (1985), 'Time-domain EM response of a 3-d body in a layered earth', *Geophysics* **50**(2), 272–272.
- Newman, G. A., Hohmann, G. W. & Anderson, W. L. (1986), 'Transient electromagnetic response of a three-dimensional body in a layered earth', *Geophysics* **51**(8), 1608–1627.
- Nicol, D. & Saltz, J. (1990), 'An analysis of scattered decomposition', *IEEE Transactions on Computers* **39**(11), 1337–1345.
- Nye, J. F. (1957), *Physical properties of crystals*, Oxford.
- Oliver, D. (1994), 'Application of a wave transform to pressure transient testing in porous media', *Transport in Porous Media* **16**(3), 209–236.
- Orsinger, A. & Nostrand, R. V. (1954), 'A field evaluation of the electromagnetic reflection method', *Geophysics* **19**, 478–489.
- Pai, D. M., Ahmad, J. & Kennedy, W. D. (1993), '2-dimensional induction log modeling using a coupled-mode, multiple- reflection series method', *Geophysics* **58**(4), 466–474.
- Qian, W. (1994), 'On small-scale near-surface distortion in controlled-source tensor electromagnetics', *Geophysical Prospecting* **42**(5), 501–520.
- Qian, W. & Boerner, D. E. (1995), 'Electromagnetic modelling of buried line conductors using an integral equation', *GJI* **121**, 203–214.
- Robinson, E. A. & Treitel, S. (1980), *Geophysical Signal Analysis*, Prentice-Hall.
- Sakashita, S. & Shima, H. (1993), Controlled source magnetic susceptibility tomography using crosshole data: A numerical evaluation, *in* '63rd SEG Annual International Meeting'. expanded abstracts.
- Sakashita, S., Shima, H. & Gasnier, S. (1994), Controlled source EM tomography – an improved imaging technique for magnetic susceptibility and resistivity, *in* '56th Meeting, EAEG'. Abstract number IO27.
- Salmon, J. (January 1988), A mathematical analysis of the scattered decomposition, *in* 'The third Conference on Hypercube Concurrent Computers and Applications', Vol. 1, ACM Press, pp. 239–284.
- Schenkel, C. J. & Morrison, H. F. (1994), 'Electrical-resistivity measurement through metal casing', *Geophysics* **59**(7), 1072–1082.
- Schnegg, P. A. & Sommaruga, A. (1995), 'Constraining seismic parameters with a CSAMT method.', *Geophysical Journal International* **122**(1), 152–160.
- Schouten, J. P. (1935), 'A new theorem in operational calculus together with an application of it', *Physica* **2**, 75–80.
- Sena, A. G. & Toksoz, M. N. (1990), 'Simultaneous reconstruction of permittivity and conductivity for crosshole geometries', *Geophysics* **55**(10), 1302–1311.

- Sheriff, R. E. (1984), *Encyclopedic Dictionary of Exploration Geophysics*, Society of Exploration Geophysics.
- Slob, E. (1994), Scattering of Transient Diffusive Electromagnetic Fields, PhD thesis, TU Delft.
- Slob, E., Habashy, T. M. & Torres-Verdin, C. (1995), A new stable numerical procedure for computing the Q-transform of TEM data, in '57th Meeting, EAEG'. Extended Abstract number D053.
- Spies, B. R. (1989), 'Depth of investigation in electromagnetic sounding methods', *Geophysics* **54**(7), 872–888.
- Spies, B. R. & Greaves, R. J. (1991), 'Numerical modeling of surface-to-borehole electromagnetic surveys for monitoring thermal enhanced oil-recovery', *Geoexploration* **28**(3-4), 293–311.
- Stehfest, H. (1970), 'Algorithm 368, numerical inversion of laplace transforms', *Communications of the ACM* **13**, 47–49.
- Strack, K. M. (1992), *Exploration with Deep Transient Electromagnetics*, number 30 in 'Methods in Geochemistry and Geophysics', Elsevier.
- Strack, K. M. & Vozoff, K. (1992), Integrating long-offset transient electromagnetics (LOTEM) with seismic in an exploration environment, in '54th Meeting, EAEG', pp. 426–427. Abstract number G014.
- Strack, K. M., Hanstein, T., Brocq, K. L., Moss, D. C., Vozoff, K. & Wolfgram, P. A. (1989), 'Case histories of LOTEM surveys in hydrocarbon prospective areas', *First Break* **7**(12), 467–477.
- Strack, K. M., Hördt, A., Vozoff, K. & Wolfgram, P. A. (1991), 'Integrated electromagnetic and seismic methods for petroleum exploration', *Exploration Geophysics* **22**, 375–378.
- Sumner, J. S. (1985), *Principles of Induced Polarization for Geophysical Exploration*, Elsevier.
- Szarka, L. & Nagy, Z. (1992), 'A possibility of an electromagnetic technique to locate oil reservoir boundaries on basis of analogue modeling experiments', *Acta Geod. Geoph. Mont. Hung.* **27**(1), 131–138.
- Szarka, L., Nagy, Z. & Szala, S. (1994), 3D CSAMT analogue modelling studies, in '56th Meeting, EAEG'. Abstract number P121.
- Tournerie, B. & Gibert, D. (1995), 'Inversion of the COPROD2 magnetotelluric data using a diffusive-to-propagative mapping (DPM)', *Geophysical Research Letters* **22**(16), 2187–2190.
- Vaughan, P. J., Udell, K. S. & Wilt, M. J. (1993), 'The effects of steam injection on the electrical-conductivity of an unconsolidated sand saturated with a salt solution', *Journal of Geophysical Research-Solid Earth* **98**(B1), 509–518.
- Velikov, Y. P., Zhdanov, M. S. & Frenkel, M. A. (1987), 'Interpretation of MHD-sounding data from the Kola Peninsula by the electromagnetic migration method', *Physics of the Earth And Planetary Interiors* **45**, 149–160.
- Villinger, H. (1985), 'Solving cylindrical geothermal problems using the gaver-stehfest inverse laplace transform', *Geophysics* **50**(10), 1581–1587.
- Vozoff, K. & Jupp, D. L. B. (1975), 'Joint inversion of geophysical data', *Geophysical Journal Roy. Astr. Soc.* **42**, 977–991.
- Walker, P. W. & Groom, R. W. (1995), The importance of correctly formulating inductive and galvanic scattering in EM simulation, in '57th Meeting, EAEG'. Abstract number D049.

- Ward, S. H. & Hohmann, G. W. (1987), Electromagnetic theory for geophysical applications, in M. N. Nabighian, ed., 'Electromagnetic Methods in Applied Geophysics', Investigations in Geophysics, SEG, pp. 131–311. Volume I, Theory.
- Warren, R. K. (1996), 'A few case histories of subsurface imaging with emap as an aid to seismic processing and interpretation', *Geophysical Prospecting* **44**(6), 923–934.
- Wayland, J. R., Lee, D. O. & Cabe, T. J. (1985), 'Mapping of a steamflood in a Utah tar sand by controlled source audio magnetotelluric survey', *In Situ* **9**(1), 53–73.
- Wayland, J. R., Lee, D. O. & Cabe, T. J. (1987), 'CSAMT mapping of a Utah tar sand steamflood', *Journal of Petroleum Technology* **39**(3), 345–352.
- Webb, S., Edwards, R. & Yu, L. (1993), 'First measurement from a deep-tow transient electromagnetic sounding system', *Marine Geophysical Research* **15**, 13–26.
- Weidelt, P. (1972), 'The inverse problem of geomagnetic induction', *Zeit. fur Geophysik* **38**, 257–289.
- Weir, G. (1980), 'Transient electromagnetic fields about an infinitesimally long grounded horizontal electric dipole on the surface of a uniform half-space', *Geophys. J. Roy. Astr. Soc.* **61**, 41–56.
- West, G. F., Macnae, J. C. & Lamontagne, Y. (1984), 'A time-domain EM system measuring the step response of the ground', *Geophysics* **49**(7), 1010–1026.
- Wilson, A. J. S. (1994), Seismic processing of multichannel transient electromagnetic data, in '56th Meeting, EAGE'. Abstract number P123.
- Wilson, A. J. S., Mills, J. G. & Norman, M. G. (1991), *Bodyscan*: A transputer based 3D image analysis package, in 'Applications of Transputers 3', Vol. 2, IOS, pp. 130–135.
- Wilson, A. J. S., Ziolkowski, A., Hobbs, B. & Sharrock, D. (1995), Time-lapse EM, in 'International Symposium on 3D Electromagnetics'.
- Wilt, M. J., Alumbaugh, D. L., Morrison, H. F., Becker, A., Lee, K. H. & Deszczpan, M. (1995), 'Crosswell electromagnetic tomography - system-design considerations and field results', *Geophysics* **60**(3), 871–885.
- Wilt, M., Morrison, H. F., Becker, A., Teng, H. W., Lee, K. H., Torres-Verdin, C. & Alumbaugh, D. (1995), 'Crosshole electromagnetic tomography: A new technology for oil field characterization', *Geophysics: The Leading Edge of Exploration* **14**(3), 173–177.
- Withers, R., Eggers, D., Fox, T. & Crebs, T. (1994), 'A case-study of integrated hydrocarbon exploration through basalt', *Geophysics* **59**(11), 1666–1679.
- Wu, X. & Habashy, T. M. (1994), 'Influence of steel casings on electromagnetic signals', *Geophysics* **59**(3), 378–390.
- Yan, L., Su, Z. & Hu, J. H. W. (1997), 'Field trials of lotem in a very rugged area', *Geophysics: The Leading Edge of Exploration* **16**(4), 379–380.
- Yost, W. J. (1952), 'The interpretation of electromagnetic reflection data in geophysical exploration – Part I: general theory oscillating dipole', *Geophysics* **17**, 89–106.
- Yost, W. J., Caldwell, R. L., Beor, C. L., McChere, C. D. & Skomal, E. N. (1952), 'The interpretation of electromagnetic reflection data in geophysical exploration – Part II: metallic model experiments', *Geophysics* **17**, 806–826.
- Yu, L. & Edwards, R. (1992), 'The detection of lateral anisotropy of the ocean floor by electromagnetic methods', *Geophysical Journal International* **108**, 433–441.

- Zhdanov, M. S. & Frenkel, M. A. (1983), 'The solution of the inverse problems on the basis of the analytical continuation of the transient electromagnetic field in reverse time.', *Journal of Geomagn. Geoelectr.* **35**, 747–765.
- Zhdanov, M. S. & Frenkel, M. A. (1988), 'Phase-field imaging - the electromagnetic equivalent of seismic migration - discussion', *Geophysics* **53**(6), 863.
- Zhdanov, M. S. & Keller, G. V. (1994), *The Geoelectrical Methods in Geophysical Exploration*, number 31 in 'Methods in Geochemistry and Geophysics', Elsevier.
- Zhdanov, M. S., Traynin, P. & Portniaguine, O. (1994), Migration and analytic continuation in geoelectric imaging, in '64th SEG Annual International Meeting', pp. 357 – 360. expanded abstract number EM1.4.
- Zhdanov, M., Traynin, P. & Booker, J. (1996), 'Underground imaging by frequency-domain electromagnetic migration', *Geophysics* **61**(3), 666–682.
- Ziolkowski, A. (1987), 'The determination of the far-field signature of an interacting array of marine seismic sources from near-field measurements — results from the Delft Air Gun Experiment', *First Break* **5**(1), 15–29.
- Ziolkowski, A. M. (1993), 'Personal communication'.
- Ziolkowski, A. M., Hobbs, B., Chisholm, I., Wilson, A. J. S., Sharrock, D., Rüter, H., Hördt, A., Neubauer, F., Vozoff, K., Helwig, S. & Andrieux, P. (1996), Time-lapse multichannel transient electromagnetic experiment over an underground gas storage reservoir in france, in '5th European Union Hydrocarbons Conference'.
- Ziolkowski, A. M., Peet, W., Strack, K. M., Andrieux, P. & Vozoff, K. (1992), Structure, stratigraphy, fluid content and field procedures for seismic and EM, in '54th Meeting, EAEG', pp. 424–425. Abstract number GO13.
- Zorgati, R., Duchene, B., Lesselier, D. & Pons, F. (1991), 'Eddy-current testing of anomalies in conductive materials (I) qualitative imaging via diffraction tomography techniques', *IEEE Transactions On Magnetism* **27**(6), 4416–4437.
- Zorgati, R., Lesselier, D., Duchene, B. & Pons, F. (1992), 'Eddy-current testing of anomalies in conductive materials, (II) quantitative imaging via deterministic and stochastic inversion techniques', *IEEE Transactions on Magnetism* **28**(3), 1850–1862.
- Zou, Z. (1993), The Cylindrical Bender Source in a Fluid-Filled Borehole, PhD thesis, TU Delft.

Appendix A

Time-Lapse Electromagnetics

A.J.S.Wilson, A.M.Ziolkowski, B.A.Hobbs and D.S.Sharrock

Reprinted, with permission, from proceedings of the
International Symposium on 3D Electromagnetics
held at Schlumberger-Doll Research, Ridgefield, Connecticut, USA.
October 1995.

Time-Lapse EM

Andrew J S Wilson, Anton Ziolkowski, Bruce A Hobbs and Dave S Sharrock

*Department of Geology and Geophysics,
University of Edinburgh, The Kings Buildings, Edinburgh EH9 3JW, UK.
Email Andrew.J.S.Wilson@ed.ac.uk, Telephone +44 131 650 8533,
Fax +44 131 668 3184, URL <http://www.glg.ed.ac.uk/ajsw>.*

Abstract

Seismic reflection is the premier geophysical method for determining structure in sedimentary basins and the dominant geophysical exploration method for hydrocarbon prospecting. The seismic method is directly sensitive to velocity and density contrasts but only indirectly sensitive to changes in porosity and pore fluid content, and such variations are poorly resolved with seismic. Electromagnetic (EM) prospecting is directly sensitive to contrasts in bulk resistivity due to, for example, a change in pore fluid from brine to oil. This suggests that EM methods can be used in addition to seismic and other geophysical measurements to determine the fluid content within a reservoir and thus map the hydrocarbon reserves.

This proposition is being tested at an underground gas-storage site in France. During the summer gas is pumped into an underground sandstone reservoir. Gas reserves peak in autumn and are then depleted during winter as the rate at which the gas is consumed exceeds the rate of supply. Reserves reach a minimum in spring, the space formerly occupied by gas being replaced by natural salt water in the reservoir. The primary objective of the experiment is to demonstrate that changes in the reservoir can be monitored using repeated surface electromagnetic surveys, which we call the *time-lapse EM* method. The aim is to perform two surveys over the reservoir and map in space the changes in resistivity observed between the two surveys. These should occur mainly in the reservoir rock and should be related directly to the movement of the gas-water interface, which can also be measured directly in control boreholes.

In order to map the movement of the gas-water interface, two surveys are being collected using the latest generation of multichannel transient electromagnetic acquisition systems. 3D modelling indicates that the difference between the two data sets should be of the order of 5% over an appropriate time/offset range. We believe it is possible to obtain repeatable measurements with less than 1% noise. This means that this effect is detectable and that it will be possible to obtain a reasonable resolution of the gas movement.

The first survey, conducted in September/October 1994, yielded unprecedented production levels, data coverage and data volumes for an EM survey — in total 4.5 GBytes of data were collected. Traditional interpretation approaches, based on inverse modelling, struggle with such large data sets. We have decided to transform our EM data to a form that allows us to manipulate and process it as if it were seismic data — thus taking advantage of extremely well developed seismic data processing packages. One such approach is to use the wave transform.

The wave transform relates the response of a diffusive medium to the response of an equivalent wave propagation medium. Wave transform inversion of transient EM data recovers an equivalent wavefield to which seismic data processing systems may be applied to process and interpret the data, making best use of the dense spatial coverage. This is illustrated for one common source gather.

A warm winter resulting in reduced gas demand meant that the reservoir was still full at the time of the planned return to the site in spring 1995. With the kind permission and support of the sponsors the project time-scale has been extended, and the second survey is now planned for spring 1996. We expect at the conclusion of this experiment to demonstrate that time-lapse EM surveying will allow the movement of fluids in reservoirs to be monitored.

1 Introduction

The development of a new exploration geophysics methodology begins with the identification and description of a geological target and investigation of its geophysical response. Then follows the development of an innovative surveying method including construction of apparatus and procedure for acquiring data, and theory and procedure necessary for processing and interpreting the data. Proving the worth of the new methodology requires the measurement of data in the field and interpretation to a geological model.

The University of Edinburgh, in collaboration with The University of Cologne, Deutsche Montan-Technologie (DMT), and Compagnie Générale de Géophysique has a European Commission THERMIE project entitled *Delineation and Monitoring of Oil Reservoirs using Seismic and Electromagnetic Methods* (Contract Number OG/0305/92/NL-UK). This project is primarily concerned with the development of an exploration methodology which may be routinely used to detect and monitor financially recoverable hydrocarbon reservoirs directly using multichannel transient electromagnetics (MTEM) in combination with complementary data sets such as well logs and exploration seismology. This paper reports progress towards proving this new methodology.

Reflection seismology is the single most effective tool for mapping subsurface structures in sedimentary basins, including salt domes, folds and basement highs. Such structures can control the location of hydrocarbon accumulations and consequently reflection seismology is the dominant geophysical method for hydrocarbon exploration.

The seismic method is directly sensitive to velocity and density contrasts but only indirectly sensitive to changes in porosity and pore fluid, and such variations are poorly resolved by seismic data. Seismic reflection has a proven track record in mapping structure, but has not had great success in direct hydrocarbon detection, except in identifying gas in certain special environments (for example, by “bright spots” and by AVO anomalies.)

Electromagnetic (EM) methods are sensitive to variations in bulk resistivity due to, for example, variations in lithology, porosity or pore fluid. EM prospecting, being a diffusive process, lacks the intrinsic resolution of the seismic method and is typically not used beyond initial, large scale, exploration, if at all.

Despite these difficulties EM methods do have an ability which makes them attractive for hydrocarbon exploration. The seismic method is generally poor at determining fluid content because there is very little acoustic contrast between rock saturated with oil and rock saturated with water. Well logs and laboratory studies show that electrical conductivity can vary enormously within a porous medium, depending on both the porosity and the fluid content. Salt water is much more conductive than oil or gas. The direct sensitivity of EM methods to variations in porosity and pore fluid is a property, not possessed by the seismic method, which offers the possibility of the direct detection of resistivity anomalies associated with hydrocarbon reservoirs.

Interest in using electrical and electromagnetic methods for direct hydrocarbon detection has long existed (Keller 1968). Model studies conclude that both controlled source and natural source surface EM methods have the potential to detect financially recoverable hydrocarbon reservoirs at moderate depths. Monitoring small variations in reservoir properties during production of hydrocarbons is a more difficult task. The development of such an EM methodology has been made possible by advances in EM acquisition, processing and interpretation technology.

Dense galvanic controlled source measurements are the most promising surface EM methods with which to tackle the problem. Modelling shows that it should be feasible to monitor shallow variations in reservoir properties during the production of hydrocarbons, either from a new field or from an underground gas storage reservoir provided repeatable measurements with less than 1% noise can be made (Hördt et al. 1995). Multichannel acquisition systems originally developed for use in exploration seismology have been adapted for use in MTEM surveys and it is now possible to collect much larger amounts of data than ever before. Improved instrumentation also allows acquisition

configurations which were not previously possible. Techniques for improving signal-to-noise ratio allow surveying in areas where noise levels would have previously rendered data un-interpretable.

A first field season with the new TEAMEX MTEM system has acquired high quality data at an underground gas-storage site in France. We believe it is possible to obtain repeatable measurements with less than 1% noise. This means that changes in bulk resistivity due to movement of the gas-water contact are detectable and that it will be possible to obtain a reasonable resolution of the gas movement. The final step in the proving of this new methodology will be the acquisition of a second survey over our field site and subsequent processing to image resistivity changes, finally yielding a geological interpretation.

Previous data processing and interpretation leant heavily on inverse modelling which, for 2D and 3D models, is difficult and computationally expensive. Wave transform inversion allows calculation of an equivalent wavefield from diffusive transients. The equivalent wavefield may then be processed and interpreted using seismic techniques. This avoids the need for inverse modelling.

The remainder of this paper describes our experiment, beginning with the MTEM acquisition methodology and the TEAMEX MTEM acquisition system. The results of some feasibility studies of our target are then outlined. The experience of the first field survey, including field parameters, production rates, data quality and pre-processing are discussed in some detail. New data processing methodologies being developed to process these unusually large, high quality, and dense data sets are then introduced and conclusions are drawn.

2 MTEM Acquisition with the TEAMEX System

The TEAMEX system for MTEM sounding (Figure 1) was developed by DMT, based on their SEAMEX system for seismic exploration. Many TEAMEX receivers can be linked together in a spread. Each receiver converts analogue signals for digital transmission to a central PC which controls the action of the entire spread. This new technology greatly speeds the data acquisition process. This allows many more transmitter locations to be occupied than was previously economically feasible, resulting in a dramatic increase in the spatial density of data collected. The increased dynamic range of the TEAMEX receiver units also allow data to be recorded at much nearer offsets than was previously possible. Synchronisation between the transmitter and receiver systems can be achieved using high precision clocks. This removes the necessity for a physical connection or line-of-sight between the transmitter and receiver crews.



Figure 1: TEAMEX receiver unit installation.

A typical 2D acquisition configuration is schematically presented in Figure 2. The transmitter and receivers are laid out along a line over the target. Each TEAMEX receiver unit measures E_x , the horizontal component of the electric field parallel to the transmitter orientation, and one additional component, which is alternately the horizontal component of the electric field perpendicular to the transmitter orientation or the rate of change with respect to time of the vertical component of the magnetic field, denoted dH_z/dt . A bipolar transmitter current wave form $I(t)$ is employed, which induces transient EM signals whose decay reveals the subsurface resistivity structure.

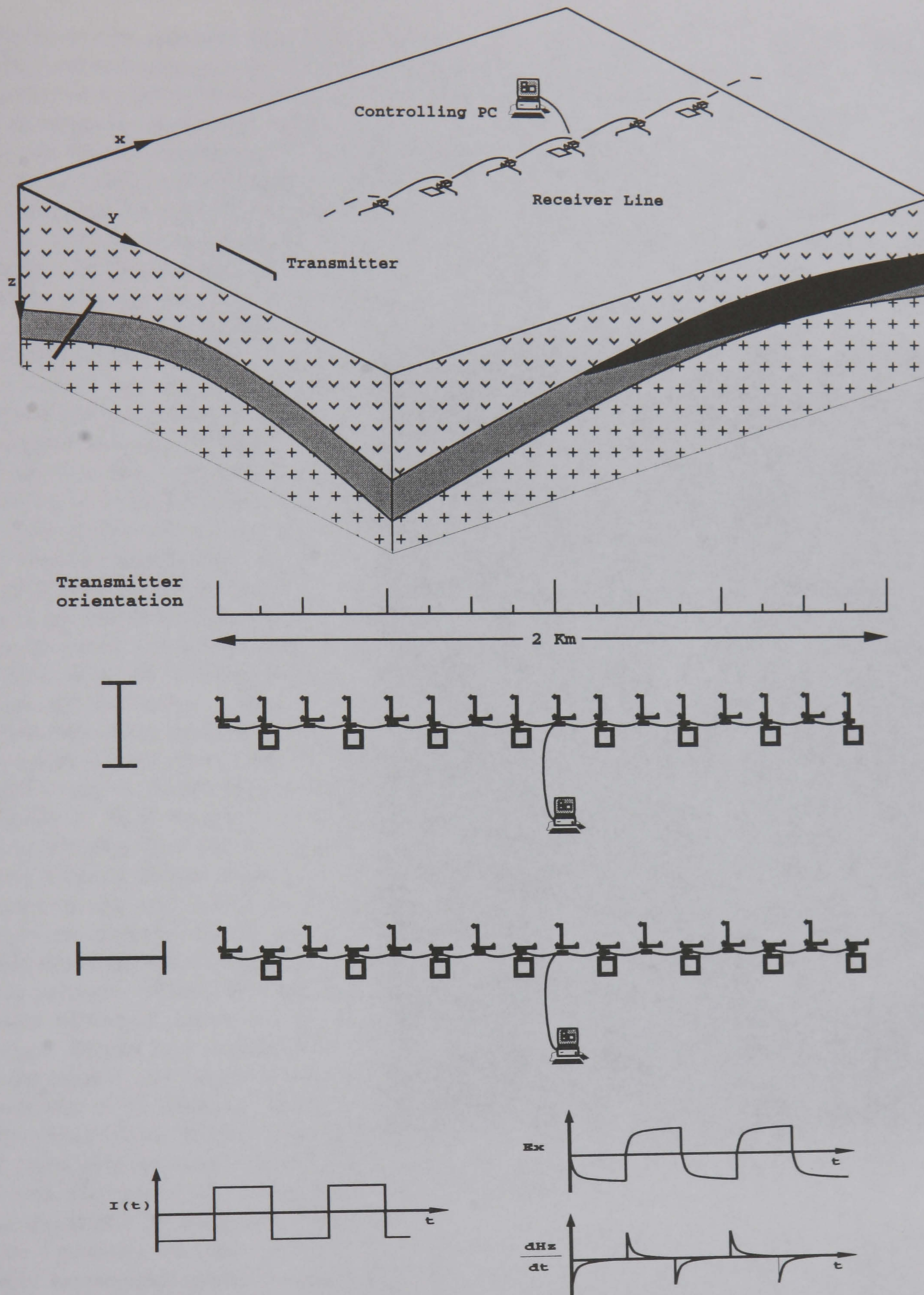


Figure 2: Surface to surface MTEM data acquisition configuration.

3 Feasibility Studies

Model studies conclude that both controlled source (Hördt et al 1995) and natural source (Eadie 1981) surface EM methods have the potential to detect financially recoverable hydrocarbon reservoirs at moderate depths. Monitoring small variations in reservoir properties during production of hydrocarbons is a more difficult task. Eadie (1981) and Kaufman and Keller (1983) develop theory indicating that for the surface-to-surface acquisition configuration resistive units, such as hydrocarbons, are best resolved by MTEM methods with galvanic sources. That is, sources which couple galvanically with the Earth resulting in significant vertical current flow. Accordingly a grounded electric bipole source is employed.

Modelling the response of layered Earth models can determine the magnitude of the geophysical response to a geological anomaly of infinite extent. This allows a first estimate of the detectability of a resistivity anomaly due to a large hydrocarbon reservoir. Table 1 lists the depths and resistivities for 1D Earth model H which represents a gas saturated reservoir. This model is based upon well logs from the field area, an underground gas-storage site in France. The anticlinal structure of the reservoir is known from sparse seismic data and over 40 boreholes and is shown schematically in Figure 3. It is known from borehole monitoring that the reservoir is "open" allowing the gas-water contact to move up-dip and down-dip as gas reserves are depleted during the winter and then replenished during the following summer. Model W represents a water saturated reservoir and has the same depths and resistivities except for layer 5, the target, which has a resistivity of 10 Ohm m. Synthetic in-line dipole-dipole MTEM responses were calculated for cases without (W) and with (H) gas in the target layer using the MODALL program (Strack 1992).

Figure 4 presents the ratio of in-line Ex components for models H and W as a contour plot. At optimal transmitter-receiver configurations the ratio between responses with and without the hydrocarbon bearing layer can be as much as 50% for a fully saturated target layer of 30 m thickness.

The response due to a reservoir of finite extent is, of course, smaller. Variations in the saturation or areal extent of a finite reservoir will have a response which is smaller still. Careful 3D modelling of the project field area indicates that the response due to expected seasonal variations in the volume

layer	depth (m)	resistivity (Ohm m)
1	0-140	50
2	140-160	15
3	160-310	50
4	310-490	10
5	490-520	200
6	520-	10

Table 1: Layer depths and resistivities for model H.

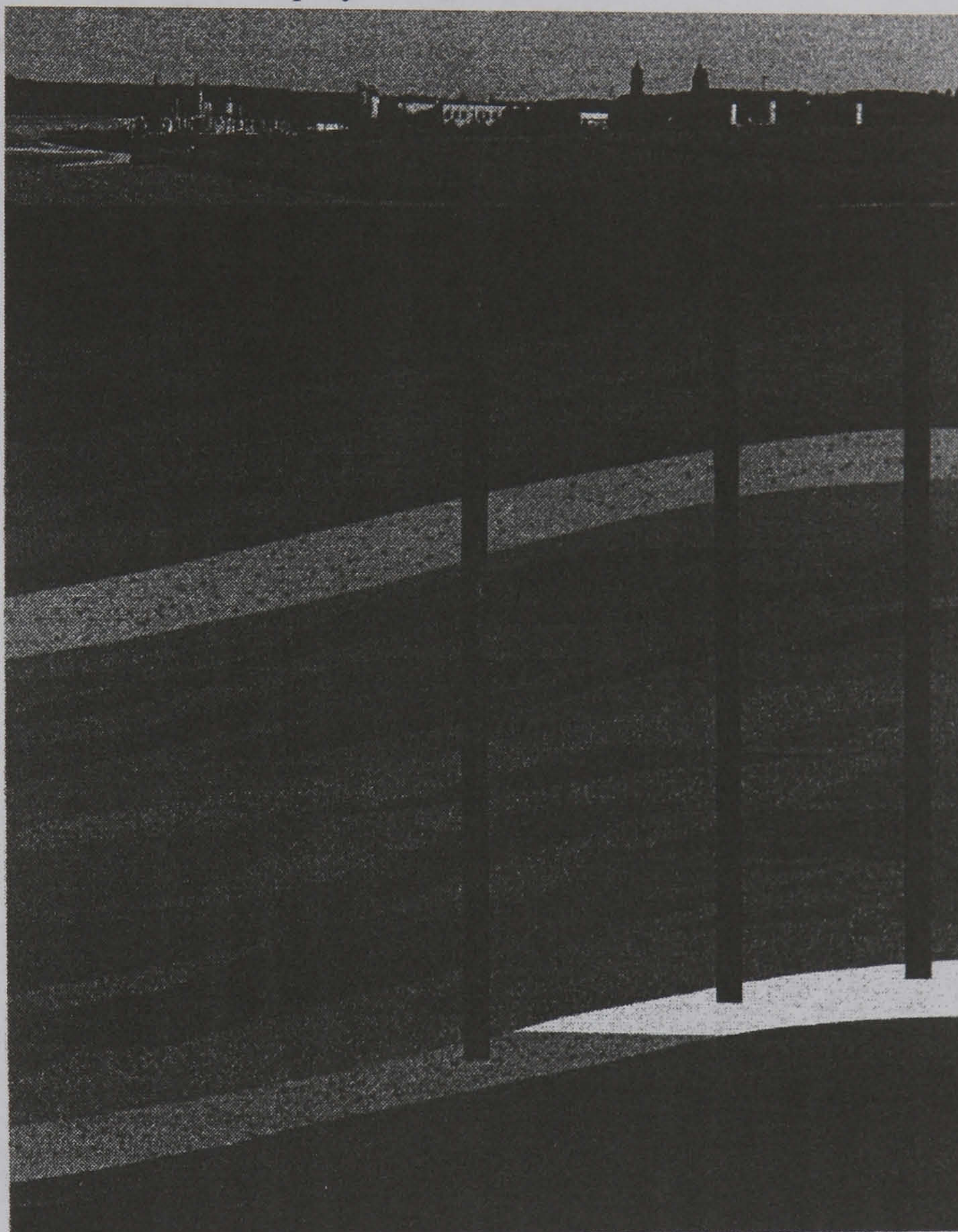


Figure 3: Anticlinal structure of field site showing wells used for injection, production and monitoring of gas in the reservoir. After Gaz de France illustration.

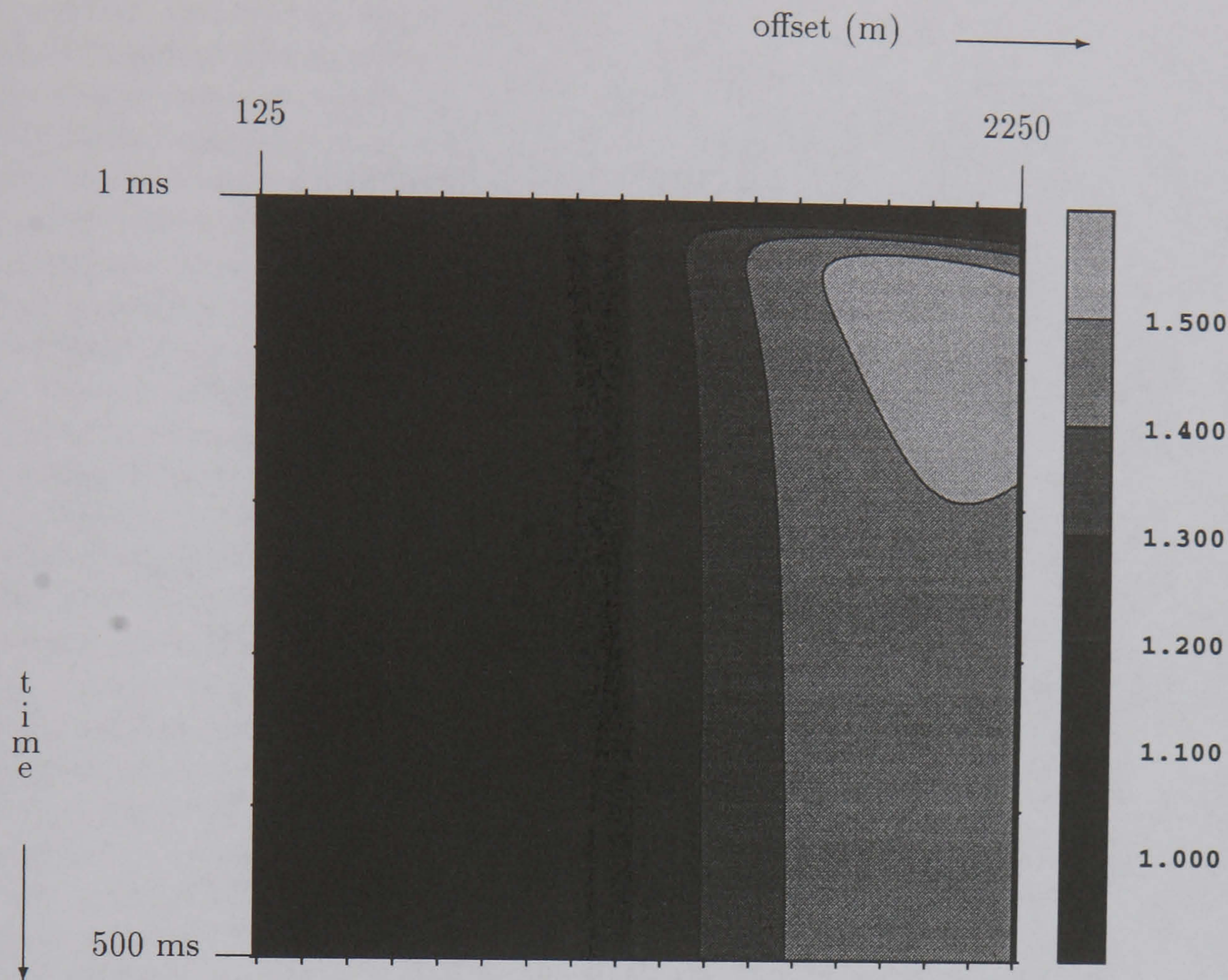


Figure 4: The ratio of in-line Ex components for models H and W presented as a contour plot. Receivers are plotted against time with receiver offset increasing from left to right and time increasing down the page. Receiver offsets varies from 125 m to 2250 m in intervals of 125 m, while the time range is from 1 ms to 500 ms in intervals of 1 ms.

of gas stored will be around 5% (Hördt et al. 1995). Although the response will be small it will retain a characteristic spatial variation and should be detectable provided that good data can be acquired with an uncertainty less than, say, 1%.

4 Field Acquisition, Data Pre-processing and Data Quality

The first field campaign was conducted in 3 weeks over September/October 1994. The acquisition was performed by Compagnie Générale de Géophysique and their sub-contractors, including HarbourDom Consulting GmbH, to a specification drawn up by the project partners.

Acquisition focused on a single profile over the target. Two receiver spreads were employed, lying contiguous to give continuous receiver coverage over the centre 4 km of the profile. 19 TEAMEX receiver units were taken to the field. At any one time up to 16 units were in use, with the remainder being held in reserve in case of failure. The receiver unit spacing in each spread was 125 m, giving an individual spread length of 2 km. Each receiver unit measured two channels. Telluric channels employed receiver dipoles of 125 m length and copper/copper-sulphate electrodes, while 50 m square

loops of modified multi-core seismic cable were laid flat on the ground to record magnetic fields. Each receiver unit records two transients every time the bipolar current waveform is switched. A transient length of 2048 samples at a sampling rate of 1 ms was selected. Of these approximately 384 are pre-trigger samples, which allow accurate identification and backing off of residual bias signal.

The main transmitter run was also centred along the same profile. Transmitters orientated parallel (in-line) and orthogonal (broad-side) to the profile were deployed at intervals of 250 m. Each transmitter electrode installation employed two 3 m long pipes sunk into drill holes and surrounded with bentonite mud. A transmitter dipole length of 250 m was employed, with transmitter current varying according to the maximum which could be safely and repeatedly injected at each site. A bipolar waveform was employed, switching alternately between positive and negative current (Strack 1992). Peak to peak transmitter currents of between 20 A and 60 A were achieved, depending upon surface resistivity and generator power. In addition to the main transmitter run, a further four transmitter stations were occupied forming a cross on each side of the profile.

In total 64 receiver channels and 57 transmitter stations were occupied. Such dense spatial data coverage is unprecedented in a transient electromagnetic survey.

The raw transients contain a significant amount of periodic noise. Principal among these is 50 Hz noise from mains power sources and its higher harmonics, but there is also significant periodic energy at other frequencies. This may be removed using notch filters, but the distortion associated with the application of many notch filters to a single signal is to be avoided.

In order to improve the signal-to-noise ratio many transients are recorded for one transmitter-receiver configuration and then *vertically* stacked. Since the noise is not phase stable between transmitter switchings a simple averaging of an adequate number of relatively clean transients is effective in improving the signal-to-noise ratio. The length of time each transmitter station was occupied depended upon the transmitter dipole moment, noise environment and the offset to the farthest receiver. Between 55 and 190 transients were recorded for each transmitter position, resulting in a total data volume of approximately 4.5 GBytes. Overall data quality is very good and from the stacking statistics the uncertainty for most of the transients is below the 1% level which was targeted (see Figure 5 and Hördt et al. 1995).

More sophisticated noise-reduction approaches may also be taken. Since the noise is (largely) stationary within one trace, predictive deconvolution can be used to remove the predictable component of the noise. There are also a number of algorithms which try to remove non-stationary noise by attempting to identify and remove uncharacteristic samples (outliers) due to noise bursts (Strack 1992).

Geological noise, topography and the presence of pipelines mean that, as would be expected, the measured data does not match exactly the response to the reservoir which was estimated by 3D modelling. Principal among these distorting factors are about 40 wells, and associated surface pipes. While the EM response of pipelines is broadly understood the quantitative evaluation and removal of pipeline effects in EM surveys remains an area of active research (Qian and Boerner 1995). Certainly it would be a very non-routine task to interpret and eliminate the effects of 40 wells and the conclusivity of the results might still be held in question. However these distorting features will all remain the same during the second survey. Taking the difference between the data collected in the two surveys will eliminate effects from pipelines and uncover the response to changes in the reservoir. This should reveal the movement of the gas-water contact in the time between the two surveys.

5 Data Processing and Interpretation

So-called *inverse* modelling — the iterative refinement of a model through *forward* modelling until a good fit with the experimentally acquired data is achieved — continues to be the mainstay of many

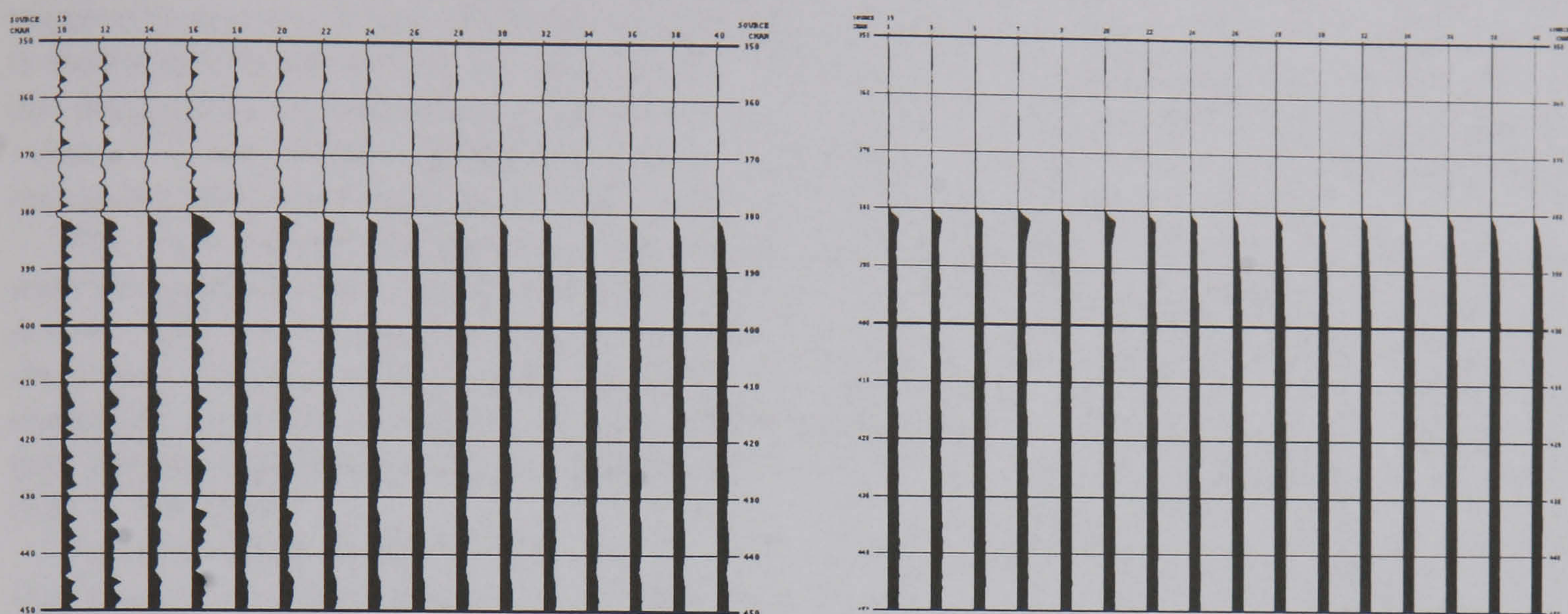


Figure 5: Common source gather of E field components in-line with transmitter 19, presented in the style of a seismic common source gather. In each figure offset from the transmitter increases from right to left in intervals of 125 m, starting from 1 km. Time increases from top to bottom in intervals of 1 ms while timing lines are set at 10 ms intervals. On each trace is apparent a number of pre-trigger samples followed by onset of the pulse from the transmitter. Left: the first raw trace recorded at each receiver. Right: the result of vertical stacking all the traces at each receiver, demonstrating a greatly improved signal-to-noise ratio.

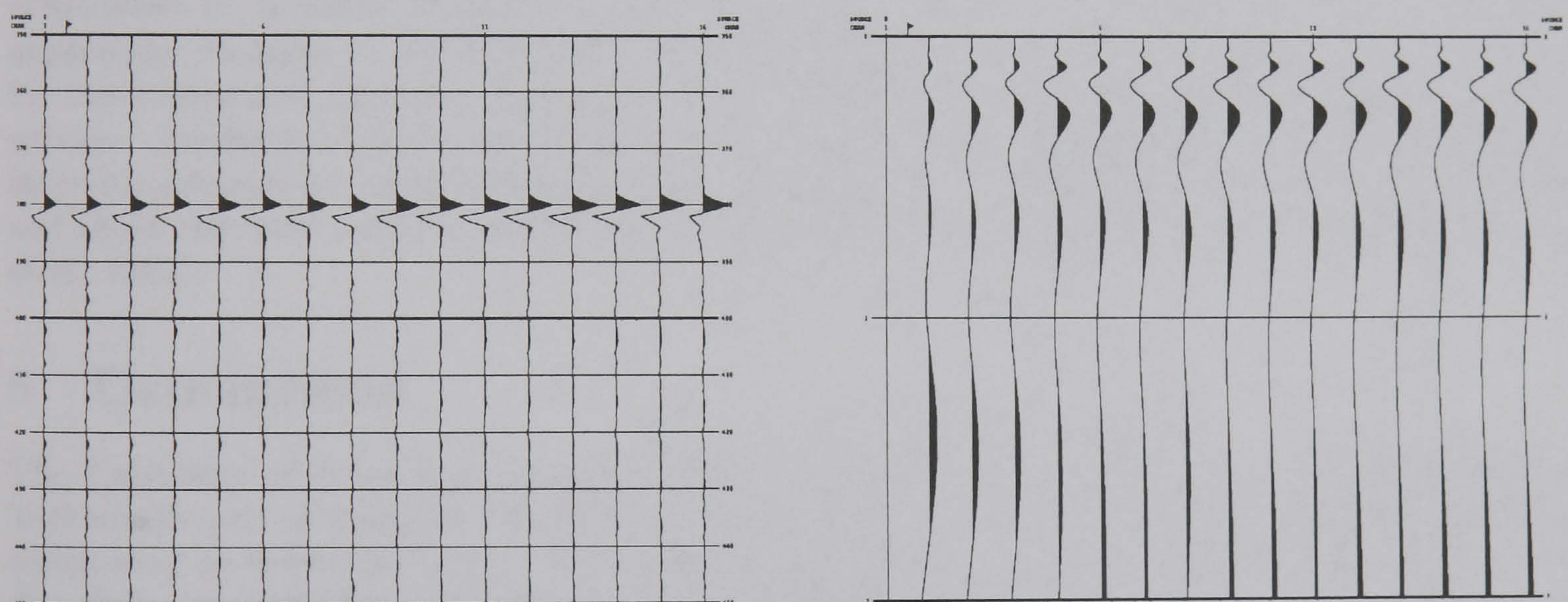


Figure 6: Common source gather of E field components in-line with transmitter 19 after processing. In each figure offset from the transmitter increases from right to left in intervals of 125 m, starting from 1 km. Left: second derivative of stacked traces plotted with against time with timing lines set at 10 ms intervals increasing down the page. Right: Equivalent wavefield calculated from second derivative of stacked traces using wave transform inversion by deconvolution in log time. The equivalent wavefield is plotted against the time-like variable q which has units of \sqrt{s} . q increases down the page with timing lines at $1 \sqrt{s}$ intervals.

EM interpretation schemes. While 1D inverse modelling is tractable using moderate computer power, computational expense makes 2D and 3D inverse modelling a slow and painful task. The problem is exacerbated by the dramatic increase in data volumes resulting from the multichannel surveys required to resolve 2D and 3D features (Schnegg and Sommaruga 1995, Hördt et al. 1995). Although it would not be impossible to apply methods developed to interpret traditional surveys, they are not designed to exploit dense spatial sampling and would struggle to process the much larger data volumes. There remains at the present time a need to develop a more satisfactory methodology for processing and interpretation of these unusually large and dense MTEM surveys.

The wave transform relates the response of a diffusive medium to the response of an equivalent wave propagation medium, provided the sources, geometry and boundary conditions in both domains match. The wave transform may be inverted to calculate an equivalent wavefield from diffusive transients and then seismic data processing and interpretation techniques may be applied to the equivalent wavefield to recover the equivalent velocity $c(\mathbf{r})$. For EM data a resistivity profile $\sigma(\mathbf{r})$ may then be calculated using the relationship $\mu\sigma(\mathbf{r}) = c(\mathbf{r})^{-2}$ where μ is the magnetic permeability (Lee & Xie 1993).

Figure 6 shows on the left the second derivative of the stacked data set of Figure 5, illustrating that most of the information is contained in a small fraction of the samples on each trace. These data have then been transformed by applying wave transform inversion by deconvolution in log time (Jia et al. 1995) to each trace. The resulting data are plotted on the right of figure 6 against the time-like variable q .

The surface-to-surface MTEM response resembles seismic refraction more closely than seismic reflection. As a first step in the interpretation of the data, we intend to combine common-source gathers, similar to the seismic refraction method, enabling the layer thicknesses and resistivities to be inverted using conventional travel time tomography (Palmer 1980).

Wave transform inversion remains an area of active research. Different schemes introduce differing constraints on possible solutions in order to improve resolution and tractability. Exciting new approaches continue to be developed (Gershenson 1993, Slob et al. 1995) and there remains scope for developing new inversion schemes to take advantage of the dense spatial sampling of MTEM surveys. Inversion of the wave transform is well known to be an inherently ill-posed problem and inversion schemes are often computationally expensive. Many schemes treat each trace individually and these can quite easily be implemented on parallel computers to reduce computation time (Jia et al. 1995).

6 Conclusions

The University of Edinburgh, in collaboration with The University of Cologne, Deutsche Montan-Technologie and Compagnie Générale de Géophysique are developing an exploration methodology which may be used routinely to detect and monitor financially recoverable hydrocarbon reservoirs directly using multichannel transient electromagnetics (MTEM).

A first field survey over an underground gas storage site yielded unprecedented production levels, data coverage and data volumes for an EM survey. Data quality is very good and from the stacking statistics the uncertainty for most of the transients is below 1%.

3D modelling of the site indicates that the response due to expected seasonal variations in the volume of gas stored will be around 5%. We believe it is possible to obtain repeatable measurements with less than 1% noise. This means that the effect of variations in the volume of gas stored is detectable and that it will be possible to obtain a reasonable resolution of the gas movement.

The 4.5 GBytes of data collected spurred development of new processing systems designed to exploit the large data volumes and dense spatial coverage. Wave transform inversion allows calculation of an equivalent wavefield from diffusive transients. The equivalent wavefield may then be

processed and interpreted using existing seismic processing systems. This may avoid the need for inverse modelling.

Unusually warm weather resulted in little depletion of gas reserves during the 1994/1995 winter. With the support of the sponsors the project time-scale has now been extended, and a second survey which should reveal interim movement of the gas-water contact is now planned for spring 1996.

We expect this experiment to demonstrate that time-lapse EM surveying will allow the movement of fluids in reservoirs to be monitored. It may also demonstrate that the method can be used as a direct hydrocarbon indicator. We also expect it to be useful for hydrocarbon exploration, delineation of salt domes and groundwater surveying.

7 Acknowledgments

This work is currently supported by European Community THERMIE research grant number OG/0305/92/NL-UK, and Elf Enterprise Caledonia contract number CA5527. Anton Ziolkowski thanks the Petroleum Science and Technology Institute for funding his position as Professor of Petroleum Geoscience at the University of Edinburgh. David Sharrock is employed under subcontract to DeutscheMontanTechnologie. The authors are indebted to their collaborating partners at the University of Köln, DeutscheMontanTechnologie and Compagnie Générale de Géophysique. We would like to thank Gaz de France for their help in planning and carrying out the field operations. The cooperation of the Research and Development team in charge of this site, headed by Frederic Huguet and from the management of the production unit, headed by M. Laroche was invaluable in ensuring the smooth and efficient running of the survey.

8 References

- Eadie, T., 1981. Detection of hydrocarbon accumulations by surface electrical methods: a feasibility study. *Research in Applied Geophysics*.
- Gershenson, M., 1993. Simple Interpretation of Time-Domain Electromagnetic Sounding Using Similarities Between Wave and Diffusion Propagation. In proceedings of *SEG Annual International Meeting* 1993, 1342–1345. Extended Abstract number SS2.34.
- Hördt, A., Vozoff, K. & Neubauer, F. M., 1995. Multichannel transient electromagnetics for underground gas storage monitoring, in 57th Meeting, EAEG. Abstract number D051.
- Lee, K. H. & Xie, G. Q., 1993. A new approach to imaging with low-frequency electromagnetic fields. *Geophysics*, 58(6):780–796.
- Jia, P., Flockhart, I. W. & Wilson, A. J. S., 1995. Automatic parallelisation of multichannel transient EM processing, in *International Symposium on Three-Dimensional Electromagnetics*.
- Kaufman, A. A. & Keller, G. V., 1983. *Frequency and transient soundings*, Elsevier.
- Keller, G. V., 1968. Electrical prospecting for oil, *Quarterly of the Colorado School of Mines*.
- Palmer, D., 1980. The generalized reciprocal method of seismic refraction interpretation. *Society of Exploration Geophysicists*.
- Qian, W. & Boerner, D. E., 1995. Electromagnetic modelling of buried line conductors using an integral equation. *Geophysical Journal International*, 121, 203–214.
- Slob, E. C., Habashy, T. M. & Torres-Verdin, C., 1995. A New Stable Numerical Procedure for Computing the Q-transform of TEM data. In proceedings of 57th Meeting, EAEG, June, 1995 Glasgow. Abstract number D053.
- Strack, K. M., 1992. *Exploration with Deep Transient Electromagnetics*, Elsevier.
- Schnegg P. -A. & Sommaruga A., 1995. Constraining Seismic Parameters with a CSAMT method. *Geophysical Journal International*, 122(1):152–160.

Appendix B

Related Problems in Partial Differential Equations

In this section a new relationship between the solutions of related initial value problems is derived. This extends the result of Bragg & Dettman (1968*b*), essentially by employing the approach of Schouten (1935) but with a simpler and more concise derivation than either of these previous works.

B.1 Generalising the Q Transform

Let D_r be a linear differential operator which is independent of t . That is, let $D_r = (D_1, D_2, \dots, D_n)$ where each D_j is some collection of powers of the space variable \mathbf{x} and $\partial_i, i = 1, \dots, n$ the partial derivative with respect to the i^{th} component of \mathbf{x} . Let P_1 and P_2 be polynomials with coefficients $a_i, i = 1, \dots, N$ and $b_i, i = 1, \dots, M$ respectively. Finally, let $\partial\mathcal{V}$ be the boundary of the volume \mathcal{V} .

We are interested in deriving a relationship between solutions to the two related initial value problems

$$\begin{aligned} D_r\{\mathbf{F}(\mathbf{x}, t)\} + P_1(\partial_t)\{\mathbf{F}(\mathbf{x}, t)\} &= \mathbf{S}(\mathbf{x}, t), \\ \mathbf{x} &\in \mathcal{V}, t > 0 \\ \frac{\partial^i \mathbf{F}(\mathbf{x}, 0)}{\partial t^i} &= \boldsymbol{\alpha}_i(\mathbf{x}), \\ \mathbf{x} &\in \mathcal{V}, i = 1, \dots, N \\ \mathbf{F}(\mathbf{x}, t) &= \mathbf{f}(\mathbf{x}, t), \\ \mathbf{x} &\in \partial\mathcal{V}, t > 0, \end{aligned} \tag{B.1}$$

and

$$D_r\{U(\mathbf{x}, q)\} + P_2(\partial_q)\{U(\mathbf{x}, q)\} = \mathbf{T}(\mathbf{x}, q),$$

$$\mathbf{x} \in \mathcal{V}, q > 0$$

$$\frac{\partial^i U(\mathbf{x}, 0)}{\partial q^i} = \beta_i(\mathbf{x}), \quad (B.2)$$

$$\mathbf{x} \in \mathcal{V}, i = 1, \dots, M$$

$$U(\mathbf{x}, q) = u(\mathbf{x}, q),$$

$$\mathbf{x} \in \partial\mathcal{V}, q > 0.$$

Taking the Laplace transform of problems (B.1) and (B.2) with respect to t and q with transform parameters s and p respectively we obtain

$$\begin{aligned} D_r\{\hat{\mathbf{F}}(\mathbf{x}, s)\} + P_1(s)\hat{\mathbf{F}}(\mathbf{x}, s) = \\ \sum_{i=0}^{N-1} \sum_{j=0}^i a_i s^{i-j} \alpha_j(\mathbf{x}) \\ + \hat{\mathbf{S}}(\mathbf{x}, s), \quad \mathbf{x} \in \mathcal{V} \end{aligned} \quad (B.3)$$

$$\hat{\mathbf{F}}(\mathbf{x}, q) = \hat{\mathbf{f}}(\mathbf{x}, q), \quad \mathbf{x} \in \partial\mathcal{V}$$

and

$$\begin{aligned} D_r\{\hat{\mathbf{U}}(\mathbf{x}, p)\} + P_2(p)\hat{\mathbf{U}}(\mathbf{x}, p) = \\ \sum_{i=0}^{M-1} \sum_{j=0}^i b_i p^{i-j} \beta_j(\mathbf{x}) \\ + \hat{\mathbf{T}}(\mathbf{x}, p), \quad \mathbf{x} \in \mathcal{V} \end{aligned} \quad (B.4)$$

$$\hat{\mathbf{U}}(\mathbf{x}, q) = \hat{\mathbf{u}}(\mathbf{x}, p), \quad \mathbf{x} \in \partial\mathcal{V}.$$

Let $\varphi(s)$ be such that $P_2(\varphi(s)) = P_1(s)$ and the inverse Laplace transform of $\exp(-\varphi(s))$ with respect to transform parameter s exists. Substituting $p = \varphi(s)$ in (B.4) we obtain

$$\begin{aligned} D_r\{\hat{\mathbf{U}}(\mathbf{x}, s)\} + P_2(\varphi(s))\hat{\mathbf{U}}(\mathbf{x}, s) = \\ \sum_{i=0}^{M-1} \sum_{j=0}^i b_i (\varphi(s))^{i-j} \beta_j(\mathbf{x}) \\ + \hat{\mathbf{T}}(\mathbf{x}, \varphi(s)), \quad \mathbf{x} \in \mathcal{V} \end{aligned} \quad (B.5)$$

$$\hat{\mathbf{U}}(\mathbf{x}, q) = \hat{\mathbf{u}}(\mathbf{x}, \varphi(s)), \quad \mathbf{x} \in \partial\mathcal{V}$$

Define the quantity $\hat{\mathbf{R}}(\mathbf{x}, s)$ by

$$\hat{\mathbf{R}}(\mathbf{x}, s) \equiv \hat{\mathbf{F}}(\mathbf{x}, s) - \hat{\mathbf{U}}(\mathbf{x}, \varphi(s)). \quad (\text{B.6})$$

By subtracting equations (B.5) from (B.3) we see that $\hat{\mathbf{R}}(\mathbf{x}, s)$ obeys

$$\begin{aligned} D_r\{\hat{\mathbf{R}}(\mathbf{x}, s)\} + P_1(s)\hat{\mathbf{R}}(\mathbf{x}, s) = \\ \sum_{i=0}^{N-1} \sum_{j=0}^i a_i s^{i-j} \boldsymbol{\alpha}_j(\mathbf{x}) \\ - \sum_{i=0}^{M-1} \sum_{j=0}^i b_i(\varphi(s))^{i-j} \boldsymbol{\beta}_j(\mathbf{x}) \\ + \hat{\mathbf{S}}(\mathbf{x}, s) - \hat{\mathbf{T}}(\mathbf{x}, \varphi(s)) \\ \hat{\mathbf{R}}(\mathbf{x}, s) = \hat{\mathbf{f}}(\mathbf{x}, s) - \hat{\mathbf{u}}(\mathbf{x}, \varphi(s)), \mathbf{x} \in \partial\mathcal{V}. \end{aligned} \quad (\text{B.7})$$

Let us require that the boundary, and source terms in (B.7) match, i.e.

$$\hat{\mathbf{f}}(\mathbf{x}, s) - \hat{\mathbf{u}}(\mathbf{x}, \varphi(s)) = 0 \quad (\text{B.8})$$

and

$$\hat{\mathbf{S}}(\mathbf{x}, s) - \hat{\mathbf{T}}(\mathbf{x}, \varphi(s)) = 0. \quad (\text{B.9})$$

Now consider the, often relevant, case where we have $\boldsymbol{\alpha}_j(\mathbf{x}) \equiv 0, j = 1, \dots, N$ and $\boldsymbol{\beta}_j(\mathbf{x}) \equiv 0, j = 1, \dots, M$. In this case there are no remaining terms on the right hand side of equations (B.7) and clearly $\hat{\mathbf{R}}(\mathbf{x}, s) \equiv 0$ is a solution for the problem (B.7).

In the situation where we have some initial conditions $\boldsymbol{\alpha}_j(\mathbf{x})$ which are non-zero we require $\boldsymbol{\beta}_j(\mathbf{x})$ such that each power of s in (B.3) and (B.5) has the same coefficient. In order to aid later analysis we note here that this requirement may be re-written as

$$\begin{aligned} \sum_{k=0}^{N-1} s^k \sum_{j=0}^{N-1-k} a_{j+k} \boldsymbol{\alpha}_j(\mathbf{x}) - \\ \sum_{k=0}^{M-1} (\varphi(s))^k \sum_{j=0}^{M-1-k} b_{j+k} \boldsymbol{\beta}_j(\mathbf{x}) = 0. \end{aligned} \quad (\text{B.10})$$

If it is possible to expand $\varphi(s)$ in terms of powers of s then this formulation yields a system of equations to solve for $\boldsymbol{\beta}_j(\mathbf{x})$. Note that this system does not always have a solution.

Given that we can satisfy (B.10), we return our attention to (B.7). If this problem is such that it has a unique solution, then $\hat{\mathbf{R}}(\mathbf{x}, s) \equiv 0$ must be the only solution and in this case

$$\hat{\mathbf{F}}(\mathbf{x}, s) = \hat{\mathbf{U}}(\mathbf{x}, \varphi(s)) \quad (\text{B.11})$$

which by the definition of the Laplace transform implies that

$$\hat{\mathbf{F}}(\mathbf{x}, s) = \int_0^\infty \mathbf{U}(\mathbf{x}, q) e^{-\varphi(s)q} dq. \quad (\text{B.12})$$

Taking the inverse Laplace transform we obtain our result

$$\mathbf{F}(\mathbf{x}, t) = \int_0^\infty \mathcal{L}^{-1}\{e^{-\varphi(s)q}\} \mathbf{U}(\mathbf{x}, q) dq \quad (\text{B.13})$$

which we call the generalised Q transform.

B.2 Correspondence of Sources

Recall equation (B.9) which stated that for source functions to match we require

$$\hat{\mathbf{S}}(\mathbf{x}, s) = \hat{\mathbf{T}}(\mathbf{x}, \varphi(s)). \quad (\text{B.14})$$

By the definition of the Laplace transform (0.7) Equation (B.14) implies that

$$\hat{\mathbf{S}}(\mathbf{x}, s) = \int_0^\infty \mathbf{T}(\mathbf{x}, q) \exp(-\varphi(s)q) dq. \quad (\text{B.15})$$

B.3 Singular Value Expansion Analysis of The Generalised Q Transform

We can now make some observations on the applicability of the generalised Q transform. Consider the case where the two initial value problems (B.1) and (B.2) are significantly different. To be specific, let us require $M > N$ so that $\varphi(s)$ must be such that the transformation $s \rightarrow \varphi(s)$ maps a polynomial of degree M in s onto a polynomial of degree N .

I conjecture that if $m > n$ and $\varphi^{-1}(s)$ is such that $s = \varphi^{-1}(\varphi(s)) = \varphi(\varphi^{-1}(s))$ then $\exp(-\varphi(s)q)$ has an inverse Laplace transform but $\exp(-\varphi^{-1}(s)q)$ does not. This conjecture is true for a number of cases of interest — see for example section 7.1 — and implies that given a pair of problems, it will only be possible to derive a transform equation in one direction. Therefore it is of interest to consider how Equation (B.13) might be inverted to find $\mathbf{U}(\mathbf{x}, q)$ given an unknown $\mathbf{F}(\mathbf{x}, s)$.

Considered from a situation where it is desired to calculate $\mathbf{U}(\mathbf{x}, q)$ given an unknown $\mathbf{F}(\mathbf{x}, s)$ the generalised Q transform (B.13) is a Fredholm integral equation of the first kind Kress (1989). This is a class of problems which are inherently ill-posed. In order to demonstrate

this we examine a generic Fredholm integral equation of the first kind,

$$f(t) = \int_a^b K(t, q)u(q) dq, \quad (\text{B.16})$$

and employ a singular value expansion (SVE) in order to analyse the stability of the inverse problem of determining $u(q)$ given $f(t)$.

A kernel $K(t, q)$ may be expanded in terms of its nonzero singular values ν_i , and left and right singular functions \mathbf{u}_i and \mathbf{v}_i as

$$K(t, q) = \sum_{i=1}^{\infty} \nu_i \mathbf{u}_i(t) \mathbf{v}_i(q). \quad (\text{B.17})$$

Picard's theorem (Kress 1989, theorem 15.18, page 234) states that (B.16) is solvable only if¹

$$\sum_{i=1}^{\infty} \frac{1}{\nu_i^2} |(f, \mathbf{u}_i)|^2 < \infty \quad (\text{B.18})$$

where (f, \mathbf{u}_i) denotes the scalar product of f and \mathbf{u}_i and $|a|$ denotes the modulus of a . In this case the solution is

$$u = \sum_{i=1}^{\infty} \frac{1}{\nu_i} (f, \mathbf{u}_i) \mathbf{v}_i. \quad (\text{B.19})$$

In order to demonstrate that (B.16) is ill-posed consider equation (B.19). If we perturb the left hand side of (B.16) by adding $f_i^\delta = \delta \mathbf{u}_i$ then the change in the solution is $u^\delta = \frac{1}{\nu_i} \delta \mathbf{v}_i$. Since the singular values ν_i tend to zero, the influence of a small change f_i^δ can be made arbitrarily large simply by taking large enough i . Hence the problem is ill-posed since an infinitesimal change in the input can cause a large change in output.

¹If the condition that $f \in \mathcal{N}(A^*)^\perp$ where A is the linear operator $f \rightarrow \int_a^b K(t, q)u(q) dq$ is added, then this “only if” becomes an “if and only if”.

Appendix C

Geophysical Modelling and Simulation on High Performance Computers

Numerical simulation is used extensively in the design and interpretation of geophysical surveys. The integral equation method is well suited to numerical modelling of 3D anomalies of limited spatial extent and with uniform internal properties. The finite difference formulation is well suited to numerical modelling of Earth models with smoothly varying properties.

The development of exploration geophysics has been intimately linked to the development of high performance data acquisition systems and high performance computers to model and process the ever-increasing volumes of data. It is possible to increase the performance of a computer either by spending money on a faster processor or by spending money on more processors and the software development necessary to use them effectively. For many numerical modelling problems in geophysical, it is more effective to take the latter course and employ a parallel computing approach.

This appendix opens with a brief introduction to parallel computers and some of the concepts and terminology relevant to their effective use. The formulation of the electromagnetic induction problem using integral equations is introduced and its suitability for modelling the response of different geological targets is outlined. The formulation of the electromagnetic induction problem using finite differences is introduced and its suitability for modelling the response of different geological targets is outlined.

The EM3D integral equation electromagnetic modelling program and the EMAFD finite difference electromagnetic modelling program have been parallelised using task farms. Performance results show that this allows such diverse systems as departmental workstation clusters and massively parallel supercomputers to be used effectively for electromagnetic modelling.

C.1 High Performance (Parallel) Computers

It is possible to increase the power of a computer either by spending money on a faster processor or by spending money on more processors and the software development necessary to use them. For many modest problems it is cheaper to take the latter course. For applications demanding ultimate performance the solution is to take the fastest processors available and use as many of them as can be afforded.¹ For these reasons parallel computing has matured from a research topic into a mainstream technology. This section provides a brief introduction to parallel computers and some of the concepts and terminology relevant to their effective use.

The section opens in section C.1.1 with Flynn's taxonomy of computer architectures and then focuses on distributed memory, multiple instruction stream, multiple data stream parallel computers or *multicomputers*. Section C.1.2 surveys parallel programming paradigms, contrasting functional and data decomposition and investigating different data decomposition techniques. Load balancing techniques, which aim to minimise execution time by ensuring that all processors have the same amount of work to perform, are discussed in section C.1.3.

C.1.1 Computer Architectures

Flynn's Taxonomy

Flynn's taxonomy (Flynn 1972) categorises computer architectures according to whether they have single or multiple instruction and data streams. Conventional computers employ the single instruction stream, single data stream (SISD), or Von Neumann programming model (Flynn 1972). SIMD machines retain a single instruction stream, but have multiple data streams all of which are acted upon at the same time, and in the same way, by a large number of processors. In the MIMD, or multiple instruction stream, multiple data stream architecture, a number of processors work independently, with each processor taking instructions from its own instruction cache and operating on different data in its own data stream.

At the present time the use of SIMD parallel computers for general purpose supercomputing is declining. Meanwhile there is an increasing range number of MIMD computers marketed by vendors including Cray, DEC, Hitachi, HP-Convex, IBM, Intel, NEC and Sun. In addition modestly-parallel computing is spreading down-market from supercomputers into systems such as multi-processor PC-compatible servers.

Distributed Memory MIMD

In a distributed memory MIMD (DM-MIMD) architecture, each processor has direct and exclusive access to its own memory bank. Processors share data and communicate with each other by *message passing* through some interconnect device. This architecture can be considered

¹Today the most powerful computers are without exception massively parallel (Dongarra, Meuera & Stromaier 1995).

as simply many traditional sequential computers acting in concert and is sometimes termed a *multicomputer* — see figure C.1.

At the time of writing production-strength parallelising compilers machines do not exist for the DM-MIMD programming, and it is unlikely that they will exist in the near future. The need to perform explicit message passing means that DM-MIMD programming is widely considered more difficult than SIMD or SMP programming.

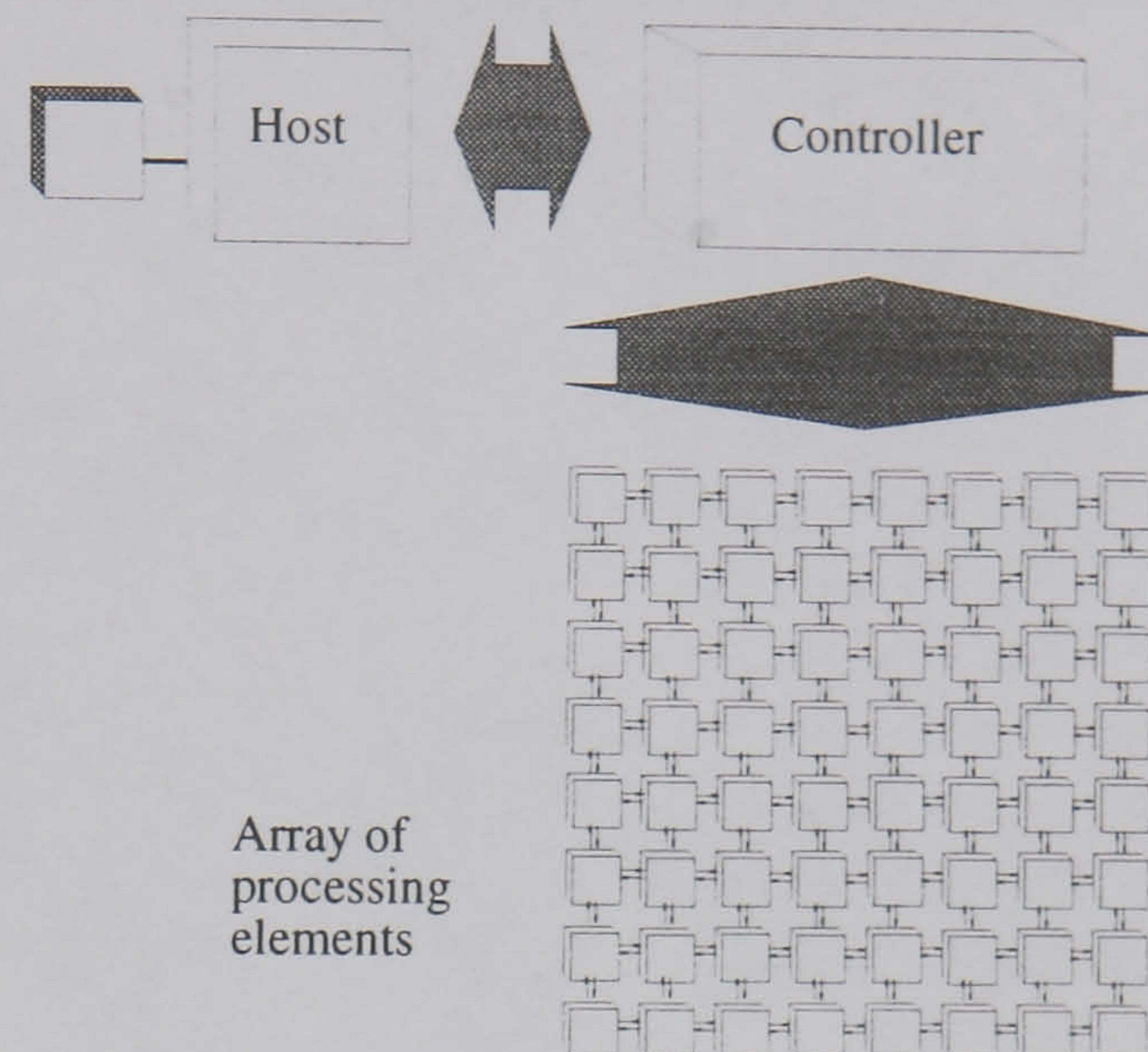
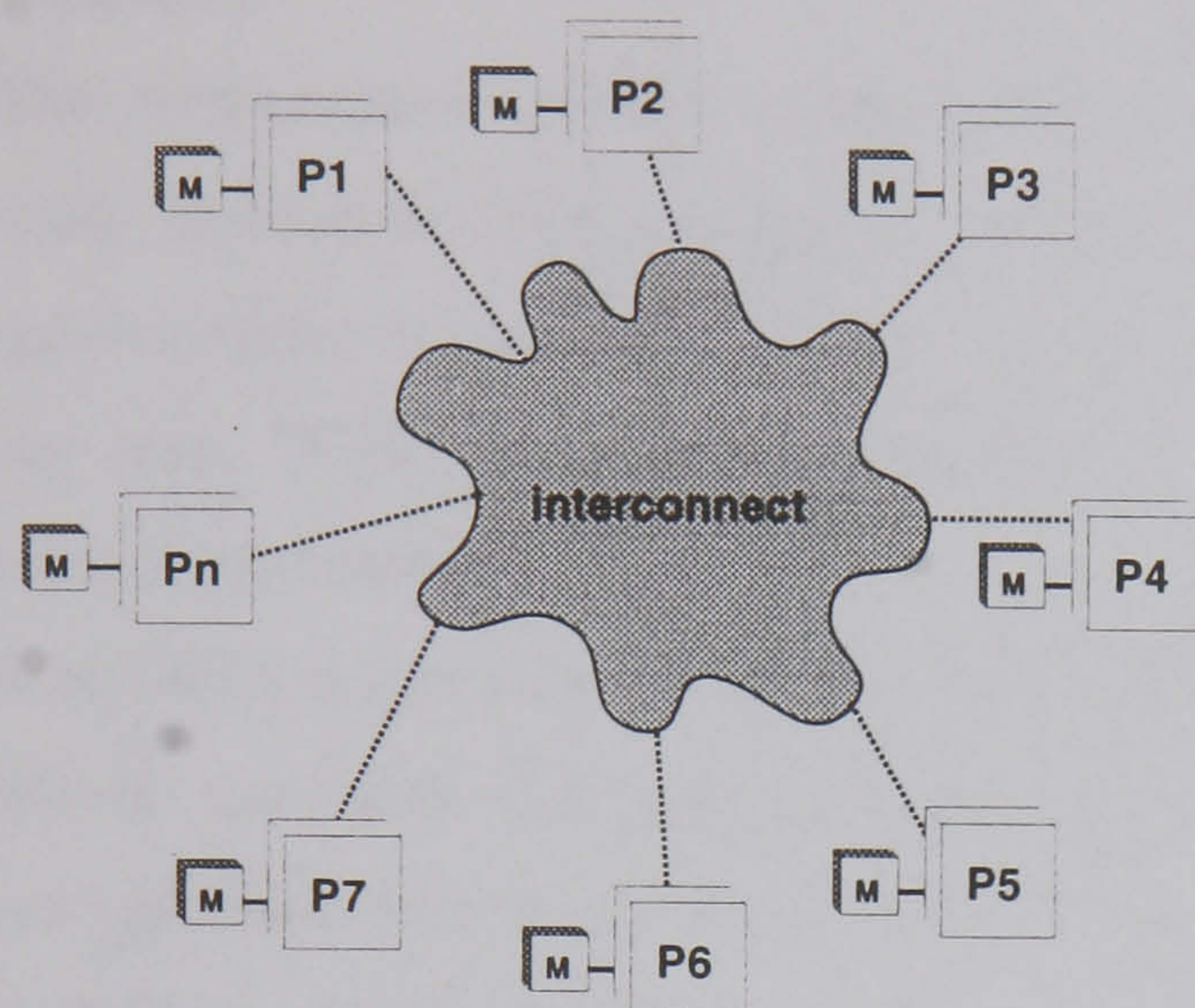


Figure C.1: Schematic DM-MIMD architecture.

Figure C.2: Schematic SIMD architecture.

The *communication to computation* ratio of a multicomputer is determined by the relative speed of the processors and the interconnect between them and is regarded by many as an important yardstick with which to gauge a multicomputer. Some applications require relatively little communication between processors when considered in proportion to the volume of computation which is required. These applications may perform well on *loosely coupled* multicomputers such as a network of workstations where the communication/computation ratio is low. However many applications require a more *tightly coupled* architecture to achieve good processor utilisation.

The Cray T3D sited at Edinburgh is currently the most powerful computer in Europe. Each of its 512 processors is a 150 MHz DEC alpha processor with 64 Mb of memory. These are paired into nodes from each of which six links running at up to 300 MBytes/s carry data to other nodes and, through a Cray Y-MP host, to other systems.

Shared Memory MIMD

When exploiting multiple processors, one approach is to give all processors access to a single memory space. This is commonly achieved through the use of a global memory bank accessed by a bus — see Figure C.3. This style of MIMD architecture is termed a symmetric multipro-

cessor (SMP).

Sophisticated compilers and code development tools have been developed which support the task of implementing applications on SMP machines. An example of this support is the automatic distribution of loops by sophisticated compilers.

The performance of SMP architectures is typically limited by bus contention and by the

synchronisation required to ensure two processors cannot simultaneously update a single memory area. With current technology the SMP programming model is efficient only up to a few tens of processors.

Non-uniform memory access (NUMA) computers blur the distinction between SMP and DM-MIMD machines. Through a combination of hardware and software NUMA architectures support global access to a distributed memory, some of which is local (fast access) and some remote (relatively slower access).

C.1.2 Fine and Coarse Grain Parallelisation Techniques

To parallelise a problem it must be decomposed into parts or *grains* which can be executed simultaneously on different processors. Several different paradigms for decomposition have evolved, and with them techniques to estimate the effectiveness of a particular parallelisation strategy on a particular problem, without actually implementing the parallel program. These techniques aid when planning the parallelisation of a new problem.

Parallelisation techniques can be classified according to whether the problem is divided on the basis of functionality or data, and on the number and/or “size” of the grains into which the problem is decomposed. A coarse-grained parallelisation technique divides the problem into a few large grains. This limits the number of processors which can be profitably employed. A fine-grained parallelisation divides the problem into very many grains. This offers a high degree of parallelism and the possibility that performance will scale well as the parallel platform is scaled up to a large number of processors. However the computation of each grain must be managed and this overhead can grow quickly with the increasing number of grains.

When choosing a parallelisation technique it is important to match the technique to the problem and machine being targeted. SIMD computers often provide very effective support for fine-grained parallelisation of mesh-based problems. However, because this is essentially provided by hardware, often it can support only very simple computations. DM-MIMD computers are more flexible but generally recognised as more difficult to program.

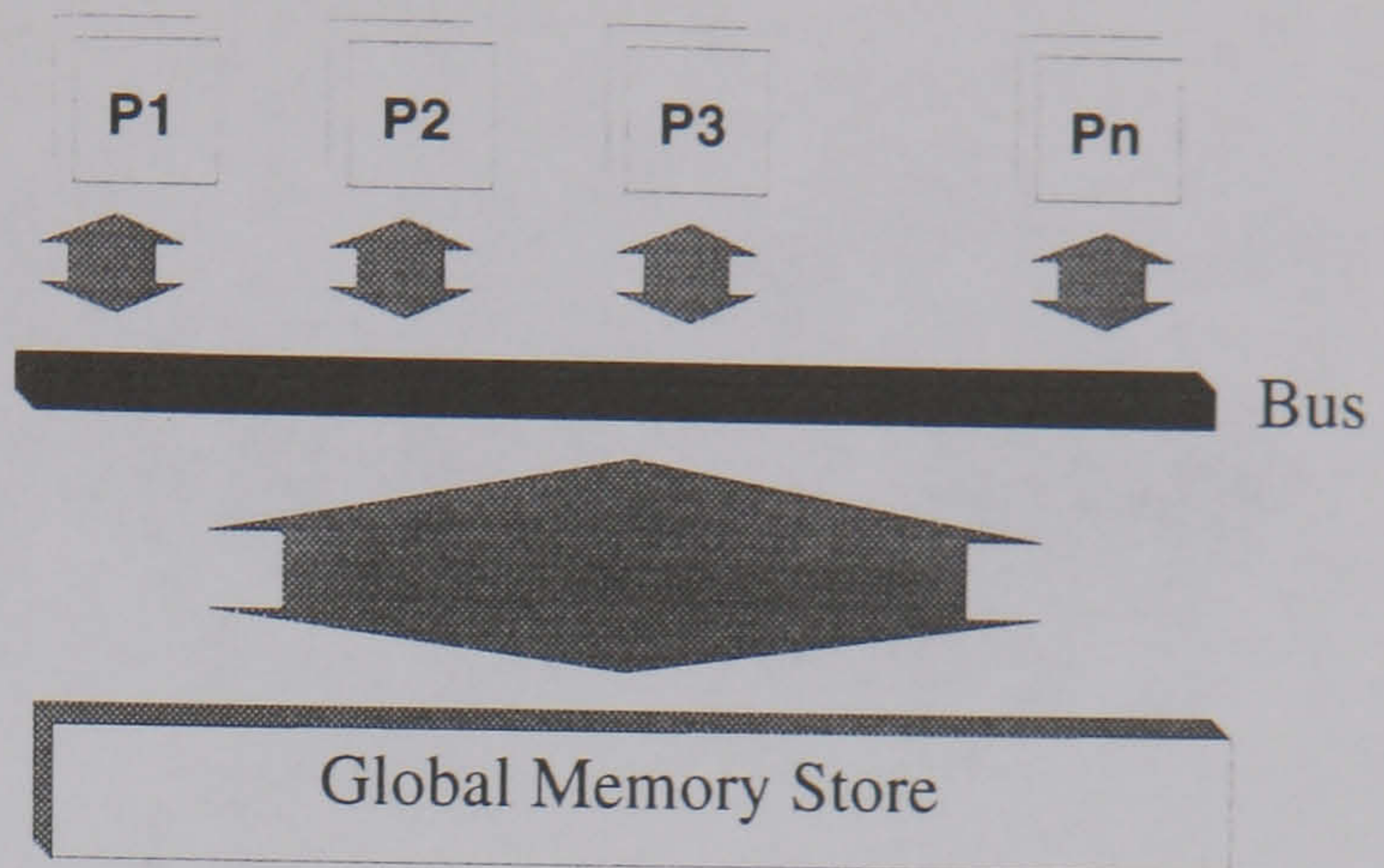


Figure C.3: Schematic SMP architecture.

Functional Decomposition

Functional (or algorithmic) decomposition breaks up a program into a number of sub-programs.

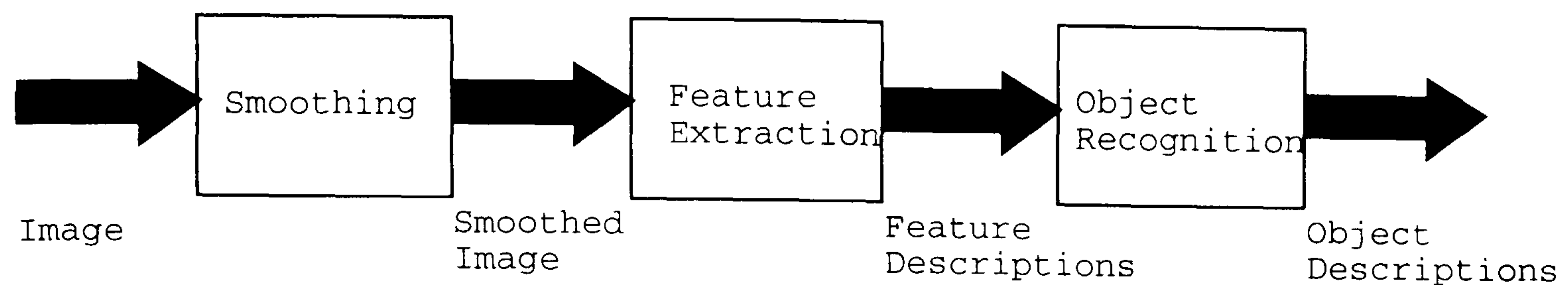


Figure C.4: A functional pipeline.

A simple form of functional decomposition is the *pipeline* — see figure C.4. In a pipeline the processing of data are broken down into a series of functional units through which the data is passed. When the first functional unit has completed processing a parcel of data the results are passed to a second unit that uses separate hardware and the first-step hardware is now free to begin processing new data. A high throughput can be achieved by breaking up a data processing job into many parcels.

However the extent to which extra hardware can be exploited by this scheme is limited by the amount of functional parallelism inherent in the problem being tackled and in general this leads to poor scalability.

The Task Farm

If the main stage of a calculation can be decomposed into several independent tasks then there is no need for communication between processes executing each task and *task farming* may be employed. A classical task farm consists of one *source* process which generates tasks, one or more *worker* processes which service them to produce results, and one *sink* process which handles results. Each worker requests a task from the source process, executes it and passes the results on to the sink

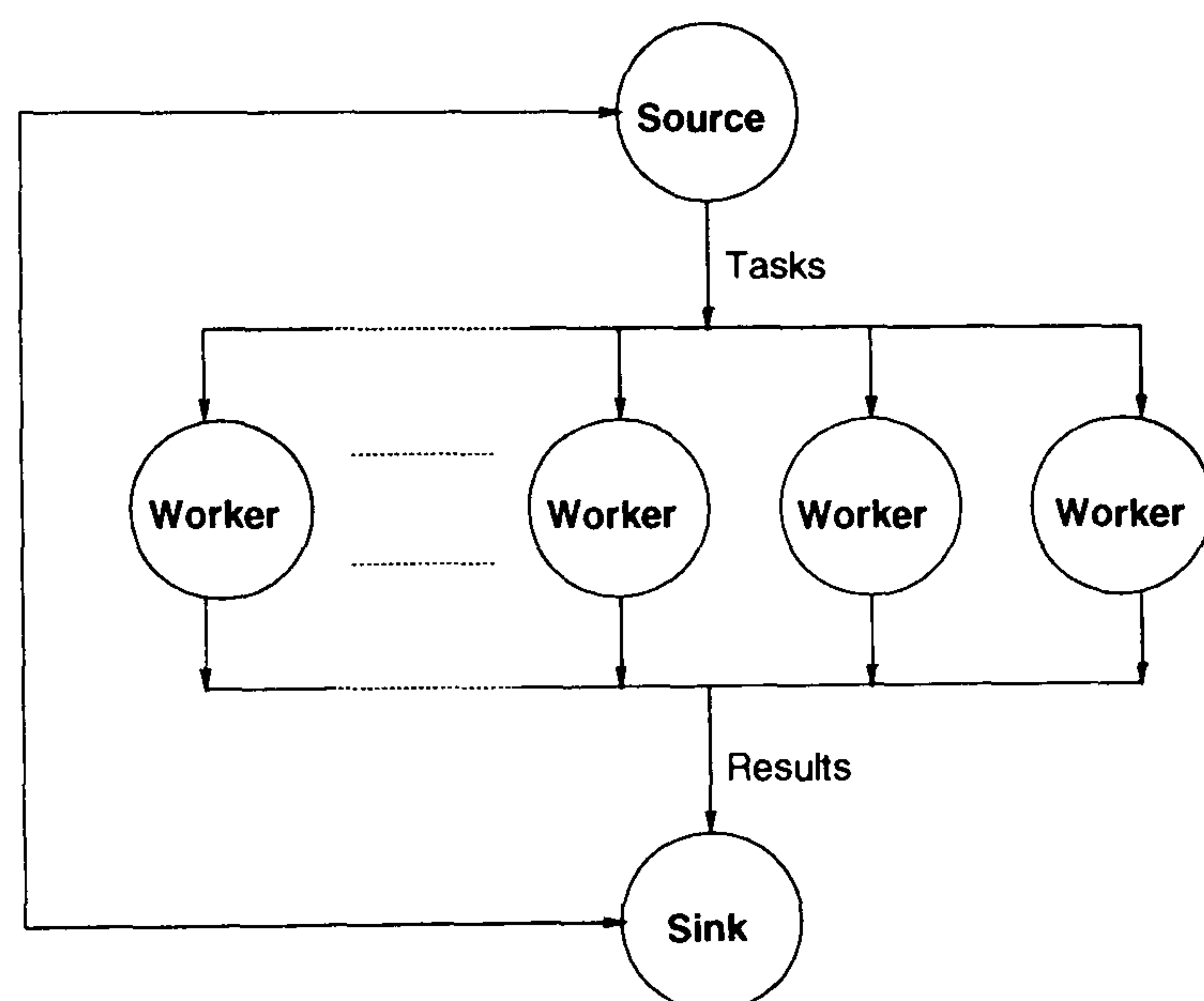


Figure C.5: The classic task farm.

process and then requests the next task from the source process. This cycle repeats until all tasks have been completed. Task farming is generally considered a coarse-grain approach, well suited to DM-MIMD computers.

Data Decomposition

Many simulations apply similar or identical operations to every member of a large data set. A common example is the solution of partial differential equations using a mesh discretisation and finite difference approximations. If the calculation for several mesh sites can proceed at

the same time then the simulation can be parallelised by decomposing the mesh over several processes so that every process is responsible for storage and computation of one portion of the mesh.

This is often termed *data decomposition* or *domain decomposition* with the latter terminology being more common when referring to data which is associated with a spatial domain which has been discretised as, for example, a regular grid.

Regular Domain Decomposition

The term *regular domain decomposition* usually refers to a data parallel paradigm in which a rectangular mesh, usually stored as a multidimensional array in serial programs, is decomposed over processes in such a way that every process is responsible for storage of, and operations upon, one contiguous rectangular portion of this mesh — see figure C.6. Problems which are amenable to this kind of parallel execution frequently arise in the physical sciences, especially where partial differential equations are solved using finite difference methods.

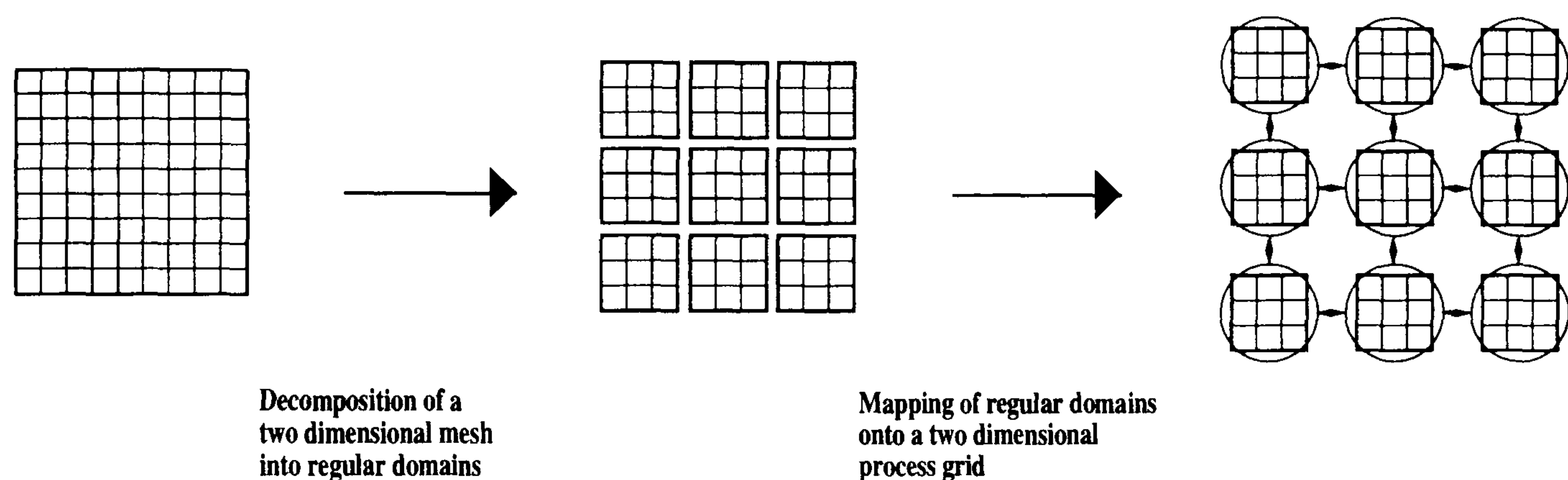


Figure C.6: Geometric domain decomposition in two dimensions.

Geometric domain decomposition is a special case of regular decomposition where grains which neighbour each other in the real world are placed onto neighbouring processes in the logical process grid, the motivation for this being to minimise communication costs.

When boundary data are communicated between neighbouring processes they tend to become *loosely synchronised*. That is, although the processes on a MIMD machine execute asynchronously, they are limited in their freedom to do so by the local interactions between them.

Note that regular domain decomposition may not provide an even distribution of computation among processors, as the amount of computation required may vary with location.

Mixed-mode Parallelism

Data decomposition and functional decomposition techniques are not mutually exclusive and many parallel programs combine them by creating a number of functional units and applying data decomposition to each unit. A common example is the *master* and *slave* paradigm where there are two functional units — the master and the slave. The master unit handles all I/O,

including the user interface and file system. Data is *broadcast* from the master to the slaves, each of which performs the work upon its domain. Results are then *gathered* or *combined*.

Reproducibility

Parallel and sequential implementations of an algorithm may produce slightly different results, depending on the method of parallelisation. For example, it is not uncommon to make slight changes in linear-solver algorithms to allow improved parallel efficiency.

However, programmers writing MIMD software should also address the issue of *reproducibility*. Precise times to perform operations tend to be non-deterministic on all computers, particularly with regard to I/O and in multi-user environments. Moreover, the resources (number of processors, memory, processor clock speed) available to a MIMD program may vary from run to run. Consequently, because MIMD machines are asynchronous, the order in which operations occur is also, by default, non-deterministic. If this is not permissible, it is necessary to use synchronisation to enforce ordering of the operations.

C.1.3 Load Balancing Techniques

Parallel programs often run at the speed of the most heavily loaded process, and this introduces the problem of *load balancing*.

For a functional decomposition, load balancing depends very much on the problem in hand. Typically it is necessary to be very careful to balance the scope of each functional unit. Alternatively, each functional unit may be data-decomposed allowing load balancing by allocating suitable numbers of processors to each functional unit.

It should be noted that many problems in physics and image processing are inherently well balanced under regular domain decomposition and no special effort to ensure load balancing is necessary.

Task farms will to some degree perform automatic load balancing, since a task farm worker process is only assigned additional work packets once it has completed its previous work packet. This means that the time elapsed between the first worker finishing and the last worker finishing can only be as long as the time taken to complete the longest work packet. Therefore, if a very fine grain decomposition is employed, that is, if the problem is divided into many very small work packets, we can expect the load balancing to be good. However there are overheads associated with managing the division of the problem into work packets and the recombining of results. The cost of these overheads must be balanced against the cost of load imbalance.

Some problems require the programmer to work a little harder to achieve good load balancing. Consider figure C.7 where the work associated with a data set is concentrated in one region. The problem is inherently unbalanced and if a simple geometric decomposition is used some processors receive much more work than others, leading to load imbalance.

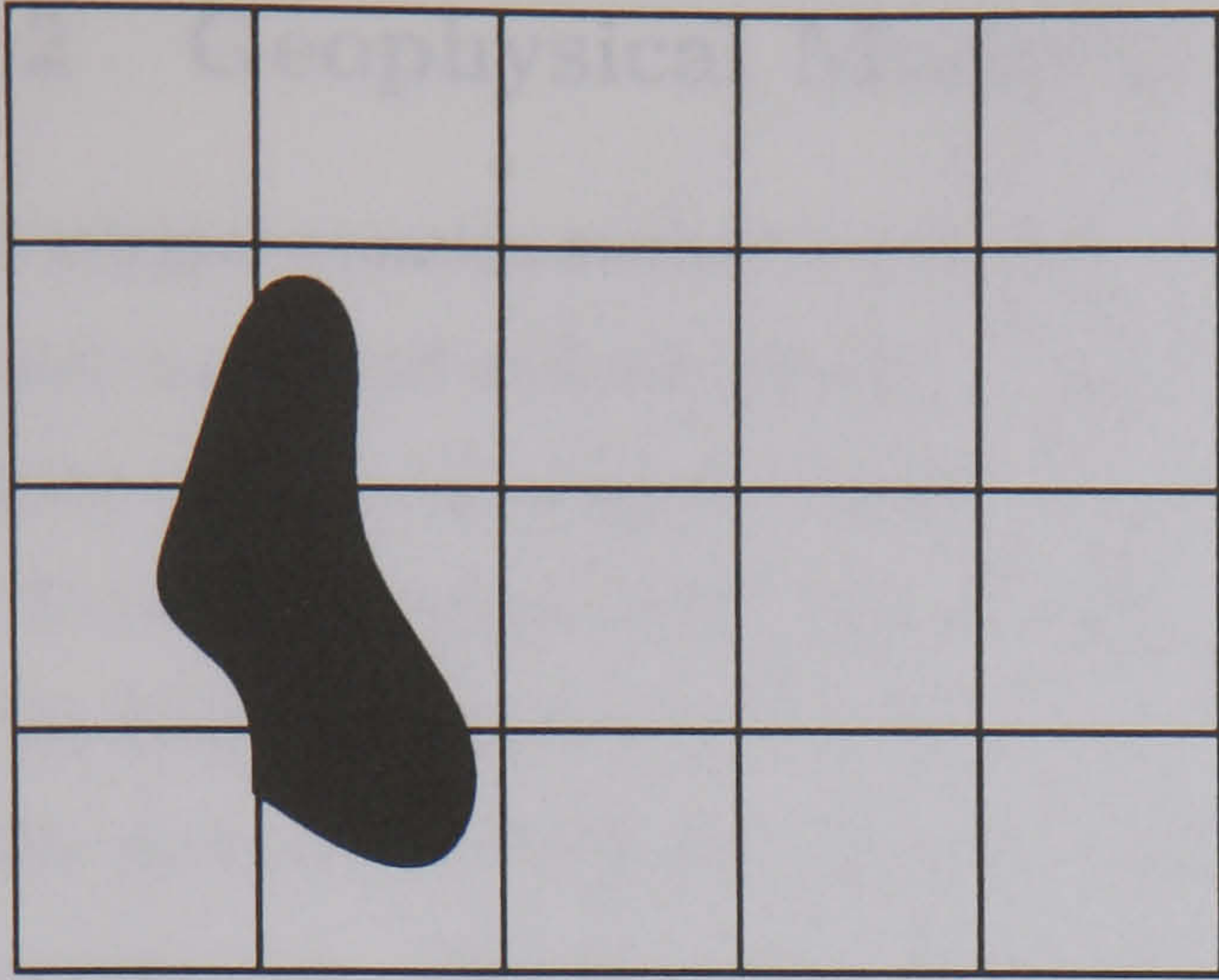


Figure C.7: The work associated with this data is concentrated in the dark region. If a geometric decomposition is employed, certain processors receive much more work than others.

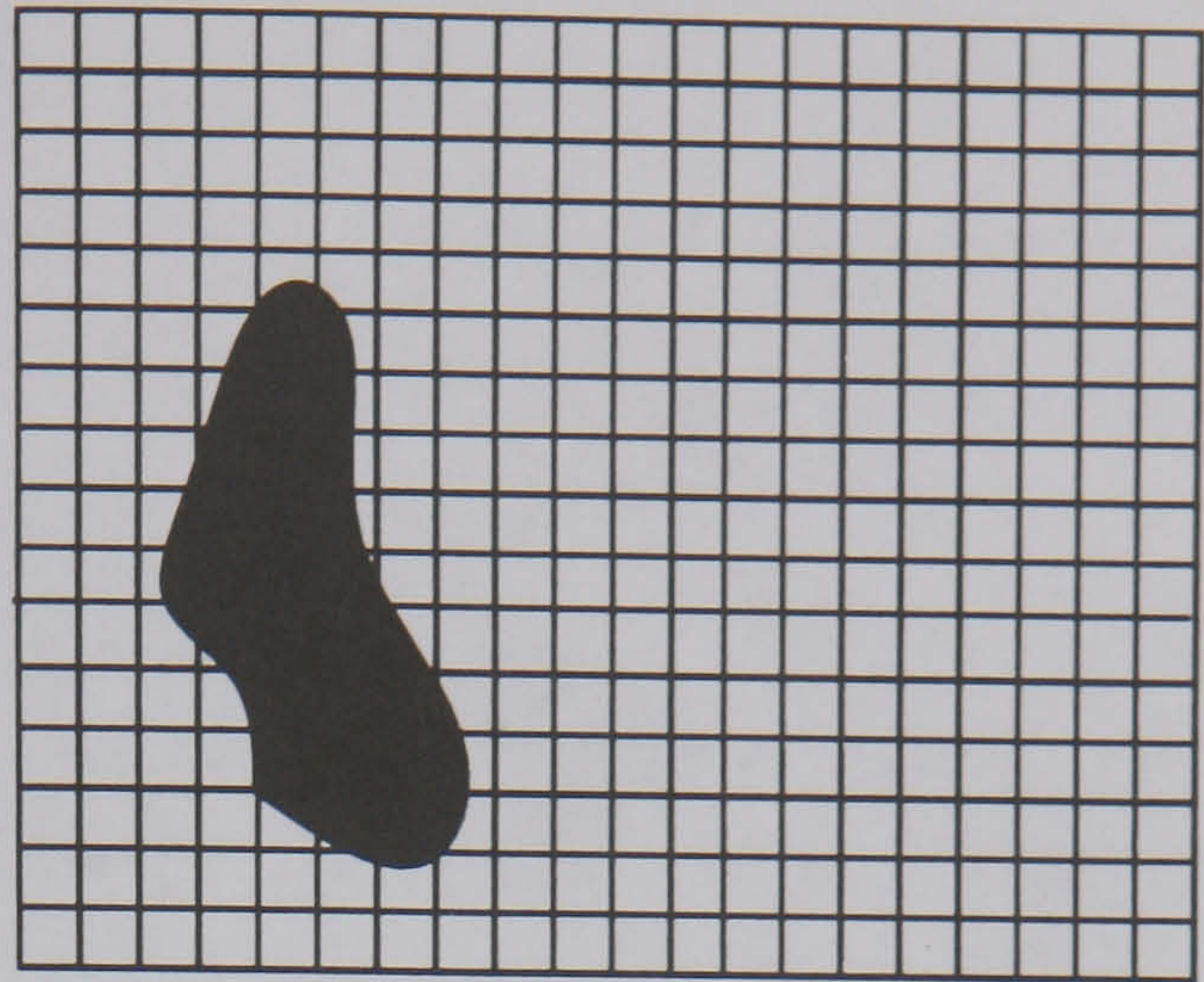


Figure C.8: A scattered spatial decomposition divides the data much more finely and then scatters it, either at random or according to some scheme, thus distributing the work more evenly.

It is important to distinguish between *static* and *dynamic* load balancing. The former seeks to achieve a good load balance solely by judicious mapping of domains to processes. Dynamic load balancing involves the appropriate allocation (or re-allocation) of work to processes while the program is running and is in general a more difficult technique.

One technique which uses a static decomposition is *scattered spatial decomposition* (Salmon January 1988, Nicol & Saltz 1990). This technique aims, as (Nicol & Saltz 1990) suggests, to balance workload without ever actually analysing it. Under this scheme the data set is broken into many more domains than there are processors and each domain is then allocated randomly or cyclically to processors in the hope that each processor will have an approximately equal work-load — see figure C.8. As with task farming, there is a trade-off between using a fine grain decomposition to achieve an even load balance and keeping down the overheads associated with managing too fine a decomposition (Wilson, Mills & Norman 1991).

C.2 Geophysical Modelling with Integral Equations

The integral equation method is well suited to geophysical modelling of 3D anomalies of limited spatial extent and uniform internal properties. It is not suitable for bodies of infinite or semi-infinite extent such as quarter spaces separated by a fault, or a semi-infinite layer.

To recap on terminology, the *primary field* is a source field which is generated externally to the Earth's surface. The *secondary field* is induced by the primary field. The *normal field* is the primary field plus the secondary field induced in a one-dimensional or layered Earth approximation. The total field resulting from a 3D Earth model may be divided into the *normal field* resulting from a layered Earth plus the *anomalous field* resulting from additional (3D) heterogeneities. Usually it is “easy” to solve for the normal field. The anomalous field may then be formulated in terms of anomalous scatterers and Green's functions.

C.2.1 Formulating the EM Induction Problem Using Integral Equations

The EM3D package calculates the frequency domain response of a model using an integral equation formulation (Newman *et al.* 1986). A variety of sources can be constructed using finite length grounded electric dipoles, and receivers can be placed in or over a layered Earth model containing a body of finite extent which is discretised using a number of cuboidal cells.

The total electromagnetic field \mathbf{E}_t resulting from a 3D Earth model may be divided into the normal field \mathbf{E}_n resulting from a suitably chosen layered Earth background, and the anomalous field \mathbf{E}_a resulting from additional (3D) heterogeneities. The normal field incident upon the scattering anomalies then forms the source term for the anomalous field.

This formulation divides the conductivity σ into the normal conductivity σ_n and the anomalous conductivity σ_a ,

$$\sigma(\mathbf{x}) = \sigma_n(\mathbf{x}) + \sigma_a(\mathbf{x}). \quad (\text{C.1})$$

$\mathbf{J}_a = \sigma_a \mathbf{E}_t$ is the (fictional) scattering current in the anomalous body. The anomalous field \mathbf{E}_a may be written as the integral over the scattering body of the contributions from the scattering current,

$$\mathbf{E}_t(\mathbf{x}) = \mathbf{E}_n(\mathbf{x}) + \mathbf{E}_a(\mathbf{x}) \quad (\text{C.2})$$

$$= \mathbf{E}_n(\mathbf{x}) + \int_V \mathcal{G}(\mathbf{x}, \mathbf{x}') \mathbf{J}_a(\mathbf{x}') d\mathbf{x}' \quad (\text{C.3})$$

where $\mathcal{G}(\mathbf{x}, \mathbf{x}')$ is the Green's tensor which describes the field at a point \mathbf{x} due to an infinitesimal scattering current at \mathbf{x}' .

The only unknown in the right hand side of Equation (C.3) is the scattering current \mathbf{J}_a . In

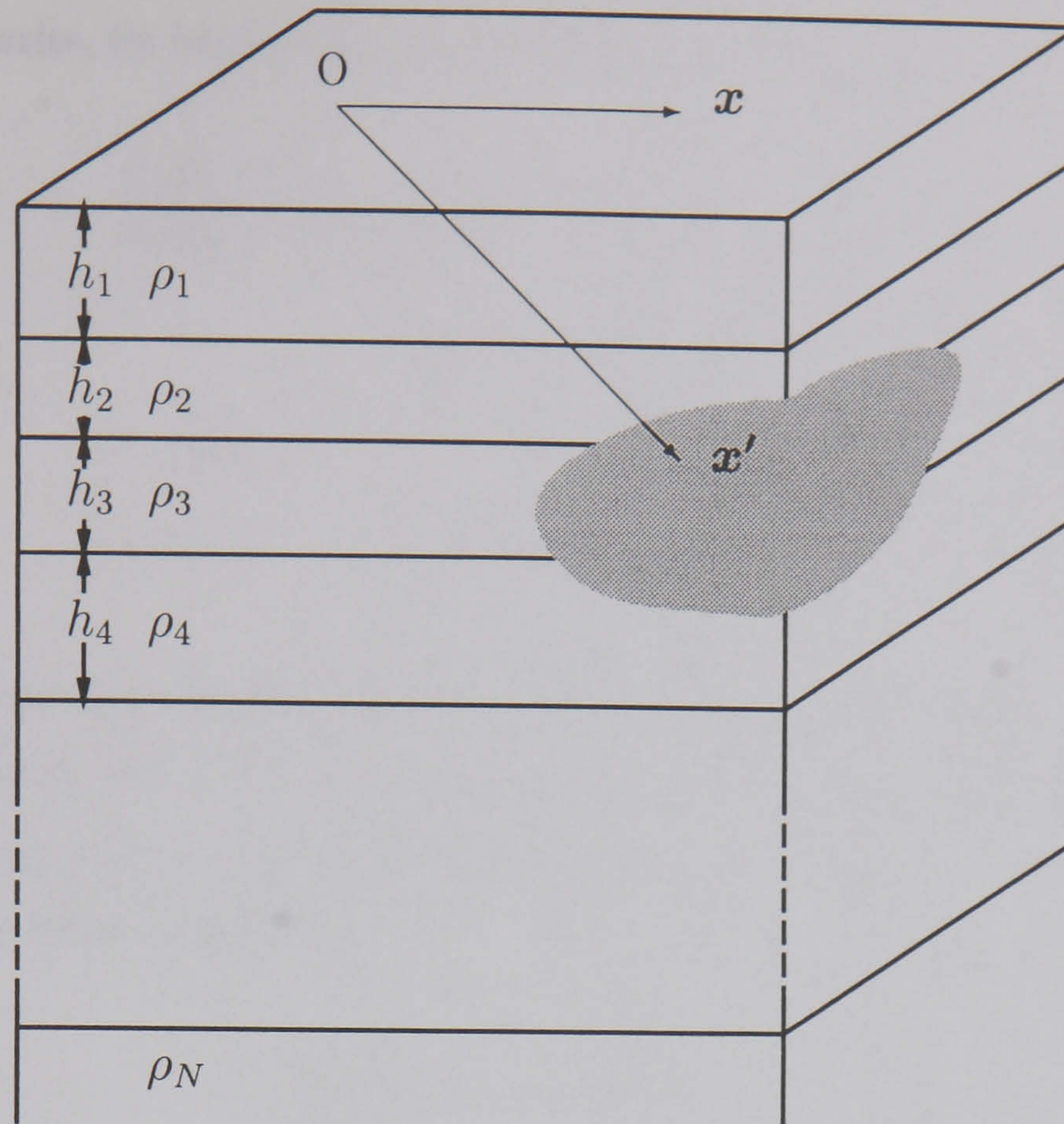


Figure C.9: The Green's tensor $\mathcal{G}(\mathbf{x}, \mathbf{x}')$ describes the field at a point \mathbf{x} due to a infinitesimal scattering current at \mathbf{x}' . The additional field \mathbf{E}_a due to an anomaly may be written as the integral over the scattering body of the product of the Green's tensor \mathcal{G} , the incident (normal) field \mathbf{E}_n and the conductivity anomaly σ_a .

the anomalous body we can calculate \mathbf{J}_a using

$$\frac{\mathbf{J}_a(\mathbf{x})}{\sigma_a(\mathbf{x})} = \mathbf{E}_t(\mathbf{x}) \quad (\text{C.4})$$

$$= \mathbf{E}_n(\mathbf{x}) + \int_V \mathcal{G}(\mathbf{x}, \mathbf{x}') \mathbf{J}_a(\mathbf{x}') d\mathbf{x}'. \quad (\text{C.5})$$

This equation is implicit, since the scattering currents which we seek to calculate appear on both sides of the equation. In order to solve this equation we make a series of approximations which ultimately will yield a system of simultaneous linear equations.

First, the anomalous body is divided into a number of regions V^n . In each region the scattering current is approximated by a constant \mathbf{J}_a^n .

$$\frac{\mathbf{J}_a(\mathbf{x})}{\sigma_a(\mathbf{x})} = \mathbf{E}_n(\mathbf{x}) + \int_V \mathcal{G}(\mathbf{x}, \mathbf{x}') \mathbf{J}_a(\mathbf{x}') d\mathbf{x}' \quad (\text{C.6})$$

$$\approx \mathbf{E}_n(\mathbf{x}) + \sum_{n=1}^N \int_{V^n} \mathcal{G}(\mathbf{x}, \mathbf{x}') \mathbf{J}_a^n dr'. \quad (\text{C.7})$$

Now choosing some set of vectors \mathbf{x}^m which are suitably representative of the location of each

cell V^m we may write, by making the simple substitution $\mathbf{x} = \mathbf{x}^m$,

$$\frac{\mathbf{J}_a(\mathbf{x}^m)}{\sigma_a(\mathbf{x}^m)} \approx \mathbf{E}_n(\mathbf{x}^m) + \sum_{n=1}^N \int_{V_n} \mathcal{G}(\mathbf{x}^m, \mathbf{x}') \mathbf{J}_a^n dr' \quad (\text{C.8})$$

$$= \mathbf{E}_n(\mathbf{x}^m) + \sum_{n=1}^N \Gamma(\mathbf{x}^m, \mathbf{x}^n) \mathbf{J}_a^n \quad (\text{C.9})$$

where

$$\Gamma(\mathbf{x}^m, \mathbf{x}^n) = \int_{V_n} \mathcal{G}(\mathbf{x}^m, \mathbf{x}') dr'. \quad (\text{C.10})$$

Letting $\Gamma^{m,n}$ denote the approximation of $\Gamma(\mathbf{x}^m, \mathbf{x}^n)$ resulting from the numerical integration of the Green's tensor over the cell surrounding \mathbf{x}^n we arrive at a set of simultaneous linear equations. This may now be re-arranged to give a matrix equation that may be solved to yield to the scattering current in each cell.

$$\frac{\mathbf{J}_a^m}{\sigma_a^m} = \mathbf{E}_n^m + \sum_{n=1}^N \Gamma^{m,n} \mathbf{J}_a^n \quad m = 1, \dots, N \quad (\text{C.11})$$

$$\sum_{n=1}^N \left[\Gamma^{m,n} - \frac{\delta_{mn}}{\sigma_a^m} \right] \mathbf{J}_a^n = -\mathbf{E}_n^m \quad m = 1, \dots, N \quad (\text{C.12})$$

where N is the number of cells.

Using this formulation the calculation of the total field begins with computation of the coupling matrices $\Gamma^{m,n}$, which are then factored allowing calculation of the anomalous field. The total field at the receivers is then the sum of the anomalous field with the normal (layered Earth) field, which can be calculated separately.

C.2.2 Scope of the Integral Equation Formulation

The success of the integral equation method in correctly reproducing the behaviour of the continuous geophysical fields which it approximates depends upon careful construction of the approximations which discretise the effect of the scattering body.

For large conductors which have a low contrast with the background, galvanic current flow, or *current channelling*, in the body dominates the transient response. The effect of vortex currents, which flow in closed loops in the body, is negligible (Newman & Hohmann 1985). The strength of the current channelling effect is a function of the host medium, the body's geometry and the conductivity of the background. The time dependence of the response is largely a function of the host medium's primary electric field.

Thin sheet models which assume the response to be purely inductive will give inaccurate results when the response is dominated by current channelling. Integral equation models such as EM3D (Newman *et al.* 1986) can be expected to model accurately responses dominated by current channelling but are not expected to model accurately responses dominated by induction

(Walker & Groom 1995).

The transient response for high-contrast conductors is determined by complex interactions between galvanic and vortex distributions (Filipo, Eaton & Hohmann 1985). Only formulations which accurately model induction, channelling and their interaction can give good results in all configurations.

C.3 Geophysical Modelling with Finite Differences

In the finite difference method the quantities to be modelled are approximated by a discrete representation on a grid or mesh which covers the region of interest. The differential equations which describe the behaviour of the continuous field translate into finite difference equations relating the fields at the nodes of the mesh. Such discrete representations are convenient for computers and can often be translated very effectively onto higher performance parallel computers.

In principle, the finite difference method allows any distribution of Earth properties to be represented, subject to adequate sampling by the finite difference grid. In this way it is more flexible than the integral equation method.

The success of the finite difference method in correctly reproducing the behaviour of the continuous differential equations which it approximates, depends upon careful construction of the difference equations and the finite difference mesh upon which they operate.

Coding is generally easier when a regular mesh is used, particularly for distributed memory computing systems. In addition, the symmetry of a regular mesh can often result in cancellation of terms in the expansion of the partial differential equations resulting in finite difference equations with a higher order of accuracy in the approximation than for a non-regular mesh.

C.3.1 Axi-symmetric Finite Difference Formulation

The electrical conductivity of an axi-symmetric structure is allowed to vary in the radial ρ and vertical z directions, but is independent of the azimuthal angle ϕ . If the electric dipole transmitter is sited arbitrarily, the source must be described fully in 3D. The combination of an axi-symmetric 2D structure and a finite source, the 2.5D problem, has been investigated by Goldman & Stoyer (1983), Chang & Anderson (1984), Pai, Ahmad & Kennedy (1993), Liu (1993) and others, but most compute results for a source located restrictively on the axis of rotational symmetry.

The EMAFD package was initially developed by Liming Yu and Nigel Edwards at the Geophysics Laboratory of the Department of Physics, University of Toronto (Yu 1994). EMAFD uses a finite difference approximation to calculate the response of an axisymmetric target in a double half-space background. The formulation employed by EMAFD divides the electromagnetic field into the normal field, subscript n , and the anomalous field, subscript a . The normal field is the response of a background layered Earth, while the anomalous field is the additional field caused by an anomaly.

The EMAFD code uses the Laplace transform domain, which is equivalent to imaginary frequency values. The anomalous electric and magnetic fields in the Laplace domain can be written as

$$\nabla \times \mathbf{B}_a = \mu_0 \sigma \mathbf{E}_a + \mu_0 \sigma_a \mathbf{E}_n, \quad (\text{C.13})$$

$$\nabla \times \mathbf{E}_a = -s\mathbf{B}_a, \quad (\text{C.14})$$

where σ is the total conductivity and σ_a is anomalous conductivity, the difference between the background and total conductivities.

Since the variable ϕ is periodic, it is convenient to expand the fields as a Fourier series, that is

$$F(\rho, \phi, z) = \sum_{n=-\infty}^{\infty} f_n(\rho, z) \exp(-in\phi). \quad (\text{C.15})$$

Consequently, we have

$$\frac{\partial}{\partial \phi} = -in. \quad (\text{C.16})$$

In the wavenumber domain, the ϕ -components of the electric and magnetic fields satisfy two coupled second order differential equations,

$$\begin{aligned} \frac{\partial}{\partial \rho} \left[\frac{\rho \mu \sigma}{\gamma} \frac{\partial(i\rho E_{a\phi})}{\partial \rho} \right] + \frac{\partial}{\partial z} \left[\frac{\rho \mu \sigma}{\gamma} \frac{\partial(i\rho E_{a\phi})}{\partial z} \right] - \frac{\mu \sigma}{\rho} (i\rho E_{a\phi}) = \\ \frac{n}{\gamma^2} \frac{\partial \gamma}{\partial \rho} \frac{\partial(\rho B_{a\phi})}{\partial z} - \frac{n}{\gamma^2} \frac{\partial \gamma}{\partial z} \frac{\partial(\rho B_{a\phi})}{\partial \rho} \\ - \frac{\partial}{\partial \rho} \left(\frac{n \rho \mu \sigma_a}{\gamma} E_{n\rho} \right) - \frac{\partial}{\partial z} \left(\frac{n \rho \mu \sigma_a}{\gamma} E_{nz} \right) + \mu \sigma_a (i E_{n\phi}), \end{aligned} \quad (\text{C.17})$$

and

$$\begin{aligned} \frac{\partial}{\partial \rho} \left[\frac{s \rho}{\gamma} \frac{\partial(\rho B_{a\phi})}{\partial \rho} \right] + \frac{\partial}{\partial z} \left[\frac{s \rho}{\gamma} \frac{\partial(\rho B_{a\phi})}{\partial z} \right] - \frac{s}{\rho} (\rho B_{a\phi}) = \\ \frac{n}{\gamma^2} \frac{\partial \gamma}{\partial \rho} \frac{\partial(i\rho E_{a\phi})}{\partial z} - \frac{n}{\gamma^2} \frac{\partial \gamma}{\partial z} \frac{\partial(i\rho E_{a\phi})}{\partial \rho} \\ + \frac{\partial}{\partial \rho} \left(\frac{\rho^2 s \mu \sigma_a}{\gamma} E_{nz} \right) - \frac{\partial}{\partial z} \left(\frac{\rho^2 s \mu \sigma_a}{\gamma} E_{n\rho} \right), \end{aligned} \quad (\text{C.18})$$

where $\gamma = n^2 + \rho^2 s \mu \sigma$.

EMAFD approximates these equations using finite differences and then employs an iterative numerical technique to solve for anomalous field. For a given azimuthal harmonic n and a Laplace variable value s , the electric field is first computed from Equation (C.17) neglecting the magnetic field terms. The magnetic field is then computed from the equation (C.18) using the calculated electric field. The next iteration of the equation (C.17) includes the calculated magnetic field, and so on until the fields stabilize, usually in 3 to 8 iterations. The MUDPACK finite difference package from NCAR (Adams 1989) is used to solve the differential equations at each iteration. The ρ and z components of the electric and magnetic fields are then calculated from the ϕ component and its derivatives.

Finally the fields are converted back to the time-space domain by applying inverse Fourier and Laplace transforms. The Gaver-Stehfest technique was selected to invert the Laplace transform. The Gaver-Stehfest technique is neither the most accurate nor the most generally applicable. However, the algorithm does offer the user the advantage of speed, simplicity and

perhaps most important of all, the need to compute the transform function $F(s)$ only for *real* values of the Laplace variable s . A detailed description of the algorithm may be found in (Stehfest 1970, Knight & Raiche 1982, Villinger 1985, Edwards & Cheesman 1987).

C.4 Task Farm Parallelisation of EM Simulation

C.4.1 Software Engineering

The EM3D and EMAFD codes employ a frequency domain formulation. In these programs the solution for one Fourier domain component is calculated independently of other components. Many components are required to calculate a suitable range of time domain responses. It is possible to obtain an increase in performance by simultaneously running the calculation for each different Fourier component on different processors. Normally a series of different Earth models would be investigated which further extends the number of processors which can be usefully employed.

The EM3D and EMAFD programs have been parallelised using a task farm. PUL-TF, a parallel utility library written at the Edinburgh Parallel Computer Centre (Bruce et al. 1995) was chosen as a ready built task farm implementation. Subroutines were written to perform the source, sink and worker tasks and linked to the PUL-TF libraries and the main program altered to call the PUL-TF utility which then controls and coordinates the operation of the task farm — see figures C.10, C.11 and C.12.

In this parallel implementation of EM3D every process in the task farm contains the full functionality of the application. At run-time the first process to register with the message passing system is selected as the “master” process. The master process reads in the model input file and counts how many tasks (models and frequencies) there are before passing control to PUL-TF. During operation of the task farm the master process will act as source and sink but may also act as a worker if this would help spread computation evenly over the processors. This single program multiple data (SPMD) programming model is required by some DM-MIMD computers.²

The source subroutine packs into an array a description of the next task to be executed. The worker subroutine unpacks the task description and calls the main calculation routine. This picks the specified model and frequency from the model description file, and calculates the response. Since many processes are run at the same time, all I/O had to be modified so that each process would write to a different file. This was easily achieved by using the number of the task currently being worked upon as an extension to filenames. After the main calculation for each task the worker subroutine packs into an array a confirmation that the task has been correctly completed. This is passed to the sink subroutine, which in this task farm

²Note that PUL-TF is very flexible and does not force the user to use a SPMD programming model.

[illegible]

Figure C.10: Main program section for sequential version of EM3D.

only undertakes simple book-keeping of which tasks have been completed.

The use of re-usable utilities such as PUL-TF minimises porting effort. Porting one of the simulation programs required 100 lines of new code and around 60 modified lines to port a total of 5,500 lines. However utilities such as PUL-TF cannot mitigate against poor software design. Another of the simulations required dramatic re-structuring before it could be parallelised sensibly.

In addition to reducing coding effort, PUL-TF increases portability by hiding some system dependencies. Versions of the PUL-TF library are available for all the main parallel systems and our parallel programs have been tested on networks of Sun and SGI workstations, T800 and i860 based Meiko Computing Surfaces and a Cray T3D.

C.4.2 Performance Analysis

A series of experiments was undertaken to test the effectiveness of the task farm parallelisation of the EM3D simulation on a heterogeneous workstation cluster. In order to keep the computational cost of these simulations to a reasonable level a very simple test model was chosen from the literature (figure 9, Newman et al. 1986). This model consists of a single anomalous body in a halfspace illuminated by a loop source and with a line of receivers. Symmetry is exploited to allow discretisation of the body using just 5 cells.

This model consists of a single anomalous body in a 100 Ωm halfspace. The anomaly is a 1 Ωm body $20 \times 600 \times 60$ m ($x \times y \times z$) in dimension centred below origin and buried so that the top of the body is 40 m below the surface. The 1st quadrant of the body is discretised using 5 cells, and the complete body then made up by using symmetry in two dimensions. This Earth model is illuminated using a 500 x 600 m loop source ($x \times y$) on the surface with the centre of loop offset 560 m from the origin in the negative x direction. Receivers are situated every twenty m along a line through the origin out to 90 m from the origin in the positive and negative x directions.

In order to measure the success of a parallelisation we might plot the total execution times of an n -processor implementation against n . Since the workstation cluster employed is heterogeneous, and each workstation has a different performance, it is more informative to plot against total capacity of the workstations employed. The relative performance of each workstation is gauged by running the simple test model on each workstation, recording the execution time and then normalising relative to the performance on a Sun Sparc 2 — see Table C.1.

Machine	Abbreviation	Description	Elapsed Time (minutes)	Normalised Performance
briar	b	Sparc 10	1.8	2.36
fungi	f	Sparc 2	4.3	0.99
gorse	g	Sparc 2	4.25	1.00
rose	r	Sparc 2	5.0	0.85
sitka	s	Sun ELC	5.333	0.797
sage	sg	Sun ELC	5.75	0.748
oak	o	Sun IPC	7.133	0.596

Table C.1: Timing Results for dike4 model using 1 frequency.

Also plotted in Figure C.13 is the minimum time in which the program could have been expected to complete. A more revealing measure of success is to plot the *speed up* of the program, defined as the relative speeds of an n -processor and a single-processor implementation. A perfect result would give a straight line, but Figure C.14 reveals that, eventually, using yet more processors does not yield as great an increase in performance as might be expected.

Because the task farm waits for a processor to finish its current task before allocating it further work, variations in workstation performance are compensated for, provided there are

sufficiently many tasks. As the number of processors is increased it becomes progressively harder to divide the finite number of tasks between them such that each processor is fully loaded for the entire time of the calculation.

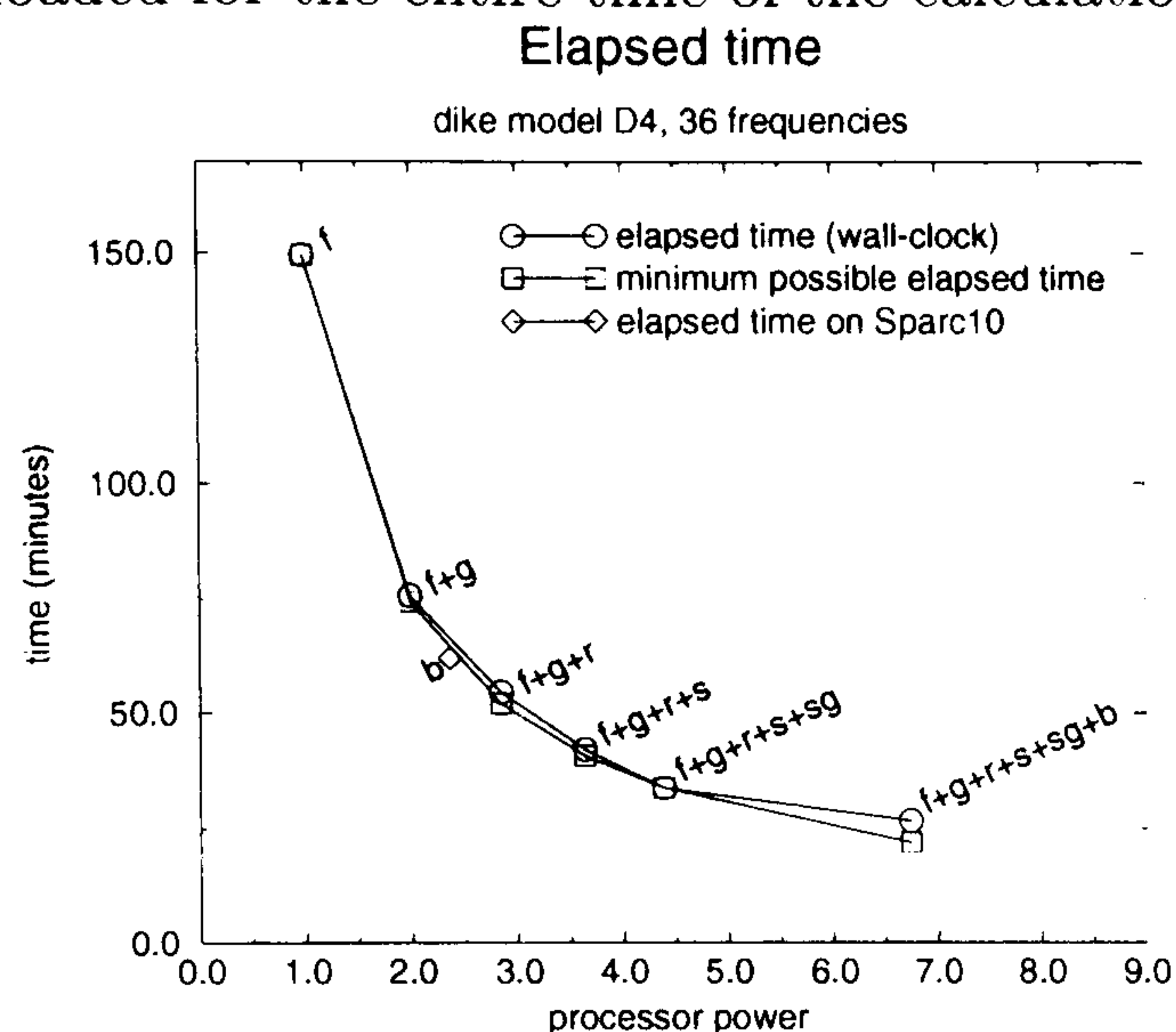


Figure C.13: Execution times of the task farm version of EM3D running dike4 model using 36 frequencies.

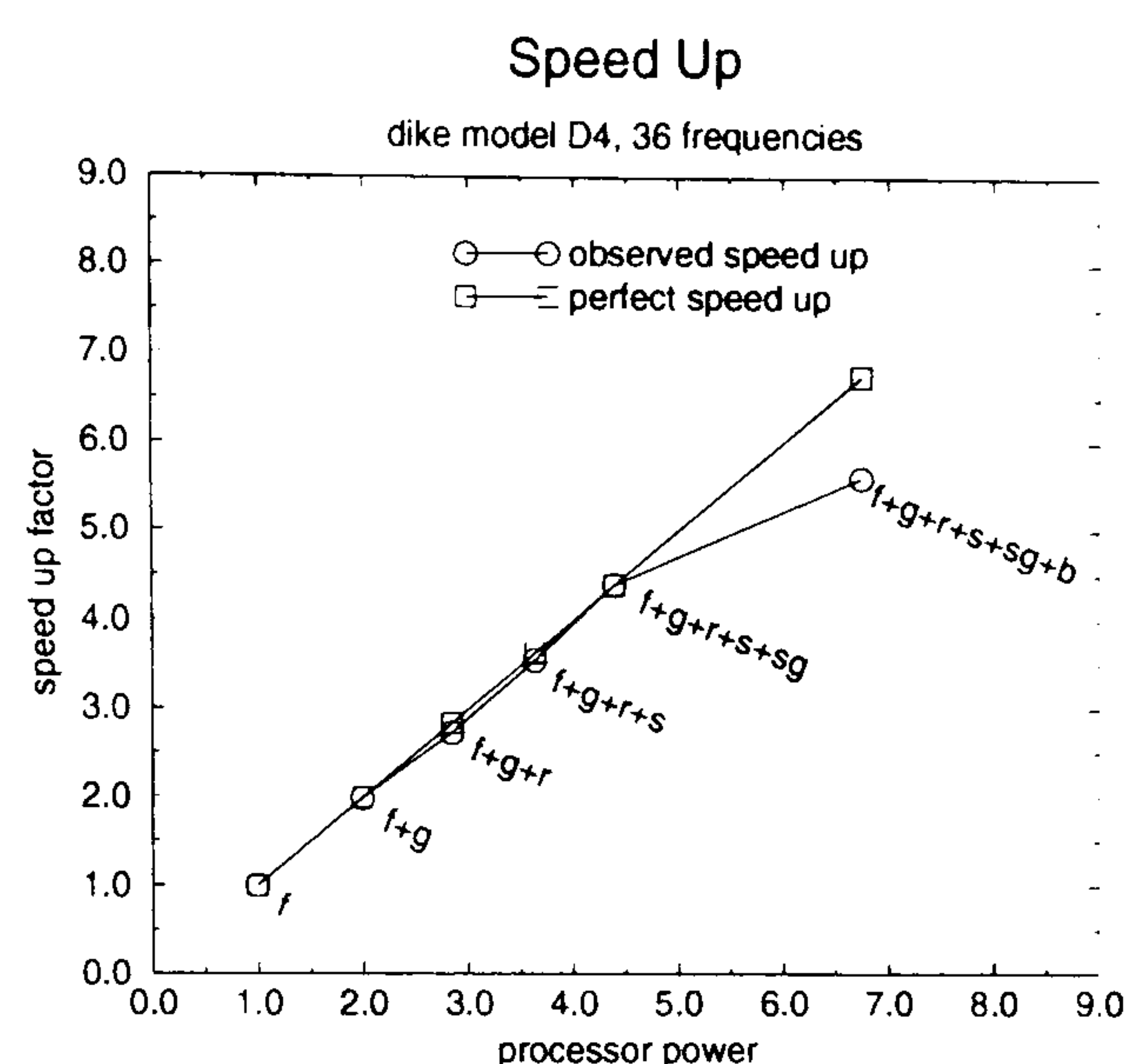


Figure C.14: Speed up of the task farm version of EM3D running dike4 model using 36 frequencies.

C.4.3 Large Scale Feasibility Studies

The EMAFD package calculates the response of a dipole source in an axisymmetric Earth model. The calculation proceeds in a transform domain where a Laplace transform is taken with respect to time and a Fourier transform with respect to azimuth. Parallelising over both temporal and azimuthal components results in several hundred independent tasks. Each task requires approximately the same amount of computation. This allows the task farm version of EMAFD to make effective use of a massively parallel computer.

The task farm version of EMAFD was ported to run on the Edinburgh Cray T3D, which contains 512 DEC Alpha processors each running at 150 MHz with 64 Mb of memory. This allowed feasibility studies to be undertaken with large scale models in a reasonable amount of time — see Section D.2.

C.5 Conclusions

The EM3D integral equation electromagnetic modelling program and the EMAFD finite difference electromagnetic modelling program have been parallelised using the task farm approach. For both programs this approach allowed an efficient numerical algorithm to be retained, and was able to run on an existing departmental workstation cluster. These computers often have spare CPU cycles waiting to be used, and this has proved an ideal method of speeding up computationally expensive tasks without purchasing financially expensive equipment. Despite using workstations of widely varying performance, the task farm did a good job of balancing the load amongst processors without requiring detailed analysis of the relative performance of processors or the amount of work to be done.

The PUL-TF utility (Bruce, Chapple, MacDonald, Trew & Trewin 1995), which provides a ready made task farm framework into which the application can be bolted, reduces porting effort and increases portability. Our task farm codes are now in use on several platforms ranging from workstation clusters to a massively parallel Cray T3D supercomputer.

Despite these achievements the coarse-grained task farm approach has a limited degree of inherent parallelism which limits the number of processors which can be usefully exercised. The parallel EMAFD program can make good use of hundreds of processors but would not sensibly scale to use thousands of processors. A highly scalable implementation might be obtained by parallelising the work of each task. Such a mixed-mode approach would ease the search for a suitable linear solver since the parallel solver need only scale efficiently to a modest number of processors, rather than to a massive number of processors. This approach would be well suited to the growing number of parallel non-uniform memory access (NUMA) computers.

Appendix D

Feasibility Studies

The feasibility of detecting a geological target using electromagnetic surveying may be investigated using analogue model studies (Szarka & Nagy 1992, Szarka, Nagy & Szala 1994) or numerical simulation. In this chapter numerical modelling techniques are applied to investigate the feasibility of detecting hydrocarbon reservoirs due to their higher resistivity than the surrounding rocks.

Eadie (1981) and Kaufman & Keller (1983) develop theory indicating that for the surface-to-surface acquisition configuration resistive units are best resolved by MTEM methods with galvanic sources. That is sources, such as a grounded electric bipole, which couple galvanically with the Earth resulting in significant vertical current flow. For such configurations the maximum depth of investigation is determined by the offset from the source to the receiver. Sub-aerial surface to surface electromagnetic methods are unlikely to be able to delineate hydrocarbon accumulations much below 3 km, due to the finite thickness of a typical reservoir (Eadie 1981). Realistic exploration depths are of the order of up to 1 km.

Two different Earth models are considered here, both of which are based upon well-logs from real hydrocarbon reservoirs. The first Earth model represents gas storage in a shallow reservoir at around 500 m depth. In this case it is assumed that the acquisition is taking place on land, with both electromagnetic sources and receivers sited at the Earth's surface.

In the final model the reservoir is under approximately 500 m of rock which in turn is below a significant depth of water, and the feasibility of detecting the reservoir using sub-marine electromagnetic soundings is studied. For this final study an axi-symmetric Earth model is used, which represents the reservoir as a disk of anomalous conductivity.

D.1 1D Modelling of a Shallow Gas Storage Reservoir

This section presents the results and conclusions of numerical modelling of the EM response of a shallow gas-storage reservoir. The geology of the area is modelled as a series of stratified layers with the gas reservoir causing a localised change within a particular layer. In the modelling described in this section, the anomalous resistivity value is initially assigned to the entire layer of interest. That is, a 1D Earth model is employed. If it is judged feasible to detect a response due to a change in the resistivity of this layer of infinite extent then this justifies further analysis using a 3D model.

D.1.1 Description of Earth Model

In order to model the effect of varying gas saturation, three models have been studied. For compactness these models are referred to as models IL10, IL100 and IL200. Table D.1 lists the thickness, depth and resistivity of each layer in model IL200. This model was prepared by blocking resistivity logs from a shallow gas-storage reservoir in France and represents a hydrocarbon saturated reservoir. Models IL10, IL100 and IL200 have identical layer thicknesses and resistivities except for layer 5, the layer of interest, which holds the gas reservoir. Model IL10 has no resistivity anomaly and represents a water saturated reservoir. Model IL200 has a significant resistivity anomaly and represents a hydrocarbon-saturated reservoir. Model IL100 has a reduced resistivity anomaly and represents a partial hydrocarbon saturation. The variation of thickness and resistivity of these layers is summarised in table D.2, and presented graphically in Figure D.1.

	thickness (m)	depth (m)	resistivity (Ωm)
layer			
1	140	0-140	50
2	20	140-160	15
3	150	160-310	50
4	180	310-490	10
5	30	490-520	200
6	-	520-	10

Table D.1: Layer thicknesses, depths and resistivities for model IL200. Layer 5 represents the hydrocarbon-saturated reservoir.

	layer 5	
	thickness (m)	resistivity (Ωm)
model		
IL10	30	10
IL200	30	200
IL100	30	100

Table D.2: Thicknesses and resistivities for layer 5 of models IL10, IL100 and IL200. All other layer thicknesses and resistivities are as model IL200.

D.1.2 Description of the Acquisition Configuration

The Earth model is illuminated by a horizontal electric current dipole transmitter, with a dipole moment of 250 A m. For convenience, and to fix our coordinate system, the dipole is centred on the origin and aligned with the x axis. In order to describe the location of receiving stations a right-handed coordinate system (x,y,z) is employed with z increasing into the ground.

Resistivity Models

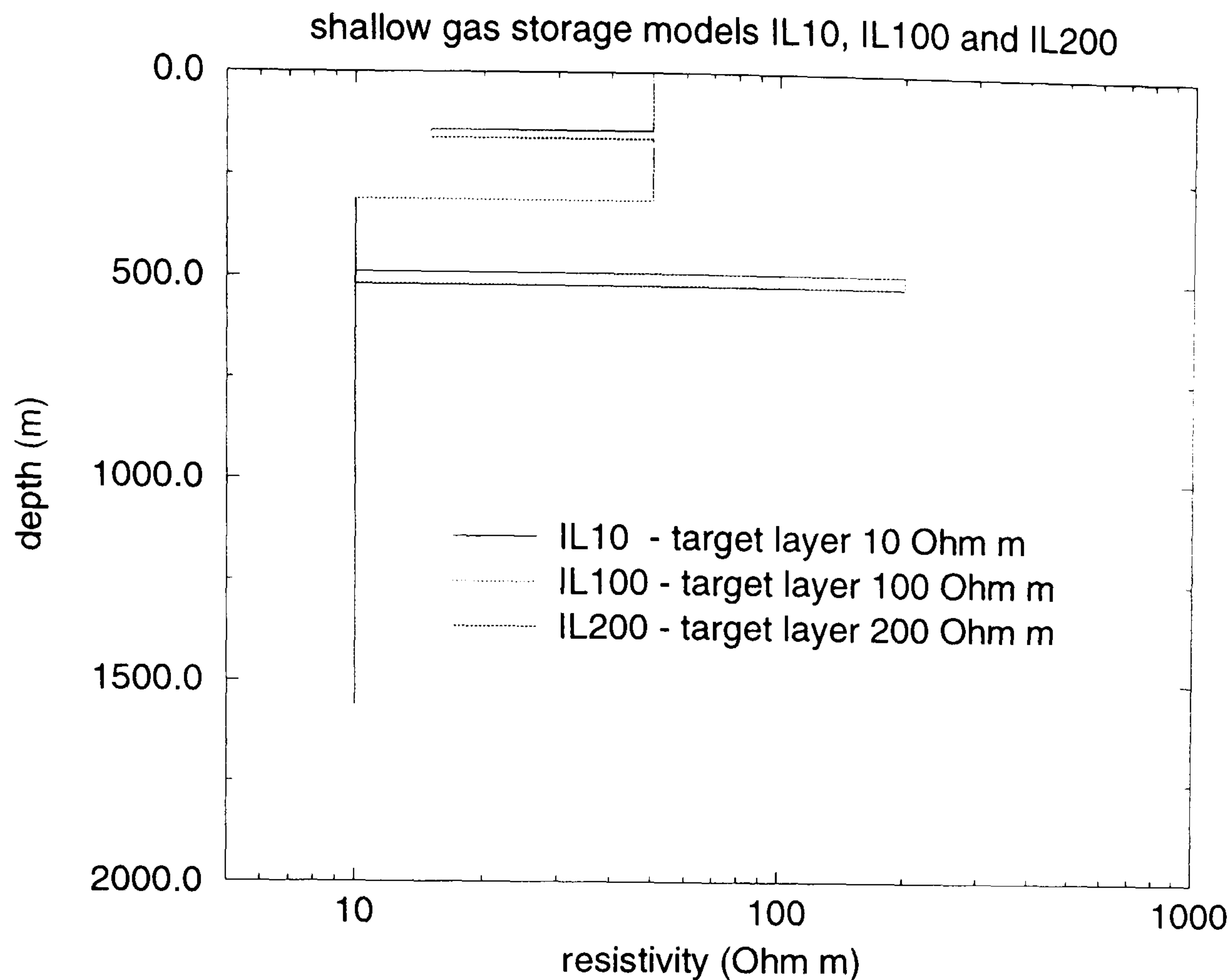


Figure D.1: Resistivity versus depth profiles for 1D Earth models IL10, IL100 and IL200. The top of the target layer is at a depth of 490 m. In model IL10 the target layer has no resistivity anomaly and represents a water saturated reservoir. Model IL200 has a significant resistivity anomaly and represents a hydrocarbon-saturated reservoir. Model IL100 has a reduced resistivity anomaly and represents a partial hydrocarbon saturation.

It is common practice in MTEM surveying to measure some horizontal component of the electric field using a grounded electric current bipole, plus the rate of change of the vertical component of the magnetic field using an induction coil (Strack 1992). Following the LOTEM naming convention E_x is used to denote the component of electric field parallel to the transmitter, E_y to denote the component of electric field orthogonal to the transmitter and dH_z/dt to denote the rate of change with time of the vertical component of the magnetic field.

Because of the symmetry of the model E_y is zero at azimuths of 0° and 90° from the transmitter direction, and so it is not useful to consider E_y . The response to the hydrocarbon reservoir is not so great for the dH_z/dt component as for the E_x component and so only results for the E_x response are presented here. Although we do not consider the dH_z/dt component here, it remains important to measure this component in the field as it provides complimentary information to the E field, and thus greatly aids interpretation of field data.¹ A total of 18 receivers has been modelled, starting at an offset of 125 m from the transmitter dipole and spreading out in-line with the transmitter at intervals of 125 m.

The modelling has been performed using the program MODALL (Strack 1992). This yields the

¹

time domain response for a *switch-on* transmitter current profile, that is, a transmitter current which is zero for negative times and constant for positive times. MTEM fieldwork is performed with a bipolar transmitter current profile, and then converted to a switch-on response during pre-processing (see section 6.2.1).

D.1.3 Results

Figure D.2 shows the switch-on response at receiver offsets from 250 m to 2250 m in intervals of 250 m for model IL200 (the fully gas saturated model). When presented on a log-log plot such as this, the characteristic fall-off of amplitude with offset is clear. Also apparent is the characteristic shape of the signal.

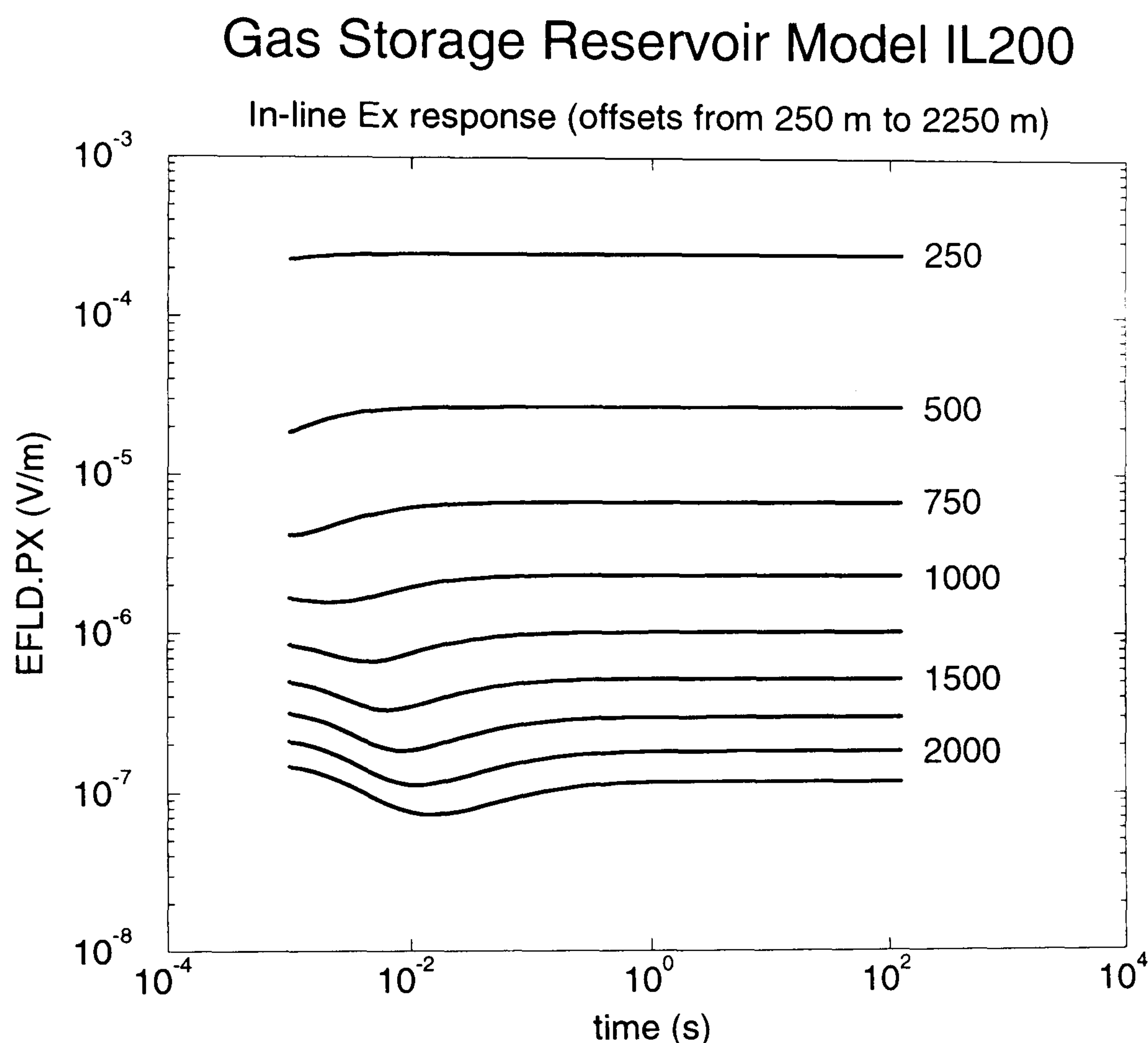


Figure D.2: The switch-on response for the in-line Ex component for model IL200, at receiver offsets from 250 m to 2250 m in intervals of 250 m. Presentation on a log-log plot such as this figure accentuates the characteristic change in signal amplitude and shape with offset from the transmitter. At the earliest and latest times the signal asymptotes to a constant. Interesting information about the Earth's response is captured within an intermediary time interval. This interval becomes later in time, and the amplitude of the response decreases, with increasing offset from transmitter to receiver.

Figure D.3 compares the switch-on response at 2000 m offset for models IL200 (the fully gas saturated model) IL100 (partially gas saturated) and IL10 (water saturated). At the earliest times, the response is determined by the near surface resistivity, while the limiting DC response

is a cumulative function of the entire section. There is a characteristic intermediate time-range at which variations in the response give information on the target zone. From this plot it is clear that there is a significant response to the hydrocarbon layer which increases with saturation.

The ratio of components for each pair of models may be plotted in order to give a better impression of the relative magnitude of this difference. The ratio of the response for model IL200 to the response for model IL10 is plotted in Figure D.4. This plot emphasises the distinct spatial pattern of the response as offset from the transmitter is varied. This pattern is dependent upon the depth and resistivity of the target layer and may be exploited using a MTEM survey to detect variations in resistivity at depth which might be unresolvable with single channel systems.

Shallow Gas Storage Reservoir Model

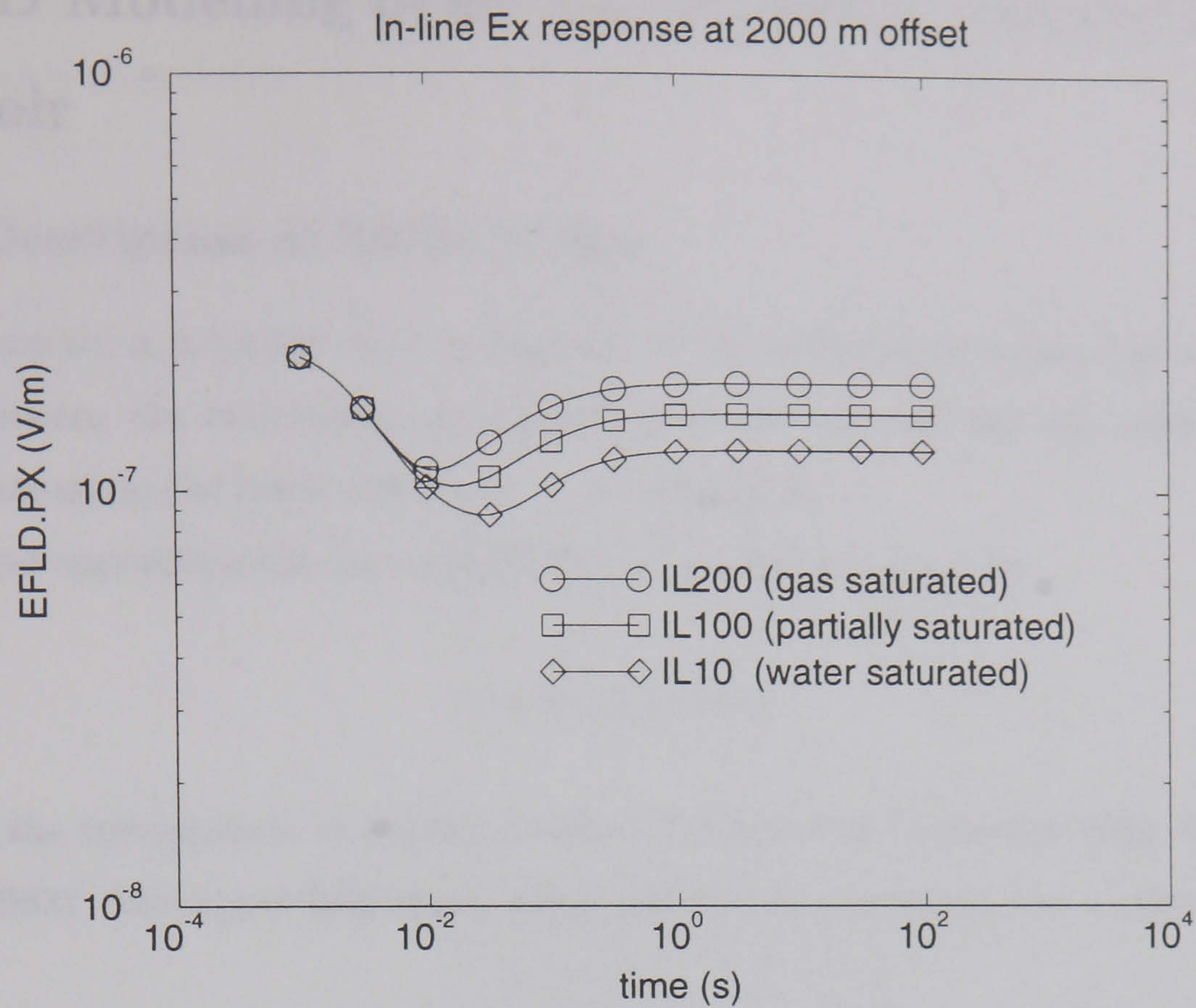


Figure D.3: Comparison of in-line Ex response for models IL10, IL100 and IL200.

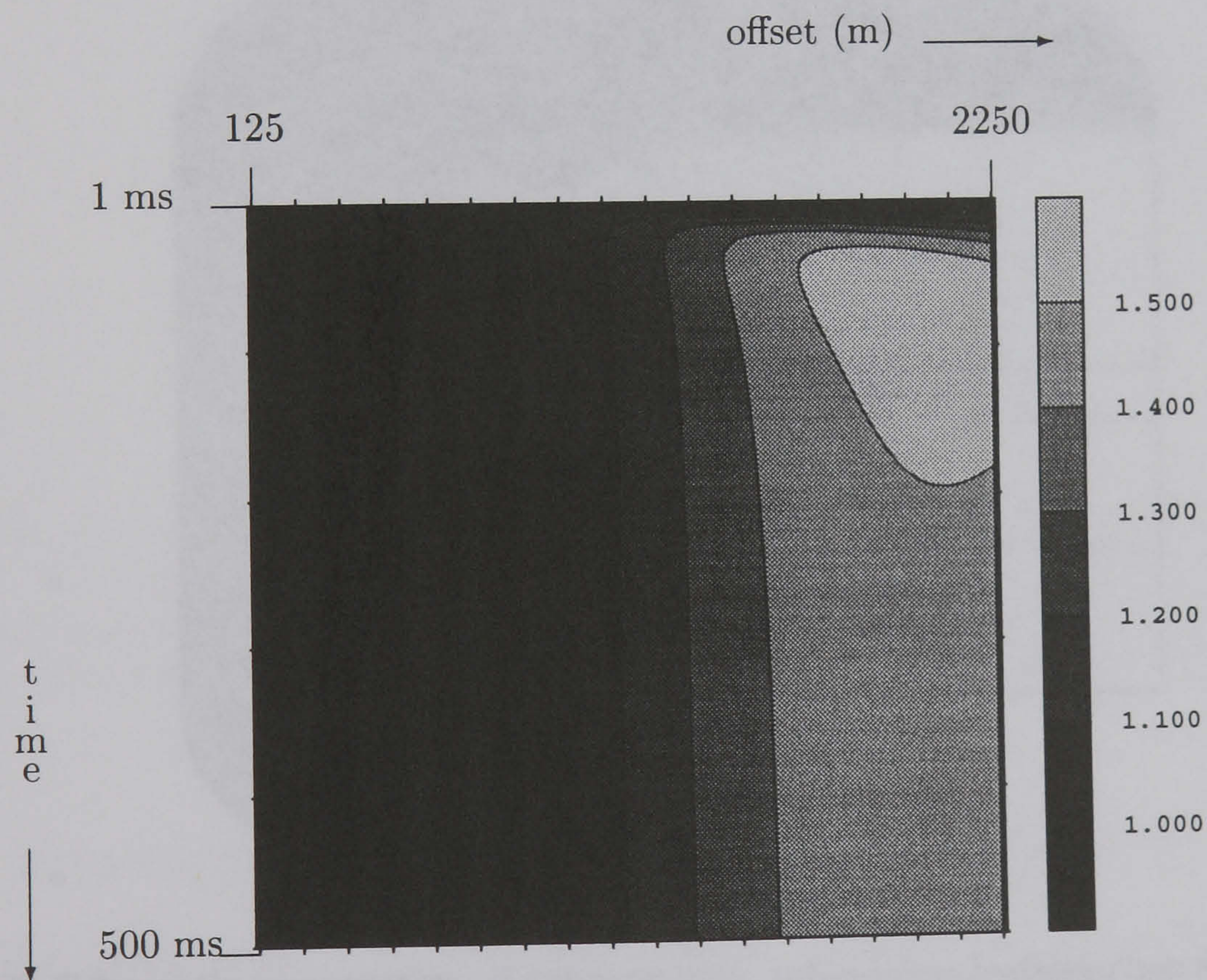


Figure D.4: The ratio of in-line Ex components for models IL200 and IL10 presented as a contour plot. Receivers are plotted against time with receiver offset increasing from left to right and time increasing down the page. Receiver offsets varies from 125 m to 2250 m in intervals of 125 m, while the time range is from 1 ms to 500 ms in intervals of 1 ms.

D.2 3D Modelling of an Axisymmetric Submarine Reservoir

D.2.1 Description of Earth Model

The configuration is modelled as a background of two uniform, isotropic, half spaces with the interface between the half spaces corresponding to the sea bed and the reservoir forming a resistive anomaly in the lower half space — see Figure D.5.

To a good approximation the conductivity of sea water is given by

$$\sigma_s = 3 + T/10Sm^{-1}, \quad (D.1)$$

where T is the temperature in degrees Celsius (Bradshaw & Schleicher 1980, Herzen, Francis & Becker 1983). The upper half space, which models the sea water, has a resistivity of $0.3125 \Omega m$.

The lower half space, which models the seabed, has a resistivity of $10 \Omega m$. The reservoir is modelled as a moderately resistive disk with a depth centred at 500 m below the sea bed, a vertical thickness of approximately 200 m and a horizontal radius of approximately 1000 m.

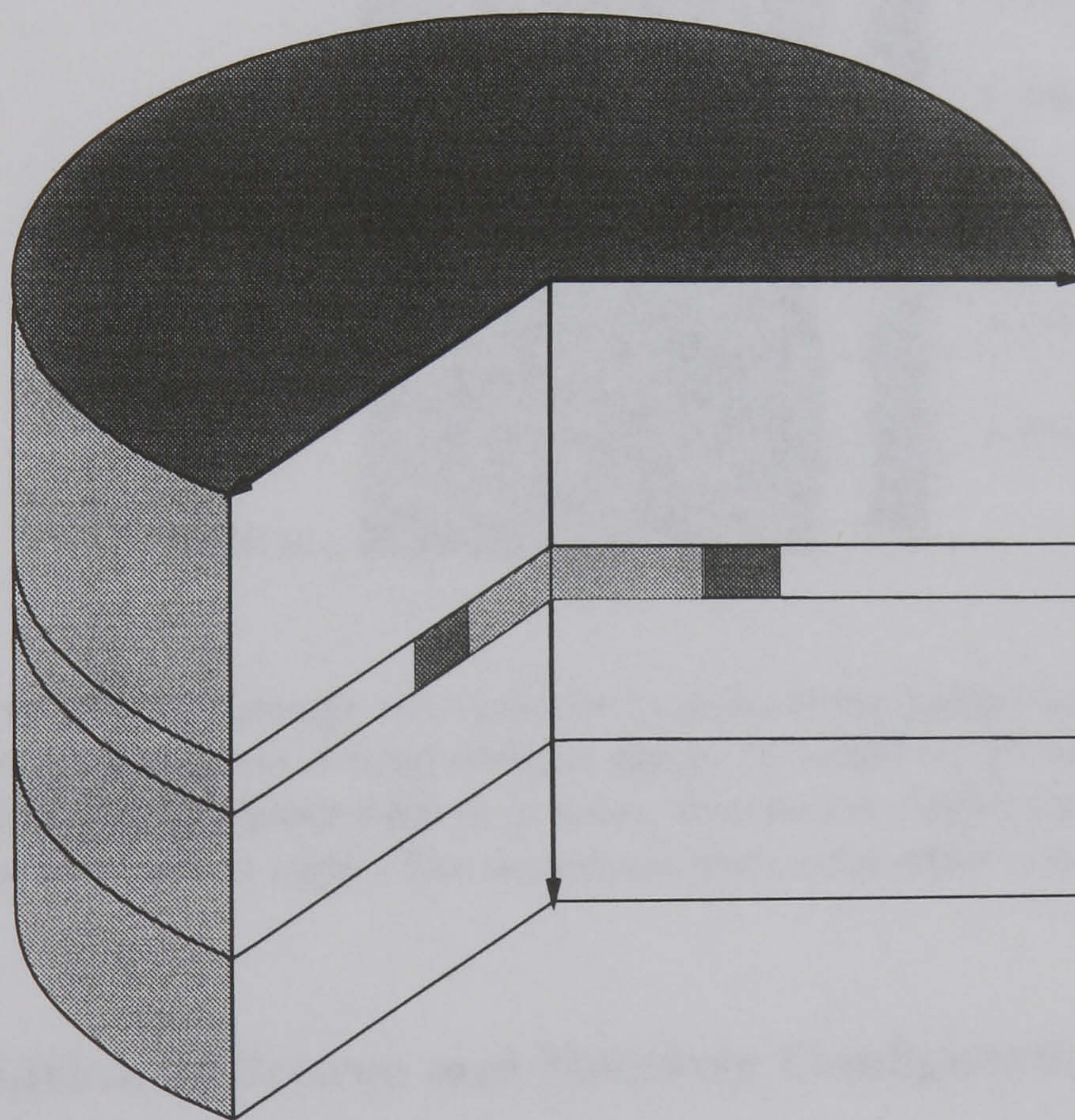


Figure D.5: Schematic presentation of axisymmetric sub-marine hydrocarbon reservoir in which subsurface resistivity is modelled as varying with depth and radial offset. If the source may be sited arbitrarily then the source must be described fully in 3D. This combination of a 2D Earth model and 3D source model is sometimes called a 2.5D problem.

Computation of the anomalous field takes place on a regular finite difference grid extending 6400 m above and 6400 m below the sea bed and with a radius of 6400 m. The grid is

discretised using a $50 \text{ m} \times 50 \text{ m}$ mesh size. In order to achieve numerical convergence of the finite difference scheme the conductivity distribution is smoothed under user control. This smoothed conductivity section is used only to calculate the secondary field — the primary field is calculated using the analytic formula for a double half space. Figure D.6 presents the smoothed conductivity section on the finite difference grid. Figure D.7 presents a vertical profile of conductivity at zero offset.

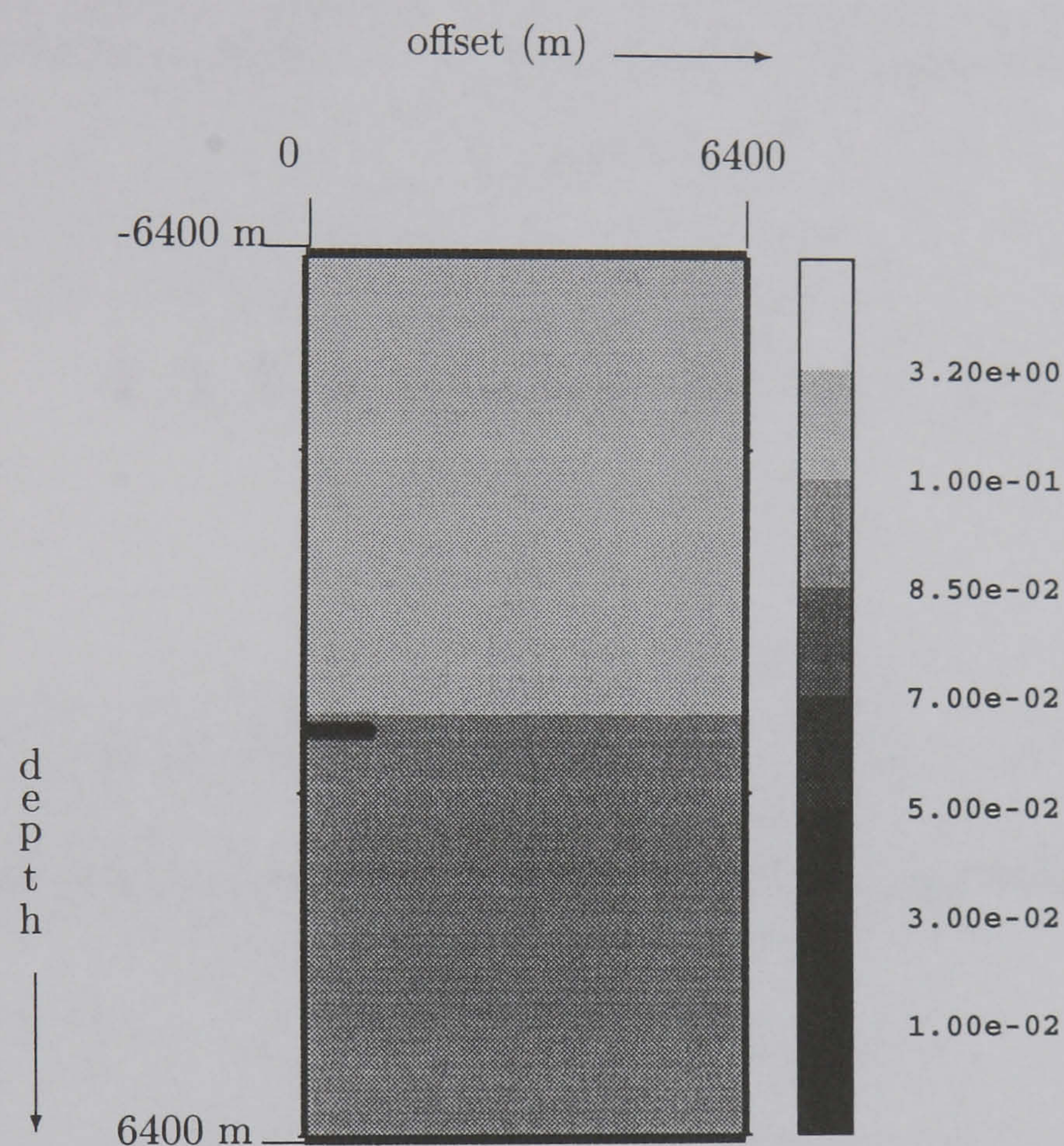


Figure D.6: Vertical section through the smoothed conductivity model for sub-marine model ilm3000b. The section represents a total vertical extent of 12800 m, of which the upper 6400 m is above the seabed and the lower 6400 m is below the seabed. Offset from the axis of radial symmetry increases from left to right. The maximum horizontal offset is 6400 m.

D.2.2 Description of Source and Receiver Configuration

A horizontal electric current dipole source is modelled lying on the sea bed, 1500 m off the axis of rotational symmetry of the Earth model. Electric dipole receivers are placed from an offset of 50 m at intervals of 50 m. The time domain response is calculated for a switch-off transmitter current profile. Broadside and collinear source-receiver configurations are investigated — see figure D.9.

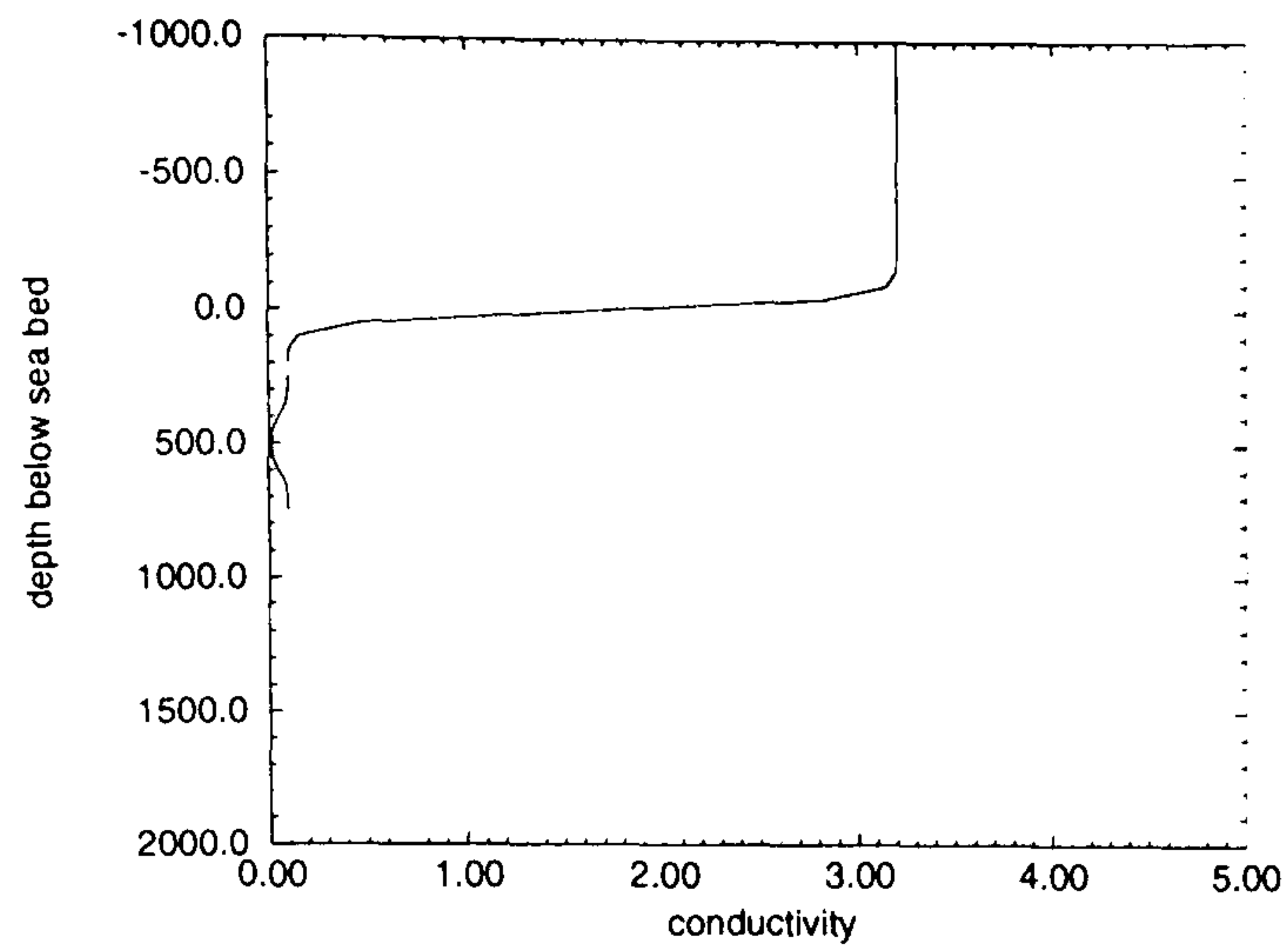


Figure D.7: Smoothed vertical conductivity profile for sub-marine model ilm3000b.

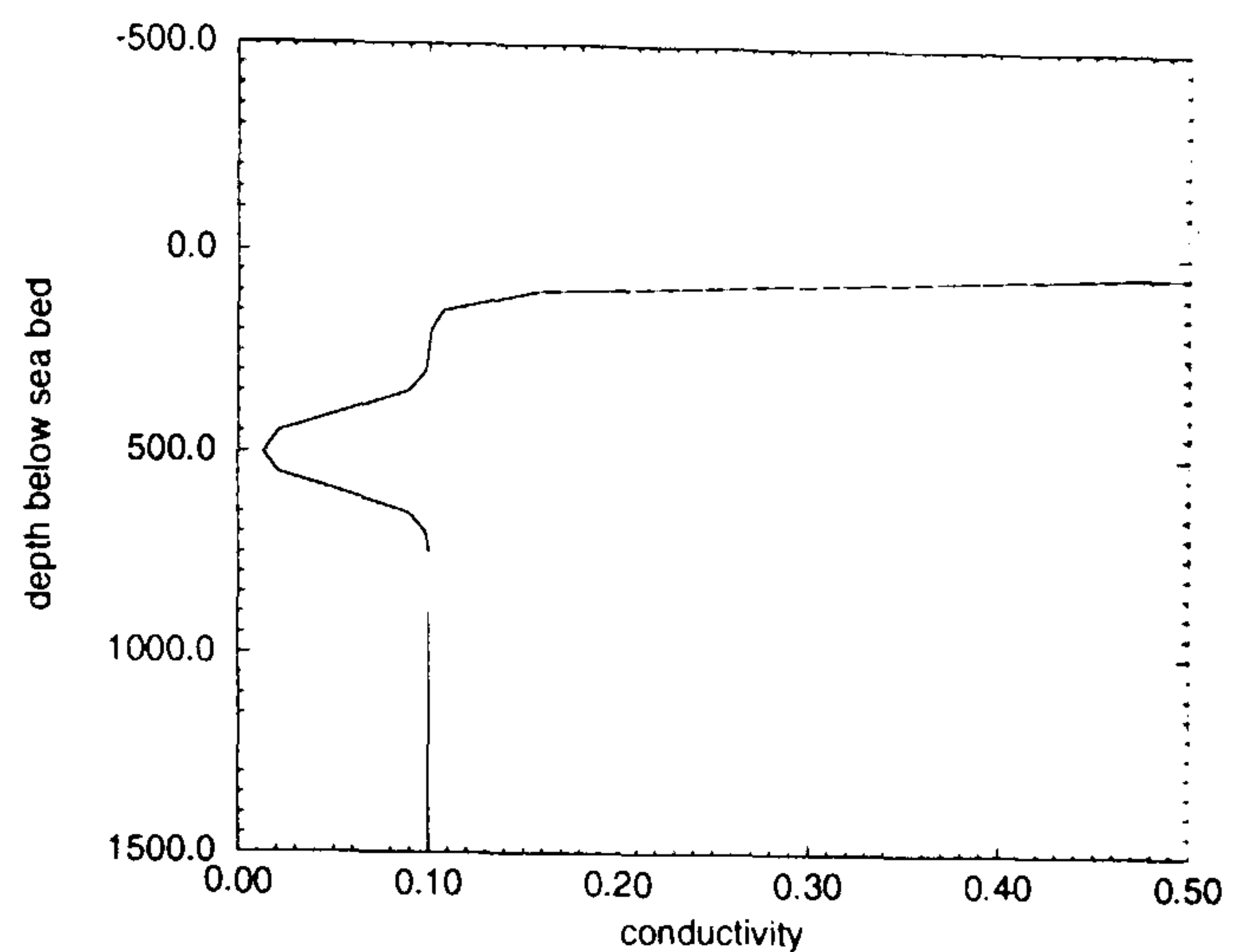


Figure D.8: Zoom on vertical profile of resistive anomaly: maximum resistivity is $75 \Omega\text{m}$.

Transmitter

Receivers

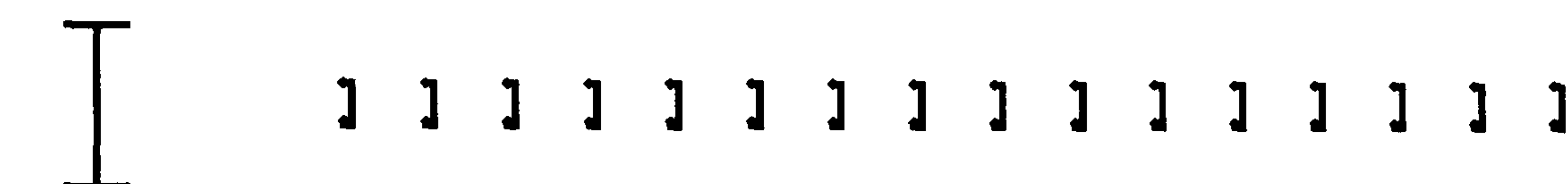


Figure D.9: Broadside (top) and collinear (bottom) alignment of transmitter and receiver dipoles.

D.2.3 Results

Depending upon the transmitter and receiver configuration a single simulation with this Earth model required 12 to 16 processor hours, a day's work for a departmental server. Use of the Edinburgh Cray T3D enabled this simulation to be run in under 10 minutes, and allowed a suite of Earth models to be simulated in a day.

D.3 Conclusions

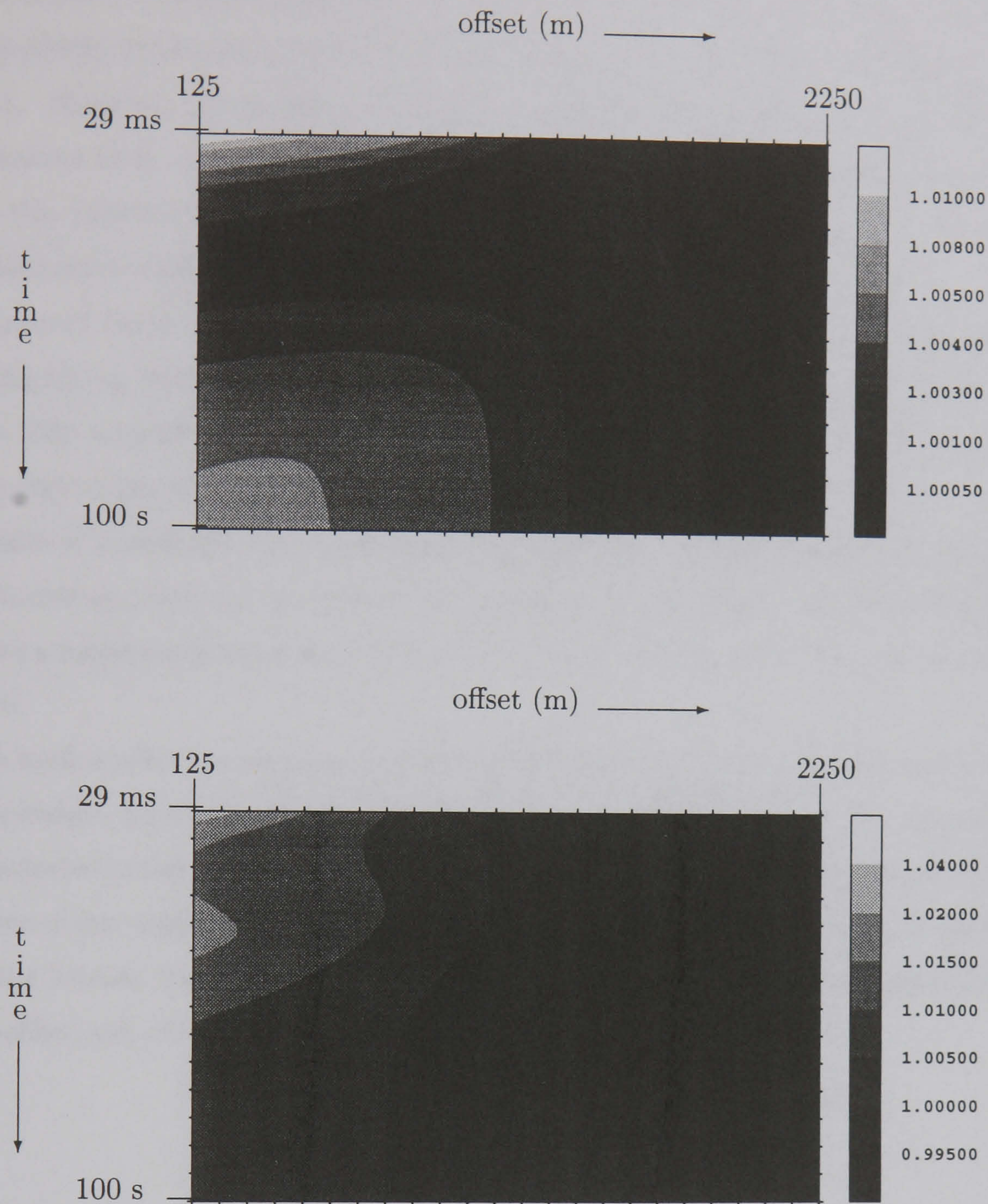


Figure D.10: The ratio of total electric field to normal electric field presented as a contour plot for broadside (top) and collinear (bottom) transmitter-receiver configurations. Receivers are plotted against time with receiver offset from the origin increasing from left to right and time increasing down the page. Receiver offsets from the origin vary from 50 m to 1200 m in intervals of 50 m, while the time range is on a logarithmic scale from 29 ms to 100 s. The horizontal electric current dipole transmitter is located beyond the right-most receiver, at an offset of 1500 m from the origin.

D.3 Conclusions

Numerical simulation of pairs of ‘layered Earth’ models can determine the change in the EM response resulting from a change in the resistivity of a target layer. It is important to recognise the difference between analysing the response to changes in the Earth’s subsurface, and analysis of the ability to resolve a particular target using a given interpretation method (Jupp & Vozoff 1975). However, 1D modelling does allow a swift first estimate of the detectability of an anomalous body of finite extent. If layered Earth modelling indicates a detectable response then this justifies further study using a 3D Earth model which is more geologically accurate, but also more computationally expensive.

Layered Earth modelling of a sub-area gas-storage reservoir at a relatively shallow depth of around 500 m, demonstrated a significant response to resistivity changes in the reservoir layer. For a fully saturated layer of 30 m thickness the ratio between responses with and without the hydrocarbon bearing layer at transmitter-receiver offsets of around 2,000 m is up to 1.5. This response is considered detectable and so further study using a 3D model is justified.

Modelling of sub-marine EM surveying over an axisymmetric hydrocarbon reservoir demonstrates a response of less than 2% for a reservoir of 2,000 m lateral extent at a depth of around 500 m.

In both studies the response to subsurface changes has a characteristic pattern. This pattern is dependent upon the depth and resistivity of the target layer. The response occurs in a characteristic time range and varies as azimuth and offset from the transmitter are varied. The pattern of the response indicates that when drawing an analogy between diffusive EM surveying and the seismic method it is more appropriate to consider wide-angle, refraction seismic than near-offset, reflection seismic surveying.

Appendix E

Euphrates: A System for Automatic Introduction of Data Parallelism into Modular Applications

Andrew J S Wilson and Ian W Flockhart

Reprinted, with permission, from

Computer Graphics

(transactions of the ACM SIGGRAPH)

special issue on

Modular Visualisation Environments (MVEs):

Past, Present and Future

May 1995.

Euphrates: A System for Automatic Introduction of Data Parallelism into Modular Applications

Andrew J S Wilson¹ and Ian W Flockhart²

To appear in **Computer Graphics** (transactions of the ACM SIGGRAPH)
special issue on
**Modular Visualisation Environments (MVEs):
Past, Present and Future**
May 1995.

Introduction

The purpose of scientific computation is not to generate numbers, but to gain insight. In the search for insight it is common to perform a computational experiment, for example to explore the behaviour of a mathematical model, or to analyse the effectiveness of a new experimental procedure, data processing sequence or visualization technique. Consequently scientists need to swiftly construct, optimise, and analyse prototype applications with a minimum of pain and without losing sight of the overall objective of gaining insight.

Modular visualisation environments (MVEs) such as apE [1] AVS [2], IRIS Explorer [3] and Khoros [4] provide an exceptionally effective environment in which to visualise data sets. In fact MVEs can be used for much more than just visualisation and can be used to prototype entire applications by simple graphical manipulation of icons representing software modules and the connections between them. This allows the user to construct, test, and refine prototype applications at high speed without becoming programming specialists.

Unfortunately MVEs are less effective once the application design has been finalised and production use begins, since they cannot handle large data sets or data parallelism. These weaknesses prevent their use for data intensive applications such as seismic data processing, where tens to hundreds of gigabytes of data may be acquired [5] and to a lesser degree, remote sensing and medical image processing. If MVEs are to realise their full potential as modular application builders (MABs) then a system is required to “*can*” a prototype application from a MVE into a stand-alone application suitable for use in a production environment.

In contrast to MVEs, distributed memory, multiple instruction stream, multiple data stream (DM-MIMD) [6] computers are generally recognised as difficult to program but well suited to computationally expensive applications which process large data volumes. By introducing a formal description of software modules and the way they are linked to form an application, we provide a painless route for migrating an application from the MAB to a stand-alone program suitable for execution on a serial or parallel computer. Topological analysis of a network of

¹Presently at University of Edinburgh, Department of Geology and Geophysics, The Kings Buildings, West Mains Road, Edinburgh EH9 3JW, UK. Email Andrew.J.S.Wilson@ed.ac.uk Telephone +44 31 650 8533 Fax +44 31 668 3184 URL <http://www.glg.ed.ac.uk/~ajsw>, formerly at Edinburgh Parallel Computing Centre

²Edinburgh Parallel Computing Centre, The University of Edinburgh, JCMB, The King's Buildings, Mayfield Road, Edinburgh, EH9 3JZ, UK. email ianf@epcc.ed.ac.uk

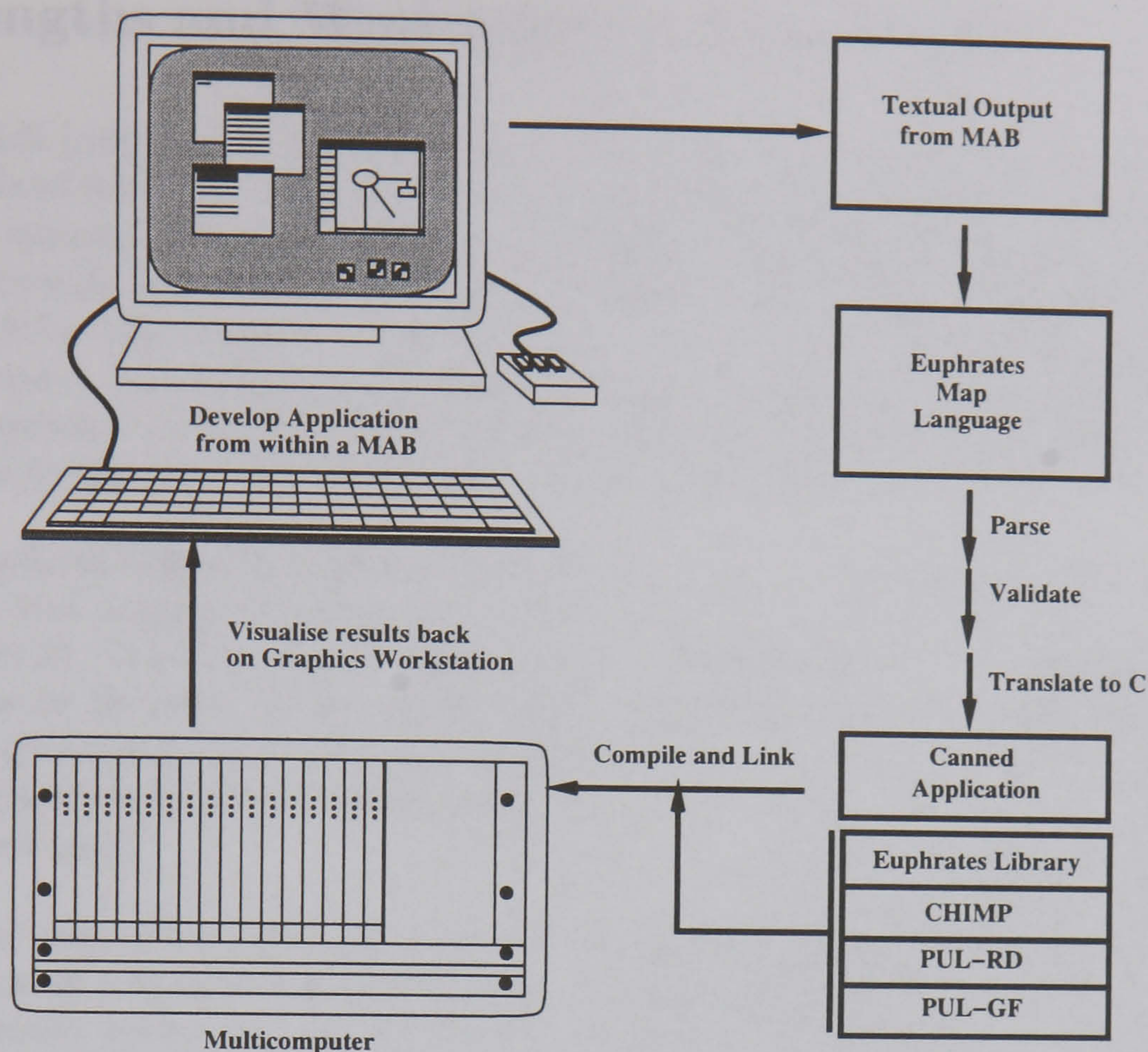


Figure 1: The Euphrates Cycle: An application prototype is interactively generated using a MAB, and then automatically canned into a production strength program, using Euphrates. The data set output from the production program is then returned to the graphics workstation for analysis.

modules allows derivation of the order in which each processing module must be applied to the input data set. Analysis of the data access patterns of each module allows estimation of memory requirements. This allows large data sets to be processed in a tile by tile fashion, on computers with relatively small amounts of memory.

The parallelisation by data decomposition of a wide class of useful processing operations is well understood and supported by a variety of parallel utility libraries. By rigorously defining the classes of operations supported, the Euphrates system is able to automatically generate parallel applications which will process arbitrarily large data sets; a capability which we believe to be unique [7]. These applications are parallelised using regular geometric data decomposition and are demonstrated to perform correctly and at increasing speed with increasing machine size. Future work will concentrate on widening the base of implemented modules and the class of supported operations.

We begin the remainder of this paper by outlining why live MABs are inherently memory inefficient, before going on to explain how a map of modules may be canned into a sequential program by generating a *calling order* in which to call the subroutines which perform the operation associated with each module. We then set out a methodology for classifying and precisely describing data access patterns. This approach goes right to the heart of Euphrates and allows the automatic parallelisation of a wide class of mesh based operations for application over arbitrarily large data sets. The concept of parallelisation by distribution of data over a number of processors is introduced. We present and analyse performance results for a simplistic 'toy' application and finally we discuss the direction of future development of Euphrates and modular application builders in general.

The Strengths and Weaknesses of Live MABs

In an MVE each icon may be considered as representing an executing process. Thus the application under development is akin to a set of communicating processes, which is at all times *live*. Once into the system, data flows down the network of links from module to module. New data arriving at a module may cause it to trigger, firing off a calculation which produces data to be output to modules downstream. At any time a module can be caused to fire again by changing one or more inputs, thus triggering a cascade of computation. This is one of the great strengths of live MAB systems and allows the interactive tuning of parameters. However it is precisely because of this feature that live MABs are memory inefficient.

Consider a simple module which inputs two data sets, A and B, and outputs two data sets $A+B$, and $A-B$ (figure 2). The process performing this calculation has to be ready to fire again when either port receives fresh data. This means that it must store the data from both input ports in case it is needed later.

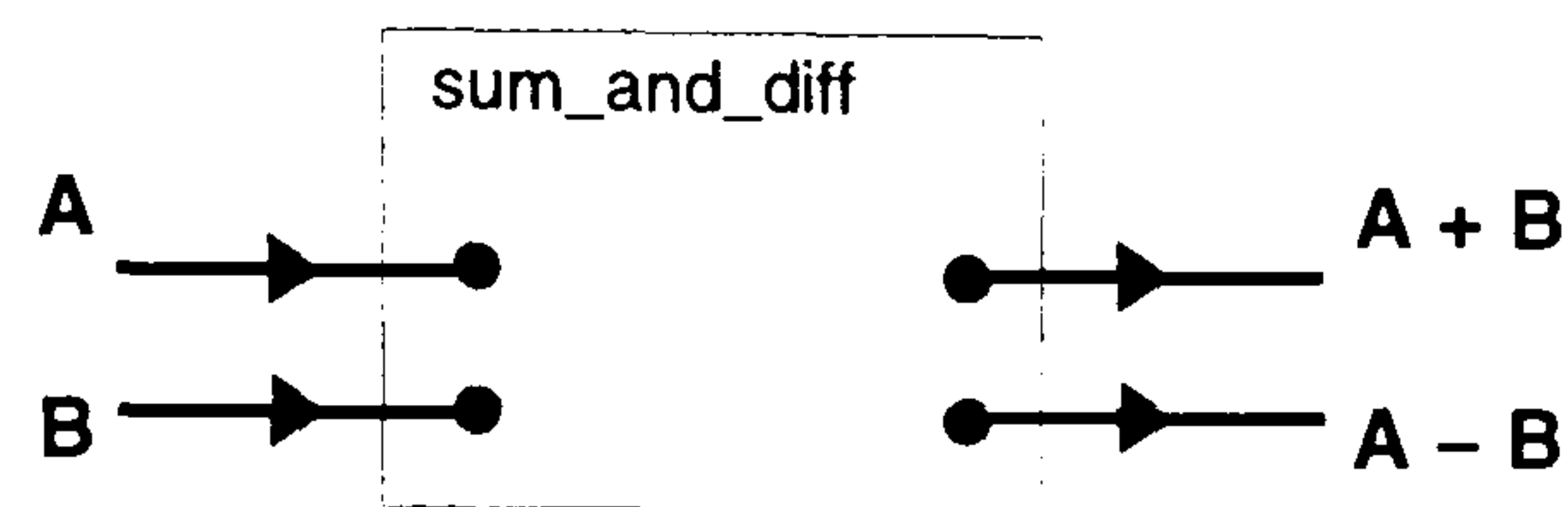


Figure 2: A simple module.

Similarly, other modules in the map may also be storing intermediate data sets. This feature means that a map containing a dozen modules, might well be using a dozen times as much memory as it really needs. By canning the live application into a fixed, stand-alone programme, this inefficiency is removed.

Calculating a Calling Order Using Topological Analysis

In the Euphrates system each module instance is associated with a single function call in the canned application. In such a system a fundamental step in converting from a live application to a canned application is the calculation of a suitable order in which to perform the actions associated with each module. The *calling order* is precisely the order in which the functions which implement the action of each module instance are called from the main program.

In a live MAB the order in which modules trigger is not explicitly pre-determined, rather it is a natural by-product of data flow and computation. In a live MAB it is possible to set up a feedback loop where downstream modules feed data back into early stages in the calculation, and data cycles in an infinite iterative loop. When analysing the map of modules such situations must be identified and handled by introducing appropriate flow control modules.

A suitable calling order may be easily and efficiently determined by topological analysis of the map of modules to generate an ordered list of modules, such that no module is downstream of a module which occurs later in the list. Typically data input modules would appear at the head of the list with data output modules appearing at the tail. This process also identifies maps which contain feedback loops.

Analysing Memory Usage

If there are parallel streams of data then there may be several possible calling orders some of which may be more effective than others. For example, the calling order can be optimised to minimise the peak memory usage. If all data output is performed as soon as possible, then this allows memory to be released, possibly reducing the overall memory requirements of the application. Further, an early start to any disk I/O will also maximise overlap of computation and disk I/O and may also help alleviate any disk I/O bottleneck.

Given a calling order it is quite easy to walk through the calling sequence noting the memory used at any one time. Once an array is no longer needed, Euphrates re-cycles that memory. An important bonus can be obtained from this analysis. By noting the peak memory usage we can gauge how large a data set can be processed on a machine with a certain total memory. If the application is such that it can be applied to a dataset on a tile-by-tile basis then an arbitrarily large data set may be processed by breaking it into machine sized chunks which can each then be processed individually and re-assembled on output.

Analysing Data Access Patterns

In order to determine if an operation can be performed on a tile by tile basis we need a formalism for analysing data access patterns. Operations on meshes can be discussed in terms of the *task* which must be performed at each site on the mesh and the *perspective* of the operation as a whole [8, 9]. Three properties of tasks can be identified which are key indicators of the efficiency which can be expected from a parallel implementation. These properties are the *spatial dependence* of each task, which describes the dependence of a task at one site upon information from other sites; the *activity* of the operation which describes the distribution of tasks across the mesh; and *precedence* which describes the order in which tasks must be executed.

Take for example the Jacobi linear solver algorithm which iteratively generates an improved approximate solution array. Each value in the updated array is calculated from the corresponding value in the previous iteration, plus some of its neighbours. Thus one iteration of the Jacobi solver has a local spatial dependence, global activity, no precedence relation and a local perspective. This iterative updating is usually terminated once a convergence criterion is satisfied and so the number of iterations is not known at compile time. Thus the algorithm as a whole has a global perspective since after sufficient iterations the dependence of one data value on those from previous generations, will have propagated across the entire array.

Parallelising Mesh Based Applications Using Data Distribution

Once a suitable calling order is determined, a canned sequential program may quite easily be constructed by associating appropriate arguments in the calls to the functions which perform the operations associated with each module instance. Parallelising the application requires a little more work. It is not possible to produce a system which will automatically parallelise an arbitrary application; this would be an all purpose parallelising compiler. The Euphrates approach has been to provide a high level of support for a wide class of well defined operations whose parallelisation is sufficiently well understood that it can be automated.

Many problems involve applying similar operations to every item in a large data set. For such applications a very effective method of parallelisation is to divide the data set between a number of processors and allow each processor to work on its portion. This approach is often termed *data decomposition* or perhaps *domain decomposition* when referring to data which is associated with a spatial domain.

In *regular domain decomposition* a regular mesh of data, usually stored as a single multidimensional array in serial programs, is decomposed over processes in such a way that every process is responsible for storage of, and operations upon, one contiguous region of the mesh. Many problems can be effectively parallelised by this method.

Operations which have local spatial dependence, global activity and no precedence relations are the easiest to parallelise and are termed *regular* since a regular geometric decomposition may be expected to provide an efficient parallelisation.

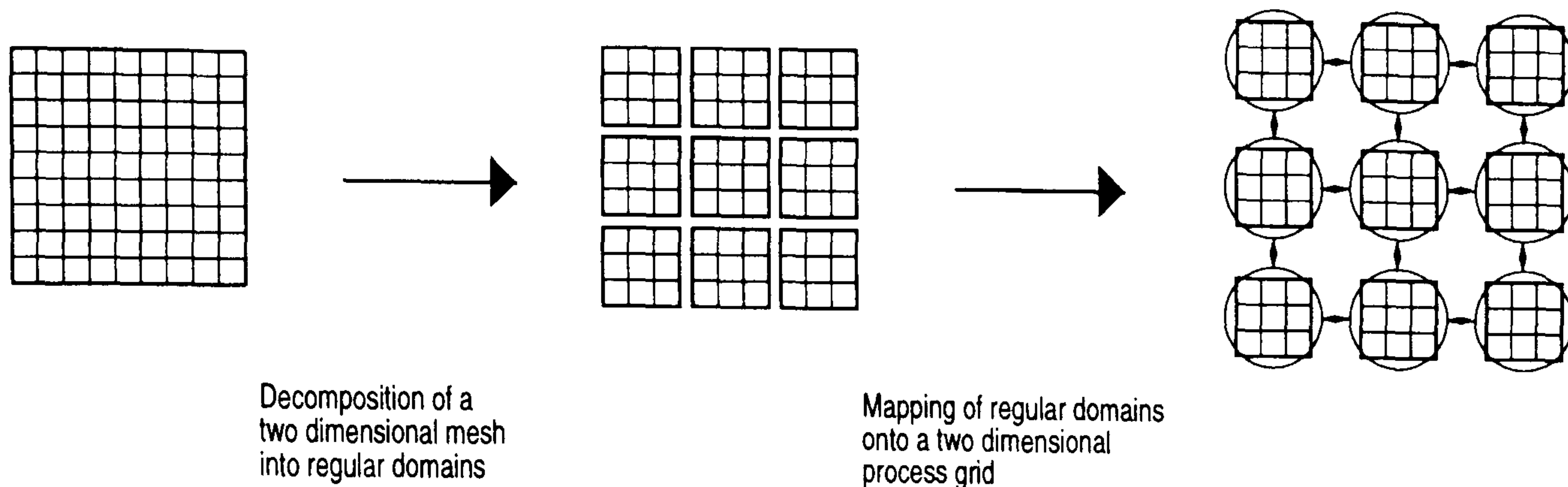


Figure 3: Geometric domain decomposition in two dimensions. A rectangular mesh corresponding to a physical domain is decomposed such that sub-domains which neighbour each other in the physical model are placed on neighbouring processes. The usual motivation behind this approach is to minimise communication costs for algorithms which require local updates.

In fact Euphrates employs two levels of data decomposition. In the *primary decomposition* an arbitrarily large data set is divided into *primary regions* each of which is small enough to be processed in the main computer memory. In the *secondary decomposition* each primary region is geometrically decomposed over the processor array

Euphrates currently supports regular operations with local perspective on arbitrarily large meshes, and operations with global spatial dependence, such as a global sum or maximum, on meshes which can be contained within primary memory. Euphrates could also be extended to support global operations on arbitrarily large data sets, but this would require the writing to secondary store of the entire data set before and after the global operation. This procedure would be necessary for any implementation and is not a feature special to the parallelisation of the process.

Results

We present performance results for a simple median filter, chosen so that the filter size may easily be enlarged, allowing performance to be assessed for increasingly processor-intensive tasks. The tests were implemented on a Meiko i860 Computing Surface [10].

Speed-up is shown for both the overall application run-time, and for the run-time of the median filter on its own (i.e. excluding input/output and other overheads, but including inter-processes communication directly related to the parallel implementation of the median filter).

Performance results for varying sizes of filter, on a 3D image of a fixed size of 150x150x150 voxels, is presented in table 1.

Filter size	5x5x5		9x9x9		11x11x11	
Number of processors	Speedup	Speedup (computation only)	Speedup	Speedup (computation only)	Speedup	Speedup (computation only)
2	1.30	1.91	1.49	2.04	1.72	2.13
4	1.56	3.84	2.18	4.22	2.58	4.33
8	1.65	6.26	2.62	8.16	3.07	8.29
16	1.69	10.27	2.86	15.01	3.85	15.93

Table 1: performance results for Euphrates for three filter sizes. The disk I/O volume remains approximately constant, but computation and interprocess communication grow with filter size.

As more processing nodes are used, more memory becomes available and Euphrates is able to process an image using fewer primary regions, which reduces computational overheads. This results in super-linear speed-up during the computational phase of the calculation. The time required for reading and writing the image to and from disk forms a substantial part of the overall runtime, and remains more or less constant regardless of the number of processors used.

The results show that this overhead becomes slightly less important as more computationally-intensive operators are used. As the median filter size is increased the computational phase of the application, which is parallelised effectively, becomes a larger part of the overall runtime. Since the other overheads remain more or less constant performance is improved. However, the performance of the system is still limited by disk access times.

Discussion and Conclusions

Performance analysis of a ‘toy’ application reveals that Euphrates makes a very efficient job of automatically parallelising computation. Indeed the computational phase of the application runs so much faster that disk I/O, which was already a significant component of the total runtime, becomes a crushing bottleneck, and barrier to further performance improvement. In some respects this is hardly surprising and might be alleviated by an improved, and inherently parallel, I/O sub-system [11, 12, 13].

However this also teaches an important lesson for designers of future modular application builders, whether parallel or sequential. If future systems are to be more widely applicable, they must be more effective at processing large data sets, such as seismic data sets where tens to hundreds of gigabytes of data can be involved. One vital aspect of this is the organisation of computation so as to allow the minimisation of disk I/O.

Consider figure 4 where three operations with local perspective process an arbitrarily large data set on a tile by tile basis. Each filter reads and writes the entire image from disk.

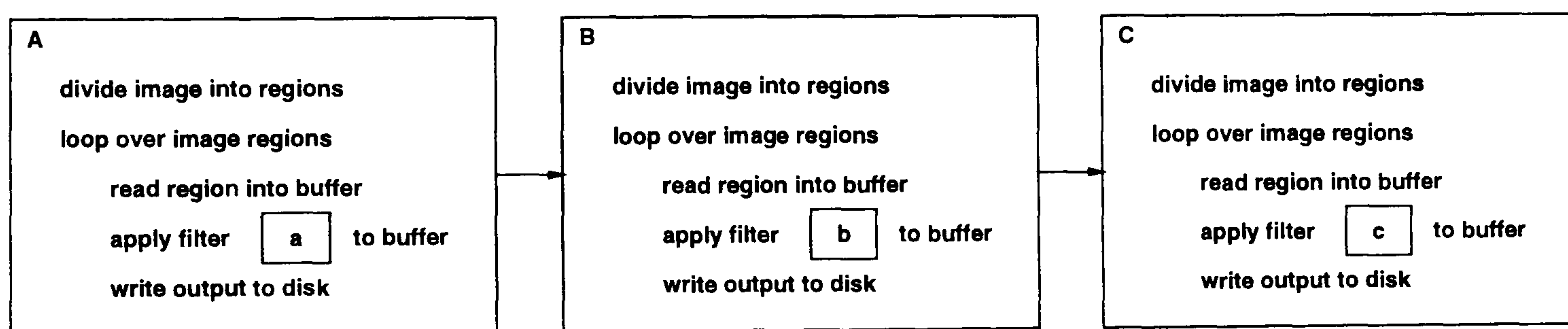
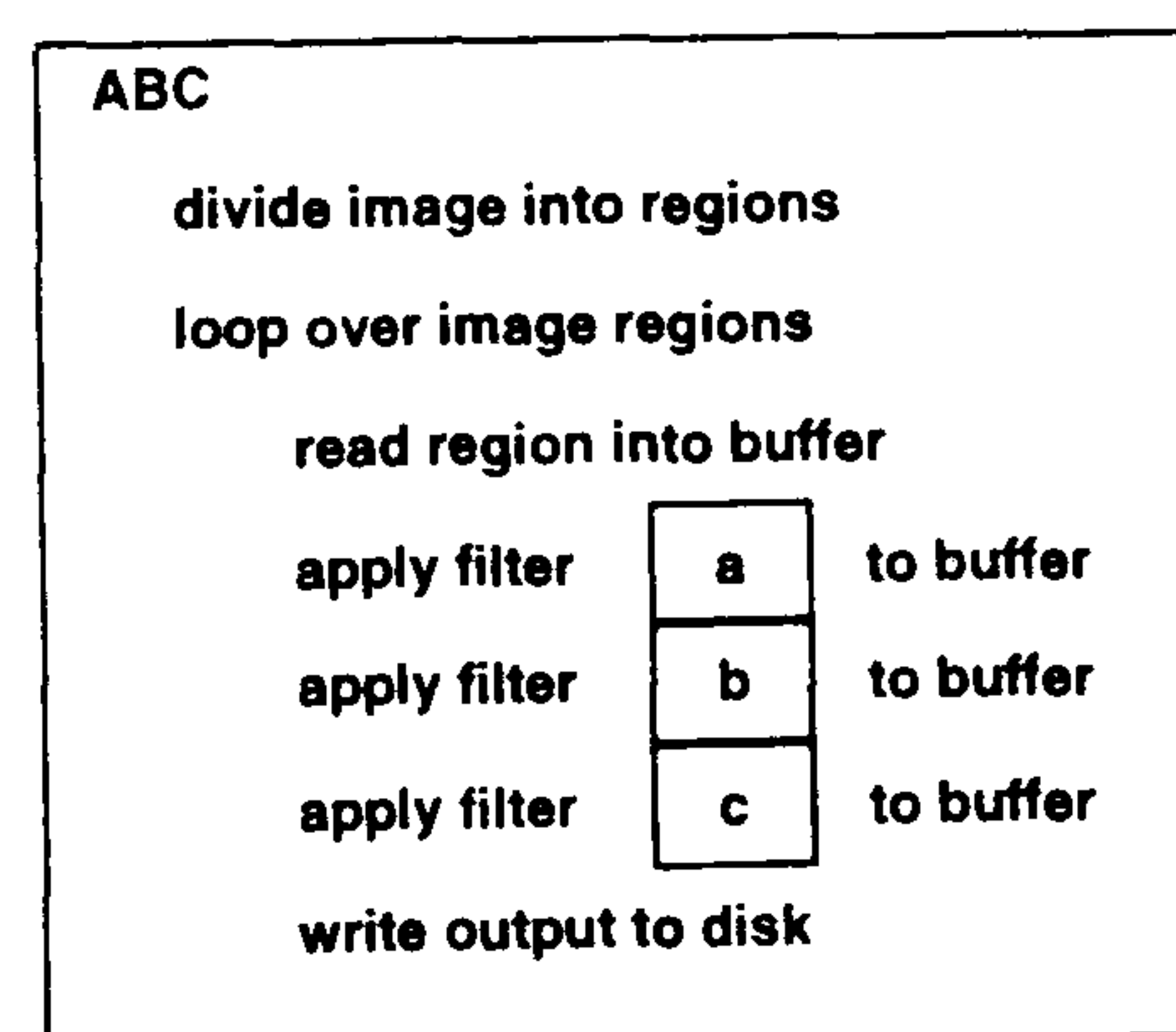


Figure 4: Each filter breaks the image up into regions small enough to be buffered in memory and operates on one region at a time. The processed image is written back to disk after each filter.

Figure 5: The volume of disk access can be reduced by re-arranging the computation so that each image region is read from disc once only and then processed by all operations before being written back to disk. If Euphrates did not employ this scheme to implement this chain of filters, then disk I/O would be at least three times its current level. For applications such as seismic data processing, which are actually fairly lightweight in terms of computational requirements per data item but process quite incredibly large data volumes, minimising disk I/O will be a critical factor in performance.



It is important to stress that it is not always possible to perform the rearrangement suggested in figure 5. If, for example, a filter was used to calculate some statistics about an image, such as mean and variance, then meaningful output cannot be generated until the filter has been applied to the entire image. An interesting adjunct to this disclaimer arises in, for example, parallel seismic migration. At first glance seismic migration has a global perspective and consequently is too expensive to implement on full-sized datasets. However by judicious approximation and massaging of the algorithm it may be implemented as a series of operations with local spatial dependence and local perspective, which may be practically implemented.

Development of the Euphrates system continues. Current work will provide improved support for seismic single-channel operations. Future work will include widening the base of implemented modules and the class of supported operations.

Acknowledgments

Edinburgh Parallel Computing Centre is an interdisciplinary focus for high performance parallel computing projects involving groups within the University of Edinburgh, industrial partners and academic users throughout Europe. The centre is supported by major grants and contracts from industry, the Commission of the European Communities, the Department of Trade and Industry, the Engineering and Physical Sciences Research Council, the Joint Information Systems Committee of the Higher Education Funding Councils and Scottish Enterprise Software Group.

Andrew J S Wilson is currently supported by European Community THERMIE research grant number OG/0305/92/NL-UK.

The authors would like to thank all those without whom the Euphrates project would not have come to fruition. Long before Euphrates was conceived Mike Norman was laying the theoretical foundations. A special mention is also reserved for Gordon Cameron who wrote the sequential package which provided the initial application functionality and Kevin Collins who managed this phase of the project. Simon Chapple and many others in the PUL team worked hard to produce the utility libraries that we needed. Our manager, Nick Radcliffe, showed divine tolerance when we ran over budget and behind time. Chris Thornborrow and Matthew White contributed greatly through much useful discussion and sage advice. Finally, none of this would have been possible without Dick Dalley, Phil Nelson and Neil Carmichael of Shell who believed in our idea and met the bottom line.

References

- [1] D. Scott Dyer. A dataflow toolkit for visualisation. *IEEE Computer Graphics and Applications*, 10(4):60–69, 1990.
- [2] C. Upson, T. Faulhaber, D. Kamis, D. Laidlaw, D. Schlegel, J. Vroom, R. Gurwitz, and A. van Dam. The application visualisation system: A computational environment for scientific visualisation. *IEEE Computer Graphics and Applications*, 9(4):30–42, 1989.
- [3] Silicon Graphics Incorporated. IRIS EXPLORER. Technical report, Silicon Graphics Incorporated, 1991.
- [4] Rasure and Kubica. The Khoros application development environment. In H.I Christensen and J.L Crowley, editors, *Experimental Environments for Computer Vision and Image Processing*. World Scientific, 1994.
- [5] J. Makin. Parallel processing technology and its applications in geophysical exploration. *Petroleum Review*, pages 445–446, September 1992.

- [6] Michael J. Flynn. Some Computer Organisations and Their Effectiveness. *IEEE Transactions on Computers*, C-21(9):948–960, September 1972.
- [7] C. Thornborrow, A. J. S. Wilson, and C. Faigle. Developing modular application builders to exploit MIMD parallel resources. In *Visualisation 1993*, pages 134–141. IEEE, October 1993.
- [8] A. J. S. Wilson, J. G. Mills, and M. G. Norman. *Bodyscan*: A transputer based 3D image analysis package. technical report EPCC-TR91-15, EPCC, 1991.
- [9] A. J. S. Wilson, J. G. Mills, and M. G. Norman. *Bodyscan*: A transputer based 3D image analysis package. In *Applications of Transputers 3*, volume 2, pages 130–135. IOS, August 1991.
- [10] N. B. MacDonald. Meiko scientific limited. In A. Trew and G. V. Wilson, editors, *Past, Present, Parallel: A Survey of Available Parallel Computing Systems*, pages 165–175. Springer-Verlag, 1991.
- [11] Simon R Chapple. PUL-PF prototype reference manual, 1994. Ref. EPCC-KTP-PUL-PF-PROT-RM.
- [12] R. A. A. Bruce, S. Chapple, N. B. MacDonald, A. S. Trew, and S. Trewin. CHIMP and PUL: Support for portable parallel computing. To appear in *Journal of Future Generation Computer Systems*, (11.1), January 1995.
- [13] S. R. Chapple and L. J. Clarke. PUL: The parallel utilities library. To appear in *Proceedings of Scalable Parallel Libraries Conference 1994*, January 1995.

Appendix F

Automatic Parallelisation of Multichannel Transient EM Processing

Peilin Jia, Ian W Flockhart and Andrew J S Wilson

Reprinted, with permission, from proceedings of the
International Symposium on 3D Electromagnetics
held at Schlumberger-Doll Research, Ridgefield, Connecticut, USA.
October 1995.

Automatic Parallelisation of Multichannel Transient EM Processing

Peilin Jia

*Department of Computer Science, Yale University, New Haven, Connecticut.
Formerly at Edinburgh Parallel Computing Centre, University of Edinburgh.*

Ian W Flockhart

*Edinburgh Parallel Computing Centre, University of Edinburgh, The King's Buildings, Edinburgh
EH9 3JZ, UK. Email ianf@epcc.ed.ac.uk, Telephone +44 131 650 5957, Fax +44 131 650 6555.*

Andrew J S Wilson

*Department of Geology and Geophysics, University of Edinburgh, The Kings Buildings, Edinburgh
EH9 3JW, UK. Email Andrew.J.S.Wilson@ed.ac.uk, Telephone +44 131 650 8533,
Fax +44 131 668 3184, URL <http://www.glg.ed.ac.uk/ajsw>.
Formerly at Edinburgh Parallel Computing Centre, University of Edinburgh.*

Abstract

Recent hardware advances allow collection of multichannel transient electromagnetic (MTEM) surveys using simultaneous recording from one source into many receivers. Resulting data coverage and data volumes are unprecedented. Existing TEM processing systems, developed to process data from each source-receiver pair on an individual basis, are not designed to exploit dense spatial coverage and struggle with large data volumes. A new processing paradigm is required.

The wave transform relates the response of a diffusive medium, and the response of an equivalent wave propagation medium. Once wave transform inversion has been achieved, seismic data processing systems may be applied to process and interpret the data, making best use of the dense spatial coverage.

In implementing the new processing scheme advantage was taken of systems such as AVS which allow users to graphically manipulate icons representing software modules and the connections between them. This allows construction and refinement of processing sequences at high speed. However in such systems each icon corresponds to an executing process, resulting in inefficient memory use and preventing their use for data-intensive applications such as seismic or MTEM data processing.

The Euphrates system automatically extracts a processing sequence from AVS, and writes a program which may be executed on a serial or parallel computer to perform that processing sequence. In addition Euphrates supports the application of a well-defined class of operations to arbitrarily large data sets; a capability we believe to be unique. Thus the Euphrates system allows the operator to interactively design and test a processing sequence on a local workstation, before submitting a batch processing job to mainframe or parallel computer.

A small number of new modules were prepared which collectively implement wave transform inversion by deconvolution. In the main these are general-purpose modules applicable to many geophysical data processing situations. In addition the Euphrates framework was extended to make easier the writing of trace-based processing modules. By maximising code re-use, and providing automatic parallelisation, both development and run-time were minimised.

1 Introduction

Seismology is the premier geophysical technique for determining structure in sedimentary basins and the dominant exploration methodology in hydrocarbon prospecting. Seismics are directly sensitive to velocity and density contrasts but only indirectly sensitive to changes in porosity and pore fluid and such variations can only sometimes be inferred from seismic. Multi-channel transient electromagnetic (MTEM) prospecting is directly sensitive to contrasts in bulk resistivity due to, for example, a change in pore fluid from brine to oil. Recent adaptation of technology from exploration seismics now enable acquisition of the closely spaced MTEM data required to image hydrocarbon reservoirs. However it is currently unclear how best to process such data once acquired.

In regions of complex geology it is well known that the expense of inverse modelling — the iterative refinement of a model through forward modelling until a good fit with the experimentally acquired data is achieved — is enormous. There is clearly a need to develop a satisfactory methodology for processing and interpretation of MTEM surveys over complex geology, similar to the well-developed and well-understood methodology for processing seismic data.

The wave transform relates the response of a diffusive medium, and the response of an equivalent wave propagation medium, provided the sources, geometry and boundary conditions in both domains match. The wave transform may be inverted to calculate an equivalent wavefield from diffusive transients and then seismic data processing and interpretation techniques may be applied to the equivalent wavefield to recover the equivalent velocity $c(\mathbf{r})$. For EM data a resistivity profile $\sigma(\mathbf{r})$ may then be calculated using the relationship $\mu\sigma(\mathbf{r}) = c(\mathbf{r})^{-2}$ (Lee & Xie 1993).

Inversion of the wave transform is well known to be an inherently ill-posed, and consequently computationally expensive, problem. Inversion schemes introduce differing constraints on possible solutions in order to improve resolution and tractability.

When developing a new processing sequence, scientists need to swiftly construct, optimise, and analyse prototype applications with a minimum of pain. Modular visualisation environments (MVEs) such as AVS (Upson et al. 1989) provide an exceptionally effective environment in which to visualise data sets. In fact MVEs can be used for much more than just visualisation and can be used to prototype entire applications by simple graphical manipulation of icons representing software modules and the connections between them. This allows the user to construct, test, and refine prototype applications at high speed without becoming programming specialists.

Unfortunately MVEs are less effective once the application design has been finalised and production use begins, since they cannot handle large data sets or data parallelism. These weaknesses prevent their use for data intensive applications such as seismic data processing. If MVEs are to realise their full potential as modular application builders (MABs) then a system is required to “*can*” a prototype application from a MVE into a stand-alone application suitable for use in a production environment. In contrast to MVEs, distributed memory, multiple instruction stream, multiple data stream (DM-MIMD) (Flynn 1972) computers are generally recognised as difficult to program but well suited to computationally expensive applications which process large data volumes.

In this paper we show how, by introducing a formal description of software modules and the way they are linked to form an application, we can provide a painless route for migrating an application from the MAB to a stand-alone program suitable for execution on a serial or parallel computer. By rigorously defining the classes of operations supported, the Euphrates system is able to automatically generate parallel applications which will process arbitrarily large data sets; a capability which we believe to be unique (Thornborrow et al. 1993).

We begin the remainder of this paper by introducing the wave transform. One particular method for wave transform inversion and its implementation in Euphrates as a collection of modules is then set out, followed by an outline of how the Euphrates system converts such a network of modules into a parallel program. Results from the automatic parallelisation and execution of this processing are then presented.

2 The Wave Transform

2.1 The Equivalent Wavefield Concept

Seismic energy propagates through the earth as, to a good approximation, a non-dispersive wave motion. Seismics can often be interpreted very effectively using procedures which amount to analysis of the time seismic pulses take to travel to and from a reflecting horizon. Electromagnetic propagation in the earth is diffusive; different frequencies in an electromagnetic pulse move at different speeds and are attenuated at different rates causing the shape of the pulse to change over time. This diffusive nature limits resolution, nullifies the concept of a travel time and makes data interpretation much more difficult.

The equivalent wavefield concept states that for every electromagnetic prospecting experiment there is an equivalent wave propagation experiment with equivalent sources, receivers and boundary conditions. This experiment is entirely fictional, and the physics of the equivalent sources, equivalent receivers and equivalent boundary conditions is determined by their electromagnetic counterparts. The wave transform may be inverted to calculate an equivalent wavefield from diffusive transients and then seismic data processing and interpretation techniques may be applied to the equivalent wavefield to recover the equivalent velocity $c(\mathbf{r})$. For EM data a resistivity profile $\sigma(\mathbf{r})$ may then be calculated using the relationship $\mu\sigma(\mathbf{r}) = c(\mathbf{r})^{-2}$ (Lee and Xie 1993).

There is no suggestion that wave transform inversion can somehow lend electromagnetic prospecting the high resolution enjoyed by seismic methods; fundamental limitations on resolution will remain. However the equivalent wavefield may be significantly easier to interpret than the original diffusive data.

In figures 1a and 1b, and similar figures which follow, time is increasing down the page and offset from the source is increasing across the page from left to right. These figures depict respectively the 1D Green's functions for propagation in wave and diffusive media; these are an impulse travelling with constant velocity, and a pulse whose profile gradually changes, dispersing and broadening with increasing time.

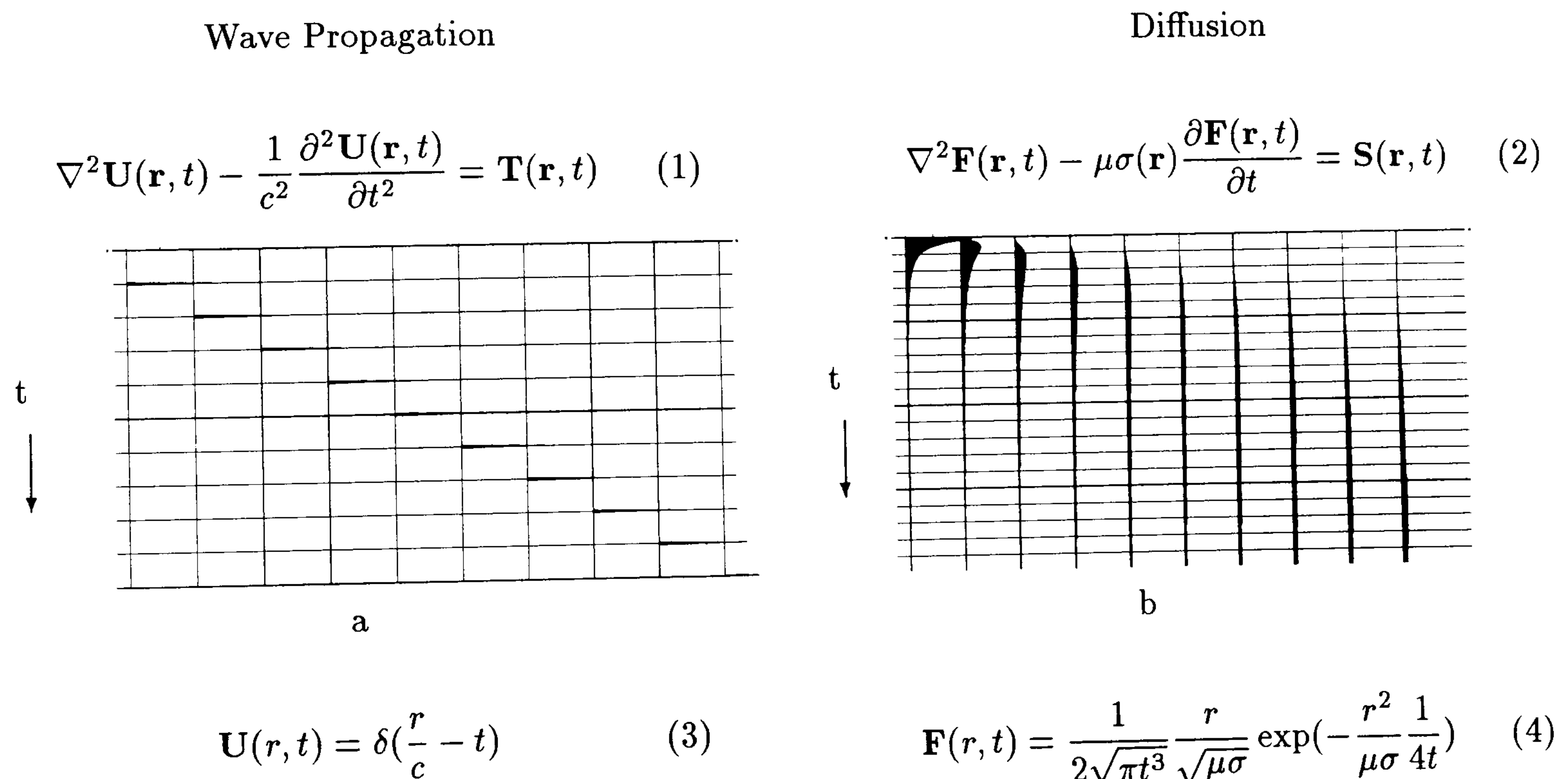


Figure 1: 1D Green's Functions for Wave Propagation and Diffusion

Any wave transform inversion process must convert the Green's function for diffusion to the Green's function for wave propagation. We approach this problem by considering the governing equations for wave propagation and diffusion in homogeneous, source free media. After taking a Laplace transform with respect to time these are

$$(\nabla^2 - \frac{p^2}{c^2})\hat{\mathbf{U}}(\mathbf{r}, p) = 0 \quad (\nabla^2 - s\mu\sigma)\hat{\mathbf{F}}(\mathbf{r}, s) = 0 \quad (5)$$

where p and s are the Laplace transform parameters for the wave and diffusive domains respectively, \mathbf{F} is the measured diffusive data and \mathbf{U} is the equivalent wavefield. To convert the diffusion equation into the wave equation we simply write $\mu\sigma = c^{-2}$, $s = p^2$ and $\hat{\mathbf{F}}(\mathbf{r}, s) = \hat{\mathbf{U}}(\mathbf{r}, p)$.

2.2 How the Wave Transform Works

Diffusive responses may usefully be expressed as a sum of exponentially decaying components. Taking the Laplace transform of one such component we obtain

$$\mathcal{L}\{\exp(-at)\}(s) = \frac{1}{s+a}, \quad a > 0. \quad (6)$$

Setting $s = p^2$ and taking the inverse Laplace transform from the transform variable p to the time-like variable q yields

$$\mathcal{L}^{-1}\left\{\frac{1}{p^2+a}\right\}(q) = \frac{\sin(\sqrt{a}q)}{\sqrt{a}}. \quad (7)$$

Thus the wave transform turns exponentially decaying signals into stationary signals. Unfortunately the inverse Laplace transform is troublesome to calculate numerically and so it is not usually convenient to calculate the equivalent wavefield through the Laplace transform domain.

2.3 Wave Transform Inversion by Deconvolution

Fortunately there is an equivalent relationship in the time domain through an integral transform

$$\mathbf{F}(\mathbf{r}, t) = \frac{1}{2\sqrt{\pi t^3}} \int_0^\infty q \exp(-\frac{q^2}{4t}) \mathbf{U}(\mathbf{r}, q) dq. \quad (8)$$

As expected the action of the transform is to progressively smooth out a pulse as it travels. Inversion of the wave transform involves the recovery of the impulse from the smooth diffusive transient. Because the action of the forward transform is to smooth out any sharp irregularities, the action of the inverse transform is to amplify any irregularities. This causes wave-transform inversion to be an ill-posed problem; a small perturbation of the input, such as the addition of some random noise, is amplified causing a dramatic change in the output. Thus small errors in the measured data can produce large changes in the solution. In order to obtain a useful processing system some kind of constraints must be applied to regularise the inversion, so that stable, but approximate, results are obtained.

By moving to a logarithmic sampling in both time and the time-like variable q the wave transform may be re-formulated as a convolution (Gershenson 1993). In effect, by moving to logarithmic time sampling, we are parameterising the inversion and the regularisation which is being imposed by this scheme is such that uniform resolution is achieved in logarithmic time. Deconvolution, the inversion of convolution equations, is a subject much studied in exploration seismology and one advantage of formulating the wave transform as a convolution is that it allows the inversion to

be performed using standard seismic deconvolution techniques. This deconvolution method is also more efficient than some previous approaches, such as discretising the wave transform as a matrix equation and applying regularised inversion. In addition, wave transform inversion by deconvolution has been demonstrated to give superior results to other techniques using known wave/diffusion pairs, synthetic diffusive transients and field data (Gershenson 1993).

2.4 Implementing the Wave Transform as a Series of Modules

In outline, the processing steps involved in wave transform inversion by deconvolution are as follows. Making the substitutions $q = \exp(v)$ and $t = \frac{1}{4} \exp(2v)$ in the wave transform above results in a convolution equation

$$\mathbf{G}(v) = \mathbf{R}(v) * W(v) \quad (9)$$

where

$$\mathbf{G}(\mathbf{r}, v) = \sqrt{\pi} \exp(v) \mathbf{F}(\mathbf{r}, \frac{1}{4} \exp(2v)), \quad (10)$$

$$\mathbf{R}(\mathbf{r}, v) = \mathbf{U}(\mathbf{r}, \exp(v)), \quad (11)$$

$$W(v) = 4 \exp(-2v) \exp(-\exp(-2v)). \quad (12)$$

After pre-processing the first step is to calculate $\mathbf{G}(v)$ from the measured transient electromagnetic data $\mathbf{F}(t)$. This is achieved by multiplying the pre-processed data by a factor which varies like the square root of time and then resampling onto a logarithmic time scale, using a splining program. Next we convolve $\mathbf{G}(v)$ with a suitable deconvolution operator M which is calculated as the (approximate) inverse of W , the convolutional kernel, using one of a number of standard techniques. This convolution yields $\mathbf{R}(v)$ which is then resampled, again using spline interpolation, to give the final output. This procedure is simply implemented using a network of standard modules — see Figure 2.

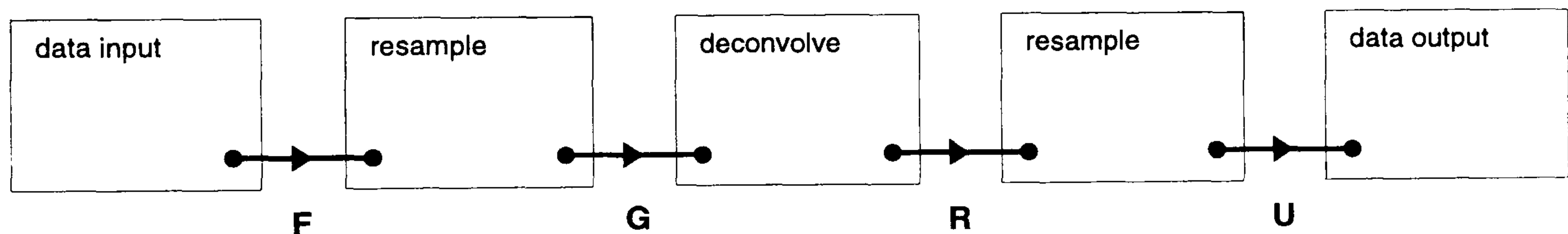


Figure 2: Implementation of wave transform inversion by deconvolution in logarithmic time as a series of simple modules.

3 Automatic Generation of a Parallel Program from a Network of Modules

3.1 Calculating a Calling Order Using Topological Analysis

In an MVE each icon may be considered as representing an executing process. Thus the application under development is akin to a set of communicating processes, which is at all times *live*. Once into the system, data flows down the network of links from module to module. Data arriving at a module may cause it to trigger, firing off a calculation which produces data to be output to modules

Consider a simple module which inputs two data sets, A and B, and outputs two data sets $A+B$, and $A-B$ (figure 3). The process performing this calculation has to be ready to fire again when either port receives fresh data. This means that it must store the data from both input ports in case it is needed later.

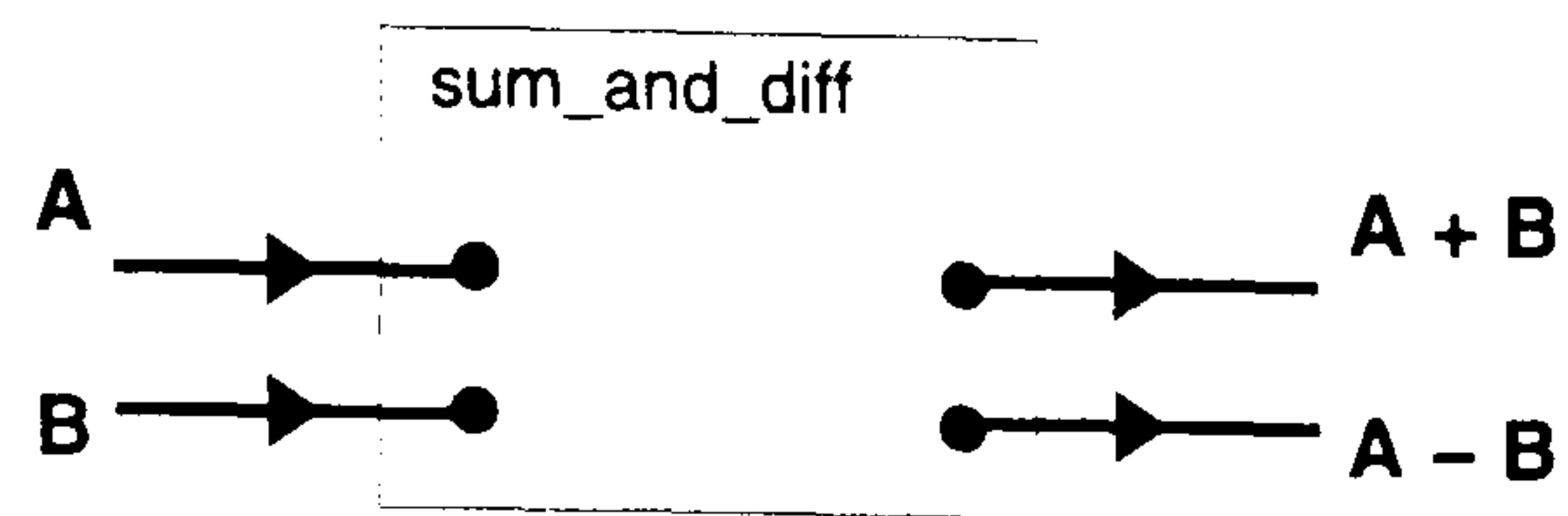


Figure 3: A simple module.

downstream. At any time a module can be caused to fire again by changing one or more inputs, thus triggering a cascade of computation. This is one of the great strengths of live MAB systems and allows the interactive tuning of parameters. However it is precisely because of this feature that live MABs are memory inefficient.

Similarly, other modules in the map may also be storing intermediate data sets. This feature means that a map containing a dozen modules might well be using a dozen times as much memory as it really needs. By canning the live application into a fixed, stand-alone programme, this inefficiency is removed.

In the Euphrates system each module instance is associated with a single function call in the canned application. A fundamental step in converting from a live application to a canned application is the calculation of a suitable order in which to perform the actions associated with each module. The *calling order* is precisely the order in which the functions which implement the action of each module instance are called from the main program.

A suitable calling order may be easily and efficiently determined by topological analysis of the map of modules to generate an ordered list of modules, such that no module is downstream of a module which occurs later in the list. Typically data input modules would appear at the head of the list with data output modules appearing at the tail. This process also identifies maps which contain feedback loops.

3.2 Analysing Memory Usage

If there are parallel streams of data then there may be several possible calling orders some of which may be more effective than others. For example, the calling order can be optimised to minimise the peak memory usage.

Given a calling order it is quite easy to walk through the calling sequence noting the memory used at any one time. Once an array is no longer needed, Euphrates re-cycles that memory. An important bonus can be obtained from this analysis. By noting the peak memory usage we can gauge how large a data set can be processed on a machine with a certain total memory. If the application is such that it can be applied to a dataset on a tile-by-tile basis then an arbitrarily large data set may be processed by breaking it into machine sized chunks which can each then be processed individually and re-assembled on output.

3.3 Analysing Data Access Patterns

In order to determine if an operation can be performed on a tile by tile basis we need a formalism for analysing data access patterns. Operations on meshes can be discussed in terms of the *task* which must be performed at each site on the mesh and the *perspective* of the operation as a whole (Wilson et al 1991). Three properties of tasks can be identified which are key indicators of the efficiency which can be expected from a parallel implementation. These properties are the *spatial dependence* of each task, which describes the dependence of a task at one site upon information from other sites; the *activity* of the operation which describes the distribution of tasks across the mesh; and *precedence* which describes the order in which tasks must be executed.

3.4 Parallelising Mesh Based Applications Using Data Distribution

Once a suitable calling order is determined, a canned sequential program may quite easily be constructed by associating appropriate arguments in the calls to the functions which perform the operations associated with each module instance. Parallelising the application requires a little more work. It is not possible to produce a system which will automatically parallelise an arbitrary application; this would be an all purpose parallelising compiler. The Euphrates approach has been to provide a high level of support for a wide class of well defined operations whose parallelisation is sufficiently well understood that it can be automated.

Many problems involve applying similar operations to every item in a large data set. For such applications a very effective method of parallelisation is to divide the data set between a number of processors and allow each processor to work on its portion. This approach is often termed *data decomposition* or perhaps *domain decomposition* when referring to data which is associated with a spatial domain.

In *regular domain decomposition* a regular mesh of data, usually stored as a single multidimensional array in serial programs, is decomposed over processes in such a way that every process is responsible for storage of, and operations upon, one contiguous region of the mesh. Many problems can be effectively parallelised by this method.

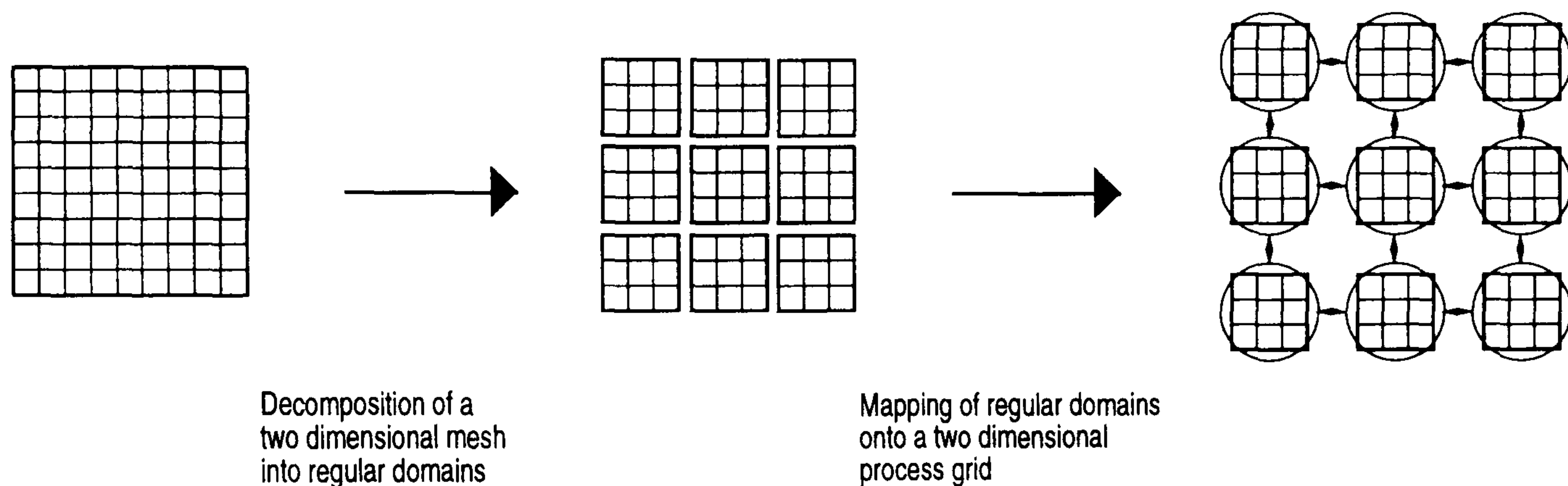


Figure 4: Geometric domain decomposition in two dimensions. A rectangular mesh corresponding to a physical domain is decomposed such that sub-domains which neighbour each other in the physical model are placed on neighbouring processes. The usual motivation behind this approach is to minimise communication costs for algorithms which require local updates.

Operations which have local spatial dependence, global activity and no precedence relations are the easiest to parallelise and are termed *regular* since a regular geometric decomposition may be expected to provide an efficient parallelisation.

In fact Euphrates employs two levels of data decomposition. In the *primary decomposition* an arbitrarily large data set is divided into *primary regions* each of which is small enough to be processed in the main computer memory. In the *secondary decomposition* each primary region is geometrically decomposed over the processor array.

Euphrates currently supports regular operations with local perspective on arbitrarily large meshes, and operations with global spatial dependence, such as a global sum or maximum, on meshes which can be contained within primary memory. Euphrates could also be extended to support global operations on arbitrarily large data sets, but this would require the writing to secondary store of the entire data set before and after the global operation. This procedure would be necessary for any implementation and is not a feature special to the parallelisation of the process.

4 Results

Performance analyses already reported in Wilson and Flockhart (1995) reveal that Euphrates makes a very efficient job of automatically parallelising computation. Accordingly this section will concentrate on the effectiveness of wave transform inversion by deconvolution in log time.

Figure 5 shows each step in the process when applied to the 1D Green’s function for diffusion. The ill-posedness of the problem means that the analytic result for the “true” equivalent wavefield, an impulse propagating with constant velocity, cannot be perfectly recovered (Slob et al 1995). However the smoothed version which is recovered can still be easily interpreted. By marking the location of the maximum amplitude on each trace in the equivalent wavefield we can easily see that the pulse is travelling outward from the source at a constant velocity which can be estimated from the slope of the line along which these maxima lie. By comparing this velocity with that used to calculate the synthetics we can confirm that the correct velocity is interpreted.

Table 1 lists the depths and resistivities for a 1D earth model based upon well logs from an underground gas storage reservoir in France. Synthetic in-line dipole-dipole MTEM responses were calculated for cases without (ilw1) and with (ilh1) gas in the target layer. Wave transform inversion of these synthetics (respectively Figures 6a and 6b) was again followed by marking the location of the maximum amplitude on each trace in the equivalent wavefield (Figures 6c and 6d). In each case two arrivals can be seen which may be interpreted using concepts from seismic refraction. The direct arrival from the source will appear as a straight line through the origin, while refracted arrivals from interface waves also appear as straight lines but will not intercept the q axis at the origin. The slope of these refracted arrivals reveals the velocity of the layer at which they refract. This very simple analysis yields estimates of 49.1 Ohm m for the top layer, and, for the model without gas 17.6 Ohm m for the next layer while for the model with gas the next layer resistivity is estimated at 110 Ohm m. These estimates compare well with the “true” values of 50 Ohm m, 15 Ohm m and 200 Ohm m, especially bearing in mind the simplicity of the wave transform inversion scheme employed.

layer	depth (m)	resistivity (Ohm m)	equivalent velocity (m/\sqrt{s})
1	0-140	50	6308
2	140-160	15	3555
3	160-310	50	6308
4	310-490	10	2821
5	490-520	200	12616
6	520-	10	2821

Table 1: Layer depths and resistivities for model ilh1. Model ilw1 has the same depths and resistivities except for layer 5, the target, which has a resistivity of 10 Ohm m.

5 Discussion and Conclusions

A major innovation in Euphrates is that it will support the processing of arbitrarily large data sets. This is particularly important when trying to process real-world data sets on DM-MIMD parallel computers which, although computationally powerful, may have limited amounts of main memory per node and no virtual memory facilities. The automatic processing of arbitrarily large data sets

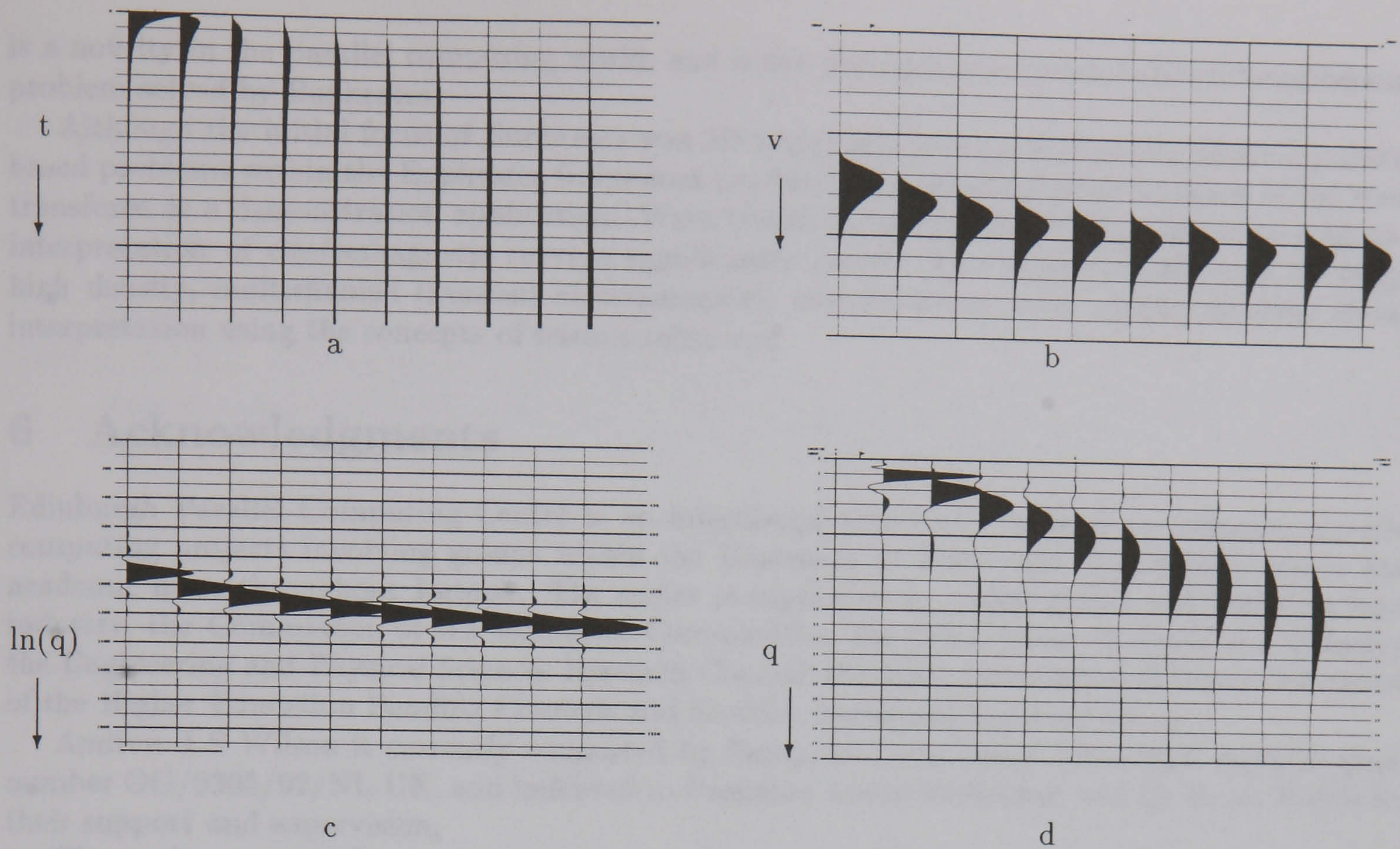


Figure 5: Wave Transform Inversion of the 1D Green's Diffusion Function

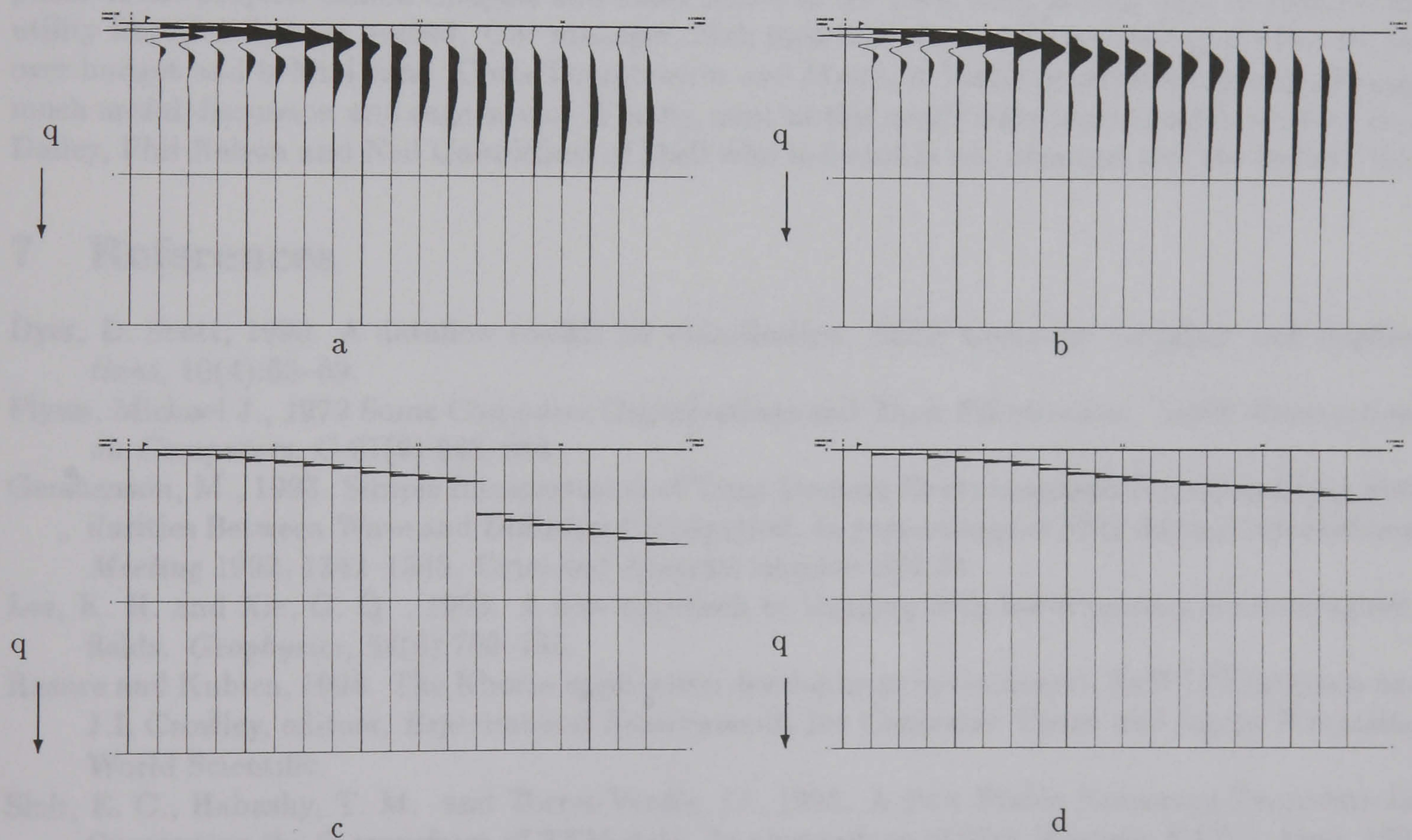


Figure 6: Interpretation of equivalent wavefield calculated from synthetics for underground gas storage reservoir.

is a novelty in the parallel computing world, and is the principle new parallel software-engineering problem solved by Euphrates.

Although the initial focus of Euphrates was 3D image processing, the viability of solving trace-based problems within the Euphrates framework has been demonstrated using inversion of the wave transform as a demonstration application. Wave transform inversion can make the processing and interpretation of electromagnetic surveys significantly easier. This is particularly true for large, high density, multichannel transient electromagnetic surveys where good spatial coverage allows interpretation using the concepts of seismic refraction.

6 Acknowledgments

Edinburgh Parallel Computing Centre is an interdisciplinary focus for high performance parallel computing projects involving groups within the University of Edinburgh, industrial partners and academic users throughout Europe. The centre is supported by major grants and contracts from industry, the Commission of the European Communities, the Department of Trade and Industry, the Engineering and Physical Sciences Research Council, the Joint Information Systems Committee of the Higher Education Funding Councils and Scottish Enterprise Software Group.

Andrew J S Wilson is currently supported by European Community THERMIE research grant number OG/0305/92/NL-UK, and indebted to Professor Anton Ziolkowski and Dr Bruce Hobbs for their support and supervision.

The authors would like to thank all those without whom the Euphrates project would not have come to fruition. Long before Euphrates was conceived Mike Norman was laying the theoretical foundations. A special mention is also reserved for Gordon Cameron who wrote the sequential package which provided the initial application functionality and Kevin Collins who managed this phase of the project. Simon Chapple and many others in the PUL team worked hard to produce the utility libraries that we needed. Our manager, Nick Radcliffe, showed divine tolerance when we ran over budget and behind time. Chris Thornborrow and Matthew White contributed greatly through much useful discussion and sage advice. Finally, none of this would have been possible without Dick Dalley, Phil Nelson and Neil Carmichael of Shell who believed in our idea and met the bottom line.

7 References

- Dyer, D. Scott, 1990. A dataflow toolkit for visualisation. *IEEE Computer Graphics and Applications*, 10(4):60–69.
- Flynn, Michael J., 1972 Some Computer Organisations and Their Effectiveness. *IEEE Transactions on Computers*, C-21(9):948–960.
- Gershenson, M., 1993. Simple Interpretation of Time-Domain Electromagnetic Sounding Using Similarities Between Wave and Diffusion Propagation. In proceedings of *SEG Annual International Meeting* 1993, 1342–1345. Extended Abstract number SS2.34.
- Lee, K. H. and Xie, G. Q. , 1993. A new approach to imaging with low-frequency electromagnetic fields. *Geophysics*, 58(6):780–796.
- Rasure and Kubica, 1994. The Khoros application development environment. In H.I Christensen and J.L Crowley, editors, *Experimental Environments for Computer Vision and Image Processing*. World Scientific.
- Slob, E. C., Habashy, T. M. and Torres-Verdin, C., 1995. A New Stable Numerical Procedure for Computing the Q-transform of TEM data. In proceedings of 57th Meeting, EAEG, June, 1995 Glasgow. Abstract number D053.

- Thornborrow, C., Wilson, A. J. S. and Faigle, C., 1993. Developing modular application builders to exploit MIMD parallel resources. In *Visualisation 1993*, pages 134–141. IEEE, October 1993.
- Upson, C., Faulhaber, T., Kamis, D., Laidlaw, D., Schlegel, D., Vroom, J., Gurwitz, R. and van Dam A., 1989. The application visualisation system: A computational environment for scientific visualisation. *IEEE Computer Graphics and Applications*, 9(4):30–42.
- Wilson, A. J. S., Mills, J. G. and Norman, M. G., 1991. *Bodyscan*: A transputer based 3D image analysis package. In *Applications of Transputers 3*, volume 2, pages 130–135. IOS, August 1991.
- Wilson, A. J. S. and Flockhart, I. W., 1995. Euphrates: A System for Automatic Introduction of Data Parallelism into Modular Applications. *Computer Graphics*, special issue on ‘Modular Visualisation Environments: Past, Present and Future’, 29(2):37–40.